A Lorentz microscopy study of chiral magnetic textures stabilised in thin films by an interfacial Dzyaloshinskii-Moriya interaction

Kayla Fallon

Materials and Condensed Matter Physics Group
School of Physics and Astronomy
University of Glasgow

Submitted in fufilment of the requirements for the Degree of

Doctor of Philosophy

December 2019

Abstract

The Dzyaloshinskii-Moriya interaction (DMI) is an antisymmetric exchange interaction that arises at interfaces between ferromagnets and heavy metals which possess strong spin-orbit coupling. Interface-driven DMI promotes Néel type magnetic textures with a fixed chirality, including skyrmions: particle-like magnetic objects. These chiral magnetic structures have promising properties for applications in spintronic devices. For skyrmions, these favourable properties include their small size, their fast and efficient motion under spin-polarised currents and the possibility of electrical detection. This thesis presents a number of studies on the various effects of DMI on the magnetic textures stabilised in thin films using primarily the methods of Lorentz microscopy.

The contrast expected in Lorentz microscopy from simple Néel and Bloch magnetic objects is outlined, and a theoretical method of accessing contrast directly related to the in-plane magnetisation of Néel type magnetic objects (which is not generally accessible in Lorentz microscopy) is proposed. This framework is then expanded upon to quantify 'hybrid chiral' wall structures that can be stabilised in multilayers where the DMI energy and dipolar energy are similar orders of magnitude. The presence and extent of the hybrid structure is assessed for three distinct multilayered systems and identifies a Bloch twist, indicative of hybrid chirality, in multilayers comprised of 10 and 15 repeats but not in a multilayer with five repeats. This information is critical in permitting an informed choice on the spin-injection geometry best suited for motion of the skyrmions.

Field-induced skyrmion nucleation at artificial nanoscale defects, created in a controlled and repeatable manner with focused ion beam (FIB) irradiation, was studied using Lorentz microscopy and correlated to structural information gained from standard transmission electron microscopy (TEM) images. It was found that this nucleation method has three notable advantages: (*i*) controlled localisation of nucleation; (*ii*) stability over a larger range of external field strengths, including stability at zero field; and (*iii*) existence of skyrmions in material systems where, prior to defect fabrication, skyrmions were not previously obtained by field-cycling. Additionally, it is observed that the size of defect nucleated skyrmions appears to be uninfluenced by the defect itself. All of these characteristics are expected to be useful towards the goal of realising a skyrmion-based spintronic device.

Finally the effects of DMI on magnetic vortices in planarly magnetised films are studied using micromagnetic simulations and Lorentz microscopy. Micromagnetic simulations predict that there is a DMI-dependent chiral twist (best quantified as divergence) of the magnetisation about the vortex core. Using Lorentz microscopy this effect is measured in two ways and, if attributable to DMI, the DMI strength is estimated to be $|\mathbf{D}| \approx 1$ mJm^{-2}.

Declaration

This thesis is a record of research carried out by myself within the Materials and Condensed Matter Physics group in the School of Physics and Astronomy at the University of Glasgow from 2015 - 2019. The work described herein is my own, with the exception of the following:

- Dr. Katharina Zeissler, from the University of Leeds, grew the Ir/Co/Pt-based samples studied in chapters 4 and 6 and provided the magnetometry measurements referenced in chapter 6;
- William Legrand, from CNRS/Thalés, grew the Pt/Co/Ru-based samples studied in chapters 5 and 6, provided the magnetometry measurements referenced in chapter 5 and wrote the MuMax3 scripts used as the base for the simulations presented in chapter 5;
- Sinan Azzawi, from Durham University, grew the Py-based bilayer and trilayer samples studied in chapter 7; and
- Dr. Sam McFadzean acquired the HAADF images presented in chapter 6.

Some of the work in this thesis can be found in the following papers:

1. '**Pinning and hysteresis in the field dependent diameter evolution of skyrmions in Pt/Co/Ir superlattice stacks**', K. Zeissler, M. Mruczkiewicz, S. Finizio, J. Raabe, P. M. Shepley, A. V. Sadovnikov, S. A. Nikitov, K. Fallon, S. McFadzean, S. McVitie, T. A. Moore, G. Burnell and C. H. Marrows, *Scientific Reports* **7**, 15125 (2017).
2. '**A transmission electron microscope study of Néel skyrmion magnetic textures in multilayer thin film systems with large interfacial chiral interaction**', S. McVitie, S. Hughes, K. Fallon, S. McFadzean, D. McGrouther, M. Krajnak, W. Legrand, D. Maccariello, S. Collin, K. Garcia, N. Reyren, V. Cros, A. Fert, K. Zeissler and C. H. Marrows, *Scientific Reports* **8**, 5703 (2018).

3. '**Quantitative imaging of hybrid chiral spin textures in magnetic multilayer systems by Lorentz microscopy**', K. Fallon, S. McVitie, W. Legrand, F. Ajejas, D. Maccariello, S. Collin, V. Cros and N. Reyren, *accepted for publication in Physical Review B.*

4. '**Controlled individual skyrmion nucleation at artificial defects formed by ion irradiation**', K. Fallon, S. Hughes, K. Zeissler, W.Legrand, F. Ajejas, D. Maccariello, S. McFadzean, W. Smith, D. McGrouther, S. Collin, N. Reyren, V. Cros, C. H. Marrows, and S. McVitie, *in preparation.*

This thesis has not been submitted elsewhere for any other degree or qualification.

Acknowledgements

Firstly, I would like to thank my supervisor Professor Stephen McVitie for his excellent guidance, advice and encouragement over the years. I would also like to thank Dr. Damien McGrouther for finding the time to teach, help and reassure me on the microscopes on many occasions. Similarly, I would like to thank Dr. Donald McLaren for his assistance with the AFM and for all his much appreciated and good advice. I would also like to thank Professor Bob Stamps for the insightful conversations in the early years of my time in MCMP. A massive thank you goes to Dr. Sam McFadzean for keeping all of the microscopes going despite their best efforts and always finding me new hard-drives for all that Medipix data... More recently, I would like to thank Dr. Amalio Fernández-Pacheco for being infinitely patient and understanding while I finished this thesis. I would like to thank Billy for all his help on the FIBs, and Colin for IT support and help on the T20. I'd also like to thank my examiners Dr. Ian MacLaren and Prof. Nicola Morley for making my viva far less scary than I imagined (and maybe even enjoyable...).

I would like to thank all my collaborators at CNRS/Thalés, the University of Leeds, and Durham University for all of their invaluable input; without them this work would not be possible.

I would like to thank all MCMP group members, past and present, for making my time in MCMP a good one. Special thanks goes to my office mates, Alison and Gavin, for being endlessly entertaining and restarting my computer for me more times than I can count! Special thanks also goes to all of the post docs for their helpful suggestions over the years. I'd also like to thank John in particular for all the climbing trips!

Finally, a massive thank you goes to all my friends and family. I would like to thank my Mum and Dad for their financial and emotional support and for their unwavering belief in me throughout my education. Thank you to Kristi for being my best friend and offering me endless distractions and comforts over the years. I'd also like to thank Tayte for introducing me to yoga just at the right time! I thank Matus for his love, encouragement and all the adventures on the other side of the world! And also more recently for patiently answering the question: 'Does this figure look okay?' about 100 times in the past few months... Lastly, I would like to thank all the cats (past and present) who have sat on my desk while I studied in undergrad and sat on my desk while I wrote this thesis.

Contents

List of Figures

xxx

List of Tables

List of Abbreviations

ADF . . . . . Annular dark field

AFM . . . . . Atomic force microscopy

AGFM . . . . Alternating gradient field magnetometer

BF . . . . . Bright field

BSE . . . . . Back scattered electron

CCD . . . . . Charge coupled device

CCW . . . . . Counter-clockwise

CTEM . . . . . Conventional transmission electron microscopy

CTF . . . . . Contrast transfer function

CW . . . . . Clockwise

DAC . . . . . Digital to analogue converter

DC . . . . . Direct current

DED . . . . . Direct electron detector

DF . . . . . Dark field

DMI . . . . . Dzyaloshinskii-Moriya interaction

DPC . . . . . Differential phase contrast

EDS . . . . . Energy-dispersive X-ray spectroscopy

EELS . . . . . Electron energy loss spectroscopy

FFT . . . . . Fast Fourier transform

FIB . . . . . Focused ion beam

FWHM . . . . Full-width at half-maximum

ICP . . . . . Inductively coupled plasma

GMR . . . . . Giant magnetoresistance

GPU . . . . . Graphics processing unit

HAADF . . . . High-angle annular dark field

LMIS . . . . . Liquid metal ion source

LLG . . . . . Landau-Liftshitz-Gilbert

LTEM . . . . . Lorentz transmission electron microscopy

MFM . . . . . Magnetic force microscopy

MOKE . . . . Magneto-optical Kerr effect

MRAM . . . . Magnetoresistive random access memory

PCA . . . . . Principle component analysis

PED . . . . . Precession electron diffraction

PFIB . . . . . Plasma focused electron beam

PMA . . . . . Perpendicular magnetic anisotropy

RKKY . . . . Ruderman-Kittel-Kasuya-Yosida

SAF . . . . . Synthetic antiferromagnet

SE . . . . . Secondary electron

SEM . . . . . Scanning electron microscopy

SFM . . . . . Scanning force microscopy

SNR . . . . . Signal to noise ratio

SPLEEM . . . Spin-polarised low energy electron microscopy

SPM . . . . . Scanning probe microscopy

SQUID . . . . Superconducting quantum interference device

STEM . . . . . Scanning transmission electron microscopy

STM . . . . . Scanning tunnelling microscopy

STXM . . . . . Scanning transmission X-ray microscopy

TEM . . . . . Transmission electron microscopy

XMCD . . . . X-ray magnetic circular dichroism

XRMS . . . . . X-ray resonant magnetic scattering

List of Symbols

$\mathbf{M}$	Magnetisation
χ	Magnetic susceptibility
$\mathbf{H}$	Magnetic field
$\mathcal{H}_{ex}$	Exchange energy
J	Exchange integral
$\mathbf{S}$	Spin
T_C	Curie temperature
M_s	Saturation magnetisation
M_r	Remanent magnetisation
H_c	Coercive field
$\mathbf{m}$	Reduced magnetisation ($\mathbf{m} = \mathbf{M}/M_s$)
A	Exchange stiffness
l_{ex}	Exchange length
μ_0	Permeability of free space
$\mathcal{H}_{DMI}$	Dzyaloshinskii-Moriya interaction energy
$\mathbf{D}$	Dzyaloshinskii-Moriya interaction constant
t	Thickness
$\mathcal{H}_{anis}$	Anisotropy energy
K_u	Uniaxial anisotropy constant
$\hat{\mathbf{n}}$	unit normal vector
K_v	Volume anisotropy constant
K_s	Surface anisotropy constant
$\mathbf{H_d}$	Magnetostatic field
φ	Magnetostatic potential
ρ	Volume magnetic charge

σ . . . . . Surface magnetic charge

$\mathcal{H}_{dipolar}$ . . . . . Dipolar (magnetostatic) energy

K_{eff} . . . . . Effective anisotropy constant

$\mathbf{H_{ext}}$ . . . . . Externally applied magnetic field

$\mathcal{H}_Z$ . . . . . Zeeman energy

δ . . . . . Domain wall width

w . . . . . Domain wall width parameter

λ . . . . . Wavelength

h . . . . . Planck's constant

m_0 . . . . . Rest mass (of the electron)

e . . . . . Charge (of the electron)

V . . . . . Accelerating voltage

c . . . . . Speed of light

C_S . . . . . Spherical aberration

C_C . . . . . Chromatic aberration

Z . . . . . Atomic number

$\mathbf{F_L}$ . . . . . Lorentz force

$\mathbf{v}$ . . . . . Velocity (of the electron)

$\mathbf{B}$ . . . . . Magnetic induction

β_L . . . . . Lorentz deflection

B_s . . . . . Saturation magnetic induction

ϕ . . . . . Phase shift

$\mathbf{A}$ . . . . . Magnetic vector potential

$\hbar$ . . . . . Reduced Planck's constant ($\hbar = h/2\pi$)

$\mathbf{J}$ . . . . . Current density vector

V_0 . . . . . Mean inner potential

Δ . . . . . Fresnel image defocus

α . . . . . Semi-convergence angle

ω_0 . . . . . Resonant frequency

k . . . . . Spring constant

τ . . . . . Torque

γ	Gyromagnetic ratio
κ	Damping Coefficient
$\mathbf{H_{eff}}$	Effective magnetic field
$\mathcal{H}_{total}$	Total energy
I	Image intensity
z_{lift}	Magnetic force microscopy lift height
θ, Φ	Angle (often sample tilt angle and sample rotation angle respectively)
Ψ	Angle of the internal domain wall magnetisation
p	Domain periodicity
T	Time
J	Current
n	Number of passes (ion beam)
Q_{ion}	Ion charge
A_{beam}	Area of (ion) beam at sample

1 Introduction

Over thirty years ago now, the discovery of giant magnetoresistance (GMR) [1, 2] sparked intense research into spintronics. The term spintronics, being a portmanteau of spin electronics, refers to the exploitation of the magnetic moment of electrons to provide another degree of freedom compared to conventional charge-based electronic devices. So far there are a number of notable and wide-reaching technological applications of spintronics in magnetic read heads and non-volatile magnetic random access memory (MRAM) [3].

Skyrmions are seen by many to hold great promise in the field of spintronics as information carriers. They are particle-like magnetic objects of small size (single-digit nanometer diameter skyrmions have been observed in Fe monolayers [4]), with interesting topology-related properties [5] which exhibit fast and efficient motion under spin-polarised currents [6, 7]. These properties lead many to envisage skyrmions playing a key role in high-density, low-energy spintronic devices of the future [8, 9]. They are stabilised by the Dzyaloshinskii-Moriya interaction (DMI) which arises in material systems without inversion symmetry and with strong spin-orbit coupling and fixes a chirality to the magnetic textures in the material. Though its effects were first observed in bulk non-centrosymmetric crystals, like FeGe [10] and MnSi [11] which are both B20-type crystals (see Fig. 1.1(a)), it was soon realised that DMI can also be interface-driven [12, 13] (see Fig. 1.1(b)). Interfacial

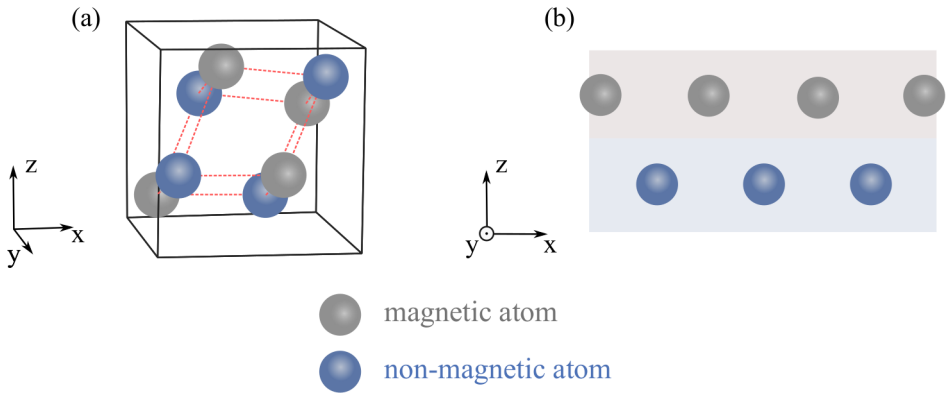

Figure 1.1: B20-type crystals and interfaces both lack symmetry and can allow non-zero DMI. (a) shows the unit cell of a cubic B20 crystal which is non-centrosymmetric and by definition has no inversion centre. (b) shows an interface which also lacks inversion symmetry with $\mathbf{z} \not\to -\mathbf{z}$.

DMI stabilises homochiral Néel walls as well as Néel type skyrmions, which both offer exciting prospects for future spintronic devices. Experimentally this interfacial DMI occurs in multilayers, where a magnetic layer is sandwiched between two dissimilar non-magnetic materials with strong spin-orbit coupling [14–16]. From an application-focused perspective, interfacial DMI is more attractive than bulk DMI because such multilayers are readily deposited using device-compatible sputtering based methods [17–19]. Furthermore multilayers are highly engineerable: the magnetic behaviour, determined by the balance of different magnetic interactions, can be controlled with layer composition and layer thickness.

With a special focus on Lorentz microscopy, this thesis will present a number of investigations into various effects of interfacial DMI in polycrystalline sputter-deposited multilayer materials. The outline of thesis thesis is given below.

Chapter 2 introduces the background physics of magnetism essential for the understanding of the results sections of this thesis. This is included together with a summary of the key outcomes of recent research on interfacial DMI stabilised magnetic objects such as homochiral domain walls and skyrmions.

Chapter 3 provides a description of the methods, experimental and simulation, that are employed in the studies presented in this thesis. This includes sample

deposition, magnetometry, focused ion beam microscopy, electron microscopy, force microscopy, micromagnetic simulations and image contrast simulations.

Chapter 4 forms the first results chapter and outlines a theoretical method to extract the handedness of Néel type domain walls directly in the transmission electron microscope (TEM) using simple one-dimensional models and Lorentz image calculations. Access to this information in the TEM is valuable as it adds to the many properties of interfacial DMI material systems that can be quantified from one session on one microscope. For example, the sign of DMI (from the wall handedness) could be determined together with the overall domain configuration, the domain wall width and relevant structural information such as the grain size and presence of defects. Experimental work is also presented, although the results are inconclusive, even after considered modifications to the experiment. As of date, measurement of Néel wall handedness in the TEM has not been realised; Lorentz microscopy can determine if walls are Néel type but the subtle image contrast which may reveal their handedness has not been successfully imaged experimentally.

Chapter 5 presents a quantitative study on 'hybrid' domain walls. To protect against thermal fluctuations, interfacial DMI systems are generally comprised of many layers stacked on top of one another. In the past year it has been noted that the increase in dipolar energy associated with many repeat layers can in fact overcome the DMI energy, leading to a flux closure three-dimensional wall structure termed a 'hybrid' wall [20–22]. This structure has important consequences on the skyrmion and wall motion under spin-polarised currents [20], therefore full quantification of this phenomenon is critical for future applications. Using Lorentz TEM, this chapter presents the first direct measurement of the Bloch type core that is characteristic of these hybrid walls. Furthermore, the number of layers over which the Bloch portion extends is quantified for a range of samples and correlated to micromagnetic simulations.

Chapter 6 presents an investigation into artificial nanoscale defects, fabricated using a focused ion beam microscope, purposed as a method of controlling skyrmion nucleation. Using the TEM, the magnetic behaviour of the magnetisation local to

defects was analysed as it evolved with an externally applied magnetic field. It was found that these artificial defects not only provide control over the location of skyrmion nucleation but increase their range of stability and even stabilise skyrmions in materials that previously supported only homochiral Néel walls, not Néel skyrmions. The magnetic behaviour of defects made with different ion doses is correlated to their structural impact on the multilayer structure.

Chapter 7 presents a curiosity-driven investigation of the DMI modification of vortex-cores in in-plane magnetised materials. Micromagnetic simulations were performed that predict an interfacial DMI induced divergent twisting of the magnetisation local to vortex cores. This is experimentally studied in micron sized Permalloy disks capped with different non-magnetic metals to both induce DMI and provide a control system with no DMI. Lowering of the external magnetic field strength required to push the vortex core out of the disks is measured together with an effective broadening of the core contrast in the TEM. With comparison to micromagnetic simulations, both of these effects provide a possible way of estimating the strength of the DMI in these materials.

The final chapter, **Chapter 8**, summarises the results of this thesis and assesses possible future research avenues.

Bibliography

[1] M. Baibich, J. Broto, A. Fert, F. Nguyrn Van Dau, and F. Petroff, "Giant Magnetorsistance of (001) Fe/(001) Cr Magnetic Superlattices," *Physical Review Letters*, vol. 61, no. 001, pp. 2472–2475, 1988.

[2] G. Binasch, P. Grünberg, F. Saurenbach, and W. Zinn, "Enhanced magnetoresistance in layered magnetic structures with antiferromagnetic interlayer exchange," *Physical Review B*, vol. 39, no. 7, pp. 4828–4830, 1989.

[3] S. Bader and S. Parkin, "Spintronics," *Annual Review of Condensed Matter Physics*, vol. 1, pp. 71–88, 2010.

[4] S. Heinze, K. Von Bergmann, M. Menzel, J. Brede, A. Kubetzka, R. Wiesendanger, G. Bihlmayer, and S. Blügel, "Spontaneous atomic-scale magnetic skyrmion lattice in two dimensions," *Nature Physics*, vol. 7, no. 9, pp. 713–718, 2011.

[5] N. Nagaosa and Y. Tokura, "Topological properties and dynamics of magnetic skyrmions," *Nature Nanotechnology*, vol. 8, no. 12, pp. 899–911, 2013.

[6] X. Z. Yu, N. Kanazawa, W. Z. Zhang, T. Nagai, T. Hara, K. Kimoto, Y. Matsui, Y. Onose, and Y. Tokura, "Skyrmion flow near room temperature in an ultralow current density," *Nature Communications*, vol. 3, no. 988, 2012.

[7] F. Jonietz, "Spin transfer torques in MnSi at ultralow current densities (Science (2010) (1648))," *Science*, vol. 333, no. 6048, p. 1381, 2011.

[8] N. S. Kiselev, A. N. Bogdanov, R. Schäfer, and U. K. Röler, "Chiral skyrmions in thin magnetic films: New objects for magnetic storage technologies?," *Journal of Physics D: Applied Physics*, vol. 44, no. 39, 2011.

[9] A. Fert, V. Cros, and J. Sampaio, "Skyrmions on the track," *Nature Nanotechnology*, vol. 8, no. 3, pp. 152–156, 2013.

[10] M. Richardson, O. Beckman, V. Attia, and S. P. Bhattacherjee, "Helical Spin Arrangement in Cubic Fege," *Physica Scripta*, vol. 1, no. 1, pp. 69–72, 1970.

[11] Y. Ishikawa, K. Tajima, D. Bloch, and M. Roth, "Helical spin structure in manganese silicide MnSi," *Solid State Communications*, vol. 19, no. 6, pp. 525–528, 1976.

[12] A. Fert, "Magnetic and transport properties of metallic multilayers," in *Materials Science Forum*, vol. 59, pp. 439–480, 1990.

[13] A. Crépieux and C. Lacroix, "Dzyaloshinsky-Moriya interactions induced by symmetry breaking at a surface," *Journal of magnetism and magnetic materials*, vol. 182, no. 3, pp. 341–349, 1998.

[14] M. Bode, M. Heide, K. Von Bergmann, P. Ferriani, S. Heinze, G. Bihlmayer, A. Kubetzka, O. Pietzsch, S. Blügel, and R. Wiesendanger, "Chiral magnetic order at surfaces driven by inversion asymmetry," *Nature*, vol. 447, no. 7141, pp. 190–193, 2007.

[15] S. Heinze, K. Von Bergmann, M. Menzel, J. Brede, A. Kubetzka, R. Wiesendanger, G. Bihlmayer, and S. Blügel, "Spontaneous atomic-scale magnetic skyrmion lattice in two dimensions," *Nature Physics*, vol. 7, no. 9, pp. 713–718, 2011.

[16] A. Fert, N. Reyren, and V. Cros, "Magnetic skyrmions: Advances in physics and potential applications," *Nature Reviews Materials*, vol. 2, p. 17031, 2017.

[17] A. Hrabec, N. A. Porter, A. Wells, M. J. Benitez, G. Burnell, S. McVitie, D. McGrouther, T. A. Moore, and C. H. Marrows, "Measuring and tailoring the Dzyaloshinskii-Moriya interaction in perpendicularly magnetized thin films," *Physical Review B - Condensed Matter and Materials Physics*, vol. 90, no. 2, 2014.

[18] C. Moreau-Luchaire, C. Moutafis, N. Reyren, J. Sampaio, C. A. Vaz, N. Van Horne, K. Bouzehouane, K. Garcia, C. Deranlot, P. Warnicke, P. Wohlhüter, J. M. George, M. Weigand, J. Raabe, V. Cros, and A. Fert, "Additive interfacial chiral interaction in multilayers for stabilization of small individual skyrmions at room temperature," *Nature Nanotechnology*, vol. 11, no. 5, pp. 444–448, 2016.

[19] K. Zeissler, M. Mruczkiewicz, S. Finizio, J. Raabe, P. M. Shepley, A. V. Sadovnikov, S. A. Nikitov, K. Fallon, S. McFadzean, S. McVitie, T. A. Moore, G. Burnell, and C. H. Marrows, "Pinning and hysteresis in the field dependent diameter evolution of skyrmions in Pt/Co/Ir superlattice stacks," *Scientific Reports*, vol. 7, no. 1, pp. 1–9, 2017.

[20] W. Legrand, J. Y. Chauleau, D. Maccariello, N. Reyren, S. Collin, K. Bouzehouane, N. Jaouen, V. Cros, and A. Fert, "Hybrid chiral domain walls and skyrmions in magnetic multilayers," *Science Advances*, vol. 4, no. 7, 2018.

[21] Y. Dovzhenko, F. Casola, S. Schlotter, T. X. Zhou, F. Büttner, R. L. Walsworth, G. S. Beach, and A. Yacoby, "Magnetostatic twists in room-temperature skyrmions explored by nitrogen-vacancy center spin texture reconstruction," *Nature Communications*, vol. 9, no. 1, pp. 1–7, 2018.

[22] I. Lemesh and G. S. Beach, "Twisted domain walls and skyrmions in perpendicularly magnetized multilayers," *Physical Review B*, vol. 98, no. 10, pp. 1–8, 2018.

2

The basic physics of chiral magnetism in thin films

Contents

In this chapter, the fundamentals of magnetism are briefly introduced, before the different energetic interactions (present in the multilayers studied in this work) are each described in turn. The interplay of these interactions explains the stabilisation of the various magnetic objects encountered in this thesis such as the different types of domain wall, flux-closure vortex structures and skyrmions. A discussion of the key features and properties of these magnetic structures, together with their manipulation using spin-polarised currents, forms the last topic of this chapter.

2.1 The fundamentals of ferromagnetism

The magnetic properties of a material originate from the relative orientation of the magnetic moments of the atoms constituting the material. The magnetic moments themselves originate from the intrinsic spin and orbital angular momentum of the electrons in the atom. By Ampére's circuital law, each electron in an atomic orbital may be considered a classical current loop with an associated magnetic moment [1]. As all materials contain electrons, all materials exhibit some sort of magnetism.

In materials where the constituent atoms or ions have partially filled orbitals with unpaired electrons, each atom or ion has a net magnetic moment. These materials can be divided into two catagories: paramagnetic and magnetically ordered. In a paramagnetic materials the net magnetic moment on each atom is randomly oriented and in the absence of external magnetic fields the magnetisation $\mathbf{M}$, that is the net magnetic moment per unit volume, is zero (see Fig. 2.1(a)). However, all paramagnetic materials exhibit a net magnetisation proportional to the applied magnetic field. The magnetic response of a material to an external magnetic field $\mathbf{H}$ can be described by its susceptibility χ where:

$$\mathbf{M} = \chi \mathbf{H}. \tag{2.1}$$

Typical values of χ for a paramagnet are $\approx 10^{-5}$. Materials that possess 'spontaneous' magnetisation (that is alignment of magnetic moments in the absence of

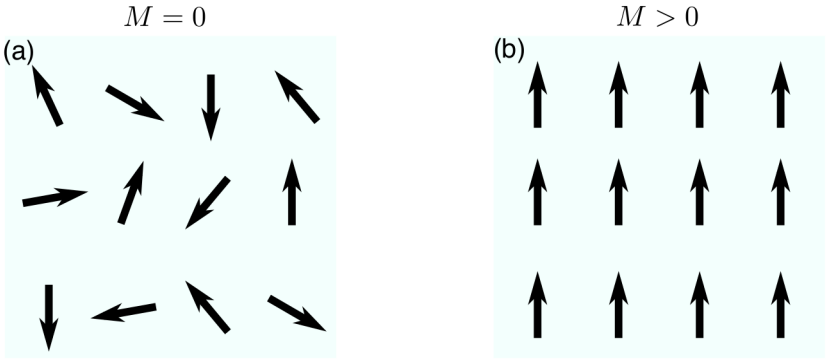

Figure 2.1: (a) The random alignment of magnetic moments in a paramagnet without any applied field. (b) The spontaneous, collinear alignment of magnetic moments in a ferromagnet.

any aligning external magnetic fields) are known as ferromagnets[1]. In ferromagnets, neighbouring magnetic moments are strongly coupled and prefer to align parallel as is sketched in Fig. 2.1(b). The magnetic susceptibility of a ferromagnet is about five orders of magnitude larger than in a paramagnet. The spontaneous alignment of magnetic moments in a ferromagnetic was explained by Heisenberg through a quantum mechanical exchange interaction [2], the Hamiltonian of which is given by

$$\mathcal{H}_{ex} = -\sum_{i<j} 2J_{ij}(\mathbf{S_i} \cdot \mathbf{S_j}). \tag{2.2}$$

In this equation J_{ij} is the material dependent exchange integral and the sum is over all interacting spins S_i and S_j. In a ferromagnet J_{ij} is positive, and it is clear that H_{ex} is minimised by parallel spins.

In ferromagnets the magnetisation is always at least locally aligned in regions called domains (which are further discussed in sections 2.2.5 and 2.3.1). The relative orientation of different domains and their reorientation in an external field leads to a complex, non-linear relationship between **M** and **H** that is concisely described by a hysteresis loop. An example of a hysteresis loop is sketched in Fig. 2.2(a), on which some key properties of ferromagnets are labelled. The magnetisation of a ferromagnet in an external magnetic field **H** reaches a maximum value known as its saturation magnetisation M_s (where all moments and domains are aligned) at some finite field external strength. The degree of magnetisation that remains when the external field is removed is called the remanent magnetisation M_r and the extra external field required bring the magnetisation back to zero is the coercive field H_c. The shape and properties of a hysteresis loop depend on both the material and its geometry.

Moreover, the saturation magnetisation of a ferromagnet is a function of temperature, and is maximum at absolute zero and reaches zero at a critical temperature known as the Curie temperature T_C. Above T_C, the thermal fluctuations destroy the alignment of the magnetic moments and the ferromagnet behaves like a paramagnet. The relationship of M_s with temperature is sketched in Fig. 2.2(b).

[1]There are, of course, different types of magnetic ordering but this thesis deals exclusively with ferromagnets therefore only ferromagnetic ordering is discussed.

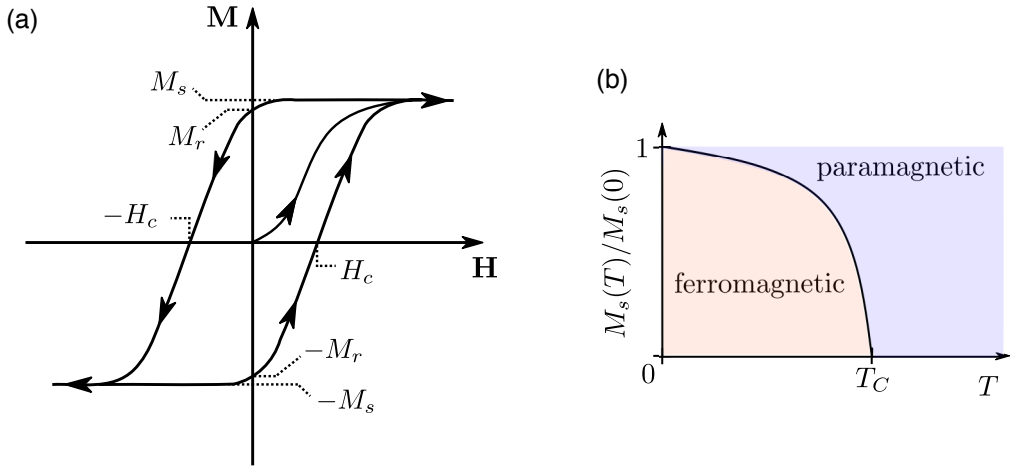

Figure 2.2: (a) A hysteresis loop showing the characteristic variance of the magnetiastion **M** of a ferromagnetic material in an applied magnetic field **H**. Key properties of the magnetic material are annotated on the loop which are further discussed in the main text. (b) The temperature variance of the magnetism of a ferromagnet is sketched: above the Curie temperature, T_c, ferromagnetic order is lost and replaced with paramagnetism.

From the transition metals Co, Ni, Fe and their alloys have sufficiently high T_C to exhibit ferromagnetism at room temperature. The rare earth metal Gd is almost ferromagnetic at room temperature with $T_C \approx 20$ °C.

2.2 Magnetic energy terms

The complex magnetic behaviour of ferromagnets is best described by the interplay of different energy terms. In each distinct material system, under different external conditions, some energy terms are stronger than others (or absent altogether). This leads to the diverse range of magnetic textures found in ferromagnets. The energy terms that underpin the magnetic behaviour of the samples studied in this thesis are ferromagnetic exchange, DMI, Ruderman-Kittle-Kasuya-Yosida (RKKY), anisotropy, dipolar and Zeeman energies. In this section the origin of each is discussed and then placed in the micromagnetic framework.

The micromagnetic framework is a continuum approximation which ignores atomic scale variations in the magnetisation [3]. The magnetisation is instead described by a smooth function $\mathbf{M}(\mathbf{r}) = M_s\mathbf{m}(\mathbf{r})$ where $|\mathbf{m}(\mathbf{r})| = 1$. This is justified by the fact that the magnetisation varies more slowly than the interatomic distances

and that, in a ferromagnet, the magnitude of the magnetic moment on each atom is fixed and simply varies in orientation [4]. The magnetic interactions that are quantum mechanical in origin (exchange, DMI, anisotropy) must be adapted to fit into the micromagnetic framework.

2.2.1 Exchange interaction

As already mentioned, the exchange interaction explains the energetic preferability of parallel spin alignment in a ferromagnet. The fundamental origin of this interaction is Coloumb repulsion between two particles with overlapping wavefuctions. Equation 2.2 provides a microscopic description of the exchange interaction. It must be noted that Heisenbergs model of the exchange interaction assumes localised spins. In transision metal ferromagnets, this assumption does not hold but nevertheless the Heisenberg formalism remains accurate to the first order and is widely used [5].

In the micromagnetic framework, the exchange energy is given by:

$$\mathcal{H}_{ex} = A \int_V (\nabla \mathbf{m})^2 \, dV \tag{2.3}$$

where A is the exchange stiffness (which is proportional to the exchange integral J of Eq. 2.2); $\nabla \mathbf{m}$ is the gradient of the magnetisation; and V is the total volume of the magnetic material. From the gradient operator in Eq. 2.3, it is clear that any deviation from parallel alignment is associated with an energy cost; however, the exchange interaction is completely isotropic therefore the direction of any deviation is of no additional impact.

The magnitude of A does vary somewhat with thickness: it is reduced in ultrathin films before building to a bulk value. For example, an experimental study found a steady increase of A with Co layer thickness before saturating at the bulk value at a Co thickness of around 7 nm [6]. To provide some examples, in the bulk limit, A $\approx$ 20 pJm^{-1} for Co [7] and $\approx$ 10 pJm^{-1} for Permalloy ($Ni_{20}Fe_{80}$) [8].

The exchange stiffness defines another useful parameter that describes ferromagnetic materials: the exchange length l_{ex}. The exchange length approximates the

distance over which the direction of the magnetisation of the material is constant, it is given by:

$$l_{ex} = \sqrt{\frac{2A}{\mu_0 {M_s}^2}}\,, \tag{2.4}$$

where μ_0 is the permeability of free space ($\mu_0 = 4\pi \times 10^{-7}$ Hm^{-1}). The exchange length varies with the material; for Permalloy a typical value is around 5 nm, and for Co about 4 nm.

2.2.2 Dzyaloshinskii-Moriya interaction

The Dzyaloshinskii-Moriya interaction (DMI) [9, 10], already introduced in Chapter 1, is present in all magnetic systems investigated as part of this thesis. Consequently, it is discussed in more depth than the other magnetic interactions. It is the driving force behind the spontaneous chiral order some magnetic materials exhibit. The Hamiltonian of the DMI interaction is:

$$\mathcal{H}_{DMI} = -\sum_{i<j} \mathbf{D_{ij}} \cdot (\mathbf{S_i} \times \mathbf{S_j}) \tag{2.5}$$

where $\mathbf{D_{ij}}$ is the DMI vector. It is clear from the form of Eq. 2.5, that the DMI energy is minimised by perpendicular alignment of neighbouring spins that rotate around the DMI vector like $\leftarrow \cdot \downarrow$ or $\leftarrow \cdot \uparrow$ where the dot represents a DMI vector normal to the page. The sense of rotation, that is clockwise ($\leftarrow\uparrow$) or counter-clockwise ($\leftarrow\downarrow$), is determined by the sign of the DMI vector. Currently the sign convention is such that positive $\mathbf{D}$ corresponds to a counter-clockwise rotation [11].

DMI is the result of strong spin-orbit coupling in low-symmetry crystalline environments. The direction of $\mathbf{D}$ is determined by the symmetry of the system. The direction of $\mathbf{D_{ij}}$, arising from two ferromagnetic atoms with spins $\mathbf{S_i}$ and $\mathbf{S_j}$ spin-orbit coupled to a third non-magnetic atom (that breaks the symmetry), was succinctly derived by Levy and Fert [12] to be $\mathbf{D_{ij}} = D_{ij}(\hat{\mathbf{r}}_\mathbf{i} \times \hat{\mathbf{r}}_\mathbf{j})$ where $\hat{\mathbf{r}}_\mathbf{i}$ and $\hat{\mathbf{r}}_\mathbf{j}$ are unit vectors between the ferromagnetic atoms and the non-magnetic atom. This is sketched in Fig. 2.3.

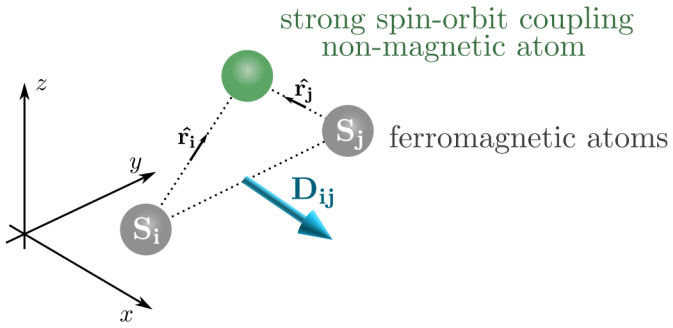

Figure 2.3: The direction of the DMI vector $\mathbf{D_{ij}}$ between two ferromagnetic atoms at sites i and j coupled to a non-magnetic atom is given by $(\hat{\mathbf{r}}_\mathbf{i} \times \hat{\mathbf{r}}_\mathbf{j})$. Equivalently, $\mathbf{D_{ij}}$ is normal to the triangle connecting the three atomic sites.

The effects of DMI are observed both in non-centrosymmetric crystals with an underlying lack of symmetry [13, 14] and in multilayers at interfaces which also naturally lack symmetry inversion [15, 16]. Respectively, these two flavours of DMI are known as bulk and interfacial DMI. The geometry of symmetry breaking that is responsible for bulk and interfacial DMI is different and therefore the direction of $\mathbf{D}$ with respect to a row of ferromagnetic atoms is different. Consequently, bulk and interfacial DMIs are responsible for different types of chiral order in magnetic systems (this is elaborated on in section 2.3.2).

DMI does not exist on its own. It competes directly with the standard ferromagnetic exchange interaction. The energetic compromise between the two is a gradual rotation of the magnetisation around the $\mathbf{D}$ vector. The tightness of this rotation depends on the relative strengths of the interactions (in the systems studied in this thesis DMI is normally around an order of magnitude smaller than the exchange interaction). For interfacial DMI, the $\mathbf{D}$ vector is parallel to the interface and the magnetisation rotates gradually around this vector. This is sketched in Fig. 2.4 where panels (a) and (b) show two bilayer systems composed of a ferromagnet and a heavy metal associated with (a) positive $\mathbf{D}$ and (b) negative $\mathbf{D}$ that introduce rotations with opposite chiralities. Pt/Co an example of an interface associated with positive $\mathbf{D}$ and Ir/Co with negative $\mathbf{D}$ [17, 18]. From Figs. 2.4(a,b) it should also be clear that reversing the stacking order of the layers inverts $\mathbf{D}$. The effect is utilised to boost the effective DMI strength by including different metals on the top

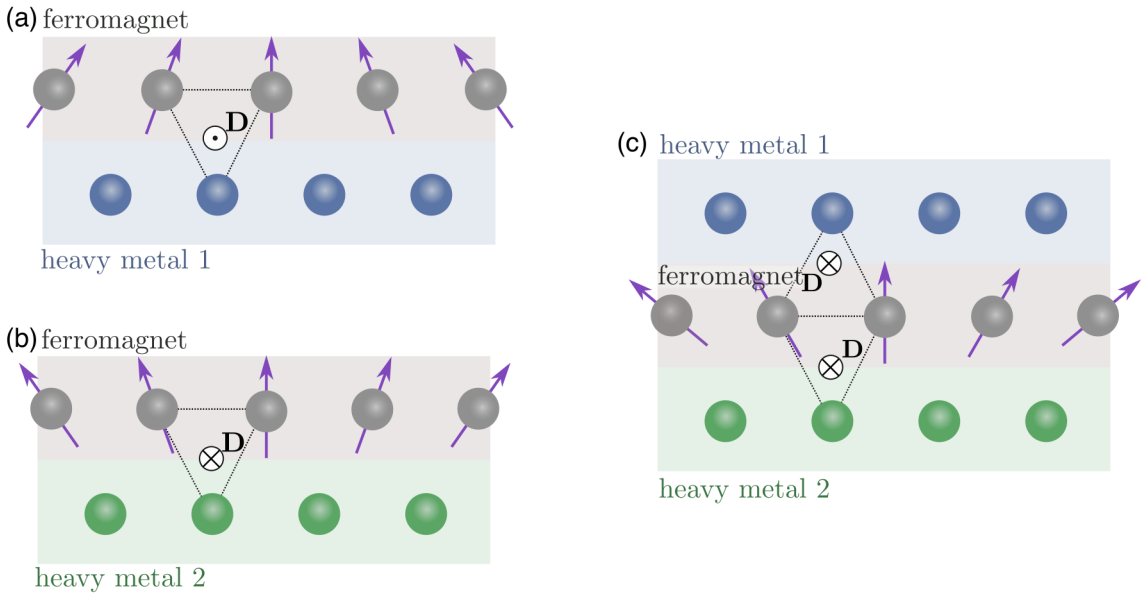

Figure 2.4: Sketches of the spin canting that results from an interface associated with (a) positive **D** and (b) negative **D**. (c) Two different metals can be combined on the top and bottom of an ferromagnet such that the DMI interaction from the two interfaces is of the same sign and combines additively.

and bottom of the ferromagnet, so the DMI from the interfaces is of the same sign and therefore 'additive' [19, 20]. Pt/Co/Ir is a typical example. This combination of interfaces is associated with $|\mathbf{D}| \approx 2$ mJm^{-2} [20]. Strong DMI of about 2 mJm^{-2} is also in found in systems based on oxides such as Pt/Co/MgO [21].

In the micromagnetic framework, the interfacial DMI energy is given by [22]:

$$\mathcal{H}_{DMI} = |\mathbf{D}| \int_V m_z(\nabla \cdot \mathbf{m}) - (\mathbf{m} \cdot \nabla) m_z \, dV, \tag{2.6}$$

where z is the direction perpendicular to the plane of the interface.

2.2.3 Ruderman-Kittel-Kasuya-Yosida interaction

The Ruderman-Kittel-Kasuya-Yosida (RKKY) interaction is an indirect exchange interaction that is responsible for long-range exchange coupling between two physically separate magnetic moments. The fundamental origin of the RKKY interaction is as follows: two magnetic moments, physically separated by some distance, couple to one another by spin-polarising the conduction electrons between the two moments [23]. Interestingly, the sign of this coupling oscillates with the distance

between the magnet moments and therefore switches between antiferromagnetic (↑↓) and ferromagnetic (↑↑) coupling.

The RKKY interaction is utilised in multilayer systems, where the exchange coupling between two ferromagnetic layers separated by a non-magnetic metal spacer layer of thickness t is tuned by varying t. The oscillatory variation of the interlayer exchange coupling J_{RKKY} with spacer layer thickness t is sketched in Fig. 2.5. RKKY coupling of separate magnetic layers is used to create synthetic antiferromagnets [24–26] and is one of the main components of GMR systems [27, 28]. In this thesis, RKKY coupling (using a Ru spacer layer) is used to control the strength of the (ferromagnetic) coupling between the Co layers of the samples studied in Chapter 5.

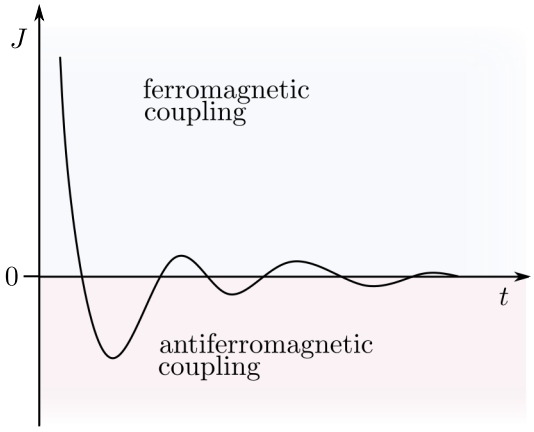

Figure 2.5: This is a sketch of the generic form of the RKKY interaction is responsible for indirect exchange coupling between to ferromagnetic layers separated by a non-magnetic spacer of thickness t. The coupling flips between ferromagnetic type and antiferromagnetic type with spacer layer thickness t.

2.2.4 Magnetocrystalline anisotropy

Like DMI, magnetocrystalline anisotropy arises from spin-orbit interactions. In this case, spin-orbit interactions couple the magnetic moment to specific directions in the crystal lattice. The resultant effect is an energetic dependence on the orientation of the magnetic moment with respect to the underlying crystal symmetry. The magnetisation direction associated with low energy is called the 'easy' axis where, conversely, the direction associated with high energy is called the 'hard'

axis. Restricting the discussion to uniaxial anisotropy, the general form of the anisotropy energy is:

$$\mathcal{H}_{anis} = -\int_V K_u(\mathbf{u}\cdot\mathbf{m})^2\,dV, \tag{2.7}$$

where $\mathbf{u}$ is the unique axis that it is preferable for the magnetisation to align with. When considering thin films, $\mathbf{u}$ is generally the sample normal $\hat{\mathbf{n}}$ and $\mathcal{H}_{anis}$ is expressed as:

$$\mathcal{H}_{anis} = -\int_V K_u(\hat{\mathbf{n}}\cdot\mathbf{m})^2\,dV. \tag{2.8}$$

In this form, $K_u < 0$ (> 0) corresponds to an in-plane (perpendicular) easy axis [29].

It is well known that magnetocrystalline anisotropy is enhanced local to interfaces because of the lowered symmetry [30]. The total anisotropy K_u, comprised of bulk and surface contributions, can be expressed phenomenologically as:

$$K_u = K_v + \frac{K_s}{t}, \tag{2.9}$$

where K_v is the bulk anisotropy constant, K_s is the surface anisotropy constant and t is the thickness of the ferromagnet. Typical value of K_v in (hcp) Co is -0.53 MJm^{-3} [31]. However, K_v is only significant in single crystal environments. In polycrystalline materials, studied exclusively in this thesis, the random orientation of the grains results in no global volume magnetocrystalline anisotropy. The volume magnetocrystalline anisotropy of each individual, but randomly oriented, grain does cause local fluctuations in the magnetisation direction known as magnetisation ripple [32, 33].

The enhanced spin-orbit coupling at interfaces with heavy metals can significantly increase K_s [34]. For example, typical values of K_s at a Co/Pt interface are ≈ 0.5 mJm^{-2} while at a Co/Vacuum surface K_s is ≈ 0.2 mJm^{-2} [34]. With sufficiently small magnetic layer thickness t, and assuming dipolar interactions (introduced in the following section) are comparatively small, the surface term will dominate. When this happens the material is said to have perpendicular magnetic anisotropy (PMA). All but one of the skyrmionic multilayers have PMA and support out-of-plane magnetisation.

The other material studied in this thesis, that is 8 nm thick polycrystalline Py, has $K_u \approx 0$. As previously mentioned, in polycrystalline films, considered as a whole, K_v is negligible; and at a thickness of 8 nm, the surface anisotropy term is very small. The magnetisation of 8 nm thick Py therefore lies in-plane because of 'shape' anisotropy. The origin of this is dipolar interactions, described next.

2.2.5 Dipolar interaction

Individual magnetic moments in a magnetic material all interact with each other through dipole-dipole interactions. Dipolar interactions are long-range. Rather than considering the effect of every magnetic moment on every other magnetic moment, a magnetostatic field $\mathbf{H_d}$ is defined where:

$$H_d = -\nabla\varphi, \tag{2.10}$$

and φ is the magnetostatic potential which is itself given by:

$$\varphi(\mathbf{r}) = \frac{1}{4\pi}\left[\int_{V'} \frac{-M_s(\nabla\cdot\mathbf{m})}{|\mathbf{r}-\mathbf{r}'|}\,dV' + \int_{S'} \frac{M_s(\mathbf{m}\cdot\hat{\mathbf{n}})}{|\mathbf{r}-\mathbf{r}'|}\,dS'\right], \tag{2.11}$$

where $\mathbf{r}$ is the position vector of the point where φ is calculated, $\mathbf{r}'$ is the position vector representing all other points, and S is the surface of the magnetic material. The magnetostatic field is both external to the sample (where it is known as the stray field) and internal (where it is known as the demagnetising field). The origin of $\mathbf{H_d}$ is the magnetic 'charge' density. Equation 2.11 features a volume charge term: $\rho = -M_s(\nabla\cdot\mathbf{m})$; and a surface charge term: $\sigma = M_s(\mathbf{m}\cdot\hat{\mathbf{n}})$. The dipolar (or magnetostatic) energy is given by:

$$\mathcal{H}_{dipolar} = -\frac{\mu_0 M_s}{2}\int_V \mathbf{H_d}\cdot\mathbf{m}\,dV. \tag{2.12}$$

Thus it is clear that the dipolar energy is minimised by reducing $\mathbf{H_d}$ which in turn is achieved by minimising the magnetic charge density. This is one of the principal reasons for domain formation in magnetic materials. Domains (covered in section 2.3.1) are finite regions (generally on the order of μms) of uniform magnetisation. A ferromagnet is generally composed of many domains oriented at some angle relative to each other to minimise the dipolar energy.

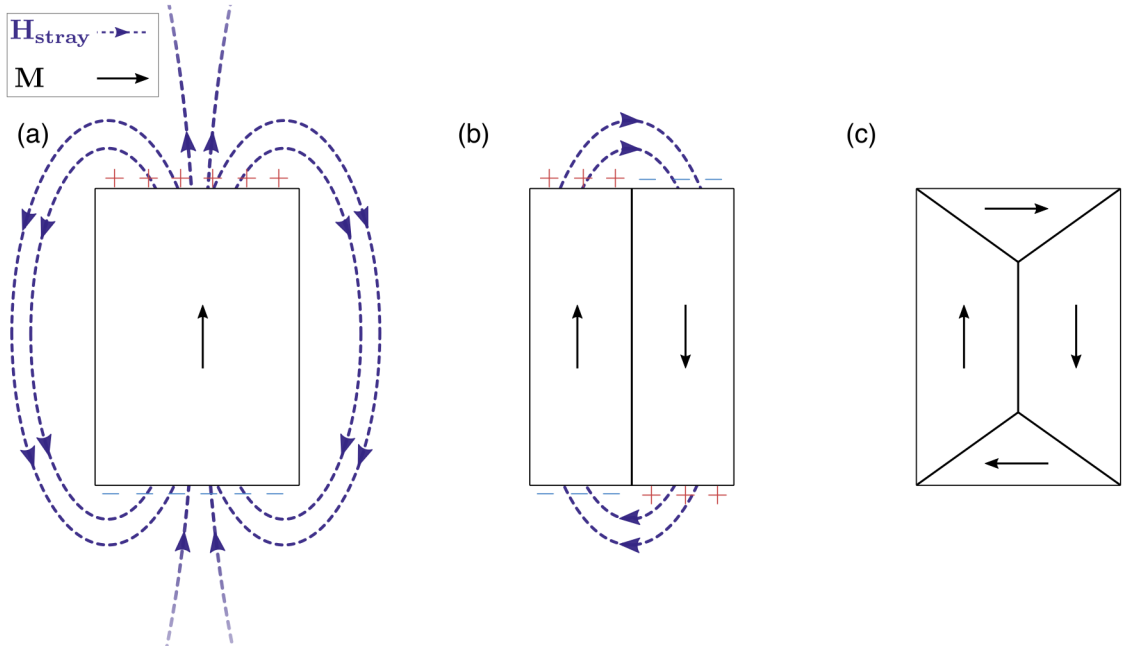

Figure 2.6: By splitting into domains, magnetic charges are redistributed and the stray field $\mathbf{H}_{\mathbf{stray}}$ is reduced. Reduction of $\mathbf{H}_{\mathbf{stray}}$ corresponds to a reduction in dipolar energy. (a) shows a single domain state associated with large dipolar energy, (b) shows a two domain state typical of a material with uniaxial anisotropy, and (c) shows a flux closure state expected in a material without magnetocrystalline anisotropy. From left to right, these magnetic state are associated with decreasing dipolar energy.

Figure 2.6(a) shows the stray field generated by a single domain state. This state is associated with a large dipolar energy and would only be stable in a large external field or if the material had a very large uniaxial anisotropy. Without these constraints, the system splits up into domains as shown in Fig. 2.6(b) and (c). Fig. 2.6(b) depicts the domain configuration expected in a material with uniaxial magnetocrystalline anisotropy parallel to the long axis of the rectangle, where the dipolar energy is reduced at the expense of the exchange energy. In the absence of magnetocrystalline anisotropy, flux closure magnetic states are generally most stable. Here there are few surface charges and consequently little stray field.

As well as the formation of domains, the dipolar energy is also responsible for 'shape' anisotropy. As with magnetocrystalline anisotropy discussed in section 2.2.4, this means the energy varies with the magnetisation direction although, because of the magnetostatic origin, it arises from the long-range alignment and depends on the boundaries of the material. It is prominent in materials with negligible

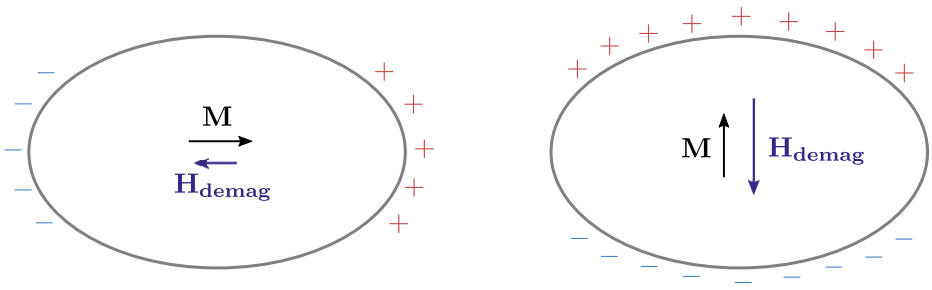

Figure 2.7: The dipolar energy an elliptical element depends on whether the magnetisation at that lies along the long or short axis of the ellipse. This is an example of shape anisotropy where the configuration on the left hand side is preferred.

magnetocrystalline anisotropy that are physically small (or thin) with a high surface to volume ratio where the second term in Eq. 2.11 - $\int_{S'} M_s(\mathbf{m}\cdot\hat{\mathbf{n}})\,dS'$ - can be a dominant source of energy. The Py samples studied in Chapter 7 have strong in-plane shape anisotropy.

The typical example of shape anisotropy is that of a uniformly magnetised ellipse, sketched in Fig. 2.7, where the dipolar energy is lowered if the magnetisation lies along the long axis of the ellipse. A perfect sphere is the only geometry without shape anisotropy. In magnetic thin films there is in-plane shape anisotropy which competes with the magnetocrystalline anisotropy, reducing the anisotropy K_u to an effective anisotropy K_{eff} [34]:

$$K_{eff} = K_u - \frac{\mu_0 {M_s}^2}{2}. \tag{2.13}$$

Typical values of this dipolar term are 1.86, 1.27 and 0.14 MJm^{-3} for Fe, Co and Ni, respectively [34]. When $K_u < \frac{1}{2}\,\mu_0 M_s^2$ i.e. the shape anisotropy dominates, the magnetisation lies in plane - this the case with the Py samples studied in this thesis.

2.2.6 Zeeman interaction

There is an energetic preference for the magnetisation to align with an externally applied magnetic field $\mathbf{H_{ext}}$. The Hamiltonian of the Zeeman interaction is as follows:

$$\mathcal{H}_Z = \mu_0 M_s \int_V (\mathbf{m}\cdot\mathbf{H_{ext}})\,dV \tag{2.14}$$

Practically, for a multidomain state, the effect of the Zeeman interaction is to enlarge domains aligned with the $\mathbf{H_{ext}}$ while shrinking domains opposed to $\mathbf{H_{ext}}$,

this is sketched in Fig. 2.8. At a sufficiently high $\mathbf{H_{ext}}$, the Zeeman energy term fully dominates the energetics of the material causing the magnetisation to be completely aligned (saturated) with $\mathbf{H_{ext}}$.

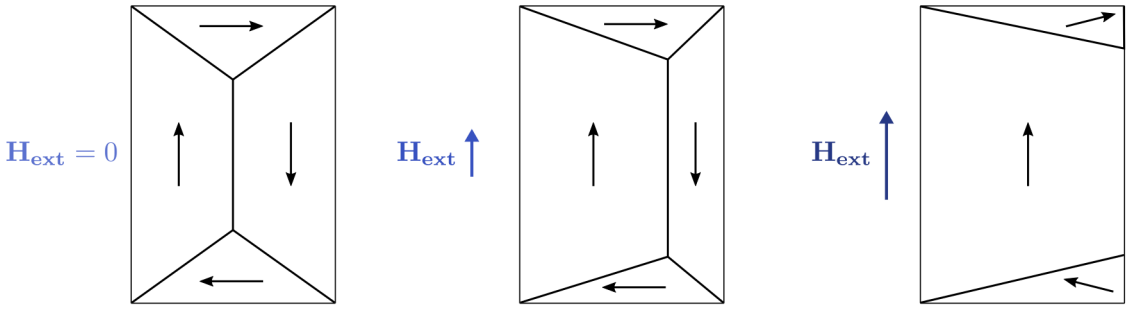

Figure 2.8: The effect of the Zeeman interaction on a multidomain magnetic configuration is to enlarge domains aligned with the external field $\mathbf{H_{ext}}$ while reducing the size of the other domains. Eventually the magnetisation by fully aligned with $\mathbf{H_{ext}}$.

2.3 Magnetic structures

In magnetic materials, the magnetic configuration depends on the energetic interplay of the different interactions. Interestingly, the multiple interactions are often of similar orders of magnitude and all somewhat influence the magnetic state supported. To summarise the most fundamental interactions: the 'direct' exchange likes neighbouring spins to be parallel, anisotropy fixes a direction of minimum energy, and the dipolar interactions like to minimise stray field generation. The exchange and dipolar energies result in the formation of finite regions of uniform magnetisation called 'domains', and generally the direction of the domains is influenced by the anisotropy. Systems with DMI add some chiral texture to the magnetisation.

Another degree of freedom is the nature of the transition between domains called domain walls. In this section, conventional domain wall structures are covered before discussing 'chiral' domain walls and skyrmions that occur in systems with DMI.

2.3.1 Domains and domain walls

In continuous thin films there are two main types of domain wall: Bloch and Néel. The two type are differentiated by a different class of rotation (with respect to the domains) as is sketched in fig. 2.9. Figure 2.9 depicts a single row of magnetic moments transitioning from pointing along $+z$ on the left to $-z$ on the right, this transition represents a 'domain wall' that by convention is defined as running along the $\pm x$ direction.

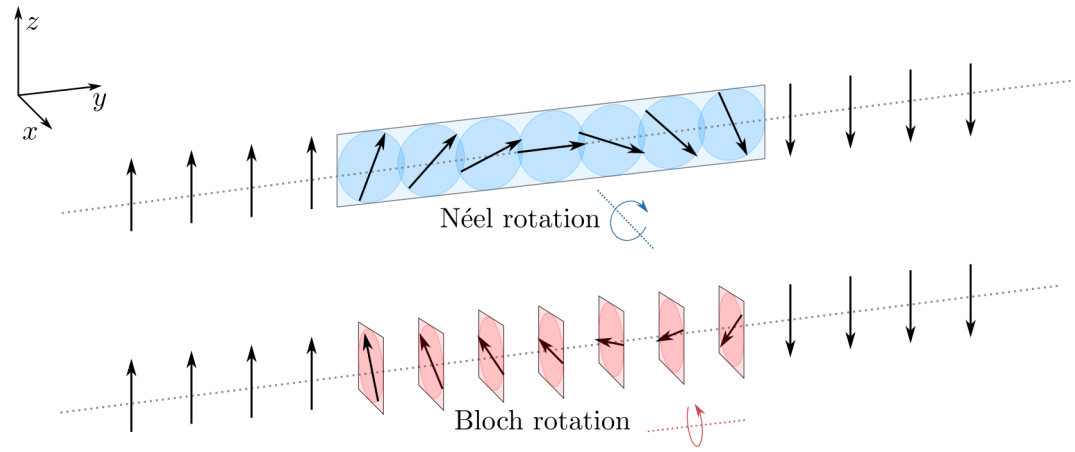

Figure 2.9: Schematic of the rotation of magnetisation associated with (top) a Néel type magnetic structure and (bottom) a Bloch type magnetic structure

In a Néel rotation, sketched in the top half of Fig. 2.9, the magnetisation twists through a single plane from the 'domain' spins along $\pm z$, around an axis perpendicular to the wall. In a Bloch rotation, sketched in the bottom half of Fig. 2.9, the magnetisation twists around an axis parallel to the wall. The magnetisation of a Bloch type rotation is divergence-less where Néel type rotations are divergent.

The type of domain wall that is energetically efficient for a given system depends on the orientation of the domains (in-plane or out-of-plane as determined by the anisotropy) and the thickness of the magnetic material. In figure 2.10, the four possible magnetisation configurations formed with two domain orientations and two wall types are sketched. The existence and position of magnetic charges is included on the diagrams. In all cases, the favoured wall type is the one that permits the largest separation of magnetic charges.

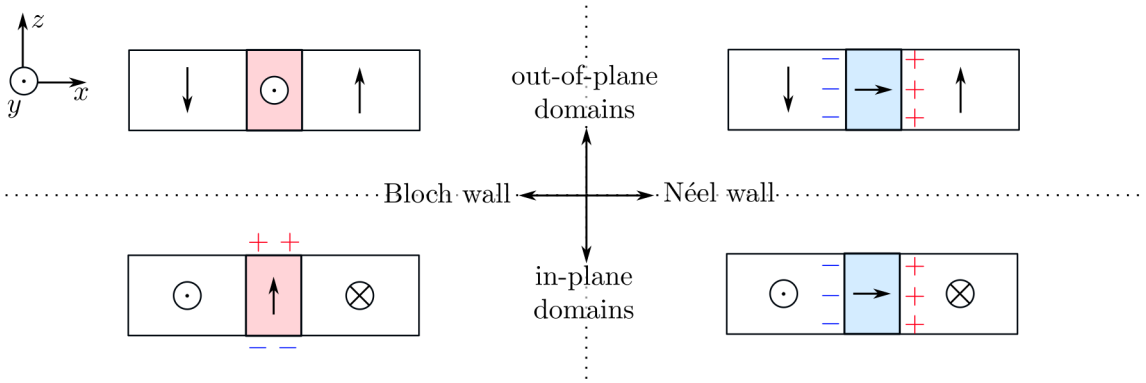

Figure 2.10: Sketches of the magnetsation and magnetic charge distribution of magnetic configurations with (starting top left and moving clockwise) out-of-plane domains with a Bloch type wall, out-of-plane domains with a Néel type wall, in-plane domains with a Bloch type wall and in-plane domains with a Néel type wall

First considering the case of in-plane domains, sketched in the lower half of Fig. 2.10, Bloch type walls result in surface magnetic charges where Néel walls result in volume magnetic charges. Therefore, simply based on maximal separation of magnetic charges, there is a threshold thickness above which Bloch walls are favoured and below which Néel walls are favoured. In Permalloy, this transition occurs at a thickness of around 60 nm [3], therefore the Py samples studied in Chapter 7 have Néel walls. It should be mentioned that around this transition 'cross-tie' walls are supported. These are more complex two-dimensional wall structures that are composed of both Bloch and Néel type rotations but are not observed in the thin film systems studied in this thesis.

When the domains are out-of-plane, sketched in the upper half of Fig. 2.10, Bloch walls are favoured this because, in this configuration, the Bloch wall is effectively charge-less. A significant DMI interaction changes this situation but discussion of this is left to the following section.

Domain wall width

There are many definitions of the domain 'wall width' because domain walls represent continuous transitions between domains [35]. Without detailing the other definitions, the precise definition of the domain wall width δ implemented in this

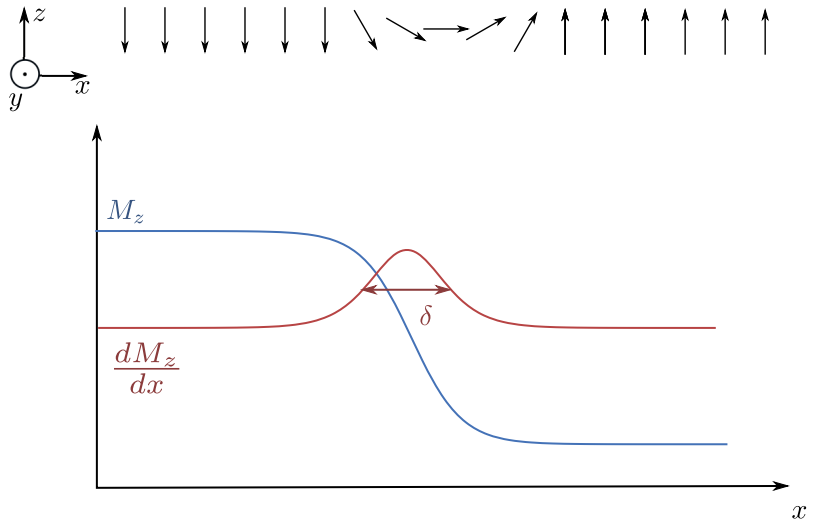

Figure 2.11: The definition of the domain wall width δ used in this thesis is the FWHM of the gradient of the domain wall profile $M_z(x)$. A schematic of the magnetic moments comprising a domain wall separating two domains in $+z$ and $-z$ is provided at the top of the figure. The domain wall profile, that is $M_z(x)$, is sketched together with its derivative (annotated with δ) in the lower half of the figure.

thesis is described here together with its relation to the experimentally accessed 'wall width parameter' w.

The wall width δ is defined as the FWHM (full width at half maximum) of the derivative of the domain magnetisation [36], this is sketched in Fig. 2.11. In this thesis, the domain wall profile is measured using DPC mode Lorentz microscopy (described in section 3.7.4). With this method, the wall width is extracted by fitting the profile to a hyperbolic tangent function of form:

$$\text{profile}(x) \propto \tanh\left(\frac{x}{w}\right). \tag{2.15}$$

where w, the wall width parameter, is equal to $(1/1.76)\,\delta$ [37].

2.3.2 Chiral domain walls and skyrmions

This section presents details of the chiral magnetic structures stabilised in material systems with DMI. As mentioned in section 2.2.2, the interaction vector **D** is oriented differently for the two types of DMI - bulk and interfacial - leading to the support of different types of chiral objects. To illustrate this, Fig. 2.9 is revisited and annotated with the direction of the bulk and interfacial **D** vectors

with respect to a row of magnetic atoms in Fig. 2.12. As per Eq. 2.5, the DMI

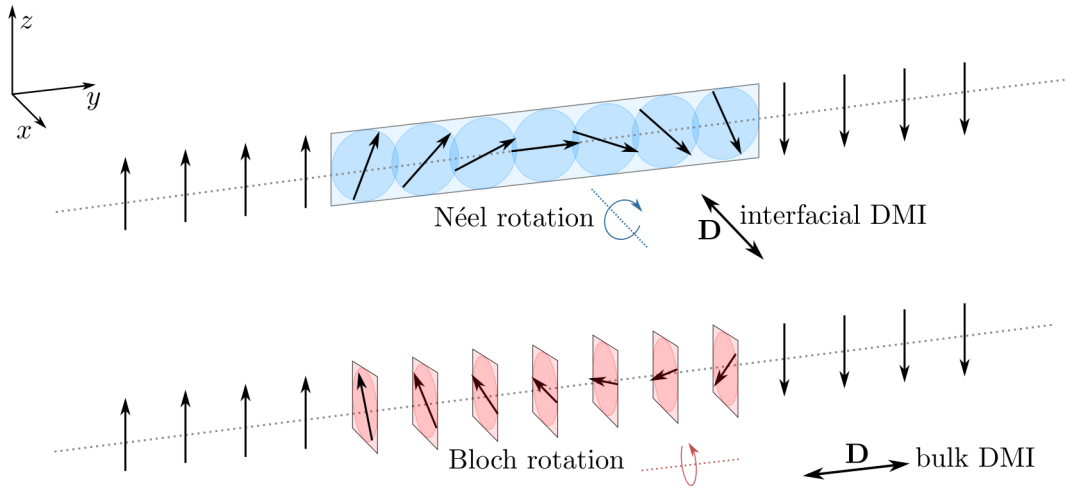

Figure 2.12: DMI energy is minimised by a rotation of the magnetisation around the **D** vector. The orientation of the **D** vector with respect to a row of magnetic atoms is included on the figure for interfacial and bulk type DMIs. Because the axis of magnetisation rotation is parallel to the **D** vector, it is clear that Néel type rotations lower interfacial DMI energy and Bloch type rotations lower bulk DMI energy.

energy is minimised by rotation of the magnetisation about an axis parallel to **D**, therefore it is clear that bulk DMI favours Bloch rotations where interfacial DMI favours Néel rotations. Because this thesis presents work on multilayers which have interfacial DMI, the rest of this section focuses on Néel type chiral objects.

Interfacial DMI stabilises 'homochiral' Néel type walls and Néel type skyrmions, schematics of both are included in Fig. 2.13. Homochiral domain walls are discussed first. The preceding section outlined the preference for thin films with PMA to form Bloch type walls but when the system also has interfacial DMI, the total energy is in fact minimised by Néel type walls with a fixed chirality [22]. These are usually referred to as homochiral Néel walls and two examples with different chiralities are sketched in Figs. 2.13(a,b). Homochiral domain walls were predicted to move at high velocities under spin-polarised currents, where the direction of motion is fixed by the chirality of the walls [22, 38, 39]. Experimentally, velocities of 700 ms^{-1} have been demonstrated in ferromagnet multilayers [40] and 1.3 kms^{-1} in ferrimagnet multilayers [41]. This is an order of magnitude faster

than the spin-polarised current driven motion of conventional domain walls [42] and requires smaller current densities [22, 43]. Therefore, homochiral domain caused considerable excitement in the field of spintronics due to their suitability as information carriers in racetrack type memory [44] which is based on domain wall motion under spin-polarised currents [45].

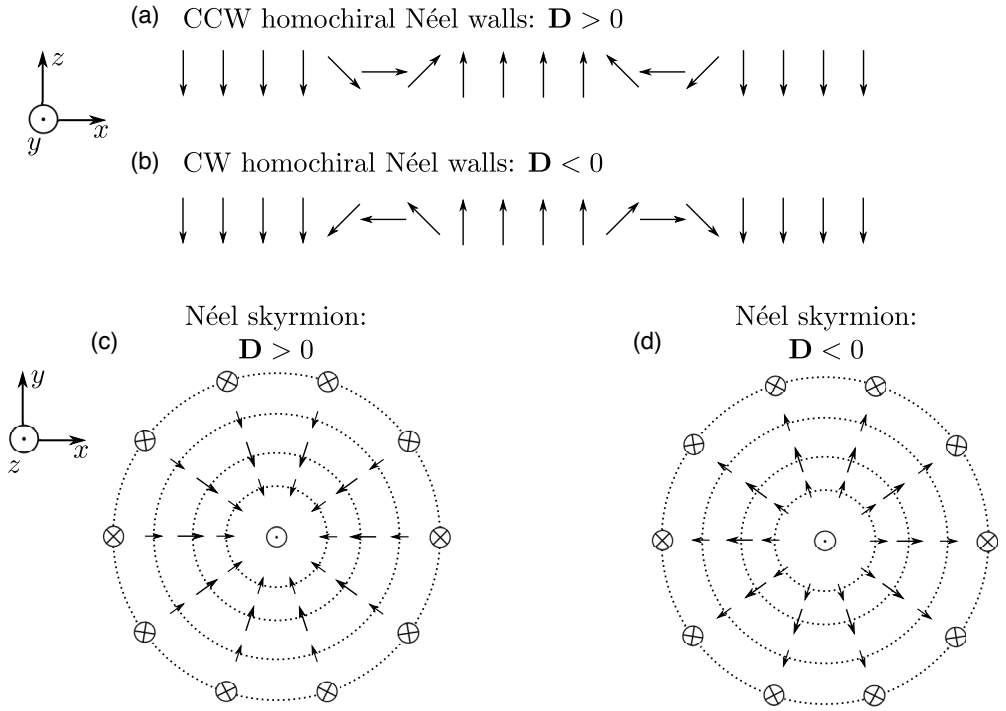

Figure 2.13: Summary of chiral magnetic objects stabilised by interfacial DMI. (a) and (b) show homochiral Néel walls, where the sense of wall rotation is fixed by the sign **D**: (a) positive **D** fixes a counter-clockwise (CCW) rotation and (b) negative **D** fixes a clockwise (CW) rotation. Similarly, (c) and (d) sketch the magnetisation of Néel type skyrmions associated with positive **D** and negative **D** respectively.

As mentioned in the introduction, skyrmions are particle-like swirls of magnetisation. As sketched in Figs. 2.13(c,d) skyrmions are circular and consist of a core, with magnetisation pointing along +(-)z, from which the magnetisation rotates through 180° (radially for Néel skyrmions) until it points along -(+)z. Additionally, they have integer topological charge (quantified by a skyrmion winding number [46]), leading to a property called 'topological protection' whereby the magnetisation cannot be continuously transformed into a configuration belonging

to another topology class i.e. uniform magnetisation[2]. Skyrmions are small; in Fe monolayers, at low temperatures, Néel skyrmions of diameter ≈10 nm have been observed. At room-temperature, in polycrystalline samples, skyrmions can be stabilised using a multilayer structure where some number of repeat layers (between five and 15 normally) increases total magnetic volume which increases their stability against thermal fluctuations. At present, the size of skyrmions in polycrystalline room-temperature systems is limited at best to around 50-100 nm [20, 47–50]. Néel skyrmions share most of their dynamic properties with homochiral Néel walls (they are however more prone to pinning and the largest measured skyrmion velocity is 50 ms^{-1} [47]). However, there is arguably more interest in skyrmions for applications because of their particle-like nature, small size and interesting topological properties. One ramification of their topology is the skyrmion Hall effect, which in analogy to the classical Hall effect, causes them to move with a curved trajectory away from the direction of applied current [51, 52]. A topology related benefit lies in the topological Hall effect, where current flowing through a skyrmion leads to measurable voltage accumulation perpendicular to the current direction [53], allowing for their electrical detection [54, 55].

In this section it must be noted that in some cases, the presence of an interfacial DMI is not enough to fix one chirality to the material. There exists a critical number of repeat layers, above which the dipolar energy competes with the DMI energy. The result is a partial reorientation of the domain wall structure to lower the dipolar energy. This was reported on last year in a number of studies [56–58], and is the focus of Chapter 5. Further discussion is left until Chapter 5.

[2]This is not true experimentally, where the nucleation and annihilation of skyrmions represents a transformation between states with different topological charges, however these actions are associated with a high energy cost [16].

Bibliography

[1] D. J. Griffiths, *Introduction to Electrodynamics*. Prentice Hall, 1999.

[2] A. Aharoni, *Introduction to the Theory of Ferromagnetism*. International Series of Monographs on Physics, Clarendon Press, 2000.

[3] J. M. Coey, *Magnetism and magnetic materials*. Cambridge university press, 2010.

[4] W. F. Brown, "Micromagnetics, Domains, and Resonance," *Journal of Applied Physics*, vol. 30, pp. S62–S69, 1959.

[5] A. Hubert, R. Schäfer, and A. Rudolf Schafer, *Magnetic Domains: The Analysis of Magnetic Microstructures*. Springer, 1998.

[6] C. Eyrich, A. Zamani, W. Huttema, M. Arora, D. Harrison, F. Rashidi, D. Broun, B. Heinrich, O. Mryasov, M. Ahlberg, O. Karis, P. E. Jönsson, M. From, X. Zhu, and E. Girt, "Effects of substitution on the exchange stiffness and magnetization of Co films," *Physical Review B - Condensed Matter and Materials Physics*, vol. 90, p. 235408, 2014.

[7] T. Devolder, J. V. Kim, L. Nistor, R. Sousa, B. Rodmacq, and B. Diény, "Exchange stiffness in ultrathin perpendicularly magnetized CoFeB layers determined using the spectroscopy of electrically excited spin waves," *Journal of Applied Physics*, vol. 120, p. 183902, 2016.

[8] P. Grünberg, C. M. Mayr, W. Vach, and M. Grimsditch, "Determination of magnetic parameters by means of brillouinscattering. Examples: Fe, Ni, Ni0.8Fe0.2," *Journal of Magnetism and Magnetic Materials*, vol. 28, pp. 319–325, 1982.

[9] I. Dzyaloshinsky, "A thermodynamic theory of "weak" ferromagnetism of antiferromagnetics," *Journal of Physics and Chemistry of Solids*, vol. 4, pp. 241–255, 1958.

[10] T. Moriya, "Anisotropic superexchange interaction and weak ferromagnetism," *Physical Review*, vol. 120, pp. 91–98, 1960.

[11] M. Heide, G. Bihlmayer, and S. Blügel, "Dzyaloshinskii-Moriya interaction accounting for the orientation of magnetic domains in ultrathin films: Fe/W(110)," *Physical Review B - Condensed Matter and Materials Physics*, vol. 78, p. 140403, 2008.

[12] A. Fert and P. M. Levy, "Role of anisotropic exchange interactions in determining the properties of spin-glasses," *Physical Review Letters*, vol. 44, pp. 1538–1541, 1980.

[13] X. Z. Yu, Y. Onose, N. Kanazawa, J. H. Park, J. H. Han, Y. Matsui, N. Nagaosa, and Y. Tokura, "Real-space observation of a two-dimensional skyrmion crystal," *Nature*, vol. 465, no. 7300, pp. 901–904, 2010.

[14] S. Mühlbauer, B. Binz, F. Jonietz, C. Pfleiderer, A. Rosch, A. Neubauer, R. Georgii, and P. Böni, "Skyrmion lattice in a chiral magnet," *Science*, vol. 323, no. 5916, pp. 915–919, 2009.

[15] S. Heinze, K. Von Bergmann, M. Menzel, J. Brede, A. Kubetzka, R. Wiesendanger, G. Bihlmayer, and S. Blügel, "Spontaneous atomic-scale magnetic skyrmion lattice in two dimensions," *Nature Physics*, vol. 7, no. 9, pp. 713–718, 2011.

[16] S. Heinze, K. Von Bergmann, M. Menzel, J. Brede, A. Kubetzka, R. Wiesendanger, G. Bihlmayer, and S. Blügel, "Spontaneous atomic-scale magnetic skyrmion lattice in two dimensions," *Nature Physics*, vol. 7, no. 9, pp. 713–718, 2011.

[17] G. Chen, T. Ma, A. T. N'Diaye, H. Kwon, C. Won, Y. Wu, and A. K. Schmid, "Tailoring the chirality of magnetic domain walls by interface engineering," *Nature Communications*, vol. 4, p. 2671, 2013.

[18] H. Yang, A. Thiaville, S. Rohart, A. Fert, and M. Chshiev, "Anatomy of Dzyaloshinskii-Moriya Interaction at Co/Pt Interfaces," *Physical Review Letters*, vol. 115, no. 26, p. 267210, 2015.

[19] A. Hrabec, N. A. Porter, A. Wells, M. J. Benitez, G. Burnell, S. McVitie, D. McGrouther, T. A. Moore, and C. H. Marrows, "Measuring and tailoring the Dzyaloshinskii-Moriya interaction in perpendicularly magnetized thin films," *Physical Review B - Condensed Matter and Materials Physics*, vol. 90, no. 2, 2014.

[20] C. Moreau-Luchaire, C. Moutafis, N. Reyren, J. Sampaio, C. A. Vaz, N. Van Horne, K. Bouzehouane, K. Garcia, C. Deranlot, P. Warnicke, P. Wohlhüter, J. M. George, M. Weigand, J. Raabe, V. Cros, and A. Fert, "Additive interfacial chiral interaction in multilayers for stabilization of small individual skyrmions at room temperature," *Nature Nanotechnology*, vol. 11, no. 5, pp. 444–448, 2016.

[21] O. Boulle, J. Vogel, H. Yang, S. Pizzini, D. De Souza Chaves, A. Locatelli, T. O. Mente, A. Sala, L. D. Buda-Prejbeanu, O. Klein, M. Belmeguenai, Y. Roussigné, A. Stashkevich, S. Mourad Chérif, L. Aballe, M. Foerster, M. Chshiev, S. Auffret, I. M. Miron, and G. Gaudin, "Room-temperature chiral magnetic skyrmions in ultrathin magnetic nanostructures," *Nature Nanotechnology*, vol. 11, no. 5, pp. 449–454, 2016.

[22] A. Thiaville, S. Rohart, É. Jué, V. Cros, and A. Fert, "Dynamics of Dzyaloshinskii domain walls in ultrathin magnetic films," *Epl*, vol. 100, p. 57002, 2012.

[23] S. Blundell, *Magnetism in Condensed Matter*. OUP Oxford, 2003.

[24] O. Hellwig, A. Berger, J. B. Kortright, and E. E. Fullerton, "Domain structure and magnetization reversal of antiferromagnetically coupled perpendicular anisotropy films," *Journal of Magnetism and Magnetic Materials*, vol. 319, pp. 13–55, 2007.

[25] R. Lavrijsen, A. Feránndez-Pacheco, D. Petit, R. Mansell, J. H. Lee, and R. P. Cowburn, "Tuning the interlayer exchange coupling between single perpendicularly magnetized CoFeB layers," *Applied Physics Letters*, vol. 100, p. 52411, 2012.

[26] W. Legrand, D. Maccariello, F. Ajejas, S. Collin, A. Vecchiola, K. Bouzehouane, N. Reyren, V. Cros, and A. Fert, "Room-temperature stabilization of antiferromagnetic skyrmions in synthetic antiferromagnets," *Nature Materials*, pp. 1–23, 2019.

[27] G. Binasch, P. Grünberg, F. Saurenbach, and W. Zinn, "Enhanced magnetoresistance in layered magnetic structures with antiferromagnetic interlayer exchange," *Physical Review B*, vol. 39, no. 7, pp. 4828–4830, 1989.

[28] M. Baibich, J. Broto, A. Fert, F. Nguyrn Van Dau, and F. Petroff, "Giant Magnetorsistance of (001) Fe/(001) Cr Magnetic Superlattices," *Physical Review Letters*, vol. 61, no. 001, pp. 2472–2475, 1988.

[29] F. Hellman, M. S. Division, L. Berkeley, A. Hoffmann, G. S. D. Beach, E. E. Fullerton, A. H. Macdonald, and D. C. Ralph, "Interface-Induced Phenomena in Magnetism," *Reviews of Modern Physics*, vol. 89, no. June, pp. 1–79, 2017.

[30] A. Fert, "Magnetic and Transport Properties of Metallic Multilayers," *Materials Science Forum*, vol. 59-60, pp. 439–480, 1991.

[31] D. Bonnenberg, K. A. Hempel, and H. Wijn, "Magnetocrystalline anisotropy: Datasheet from Landolt-Börnstein - Group III Condensed Matter · Volume 19A: "3d, 4d and 5d Elements, Alloys and Compounds"," 1986.

[32] H. W. Fuller and M. E. Hale, "Determination of magnetization distribution in thin films using electron microscopy," *Journal of Applied Physics*, vol. 31, pp. 238–248, 1960.

[33] M. Tanase and A. K. Petford-Long, "In situ TEM observation of magnetic materials," *Microscopy Research and Technique*, vol. 72, pp. 187–196, 2009.

[34] M. T. Johnson, P. J. Bloemen, F. J. Den Broeder, and J. J. De Vries, "Magnetic anisotropy in metallic multilayers," *Reports on Progress in Physics*, vol. 59, no. 11, pp. 1409–1458, 1996.

[35] A. Hubert and R. Schäfer, *Magnetic Domains: The Analysis of Magnetic Microstructures*. Berlin, Heidelberg: Springer, 1998.

[36] A. Hubert, "Stray-Field-Free and Related Domain Wall Configurations in Thin Magnetic Films (II)," *Physica Status Solidi (B)*, vol. 38, no. 2, pp. 699–713, 1970.

[37] S. McVitie and J. N. Chapman, "Measurement of domain wall widths in Permalloy using differential phase contrast imaging in stem," *Journal of Magnetism and Magnetic Materials*, vol. 83, no. 1-3, pp. 97–98, 1990.

[38] A. V. Khvalkovskiy, V. Cros, D. Apalkov, V. Nikitin, M. Krounbi, K. A. Zvezdin, A. Anane, J. Grollier, and A. Fert, "Matching domain-wall configuration and spin-orbit torques for efficient domain-wall motion," *Physical Review B - Condensed Matter and Materials Physics*, vol. 87, p. 020402, 2013.

[39] S. Emori, U. Bauer, S. M. Ahn, E. Martinez, and G. S. Beach, "Current-driven dynamics of chiral ferromagnetic domain walls," *Nature Materials*, vol. 12, no. 7, pp. 611–616, 2013.

[40] T. Ha Pham, J. Vogel, J. Sampaio, M. Vaatka, J. C. Rojas-Sánchez, M. Bonfim, D. S. Chaves, F. Choueikani, P. Ohresser, E. Otero, A. Thiaville, and S. Pizzini, "Very large domain wall velocities in Pt/Co/GdOx and Pt/Co/Gd trilayers with

Dzyaloshinskii-Moriya interaction," *EPL (Europhysics Letters)*, vol. 113, p. 67001, 2016.

[41] L. Caretta, M. Mann, F. Büttner, K. Ueda, B. Pfau, C. M. Günther, P. Hessing, A. Churikova, C. Klose, M. Schneider, D. Engel, C. Marcus, D. Bono, K. Bagschik, S. Eisebitt, and G. S. Beach, "Fast current-driven domain walls and small skyrmions in a compensated ferrimagnet," *Nature Nanotechnology*, vol. 13, pp. 1154–1160, 2018.

[42] M. Hayashi, L. Thomas, C. Rettner, R. Moriya, Y. B. Bazaliy, and S. S. Parkin, "Current driven domain wall velocities exceeding the spin angular momentum transfer rate in permalloy nanowires," *Physical Review Letters*, vol. 98, p. 037204, 2007.

[43] I. M. Miron, T. Moore, H. Szambolics, L. D. Buda-Prejbeanu, S. Auffret, B. Rodmacq, S. Pizzini, J. Vogel, M. Bonfim, A. Schuhl, and G. Gaudin, "Fast current-induced domain-wall motion controlled by the Rashba effect," *Nature Materials*, vol. 10, no. 6, pp. 419–423, 2011.

[44] S. S. Parkin, M. Hayashi, and L. Thomas, "Magnetic domain-wall racetrack memory," *Science*, vol. 320, pp. 190–194, 2008.

[45] M. Hayashi, L. Thomas, R. Moriya, C. Rettner, and S. S. Parkin, "Current-controlled magnetic domain-wall nanowire shift register," *Science*, vol. 320, pp. 209–211, 2008.

[46] H. B. Braun, "Topological effects in nanomagnetism: From superparamagnetism to chiral quantum solitons," *Advances in Physics*, vol. 61, pp. 1–116, 2012.

[47] S. Woo, K. Litzius, B. Krüger, M. Y. Im, L. Caretta, K. Richter, M. Mann, A. Krone, R. M. Reeve, M. Weigand, P. Agrawal, I. Lemesh, M. A. Mawass, P. Fischer, M. Kläui, and G. S. Beach, "Observation of room-temperature magnetic skyrmions and their current-driven dynamics in ultrathin metallic ferromagnets," *Nature Materials*, vol. 15, pp. 501–506, 2016.

[48] A. Soumyanarayanan, M. Raju, A. L. Oyarce, A. K. Tan, M. Y. Im, A. P. Petrovic, P. Ho, K. H. Khoo, M. Tran, C. K. Gan, F. Ernult, and C. Panagopoulos, "Tunable room-temperature magnetic skyrmions in Ir/Fe/Co/Pt multilayers," *Nature Materials*, vol. 16, pp. 898–904, 2017.

[49] W. Legrand, D. Maccariello, N. Reyren, K. Garcia, C. Moutafis, C. Moreau-Luchaire, S. Collin, K. Bouzehouane, V. Cros, and A. Fert, "Room-Temperature Current-Induced Generation and Motion of sub-100 nm Skyrmions," *Nano Letters*, vol. 17, no. 4, pp. 2703–2712, 2017.

[50] S. McVitie, S. Hughes, K. Fallon, S. McFadzean, D. McGrouther, M. Krajnak, W. Legrand, D. MacCariello, S. Collin, K. Garcia, N. Reyren, V. Cros, A. Fert, K. Zeissler, and C. H. Marrows, "A transmission electron microscope study of Néel skyrmion magnetic textures in multilayer thin film systems with large interfacial chiral interaction," *Scientific Reports*, vol. 8, p. 5703, 2018.

[51] W. Jiang, X. Zhang, G. Yu, W. Zhang, X. Wang, M. Benjamin Jungfleisch, J. E. Pearson, X. Cheng, O. Heinonen, K. L. Wang, Y. Zhou, A. Hoffmann, and S. G. Te Velthuis, "Direct observation of the skyrmion Hall effect," *Nature Physics*, vol. 13, pp. 162–169, 2017.

[52] K. Litzius, I. Lemesh, B. Krüger, P. Bassirian, L. Caretta, K. Richter, F. Büttner, K. Sato, O. A. Tretiakov, J. Förster, R. M. Reeve, M. Weigand, I. Bykova, H. Stoll, G. Schütz, G. S. Beach, and M. Klaüi, "Skyrmion Hall effect revealed by direct time-resolved X-ray microscopy," *Nature Physics*, vol. 13, pp. 170–175, 2017.

[53] N. Nagaosa and Y. Tokura, "Topological properties and dynamics of magnetic skyrmions," *Nature Nanotechnology*, vol. 8, no. 12, pp. 899–911, 2013.

[54] D. Maccariello, W. Legrand, N. Reyren, K. Garcia, K. Bouzehouane, S. Collin, V. Cros, and A. Fert, "Electrical detection of single magnetic skyrmions in metallic multilayers at room temperature," *Nature Nanotechnology*, vol. 13, pp. 233–237, 2018.

[55] K. Zeissler, S. Finizio, K. Shahbazi, J. Massey, F. A. Ma'Mari, D. M. Bracher, A. Kleibert, M. C. Rosamond, E. H. Linfield, T. A. Moore, J. Raabe, G. Burnell, and C. H. Marrows, "Discrete Hall resistivity contribution from Néel skyrmions in multilayer nanodiscs," *Nature Nanotechnology*, vol. 13, no. 12, pp. 1161–1166, 2018.

[56] W. Legrand, J. Y. Chauleau, D. Maccariello, N. Reyren, S. Collin, K. Bouzehouane, N. Jaouen, V. Cros, and A. Fert, "Hybrid chiral domain walls and skyrmions in magnetic multilayers," *Science Advances*, vol. 4, no. 7, 2018.

[57] Y. Dovzhenko, F. Casola, S. Schlotter, T. X. Zhou, F. Büttner, R. L. Walsworth, G. S. Beach, and A. Yacoby, "Magnetostatic twists in room-temperature skyrmions explored by nitrogen-vacancy center spin texture reconstruction," *Nature Communications*, vol. 9, no. 1, pp. 1–7, 2018.

[58] I. Lemesh and G. S. Beach, "Twisted domain walls and skyrmions in perpendicularly magnetized multilayers," *Physical Review B*, vol. 98, no. 10, pp. 1–8, 2018.

3

Instrumentation and methodology

Contents

3.1 Introduction

In this thesis a number of experimental and simulation methods are employed to study various effects and consequences of the Dzyaloshinskii-Moriya interaction on the magnetism of technologically relevant magnetic thin films. This chapter provides descriptions of all relevant experimental techniques, from sample fabrication to sample characterisation, as well as simulation methods and analytical calculations. Section 3.2 covers details of the growth of the thin films studied in this work, the following section (3.4) covers the principles of focused ion beam microscopy which is key to the work presented in Chapters 6 and 7. Leading on from this, sections 3.5 to 3.8 cover characterisation techniques used to study structural and magnetic properties of the samples including transmission electron microscopy (TEM) and scanning force microscopies (SFM). Covered in particular detail, in section 3.7.2, is Lorentz TEM. Lorentz TEM an umbrella term referring to all non-interferometric magnetic imaging techniques performed in the TEM. It is the primary experimental method employed to study the magnetic behaviour of the samples in all results chapters of this thesis, and therefore is covered in significant detail. Section 3.10.1 introduces micromagnetic simulations which are used to compute the magnetism of magnetic materials of user-defined geometry and magnetic properties, and also to simulate the magnetisation dynamics under various external stimuli. Lastly sections 3.10.3 and 3.10.4 outline how to calculate the image contrast expected when imaging (with various methods) a given magnetic configuration, supplied by micromagnetic simulations or analytical models (section 3.10.2). These image calculation tools are extremely useful for experimental image interpretation and are used widely throughout results Chapters 4, 5 and 7.

3.2 Sample Preparation

As the work presented in this thesis primarily employs methods of transmission electron microscopy (TEM) it is imperative that all samples are prepared on electron transparent substrates. In this section, therefore, electron transparent substrates are discussed before describing DC magnetron sputtering which was used to deposit all samples studied in this thesis.

3.2.1 Electron transparent substrates

For a TEM operated with an accelerating voltage of 200 kV, as in this thesis, most materials are electron transparent at thicknesses < 100 nm. For plan view studies thin films are simply deposited straight onto electron transparent substrates. Two such substrates are Si_3N_4 TEM membranes and standard TEM grids, which are sketched in Fig. 3.1(a) and (b) respectively where electron transparent areas are drawn in light grey.

Si_3N_4 membranes consist of a ≈ 35 nm thick window of Si_3N_4 (area 100 μm $\times$ 100 μm) suspended from a thicker, 2 mm square frame of Si. The window on the Si_3N_4 TEM membranes is fabricated by back etching the Si, leaving an angle around 25° between the film normal and the etched Si frame as sketched in

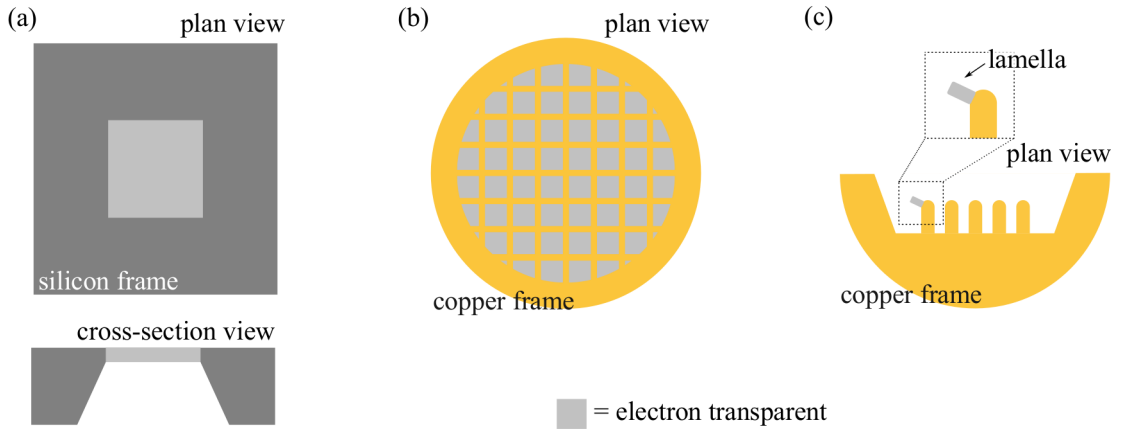

Figure 3.1: Sketches of the geometry of various electron transparent substrates. For plan view studies samples are deposited on either (a) Si_3N_4 TEM membranes or (b) standard Cu TEM grids. For cross-sectional studies electron transparent lamellas of material are fabricated and mounted onto (c) a copper Omniprobe grid. Electron transparent areas are drawn in light grey.

the lower panel of Fig. 3.1(a). This restricts the maximum sample tilt possible: above tilt angles of 25°, the electron opaque Si frame completely shadows the transparent window - preventing imaging. Consequently, for experiments requiring high sample tilt angles, samples are deposited on a 3 nm thick amorphous carbon film which is suspended from standard Cu TEM grids (sketched in Fig. 3.1(b)). The geometry of this substrate permits TEM imaging up to a 80° sample tilt. Lastly for cross-sectional studies, electron transparent lamella are extracted from bulk samples using (in this case) focussed ion beam milling (the extraction process is fully described in section 3.4.1). These electron transparent lamellas are attached to a Cu TEM omniprobe grid as sketched in 3.1(c) for TEM imaging.

3.2.2 DC magnetron sputtering

All samples studied in this thesis are polycrystalline multilayers deposited by DC magnetron sputtering by collaborators at different labs in the UK and France. The sample used in Chapter 4 and sample 1 of Chapter 6 were deposited by Katharina Zeissler at the University of Leeds. The samples in Chapter 5 and samples 2-4 in Chapter 6 were deposited by William Legrand at CNRS/Thalés. The samples in Chapter 7 were deposited by Sinan Azzawi at Durham University. Where known, the conditions used to deposit the samples grown in different labs are summarised in table 3.1 at the end of this section.

Figure 3.2 is a schematic showing the main components of a typical DC magnetron sputtering system. A DC magnetron sputtering system consists of a pair of planar electrodes: the substrate (the material on which to deposit) is situated at the anode while the target (the material to be deposited) is situated at the cathode. This system is held in a chamber which is evacuated to a low base pressure then backfilled with an inert gas, such as Ar. A high voltage bias is applied between the two electrodes which ejects electrons from the cathode which ionise the gas atoms generating a plasma. The positively charged gas ions are then accelerated into the negatively charged target. This energetic collision ejects target atoms from the target surface (sputtering) which then travel through the chamber and condense on

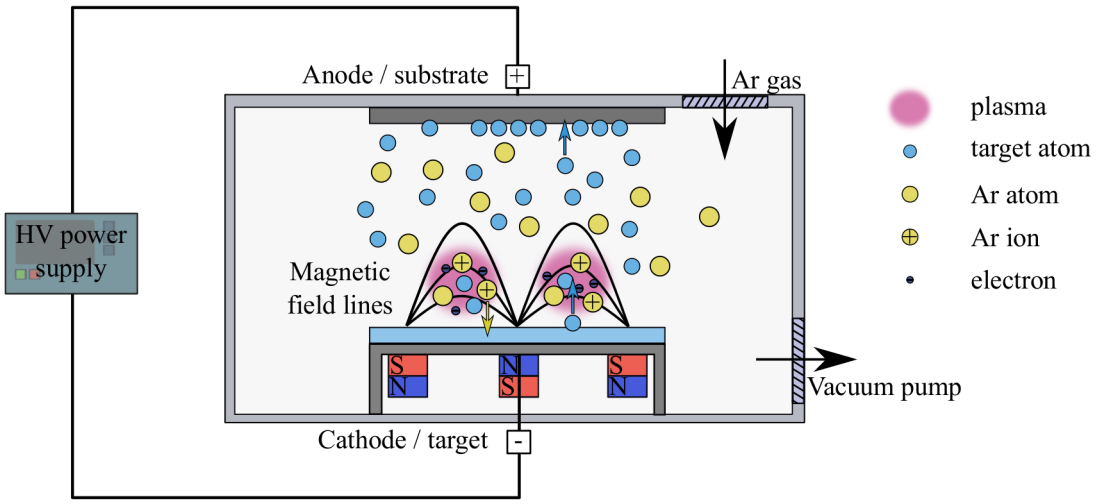

Figure 3.2: Schematic of a DC magnetron sputtering system.

the substrate (and the chamber) to form a thin film. A magnetron is situated below the target which forms a magnetic field above the target. The shape of this field traps more electrons in the vicinity of the target thus increasing the likelihood of an ionising gas atom/electron collision, generating a denser plasma which leads to an increased deposition rate [1]. The film thickness is controlled by the deposition time and the distance between the substrate and the target [2]. Furthermore multiple targets can be contained in the chamber at the same time and selected in turn to deposit multilayered samples without breaking vacuum. Deposition methods based on sputtering have key advantages over thermal deposition methods, particularly relevant here (for deposition of permalloy (Ni Fe alloys)) is that alloy targets can be deposited at stoichiometry on the substrate.

DC magnetron sputtering is often the choice deposition method for growth of thin metallic multilayer stacks because of the ease of depositing any metallic material and the high purity and uniformity of the deposited film [3]. The one drawback of sputter deposition is diffuse interfaces [4]. This should be of great concern when studying interface-driven effects like DMI, however it has been shown that DMI is actually surprisingly robust against intermixing [5] justifying further the use of sputter deposition. Moreover, DC magnetron sputtering is easily automated and scaled up, leading to wide use in commercial scale device fabrication.

Laboratory	Sample constituents	Deposition conditions		
		Base pressure	Ar pressure [flow]	Growth rate
Leeds	Ta, Pt, Co, Ir	2×10^{-6} Pa	670 Pa	0.1 nm s^{-1}
CNRS/Thalés	Ta, Pt, Co, Ru	8×10^{-6} Pa	0.25 Pa	-
Durham	$Ni_{81}Fe_{19}$, Cu, Pt, Ir	-	[0.02 Pa m^3s^{-1}]	0.9 nm s^{-1}

Table 3.1: Summary of the material composition and deposition conditions (where known) used by different labs to deposit, via DC magnetron sputtering, the samples studied in this thesis. The deposition rate depends on the material: the quoted value is from the magnetic layer.

3.3 Magnetometry

In order to extract key parameters about a magnetic material it is exceedingly useful to measure its hysteresis loop. As described in section 2.1 the hysteresis loop contains information on the materials saturation magnetisation, remanence and coercivity. Moreover from more than one loop, acquired with different directions of applied field, the anisotropy can be extracted [4]. Chapters 5 and 6 rely on, in places, magnetometry measurements made by collaborators Katharina Zeissler, University of Leeds, and William Legrand, CNRS/Thalés. Magnetometry measurements were made with both superconducting quantum interference device (SQUID) magnetometers and alternating field gradient magnetometers (AGFM). The following paragraphs briefly describe the basic working principles of each method in turn.

A SQUID magnetometer works by slowly moving the sample through a set of detector coils which are electrically connected to a SQUID (a flux-voltage converter that outputs a voltage proportional to (quanta-limited) changes in magnetic flux [6]). Graphs of the SQUID output voltage versus the sample position in the detector coils are fitted to models that allow the magnetisation to be recovered [7]. This is repeated with the sample under different applied field strengths to build a hysteresis loop.

AFGMs apply an alternating field gradient to the sample which is mounted on a mechanically resonating holder. The frequency of the alternating field gradient is adjusted until the system is at resonance, where the amplitude of the oscillation

relates directly to the magnetisation of the sample [7]. While the sample is resonating, a DC magnetic field is applied to the sample and the subsequent changes in magnetisation are measured through changes in the oscillation amplitude.

3.4 Focused ion beam microscopy

Focused ion beam (FIB) microscopes are an extremely versatile tool used for a wide range applications in academic research and in industry. In this thesis two FIB systems - an FEI Nova FIB and FEI Helios plasma FIB (PFIB) - were used for three purposes: TEM lamella fabrication, patterning and ion irradiation. After introducing the basic principles of a FIB microscope, this section will describe each of the three uses of the FIB in turn.

Both the Nova FIB (Ga^+ ions) and Helios PFIB (Xe^+ ions) microscopes are 'dual beam' systems, meaning they incorporate both a FIB column and a focused electron beam column oriented at 52° to each other as sketched in Fig. 3.3. The operating principles of both columns are similar and feature a sequence of electromagnetic lenses, apertures and scan coils to manipulate and focus a beam of charged particles onto the sample surface. When the focused ion beam is incident on the sample surface it causes sputtering (or milling) of the sample material. This ion beam/sample interaction also produces back-scattered (BSE) and secondary electrons (SE) which are collected as the ion beam is scanned over the sample and used to form an image. The contrast in these images arises from both the sample topography and variations in atomic number [8]. The nature of the ion beam/sample interaction makes FIB imaging inherently damaging and while images can be collected using a FIB, the main use of the FIB is as a highly controllable nanoscale milling machine. The focused electron beam generates BSE and SE without causing any modification to the sample, and can be used to image the sample non-destructively - this type of imaging is called scanning electron microscopy (SEM).

The geometry of the dual beam system allows for coincidence of the ion and electron beams on the sample, as depicted in the schematic in Fig. 3.3. When

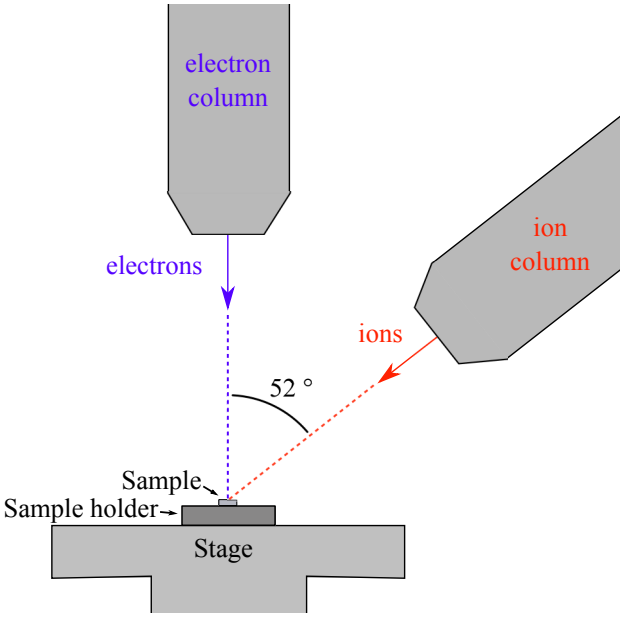

Figure 3.3: Schematic showing the geometry of a dual beam FIB/SEM system.

using the FIB to modify the sample, the stage is tilted to 52° so that the ion beam is perpendicular to the sample surface and, if using a sufficiently large electron beam current that ensures the SEs/BSEs generated by the electron beam dominate over the SEs/BSEs generated by the ion beam, the electron beam may be used to simultaneously image the sample. The ion/electron beam coincidence is tremendously useful when working with magnetic materials, as the ion dose received by simply imaging the sample can be enough to modify the magnetic behaviour of the sample [9–15]. With a dual beam system the user can easily navigate using the electron beam and expose only the area to be modified to the ion beam. The FIB/SEM system can also be used to deposit materials, Pt/W in the Nova FIB and Pt/C/Co/Fe in the Helios PFIB, via gas injection. A precursor gas is injected into the chamber close to the sample surface where it is decomposed by the ion/electron beam, resulting in deposition of the chosen material on the sample (by-products of the reaction are simply extracted by the vacuum system). This is a highly flexible deposition method with many applications [16–18], however here it is used simply to protect the sample during lamella extraction as will be described in section 3.4.1.

In this thesis the FIB instrument was used as a tool to fabricate electron transparent TEM lamellas; to create patterns in magnetic thin films; and to modify

the local magnetic behaviour of magnetic thin films with ion irradiation. The Nova FIB was used for all three FIB applications where the Helios PFIB was only used for lamella fabrication. The Helios PFIB (a more modern machine) offers advantages for TEM lamella preparation as described in a recent study [19] - but is ill-suited for patterning and small area ion irradiation because, at the low beam currents required for both of these techniques, the size of the Xe^+ probe is problematically large. For example, operated with a 30 kV accelerating voltage and a 10 pA beam current, the probe size of a Ga^+ FIB is $\approx$ 10 nm and for a Xe^+ FIB is $\approx$ 150 nm [20][1].

3.4.1 TEM lamella preparation

As mentioned in section 3.2, in general for TEM studies samples must be $<$ 100 nm thick. For cross-sectional studies of multilayer samples this means extraction of a thin lamella from a bulk substrate - in this case lamellae were extracted from the thicker Si frame area of Si_3N_4 membranes. The FIB fabrication of a TEM lamella is a standardised process [22], known as 'lift-out', and partly automated. The general procedure will be described in this section with the aid of SEM images taken at different stages of the lamella fabrication shown in Fig. 3.4.

Figure 3.4(a) shows a sample before lamella fabrication in the Helios PFIB. A variety of markers are visible, they are used to indicate the area of interest on this sample - in this case a lamella was to be extracted through lines dosed with different levels of Ga^+ ion irradiation to study the effect of ion dose on a Ir/Co/Pt based multilayer as presented in Chapter 6. To protect the underlying sample from damage, first a layer of Pt is deposited using the gas injection system and the electron/ion beams. Then trapezoid shaped trenches are milled to separate

[1]The differences in probe size at a given voltage/beam current arise from the different types of ion sources used in the two FIBs compared. The Ga^+ FIB uses a liquid source (a liquid metal ion source (LMIS)) where a sharp W needle is 'wetted' with liquid Ga and electrically biased to extract Ga^+ ions. This type of source results in small probes at small beam currents (where ions are extracted from the tip of the needle) and much large probes (of low current density) at large beam currents (ions are extracted from the sides of the needle as well as the tip). The Xe^+ FIB has a gaseous source (an inductively coupled plasma (ICP) source) where Xe^+ ions are extracted from a plasma through an aperture - the size of which limits the probe size. Therefore, the Xe^+ FIB, in comparison to the Ga^+ FIB, has larger probes at low beam currents but relatively small probes (of high current density) at higher beam currents [21].

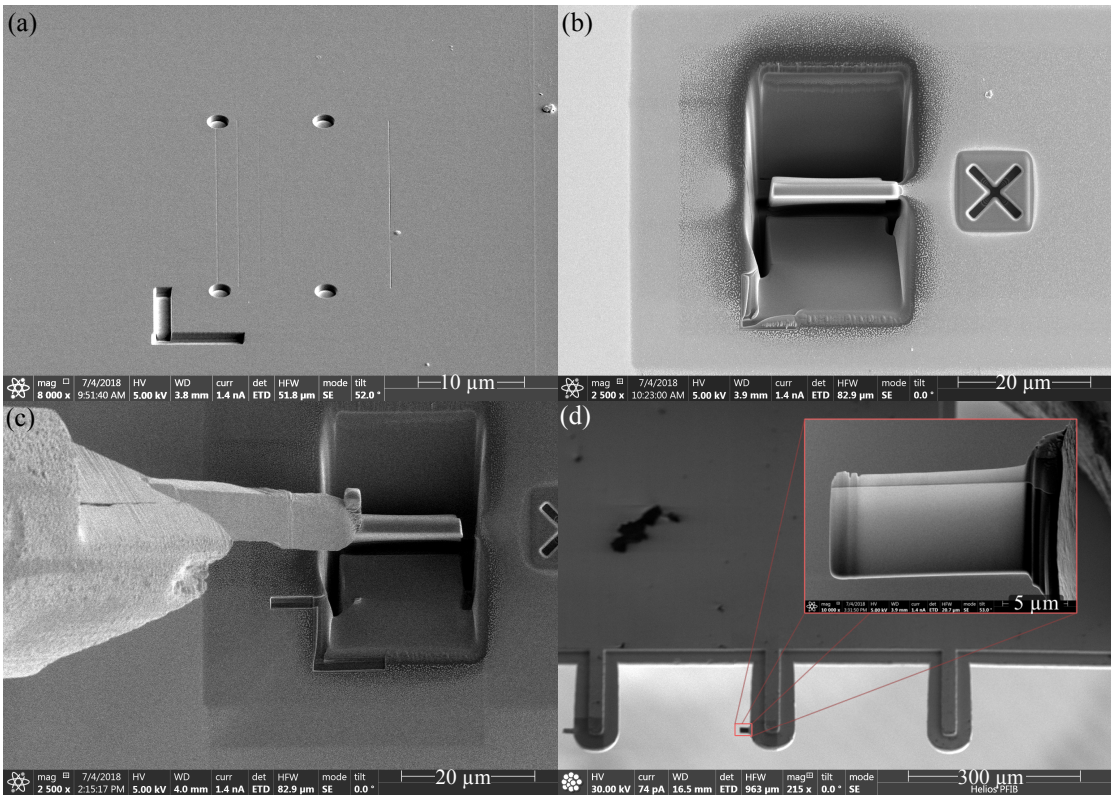

Figure 3.4: SEM images illustrating the lift-out procedure used to extract a TEM lamella from a bulk sample using the FIB. (a) the sample before lamella fabrication. (b) the sample after protective Pt was deposited and after trenches were milled either side of the area to be extracted. (c) the area to be extracted is undercut and welded to an Omniprobe® needle then moved to the Omniprobe® grid (d) where the lamella is welded to the grid and cut free from the Omniprobe® needle. The inset in (d) shows a higher magnification image of the fabricated electron transparent TEM lamella.

the lamella from the bulk sample as seen in Fig. 3.4(b). The trench milling is automated and the cross, milled on the right, is an alignment tool. Part of the protective Pt layer can be also seen in Fig. 3.4(b) on the right hand side where the lamella is still attached to the bulk sample. After the trenches are milled, the lamella is partially undercut, bonded to the Omniprobe® needle, then cut free from the bulk sample as seen in Fig. 3.4(c). While attached to the Omniprobe® the lamella is thinned to below electron transparency then welded to a TEM Omniprobe® grid and cut free from the Omniprobe® needle. Figure 3.4(d) shows a low magnification image of two lamellae attached to the Omniprobe® grid, where the inset shows a high magnification image of the final electron transparent lamella. Most of this procedure is performed with a 30kV ion beam energy and the

beam current is progressively lowered (from 6.7 nA to 230 pA) to minimise damage to the lamella. A final polishing is performed with a 5kV ion beam energy.

3.4.2 Patterning

The FIB is also used to pattern magnetic thin films. This involves the removal of areas of magnetic material to leave islands of the film magnetically separate from the uniform (and effectively infinite) thin film. Patterning introduces shape anisotropy (as described in section 2.2.5) to the energy landscape of the material and leads to the confinement and stabilisation of interesting magnetic states. Some examples found in the literature use FIB patterning to study magnetic vortices in disks [23], multi-domain states in rectangles [24]and domain wall propagation and pinning in nanowires [25, 26]. In this thesis, Chapter 7 studies the magnetic vortex structure stabilised in disks patterned into thin films of Permalloy by removing annuli of material.

In this thesis, all patterning was performed with the Nova FIB using a Ga^+ beam of energy 30 kV and current 10 pA. As is the focus of the following section (3.4.3), the magnetic properties of some materials are exceedingly sensitive to the effects of the ion beam. Therefore it is of utmost importance to only expose the area of the thin film to be removed to the ion beam - this is made simple with dual beam SEM FIB systems where the user can navigate with the electron beam and precisely set the position of the pattern without using the ion beam.

The Nova FIB has a number of in-built patterning tools, namely rectangle and circle (and annulus) tools. These allow for quick patterning but do not permit full control over the ion beam motion. The ion beam should always move parallel to the edge of the shape to be defined to create high quality patterns. If the ion beam mills perpendicular to the pattern, edge artefacts can occur as is sketched in Fig. 3.5. Figures 3.5(a) and (b) respectively illustrate a square pattern that is defined by a serpentine scan and by following the edges. The final shape resulting from the serpentine beam motion, Fig. 3.5(c), has rougher edges where the beam scanned perpendicular to the shape edge. Shapes defined by scanning parallel to edges, Fig.

3.5(d), have uniform edge roughness on all sides. By default, the circle tool allows scanning parallel to the shape edge, however for more complex shapes, parallel edge scanning is achieved using a custom program (written by Damien McGrouther) called 'edgestream'. Edgestream calculates the path required to move the ion beam parallel to the edge of any arbitrary shape and exports a 'stream file'. A stream file is simply list of beam coordinates and beam dwell times which is directly interpreted by the microscope, giving the user complete control over the beam motion.

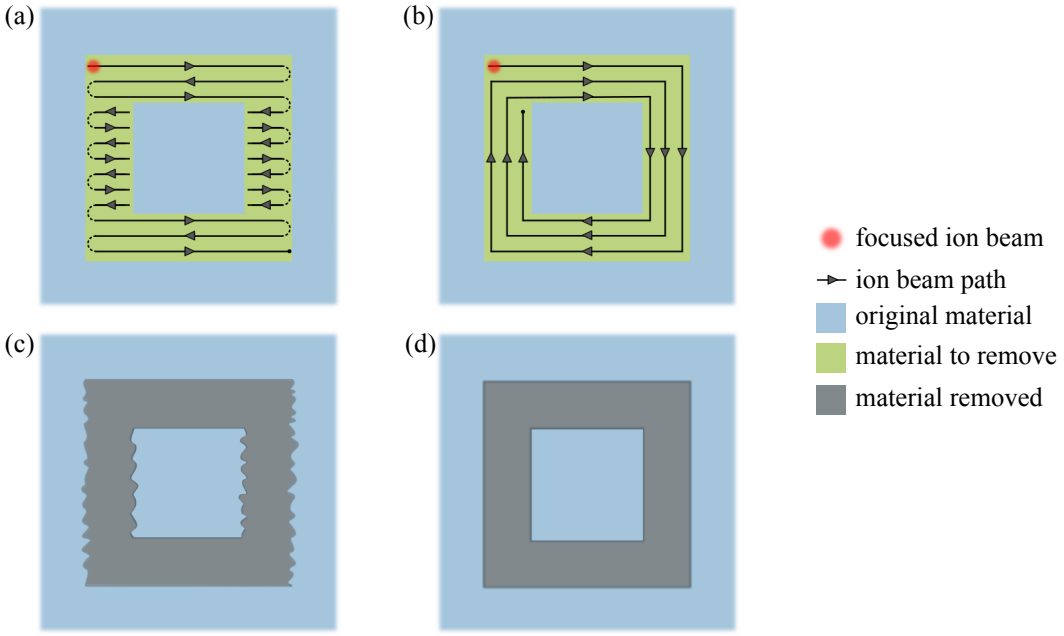

Figure 3.5: Examples of different ion beam paths: (a) a serpentine path and (b) a path that follows the edge of the structure. The direction of the beam path effects the edges of the shape defined: (c) illlustrates the non-uniform edge roughness produced by method (a) and (d) depicts the uniform edges produced by method (b).

Figure 3.6 shows an an SEM image of a FIB defined rectangle, of dimensions 2 μm by 8 μm, which is isolated from the rest of the sample (polycrystalline Permalloy) by a 1 μm trench. This pattern was defined using the edgestream code (a mistake in the input shape resulted in one line not milled to the same depth as the rest of the trench). The spotted nature of the milled areas is a consequence of preferential milling of crystallites orientated in certain directions [27, 28].

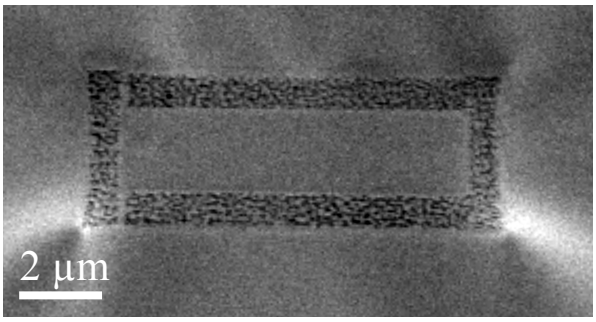

Figure 3.6: SEM image of a FIB-defined pattern in a polycrystalline thin film of Permalloy. A 2 μm by 8 μm rectangle isolated from the otherwise continuous film by milling a 1 μm wide trench.

3.4.3 Ion irradiation

The properties of some magnetic materials can be significantly modified by the FIB even at low ion doses which do not cause sputtering[2]. One ramification of this is that great care must be taken when using the FIB to pattern or fabricate cross-sections, to not unknowingly expose areas of the sample to the ion beam. Irradiation is performed much the same way as patterning, only using lower dwell times and/or number of passes to expose the sample to a lower level of ion irradiation. More precise discussion of ion irradiation is left to Chapter 6, which investigates skyrmion nucleation at artificial defects fabricated in Co-based multilayers by ion irradiation. In such cobalt based multilayers, ion irradiation is found to locally lower the magnetic anisotropy and increase the coercivity in a dose-dependent manner [9–13]. The secondary effects of ion irradiation include a number of interesting changes to the magnetic behaviour, i.e. changes in the magnetic states supported [14, 15, 29]. Another particularly interesting example is metastable face-centred cubic Fe which is paramagnetic at room temperature, and upon exposure to ion irradiation, transforms to body-centred cubic Fe which is ferromagnetic at room temperature [30, 31].

[2]The ion dose threshold, above which magnetic properties are modified, depends on the material system and on the nature of the incident ions. For example, a study by Benitez et al. detects changes in the magnetic properties of a Cr(3 nm)/Py(10 nm)/Cr(5 nm) nanowire with a Ga^+ ion dose of 4×10^{15} ions/cm^2 [14], where in Chapter 6 four different multilayer sample were studied and the 'critical' magnetic-property-altering dose of Ga^+ ions ranged from 5×10^{15} to 1×10^{17} ions/cm^2 on the different multilayers.

3.5 Transmission electron microscopy

The transmission electron microscope (TEM) is an essential tool in material science; it provides access to an extraordinary amount of information at the atomic and nano-scales including (but not limited to) structural information, chemical information and - critically for this thesis - information on the magnetic induction of the sample.

The advent of the TEM is correlated to De Broglie's revolutionary work on the theory of wave-particle duality, where he postulated that all matter can exhibit wave-like behaviour with a wavelength λ proportional to its momentum p ($\lambda = h/p$, where h is Planck's constant). Within five years De Broglie's theory was proven by electron diffraction experiments [32, 33] and within another five years, in 1932, the first TEM was built by Knoll and Ruska [34].

This section will first outline the basic operating principles of the TEM, before discussing two types of imaging key to the work presented in this thesis: structural imaging and magnetic imaging.

3.5.1 Operating principles and image formation

All electron microscopes (SEMs described in section 3.4 as well as TEMs) comprise an electron source, a series of electromagnetic lenses, apertures and detectors. There are two kinds of electron sources: thermionic and field-emission. In short thermionic sources (which extract electrons by heating) produce less coherent electrons than field-emission sources (which extract electrons by application of a large potential difference between the source and an anode). All TEM in this thesis was performed on the JEOL ARM 200cF which uses a field-emission electron source. The electron source forms part of the 'electron gun' which, as a unit, is responsible for extracting electrons from the source, accelerating them to the desired operating voltage of the TEM while also focusing the electrons to a point (known as the gun crossover).

The accelerating voltage used in all parts of this thesis is 200 kV. For electron energies above 100 kV, relativistic effects must be included and the electron wavelength is then given by

$$\lambda = \frac{h}{\sqrt{2m_0eV[1 + (eV/2m_0c^2)]}}, \tag{3.1}$$

where h is Planck's constant, V is the accelerating voltage, m_0 and e are respectively the rest mass and charge of the electron, and c is the speed of light. Using eq. 3.1, the wavelength of 200 kV electrons is 2.51 pm. The resolution of a microscope with a perfect lens system is theoretically limited by the wavelength of the illuminating radiation (be that photons/electrons/ions); microscopes that achieve this theoretical resolution are labelled 'diffraction limited'. The theoretical diffraction limited resolution d is described by Abbe's limit as

$$d = \frac{\lambda}{2n\sin(\theta)}. \tag{3.2}$$

The term $n\sin(\theta)$ is the numerical aperture, which relates to the refractive index n of the medium the imaging radiation travels through and the semi-angle θ of the spot formed by the imaging probe. Hence, one obvious advantage of TEM over conventional visible light microscopy is that the wavelength of 200 kV electrons is five orders of magnitude smaller than (400 nm wavelength) light.

In the TEM, after electrons are produced and accelerated by the electron gun, they then pass through a series of electromagnetic lenses. Because electrons are charged particles, they can be focused by electromagnetic lenses (which use magnetic fields to focus the electrons in much the same way as convex glass lenses are used to focus light). Electromagnetic lenses are imperfect and prone to aberrations which limit the resolution of TEMs to about 50 λ [35]; they are therefore aberration limited rather than diffraction limited (like most optical systems). The most serious aberration is spherical aberration C_S, which causes off-axis electrons to converge more than on-axis electrons (principally there is a radial variation in the lens focal length); followed by chromatic aberration C_C, where the convergence of the electrons varies with the electron energy (wavelength). The effects of C_C

can be minimised by improving the monochromaticity of the electron source, or by using a monochromator [36]. Correcting for C_S is more complex and can be mitigated using 'aberration-correctors' which are divergent multi-polar lenses which counteract the effects of C_S [37, 38]. The best modern TEMs now have a resolution of about 20 λ (0.05 nm) [35] - allowing routine atomic scale imaging.

There are two ways to configure a TEM. The main difference between the two is that the beam reaches the sample in one configuration as a plane wave - this is conventional TEM (CTEM) - and in the other configuration as a focused spot which is rastered over the sample - this is scanning TEM (STEM)[3]. The JEOL ARM 200cF TEM at Glasgow is C_S corrected in STEM mode only. Example ray diagrams of the TEM (based on the JEOL ARM at Glasgow) configured in both modes are supplied in Fig. 3.7, with the sample drawn in red situated around the centre of the diagrams. There are three mains sets of lenses, from the top down they are: the condenser system, imaging system and projection system. Each lens 'system' is drawn in a different colour in Fig. 3.7. The condenser system defines the beam intensity, spot size and configures the illumination to be either STEM or CTEM. CTEM mode will be described first before discussing STEM.

In CTEM mode (Fig. 3.7(a)), C2 and the upper objective lens (in this microscope the upper objective lens acts as a third condenser lens) are excited such that the electron illumination is parallel to the sample surface. After transmission through the sample, the lower objective lens focuses all electrons to a spot in its back focal plane. An objective aperture is inserted into the back focal plane of the lower objective lens which restricts the angular spread of the electrons allowed to form the final image (enhancing contrast). In the CTEM configuration the microscope can be operated in imaging mode and in diffraction mode (Fig. 3.7(a) depicts the imaging mode). Imaging and diffraction mode are selected with the intermediate lens of the projection system which, depending on its strength, selects either the back focal plane or the image plane as its object. The other lenses in the projector

[3]Outwith this chapter CTEM is simply referred to as TEM.

system are responsible for magnifying the image and selecting the camera length. In CTEM a camera is used to collect either an image or a diffraction pattern.

In STEM mode (Fig. 3.7(b)), C2 and the upper objective lens configure the illumination to be highly convergent so it reaches the sample as a focused spot. In this mode the C2 aperture is called the probe forming aperture, and defines the semi-convergence angle (and hence resolution) of the probe. Scanning coils are responsible for rastering the electron beam over the sample while simultaneously keeping the beam parallel to the optic axis as it passes through the sample. In

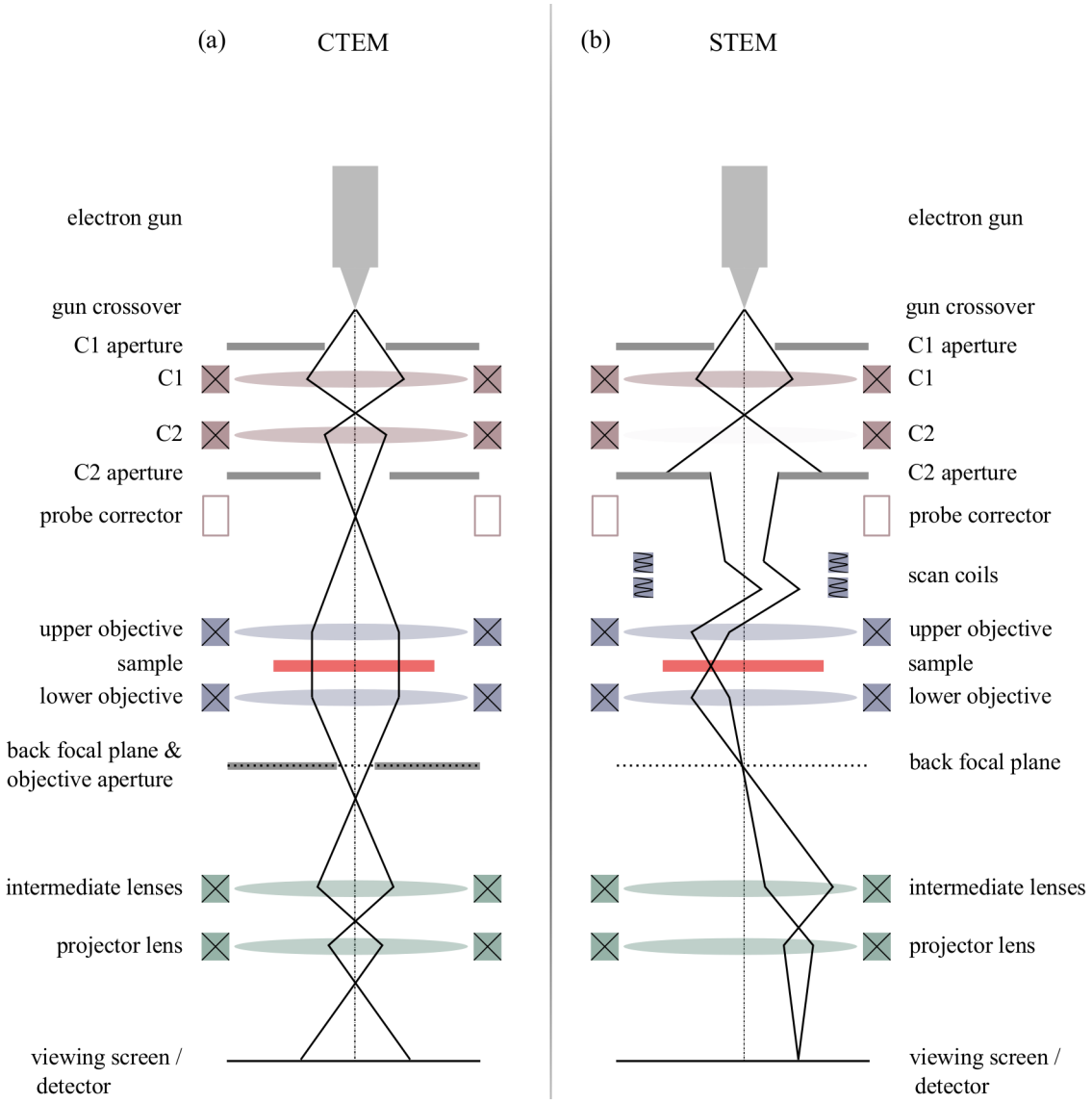

Figure 3.7: Example ray diagrams of a TEM configured in (a) conventional TEM mode and (b) scanning TEM mode.

contrast to CTEM, in STEM the microscope is always in diffraction mode and therefore the projection system is used to set the camera length. In STEM, images are built up time sequentially, pixel by pixel, as the electron beam is rastered across the sample. There is a range of specialised detectors, arranged in geometries that select different ranges of scattering angles in the diffraction pattern, available to form the final image in STEMs. As the detector geometry is specific to the imaging mode, further discussion is left to sections 3.6 and 3.7.5.

Like all microscopes, the TEM is an instrument where radiation effectively transfers information from a sample to an image. If the sample is represented by a function f($\mathbf{r}$), and the final image is represented by a function g($\mathbf{r}$) then:

$$g(\mathbf{r}) = f(\mathbf{r}) \otimes h(\mathbf{r}' - \mathbf{r}) \tag{3.3}$$

where $h(\mathbf{r}' - \mathbf{r})$ is the point spread function of the microscope. Eq. 3.3 can also be represented in Fourier (reciprocal) space as

$$G(\mathbf{k}) = F(\mathbf{k})H(\mathbf{k}). \tag{3.4}$$

where $\mathbf{k}$ is the position in reciprocal space. The term $H(\mathbf{k})$ is known as the contrast transfer function (CTF) of the microscope. It determines how well different spatial frequencies of the sample are transferred to the final image, it depends on the microscope properties. In particular, $H(\mathbf{k})$ is a function of image defocus, the chosen apertures and lens aberrations [39].

The next two sections discuss in turn the contrast mechanisms and detection methods behind the two types of TEM imaging used in this thesis: structural imaging and magnetic imaging.

3.6 Structural imaging in the TEM

Two kinds of structural imaging are used in Chapter 6: bright field (BF) TEM and high angle annular dark field (HAADF) STEM imaging. As electrons are transmitted through samples they undergo a number of elastic and inelastic scattering processes which give information on the samples structure and composition. Elastic

electron scattering (diffraction) is described by Braggs law, where the condition for constructive interference is given by:

$$n\lambda = 2d\sin(\theta), \tag{3.5}$$

where n is a positive integer, λ is the wavelength of the incident electrons, d is the separation of the atomic planes in a crystalline material, and θ is the angle of the incident electrons with respect to the aforementioned atomic plane - which, due to the elastic interaction, is equal to the scattering angle. A diffraction pattern is produced when electrons scattered from successive atomic planes interfere constructively, i.e. when Eq. 3.5 is satisfied. For a crystalline material, a diffraction pattern is an array of bright spots, known as Bragg peaks. The samples studied in this thesis are exclusively polycrystalline (consisting of many randomly orientated crystalline grains); the diffraction pattern from a polycrystalline material is then a series of concentric rings as the condition in Eq. 3.5 is satisfied radially. With 200 kV electrons, Bragg scattering angles are typically around 10 mrad.

Electron diffraction forms the basis of bright field (BF) and dark field (DF) TEM imaging, as will be explained by way of Fig. 3.8 with schematics and TEM images (used with permission from Alison Cowan) of 20 nm thick polycrystalline ($Ni_{80}Fe_{20}$) Permalloy. As described in section 3.5.1 in CTEM a diffraction pattern is formed in the back focal plane of the objective lens. This is sketched in Fig. 3.5.1(a) where upon transmission through the sample (blue) some electrons are scattered (dotted lines) and some are unscattered (full lines) all of which are focused to spots by the objective lens. Using the projector system the diffraction pattern can be imaged directly, see Fig. 3.5.1(d) for an example diffraction pattern from a polycrystalline Permalloy sample. The central (unscattered) spot is masked as it is extremely intense and can easily damage the charge coupled device (CCD) camera used for image acquisition. In imaging mode, a BF image is formed by inserting an aperture into the back focal plane which obstructs all scattered electrons so only the unscattered electrons form the final image. The ray diagram corresponding to BF image formation and an example BF image are given in Figs. 3.8(b) and (e)

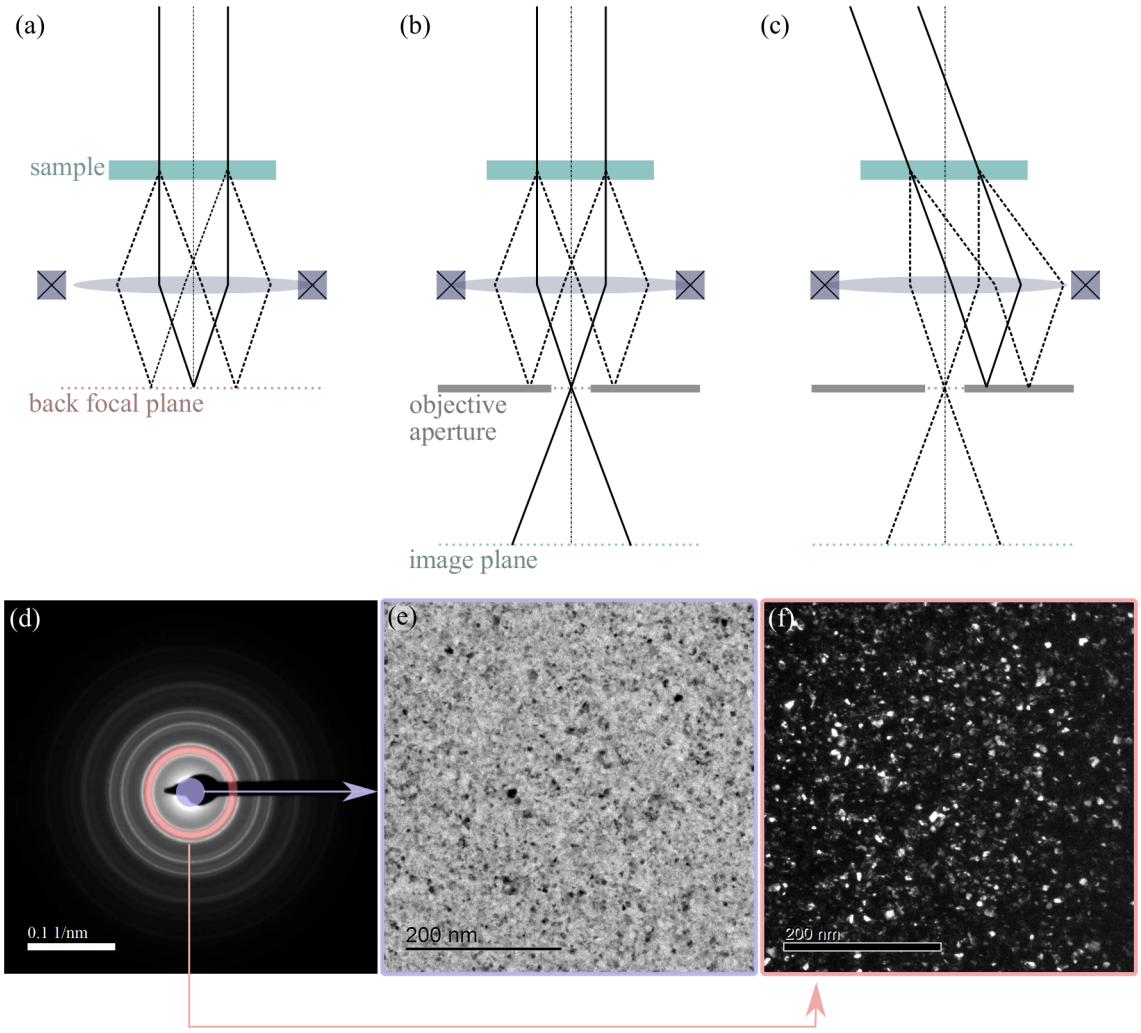

Figure 3.8: Ray diagrams illustrating diffraction, bright field (BF) imaging and dark field (DF) imaging are provided in (a), (b) and (c) respectively, where unscattered electron paths are represented by full lines and scattered electron paths by dotted lines. Corresponding experimental images are presented in the second row with: (d) a diffraction pattern, (e) a BF image, and (f) a dark field image. A purple and pink circle and annulus are overlaid on (d) to indicate what parts of the diffraction pattern form images (e) and (f). The experimental images are of 20 nm thick polycrystalline (Ni_80Fe_20) Permalloy acquired by Alison Cowan and used here with permission.

respectively. A DF image is formed by placing the aperture to allow passage of scattered electrons meeting certain (selected) diffraction conditions. This can be done in two ways: by placing the aperture off-centre; or by using a centred aperture, but tilting the beam so that scattered electrons travel on-axis. The second approach is the preferred method, named on-axis dark field imaging and sketched in 3.8(c), because off-axis electrons experience more aberrations from the electromagnetic

lenses, making it difficult to form high quality images. An example dark field image, formed from the [200] diffraction ring highlighted in pink in Fig. 3.8(d), is shown in 3.8(f). In a BF image, electrons which meet *any* Bragg conditions are dark while in a DF image, electrons that meet the *selected* Bragg condition are bright. BF images are used in Chapter 6 to evaluate the grain structure - both for finding the grain size distribution and evaluation of the impact of ion irradiation on the structure.

The above description refers to CTEM image formation but bright field imaging and dark field imaging have analogies in STEM. As described in section 3.5.1, in STEM the microscope is always in 'diffraction mode' and the focused electron beam rasters over the sample. The transmitted beam is not blocked by any objective aperture; all forward scattered electrons reach the detector plane and different types of images are formed by using detectors with different geometries. A solid detector is used to form images with only unscattered electrons (BF imaging) and an annular detector centred on the optic axis is used to collect annular dark field (ADF) images of Bragg scattered electrons at angles ≈ 10 mrad. Another annular detector surrounds the ADF detector and is set to collect electrons scattered to high angles of ≈ 100 mrad. Intuitively named, this is used for high angle dark field (HAADF) imaging. These high angle electrons result from inelastic Rutherford-like scattering from the nuclei of atoms comprising the sample. The number of electrons scattered by this mechanism varies with atomic number Z as $\approx Z^2$ [40]. Therefore, HAADF images allow Z-contrast imaging: elements of higher Z appear brighter (scatter more) compared to elements of lower Z.

An example HAADF image, of a cross-sectional lamella prepared from a Pt/Co/Pt trilayer sample, is shown in the top of Fig. 3.9(a). The sample was grown on a Si substrate, with a Ta seed layer deposited before the Pt/Co/Pt trilayer, and was capped with carbonaceous Cu to protect the sample during lamella fabrication. Each elemental change is visible in 3.9(a) through the contrast changes - Pt, the highest Z, is brightest and Si, the lowest Z, is darkest. The approximate boundaries between each element are overlaid on the line trace taken from the HAADF image

in 3.9(b). HAADF images are used in Chapter 6 to resolve the layer structure of the Pt/Co/Ir stacks and assess the impact of ion irradiation on the layer uniformity.

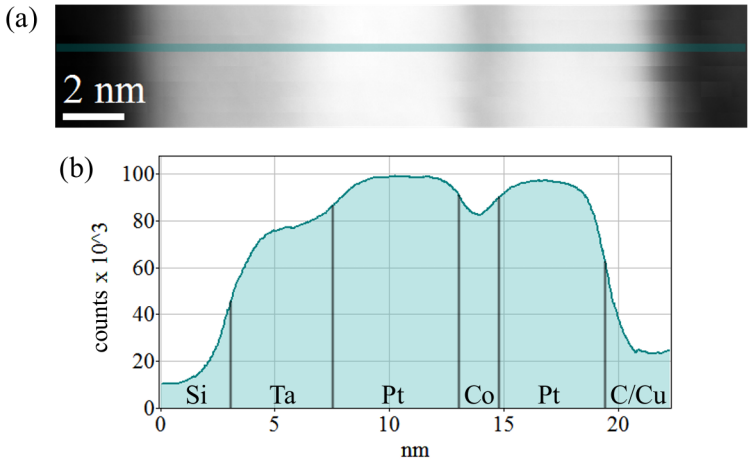

Figure 3.9: (a) An example high angle annular dark field (HAADF) image of a Pt(Z=78)/Co(Z=27)/Pt trilayer sample, grown on a Si (Z=14) substrate with a Ta (Z=73) seed layer and capped with carbonaceous (Z=6) Cu (Z=29) which shows Z contrast. (b) line trace through (a) which is annotated with the approximate elemental boundaries.

3.7 Magnetic imaging in the TEM

Given magnetic materials importance to modern society and the ongoing demand for smaller and smaller electromagnetic components, sensitive and high resolution magnetic imaging methods play a central role in current research focusing on novel magnetic phenomenon.

As already discussed in the context of electromagnetic lenses, electrons (as charged particles) change their trajectory when they pass through areas of magnetic induction. Therefore, in the TEM, transmission through magnetic samples leads to modification of the beam. This basic physics makes the TEM, with its inherent high resolution, a natural choice for imaging of magnetic materials. Later, in sections 3.8 and 3.9, alternative magnetic imaging methods are briefly discussed.

3.7.1 Field-free TEM

Samples in a TEM are situated between the two pole pieces of the objective lens, in a large magnetic field (orientated along the optic axis) that is often greater than 1 T. Magnetic fields of this magnitude are more than enough to fully saturate the vast majority of magnetic samples - erasing the magnetic features to be imaged. Therefore, to perform magnetic imaging, the TEM has to be modified. The objective lens must be switched off, leaving the sample in the remanent field of the lens which is $\approx$ 10 mT in the JEOL ARM 200cf. This strength of magnetic field will not cause modification to in-plane magnetic materials with a large demagnetising factor [41]. However, perpendicularly magnetised materials (and certain experiments) require a fully field-free environment. This is realised by specialised hardware used to manually send positive and negative values of current though the objective lens, while monitoring the resultant field in the sample area with a Hall probe [42]. This set up is used to create field-free environments and also to set field strengths between 0 - 10 mT (i.e. below the remanent field) in the sample area. Two Lorentz lenses are included in the microscope that replace the imaging functions of the objective lens, these are called the condenser mini and objective mini lenses which replace the upper and lower objective lenses respectively. These lenses are less

powerful than the objective lenses, situated further from the sample and suffer from huge spherical aberrations (C_s is four orders of magnitude larger than the standard objective lens [43, 44]). With aberration correction, resolution of 1 nm can be achieved in 200 kV field-free STEM [44]. This mode of microscope operation is often called Lorentz mode, owing to the type imaging performed in field-free and low-field environments.

The objective lens of the microscope can be partially excited to perform *in situ* magnetising experiments, where the evolution of the magnetisation under a magnetic field can be imaged in real-time. The field of the objective lens $\mathbf{H}$ is parallel to the optic axis, thus clearly suited for magnetisation experiments on perpendicularly magnetised materials. By tilting the sample by an angle θ, then a component $\mathbf{H}\sin(\theta)$ is can be introduced in the sample plane. This is sketched in Fig. 3.10. As already mentioned, for in-plane magnetic materials with a large demagnetising factor, a small out-of-plane field will not disturb most magnetic structures [41], but application of weak in-plane fields can be used intentionally manipulate the magnetic structure and move magnetic objects like domain walls and vortices (as in Chapter 7). *In situ* magnetising experiments were also performed on perpendicular magnetic materials (Chapter 6).

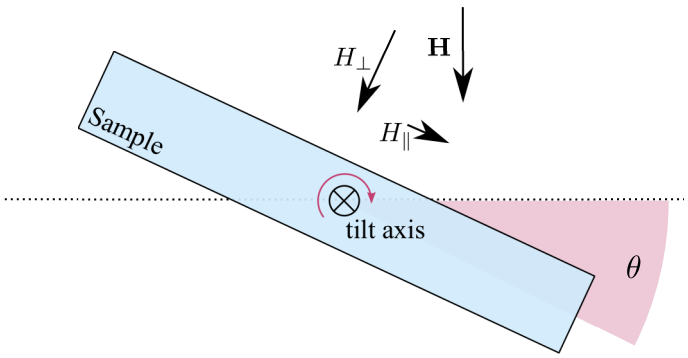

Figure 3.10: The objective lens can be weakly excited to create a field $\mathbf{H}$ at the sample parallel to the optic axis. If the sample is tilted by θ, a component $H_\parallel = \mathbf{H}\sin(\theta)$ is introduced parallel to the sample and $H_\perp = \mathbf{H}\cos(\theta)$ perpendicular to the sample. This can be used for *in situ* magnetising experiments in the TEM.

3.7.2 Lorentz TEM

Lorentz TEM is an umbrella term referring collectively to all non-interferometric magnetic imaging methods performed in the TEM. This includes Fresnel and DPC imaging, used in this work and covered in detail in sections 3.7.3 and 3.7.4, as well as Focault imaging, and low-angle electron diffraction which are discussed briefly in 3.7.6 along with electron holography which can also be used to image magnetic materials.

As electrons pass through a magnetic material they are deflected by an angle β_L as sketched in Fig. 3.11. The origin of the deflection can be considered using both classical and quantum mechanical formulations. Using classical physics, the electron deflection is explained though the Lorentz force $\mathbf{F_L}$:

$$\mathbf{F_L} = -e(\mathbf{v} \times \mathbf{B}), \tag{3.6}$$

where e and $\mathbf{v}$ are, respectively, the charge and velocity of the electron and $\mathbf{B}$ is the local magnetic induction. Two points need to be discussed with regard to equation 3.6: firstly, the electrons are deflected by the magnetic induction $\mathbf{B}$ not the magnetisation $\mathbf{M}$; and secondly, because of the cross product, components of $\mathbf{B}$ parallel to the e-beam cause no deflection. With regard to the first point, the magnetic induction $\mathbf{B}$ and magnetisation $\mathbf{M}$ are related through the expression

$$\mathbf{B} = \mu_0(\mathbf{M} + \mathbf{H}), \tag{3.7}$$

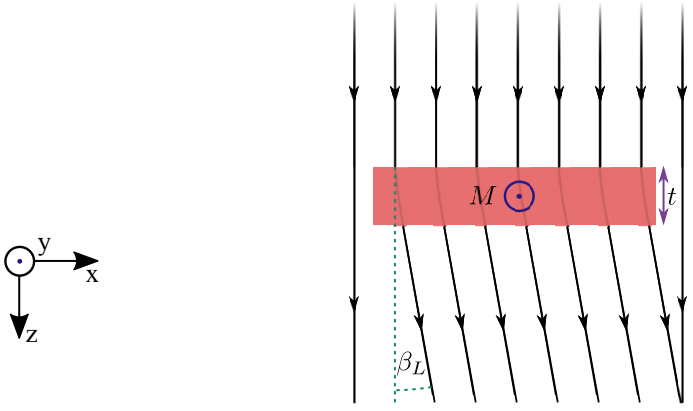

Figure 3.11: Electrons (represented by the black lines) are deflected by an angle β_L when they pass through a magnetic sample with magnetisation $\mathbf{M}$ and thickness t.

where **H** is the stray field resulting from the magnetic configuration of the sample. This means that care needs to be taken when interpreting Lorentz TEM images as contrast arises from the magnetic induction of the sample which can differ significantly from its magnetisation.

By integrating Eq. 3.6 over the electron path, and assuming the electron trajectory remains mainly along the optic axis, an expression for the deflection β_L is found:

$$\beta_L = \frac{e\lambda}{h} \int_{-\infty}^{\infty} (\mathbf{B} \times \hat{\mathbf{n}})\, d\mathbf{l}, \tag{3.8}$$

where e and λ are the charge and wavelength of the electron respectively; h is Planck's constant; $\hat{\mathbf{n}}$ is a unit vector defining the electron trajectory; and $d\mathbf{l}$ is the path of the electron. For an untilted, in-plane uniformly magnetised material of thickness t where $B_s = \mu_0 M_s$, Eq. 3.8 can be simplified significantly to

$$\beta_L = \frac{e\lambda B_s t}{h} \tag{3.9}$$

Using this equation, the expected deflection of a 200 kV electron from 10 nm thick Permalloy (B_s = 1 T) is 6.1 μrad. Clearly the assumption that electron trajectory remains predominately along the optic axis, made when deriving Eq. 3.8, is valid; furthermore, because Lorentz deflections are around four orders of magnitude smaller than typical Bragg deflections, the two sources of deflection are not easily confused.

While the classical formulation is ideal for a conceptual understanding of Lorentz microscopy, to describe Lorentz TEM quantitatively a full quantum mechanical approach is required. In this case, the sample is considered a phase object which modifies, upon transmission through the sample, the phase of the electron wave (i.e. the illuminating electron beam).

The quantum mechanical phase shift of electrons by electromagnetic potentials is described by the Aharanov-Bohm effect (illustrated in Fig. 3.12), where the phase shift ϕ between two electrons travelling from the same start point to the same end point via different routes is

$$\phi = -\frac{e}{\hbar} \int_{-\infty}^{\infty} \mathbf{A} \cdot d\mathbf{l}. \tag{3.10}$$

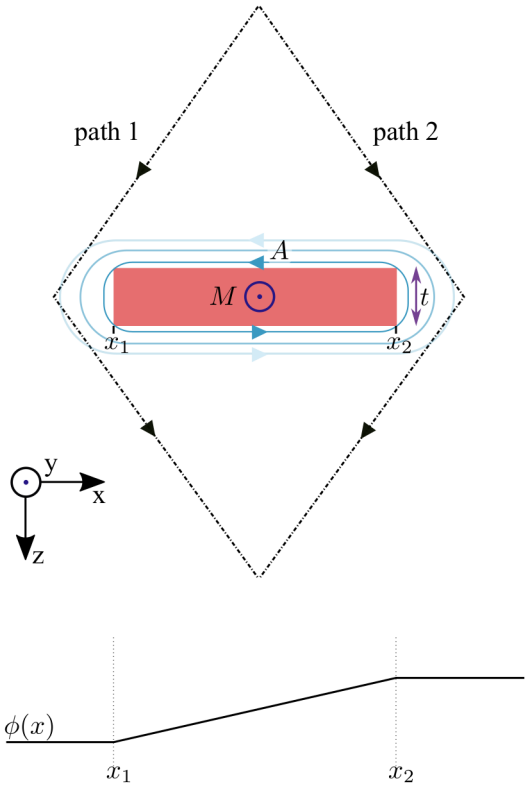

Figure 3.12: Sketch of the Aharanov-Bohm effect, where two electrons, with the same start and end point which travel different paths through a magnetic potential **A**, acquire a phase shift - as shown by the sketch in the lower half of the function $\phi(x)$ where ϕ is the phase.

In this equation $\hbar$ is the reduced Planck's constant and **A** is the magnetic vector potential where $\mathbf{B} = \nabla \times \mathbf{A}$. Counter-intuitively, due to the dependence on **A**, the phase of the electrons can be altered in regions with no electromagnetic fields. An expression relating to **B** is found by applying a two-dimensional grad operator (referring to a plane perpendicular to $\hat{\mathbf{n}}$, the electron beam trajectory) to Eq. 3.10, using standard vector calculus identities and simplifying with $\mathbf{B} = \nabla \times \mathbf{A}$:

$$\nabla_{\perp}\phi = \frac{e}{\hbar}\int_{-\infty}^{\infty}(\mathbf{B} \times \hat{\mathbf{n}})dl. \tag{3.11}$$

This equation is very similar to Eq. 3.8 and

$$\nabla_{\perp}\phi = \frac{2\pi}{\lambda}\beta_L, \tag{3.12}$$

thus demonstrating the equivalence of the quantum and classical approaches.

The expression for the phase, Eq. 3.10, may be rewritten such that the effect of the magnetisation **M** is explicit [45]. First of all, Eq. 3.10 is reformulated to depend on **J** the current density vector:

$$\phi = -\frac{e\mu_0}{\hbar 4\pi r} \otimes \int (\mathbf{J} \cdot \hat{\mathbf{n}})\, dl, \tag{3.13}$$

J is the sum of conduction currents, $\mathbf{J_C} = \nabla \times \mathbf{H}$; and Ampérian currents, $\mathbf{J_M} = \nabla \times \mathbf{M}$; and displacement currents, $\mathbf{J_D} = d\mathbf{D}/dt$. But, generally, in a TEM environment there are no conduction currents or time-varying electric fields and **J** consists of only Ampérian currents therefore:

$$\phi = -\frac{e\mu_0}{\hbar 4\pi r} \otimes \int (\nabla \times \mathbf{M}) \cdot \hat{\mathbf{n}}\, dl. \tag{3.14}$$

From this equation it is clear that the origin of contrast in Lorentz microscopy is related to the component of the Ampérian current of the sample parallel to the electron beam [45]. This is far more straightforward and convenient to consider than the integral of **B** over all space.

An additional phase change, ϕ_E, occurs when electrons pass through all materials (magnetic and non-magnetic) which is electrostatic in origin. The phase change varies with both the thickness and mean inner potential V of the sample; in full

$$\phi_E = \frac{\pi V_0 t}{\lambda V}, \tag{3.15}$$

where E is the accelerating voltage of the electrons. The total phase shift is then the sum of these two magnetic and electrostatic phase shifts. However in this thesis, in the areas of interest (assuming continuous films), the mean inner potential and thickness of the sample are non-varying and, therefore, the electrostatic phase shift is constant and does not affect any measurements.

As demonstrated, Lorentz microscopy is a branch of phase contrast imaging, though the phase changes involved are both much larger and more slowly varying than in other phase contrast imaging methods [46, 47]. The various modes of Lorentz microscopy all capture the phase change ϕ of the electrons as they pass through magnetic samples but in different ways; in Fresnel mode the contrast

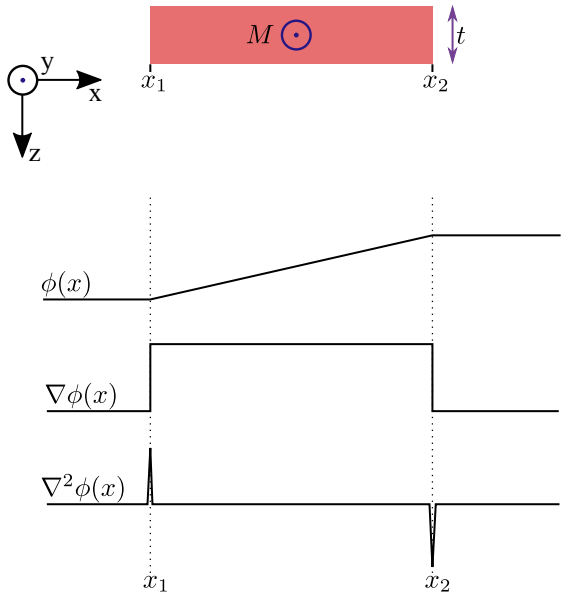

Figure 3.13: Electrons travelling along $\hat{\mathbf{z}}$ through the magnetic material sketched in red experience a phase shift ϕ. DPC mode of Lorentz microscopy is sensitive to the phase gradient $\nabla\phi$, and Fresnel mode is sensitive to the Laplacian $\nabla^2\phi$.

relates to the Laplacian of the phase $\nabla^2\phi$ and in DPC and Foucault it is related to the gradient of the phase $\nabla\phi$, as sketched in Fig. 3.13. Electron holography accesses the phase ϕ directly. Fresnel and DPC were widely used in this work and the following two sections discuss each in turn. Following this, Foucault imaging and electron holography are then briefly discussed.

3.7.3 Fresnel mode

Fresnel mode is a CTEM Lorentz microscopy technique. It is extremely straightforward to implement: so long as the conditions required for field free TEM are satisfied, it only requires defocusing the imaging lens. This is depicted schematically in Fig. 3.14, where the lens defocus is represented by Δ.

Electrons transmitted through sample areas with different magnetisation and therefore different magnetic induction (depicted to be along $\pm\ \hat{\mathbf{y}}$ in Fig. 3.14), experience different Lorentz deflections. These deflections may be imaged simply by defocussing the imaging lens to select an object plane below the sample, where the converging and diverging electrons lead to bright and dark image contrast respectively. Figure. 3.14 illustrates the formation of an over-focused image with

a positive defocus Δ. By using a negative defocus $-\Delta$, a virtual object above the sample can be imaged, this is an under-focused Fresnel image which has reversed contrast compared to an over-focused image. The position of the bright and dark contrast in the image intensity line trace correlates to the position of the domain walls in the sample, however, in Fig. 3.14 only the domain induction/magnetisation is specified and the domain walls are drawn as dark bands. This is to highlight the fact that, generally, the nature of the bright/dark contrast provides information on the direction of the domains not on the walls. With careful image interpretation, detailed information about the walls *can* be extracted from Fresnel images. This is the focus of Chapter 4 and comprises a large part of Chapter 5 and therefore detailed discussion of domain wall contrast in Lorentz microscopy is left to these chapters.

Two example Fresnel images are provided in Fig. 3.15, both taken from 8 nm of Permalloy. Figure 3.15(a) shows a Fresnel image of a three domain state where

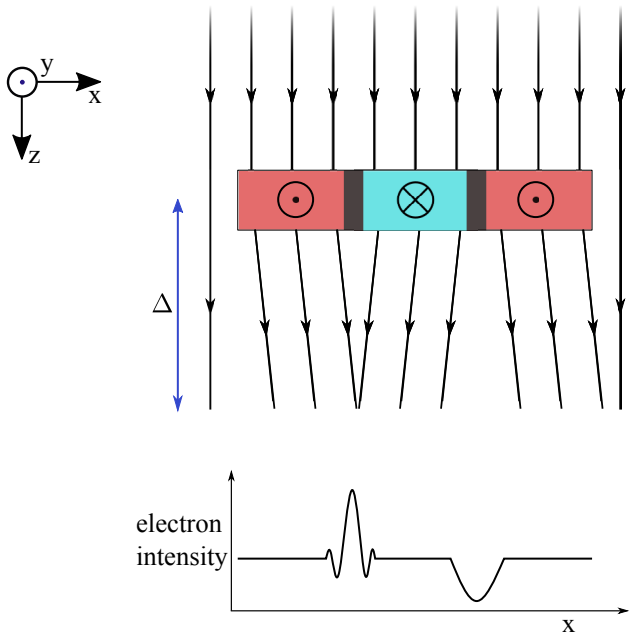

Figure 3.14: Schematic depicting Fresnel contrast in CTEM. The electrons are deflected in different directions as they pass through areas of different magnetisation, and therefore different magnetic induction. When the imaging lens is defocused by Δ the, a plane below the sample is imaged where the converging and diverging electrons resulting in bright and dark image contrast respectively. The position of the bright and dark contrast correlates with the position of the domain walls, but as is clear from the schematic, the source of the contrast is the domain magnetisation.

the magnetisation lies in-plane and the central domain is antiparallel to the two outside domains, therefore directly representing the configuration sketched in Fig. 3.14. Figure 3.15(b) shows a more complex multi-domain state supported by the FIB patterned element similar to the one given as an example in section 3.4.2.

The magnetic contrast in Fresnel images increases with increasing Δ but at the cost of blurring the image and decreasing the image resolution. Therefore, the precise value of Δ used in an experiment depends on the sample to be imaged - generally, the smallest defocus that provides a good contrast level is chosen. In most of this work, in fact in all results chapters except Chapter 7, involve materials that give only a small beam deflection (≈ 1 μrad) therefore large defoci ($\Delta > 1$ mm) must be used for sufficient magnetic image contrast. Only at small defocus values does Fresnel image contrast relate linearly to $\nabla^2\phi$, therefore it is generally considered to be a non-linear imaging mode with non-quantitative image contrast [48]. This is clear from Fig. 3.15(a) where the dark contrast is far broader than the bright contrast. The dependence on $\nabla^2\phi$ also means that areas of constant magnetisation give no Fresnel image contrast. Additionally, a particular strength of Fresnel imaging lies in imaging dynamic magnetisation processes owing to both the ease of implementation and relatively quick image acquisition time [49–52].

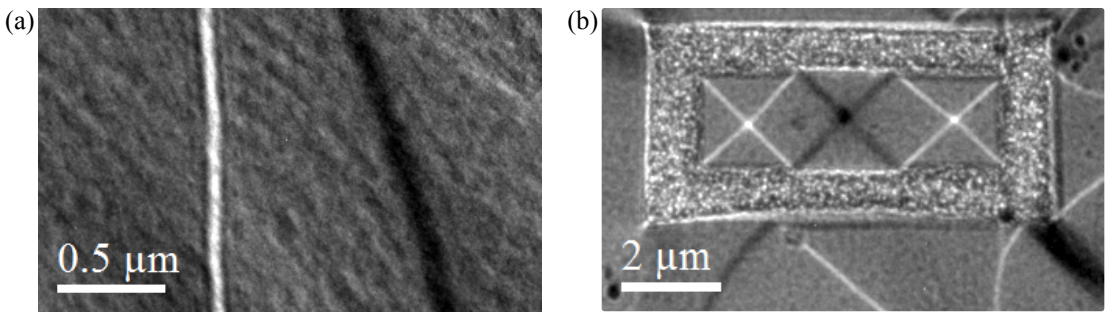

Figure 3.15: Two example Fresnel images taken from 8 nm of Permalloy with in-plane magnetisation. (a) shows a three domain state where the central domain is antiparallel to the two outer domains, and (b) shows a more complex multi-domain state stabilised in a FIB patterned rectangle.

Special cases: divergent magnetisation and out-of-plane magnetisation

Magnetisation that is either parallel to the electron beam or in-plane but divergent does not cause any phase shift, or equivalently any beam deflection[4]. These two scenarios are sketched in Figs. 3.16(a) and (b) respectively and consider electrons travelling along the z direction. Lorentz deflections arise from $\mathbf{B} \times \hat{\mathbf{z}}$ (Eq. 3.8) or equivalently $(\nabla \times \mathbf{M}) \cdot \hat{\mathbf{z}}$ (Eq. 3.14), projected through the thickness. Therefore, below Figs. 3.16(a) and (b) the configuration of the stray field and the curl of $\mathbf{M}$ is sketched (for the central domain only) to aid the following discussion of why these two scenarios do not cause a Lorentz deflection.

The configuration in Fig. 3.16(a) is considered first. In this case, most of the $\mathbf{B}$ $(= \mu(\mathbf{M} + \mathbf{H}))$ is parallel to z, therefore $\mathbf{B} \times \hat{\mathbf{z}} = 0$ and the small in-plane components of the stray field are of no effect because they cancel in projection. Considering the other formulation and Fig. 3.16(e), it is immediately obvious that no contrast is expected as $(\nabla \times \mathbf{M}) \cdot \hat{\mathbf{z}} = 0$.

The lack of phase shift from the second configuration, sketched in Fig. 3.16(b), is now considered. As sketched in Fig. 3.16(c), such a magnetisation configuration is associated with a predominantly in-plane stray field distribution that cancels in projection, i.e. $\mathbf{B} \times \hat{\mathbf{z}} \neq 0$ but $\int (\mathbf{B} \times \hat{\mathbf{z}})\, dz = 0$. Considering the formulation in Eq. 3.14 and Fig. 3.16(e) it is clear that $(\nabla \times \mathbf{M}) \cdot \hat{\mathbf{z}} = 0$

Both scenarios in Fig. 3.16 occur simultaneously in many technologically relevant thin film multilayer stacks that have out-of-plane domains separated by (divergent) Néel type walls. Such multilayered samples are the focus of Chapters 4, 5 and 6 therefore, in this section, the imaging of samples with out-of-plane and divergent magnetisation is discussed in detail.

Contrast can be generated very easily from the out-of-plane domains simply by tilting the sample as is sketched in Fig. 3.17 [53]. As depicted in Fig. 3.17, tilting around the axis sketched reconfigures the beam-sample geometry to regain

[4]Note that the following discussion is placed the context of Fresnel images specifically for ease of explaination, however, it applies equally to all TEM techniques that aim to extract magnetic information from the phase change of the electron beam

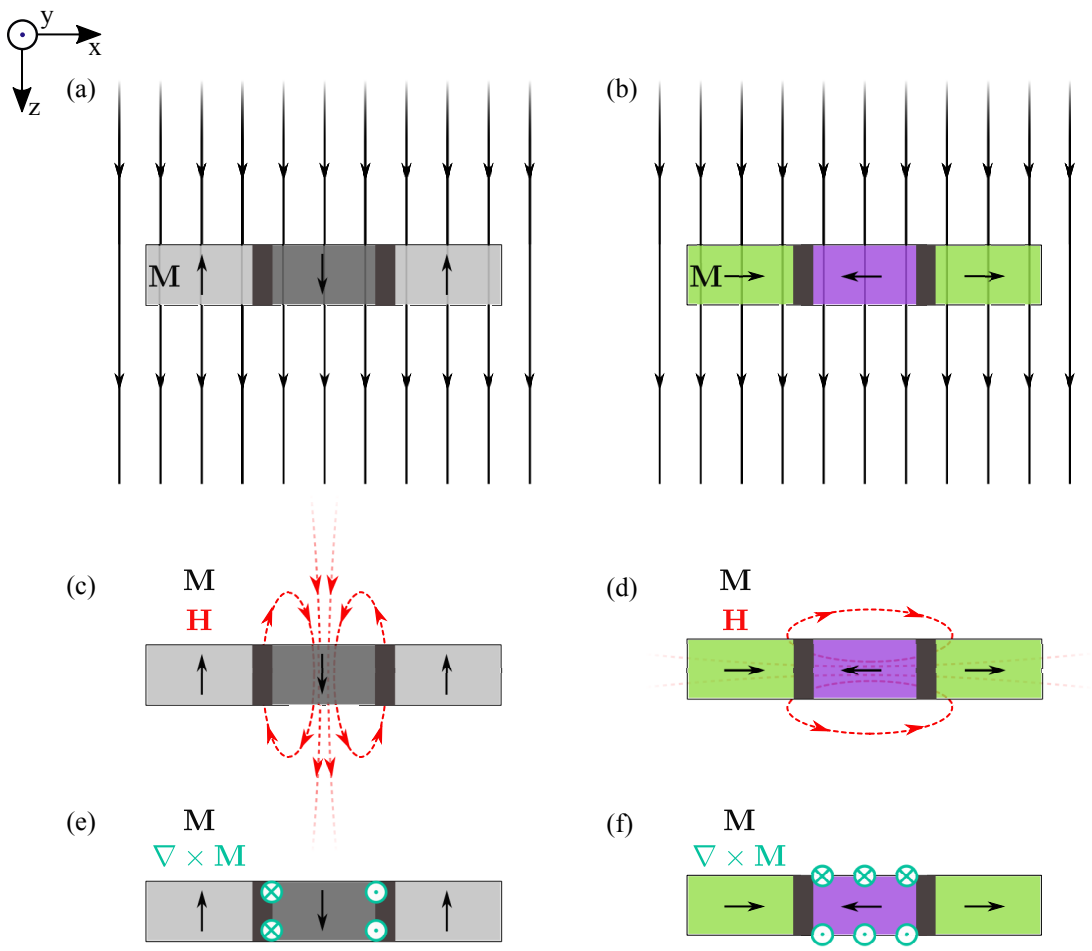

Figure 3.16: Both (a) magnetisation parallel to the electron beam and (b) divergent magnetisation distributions result in no phase shift. The stray field configuration and the curl of **M** associated with the central domain in (a) are sketched respectively in (c) and (e). Similarly, the stray field configuration and the curl of **M** associated with the central domain in (b) are sketched respectively in (d) and (f).

a non-divergent in-plane component like in Fig. 3.14. The Lorentz deflection from a sample with uniform perpendicular magnetisation tilted by θ is then

$$\beta_L = \frac{e\lambda}{h} B_s t \tan(\theta). \tag{3.16}$$

For a PMA multilayer comprised of ten 0.6 nm thick Co layers tilted by $\approx 20°$, β_L is 1 μrad. Two Fresnel images taken at zero tilt and a 20° tilt, from a sample with out-of-plane domains and Néel type walls, are shown in Fig. 3.18 respectively. The zero tilt image, Fig. 3.18(a), contains only non-magnetic information. After tilting by 20° about the axis indicated on the top left of Fig. 3.18(b), clear magnetic contrast is observed. In Fig. 3.18(b), the contrast is strongest for walls running

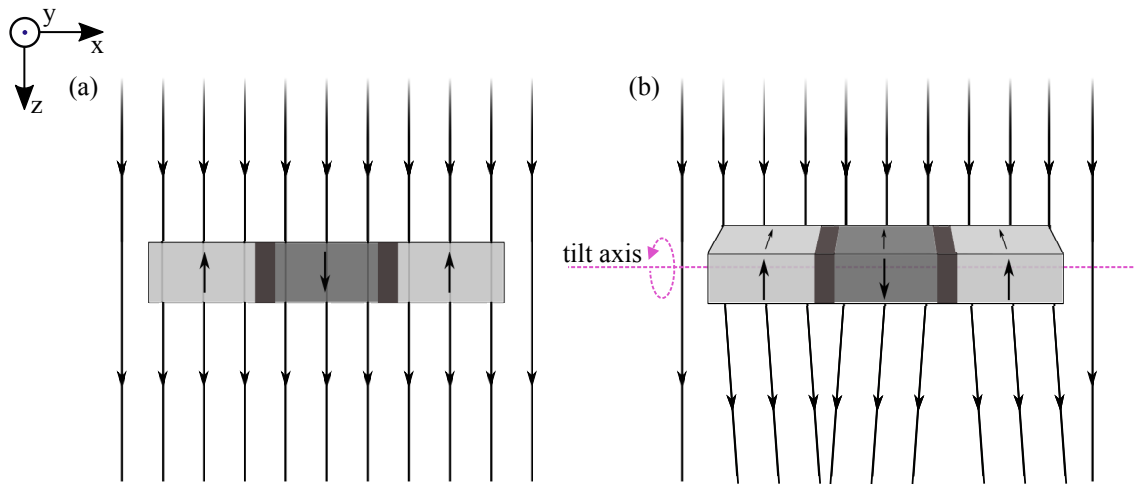

Figure 3.17: (a) Samples with out-of-plane magnetisation give no deflection in the TEM when the sample is normal to the beam trajectory. (b) If the sample is tilted, a component of the magnetisation is introduced perpendicular to the electron beam that results in a beam deflection.

perpendicular to the tilt axis and there is no contrast for walls running parallel to the tilt axis; the magnetisation orientated perpendicular to the electron beam introduced by a tilt axis parallel to the wall length is configured head to head or tail to tail, like in Fig. 3.16(b), leading to no deflection.

As explained in Chapter 2, samples with out-of-plane magnetisation that support Néel type walls and skyrmions are of great technological interest because effects arising from the fixed chirality of the walls [54, 55] and skyrmions [56–58]. It is, therefore, also of great interest to apply the high resolution and sensitive

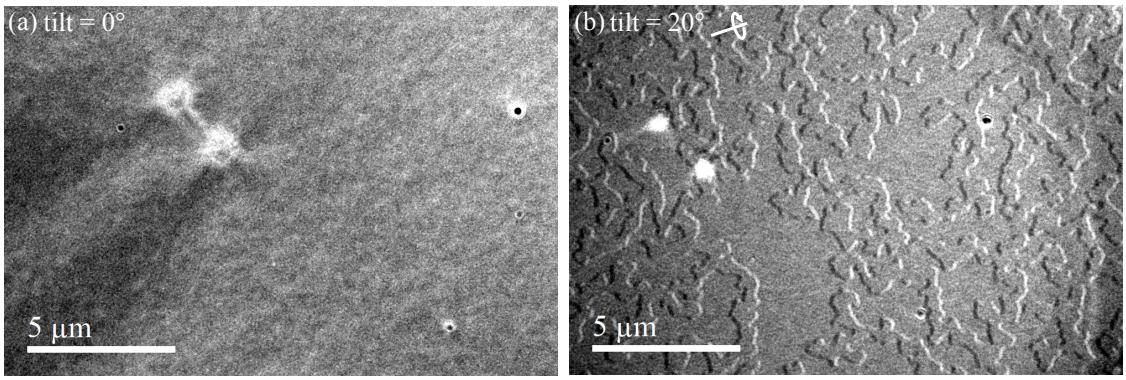

Figure 3.18: Experimental Fresnel images of a sample with out-of-plane domains and Néel walls taken at (a) zero tilt and (b) 20° tilt around the axis inset in the top left of the image.

imaging techniques of Lorentz microscopy to domain walls and skyrmion structures directly. This means extracting a contrast signature from the divergent domain walls themselves, to image their chirality. At the present time this has not been achieved experimentally but Chapter 4 details how the wall magnetisation, or equivalently wall chirality, can in principle be extracted from Fresnel images.

The microscope transfer function and determining Fresnel image defocus

The defocus of a Fresnel image is calculated retrospectively from the zeros of the contrast transfer function (CTF). The CTF $H(\mathbf{k})$ was introduced at the end of section 3.5.1 and describes how well different spatial frequencies, $\mathbf{k}$, are transferred to images. This can be written as $H(\mathbf{k}) = \sin(\chi(\mathbf{k}))$ where

$$\chi(\mathbf{k}) = \pi\Delta\lambda k^2 + \frac{1}{2}\pi C_S\lambda^3 k^4. \tag{3.17}$$

$H(\mathbf{k})$ is clearly zero when $\chi = n\pi$, where n is an integer. Assuming C_S is small compared to the defocus Δ, the first term in Eq. 3.17 dominates, then

$$\Delta = \frac{n}{\lambda {k_n}^2}, \tag{3.18}$$

where k_n is the spatial frequency corresponding to the nth zero. The CTF zeros are found by taking a fast fourier transform (FFT) of an image. The FFT of the image in Fig. 3.18(b) is given in Fig. 3.19(a), where each dark ring indicates spatial frequencies that are not transferred to the final image and therefore represents a zero of the CTF. By taking a radial average of the contrast in the FFT (example given in Fig. 3.19(b)), range of CTF zeros can be identified and Δ is obtained from the gradient of ${k_n}^2$ plotted against n. The defocus used for the image in Fig. 3.18(b) was calculated to be 2.4 mm.

3.7.4 DPC mode

Differential phase contrast (DPC) imaging is a STEM technique that provides quantitative maps of the integrated magnetic induction of the sample. It is an in-focus technique and is consequently higher resolution than Fresnel mode.

The general principle behind DPC imaging is sketched in Fig. 3.20. The

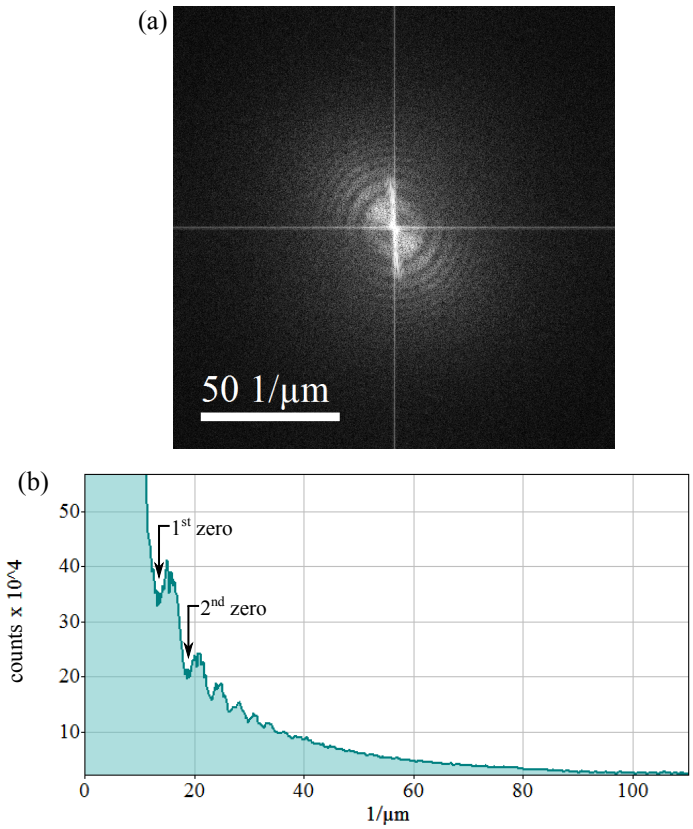

Figure 3.19: (a) FFT of a Fresnel image where the concentric dark rings are the zeros of the contrast transfer function. (b) Radial average of (a) from which the spatial frequencies of the CTF zeros can be measured out to a high order.

electron beam is focused to a fine point with a semi-convergence angle α. α is defined by the condenser aperture and determines the spatial resolution of the image: larger aperture $\equiv$ higher α $\equiv$ higher resolution. The beam deflection β_L caused by the sample is accessed directly as a shift of the transmitted beam in the detector plane of the microscope as indicated in Fig. 3.20. DPC imaging is generally performed with a long camera length so that only the central, undiffracted, disk is on the detector. Because of Eq. 3.8, the deflections measured by DPC can be converted into maps of the integrated magnetic induction $\mathbf{B}t$.

Example DPC images, mapping two orthogonal components of the integrated magnetic induction specified by the double-headed arrows in the upper left corner of the images, are provided in Fig. 3.21. These images were acquired from the same FIB patterned Permalloy element as the Fresnel image in Fig. 3.15(b). In Fig. 3.21, areas that are black or white correspond to areas with magnetisation

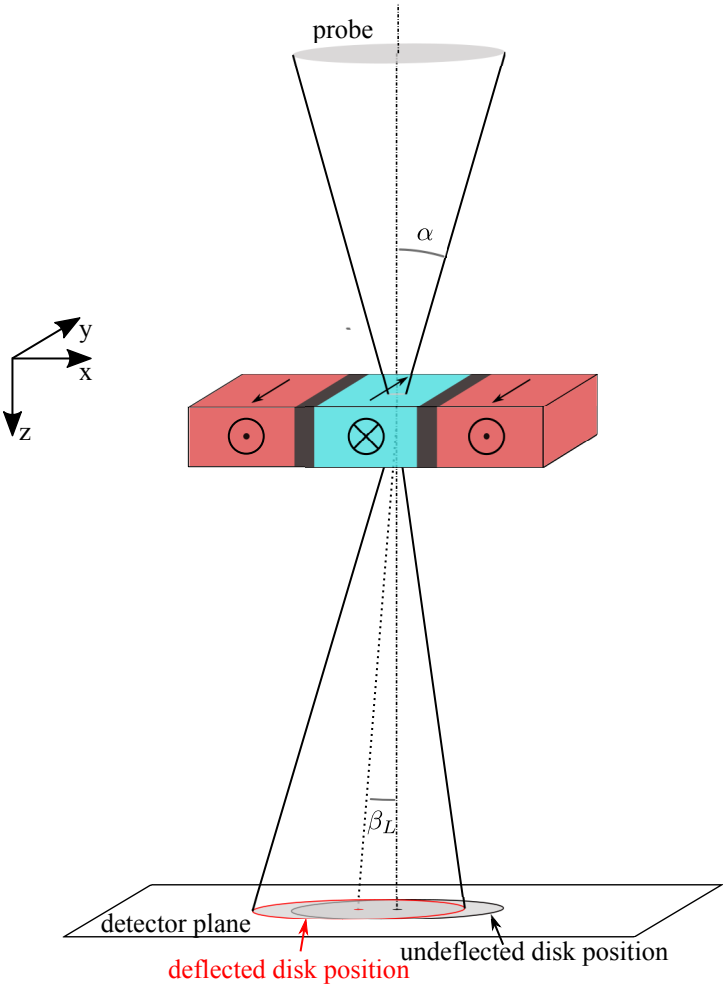

Figure 3.20: Schematic of differential phase contrast (DPC) imaging

parallel to the arrow annotated in the top left corner. Because this sample has in-plane magnetisation, the complicating factors discussed at the end of section 3.7.3 are not relevant and, in the black and white regions it is expected that $\beta_L = e\lambda B_s t/h$ where $B_s = \mu_0 M_s$.

Figure 3.21 shows clear magnetic contrast, however, there is also shorter-range background undulations present. This contribution to the contrast is diffraction-based and arises from the grains that form polycrystalline samples. Figure 3.22 shows a higher magnification BF image of the same sample in which the grains are clearly visible. In Fig. 3.21 the effect of the crystallites is slight, this is for a few reasons. Firstly, and most importantly, the deflections are measured with an advanced detection method, covered in section 3.7.5, developed precisely to

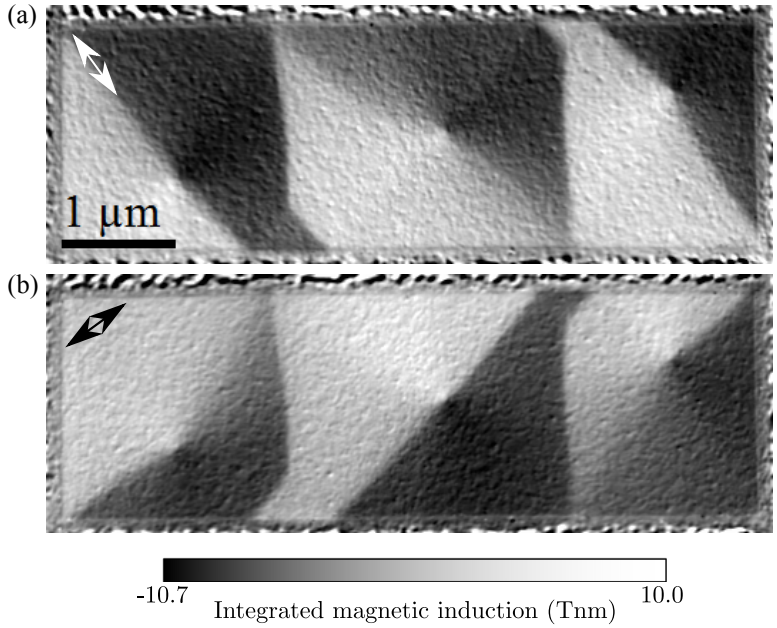

Figure 3.21: Two DPC images, mapping the integrated magnetic induction in two orthogonal directions, of a 8 nm thick FIB defined Permalloy element.

minimise this contrast. Secondly, it is a fairly low magnification DPC image, with 12 nm pixels which is larger than many of the crystallites in the sample. And thirdly, the sample is a fair thickness (8 nm) of Permalloy ($B_s \approx 1$ T) which gives a relatively large deflection of $\beta_L \approx 5$ μrad. Using standard detection methods, in high magnification images, the crystallites are no longer partially filtered by the scan sampling frequency and can obscure the magnetic contrast see Fig. 3.23 [59].

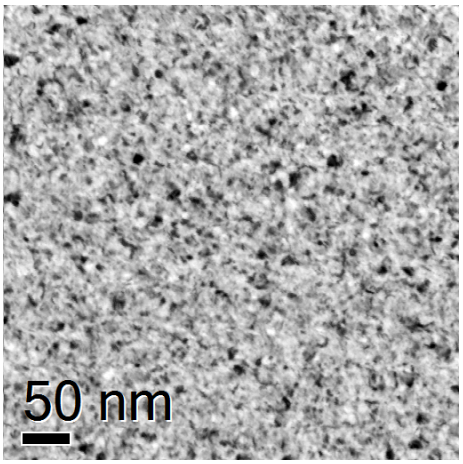

Figure 3.22: High magnification bright field image showing the grains in the polycrystalline sample used as example of DPC imaging in Fig. 3.21

The severity of this effect is, in essence, a competition between of the amount of diffraction contrast and magnitude of the Lorentz deflection. For low moment ($\mathbf{B} \lessapprox 0.5$ T) magnetic materials (or equivalently materials magnetised in the 'wrong' direction where tilting causes only a component of $\mathbf{B}$ to result in a beam deflection) and strongly scattering materials (high Z or thick) the diffraction contrast is always problematic, even at low magnifications. Skyrmionic multilayers are a material with a small Lorentz deflection and strong diffraction contrast where DPC imaging is challenging.

In the following section the detection of the beam shift is explained in detail for different detector configurations. It discusses how the beam shifts are measured with standard detectors and how the short-range electrostatic grain contrast is better isolated from the long-range magnetic contrast using pixelated detectors. These recent advances in DPC detection are highly relevant to this thesis as they enable application of quantitative DPC imaging to the study of technologically important skyrmionic multilayer materials studied in Chapters 5 and 6.

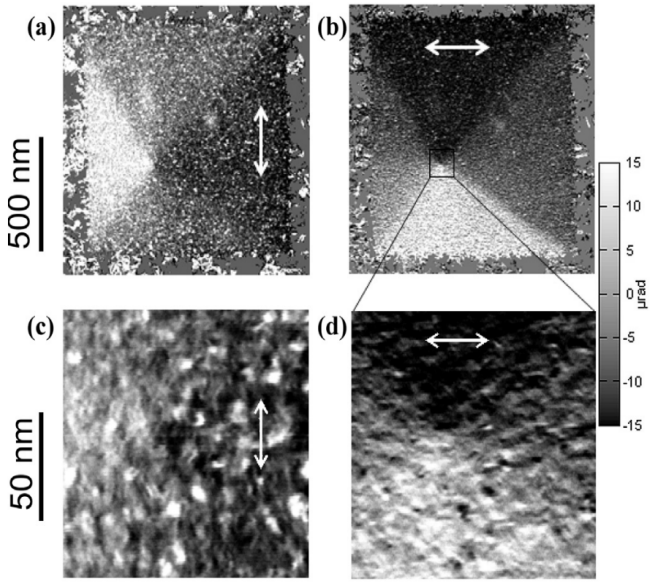

Figure 3.23: Example of diffraction contrast from crystallites in polycrystalline samples which obscures the magnetic contrast in high magnification DPC images. (a) and (b) show a pair of low magnification DPC images mapping two orthogonal directions (indicated by the double-headed arrows). (c) and (d) are high magnification images of the central area of (a) and (b) showing strong diffraction contrast. Figure reproduced from [59] under Creative Commons 4.0 licence.

3.7.5 Detectors for DPC imaging

Figure 3.24 depicts the three detector geometries used for DPC imaging. In order of development: Fig. 3.24(a) shows a quadrant detector, (b) shows an annular quadrant detector and (c) shows a pixelated detector. An idealised electron beam, shifted by β_L from the centre of each detector, is overlaid on each geometry. Note the pixels in Fig. 3.24(c) are not drawn to scale with respect to the beam size.

The quadrant (four segment) and annular quadrant (eight segment) detector both operate by summing the electron intensity that falls in each segment and then taking difference signals *between* segments to measure the beam shifts. In the quadrant detector the deflections in x and y directions are given by:

$$\begin{aligned} \beta_L(x) &= \frac{\alpha\pi}{4}\frac{(A+D)-(B+C)}{A+B+C+D}, \\ \beta_L(y) &= \frac{\alpha\pi}{4}\frac{(A+B)-(C+D)}{A+B+C+D}, \end{aligned} \tag{3.19}$$

where the letters A, B, C, D identify the quadrants labelled in Fig. 3.24(a) and α is the semi-convergence angle of the probe. The difference signal is normalised by the sum signal to account for intensity variations between probe positions. The annular quadrant detector measures deflections similarly but using only the outer

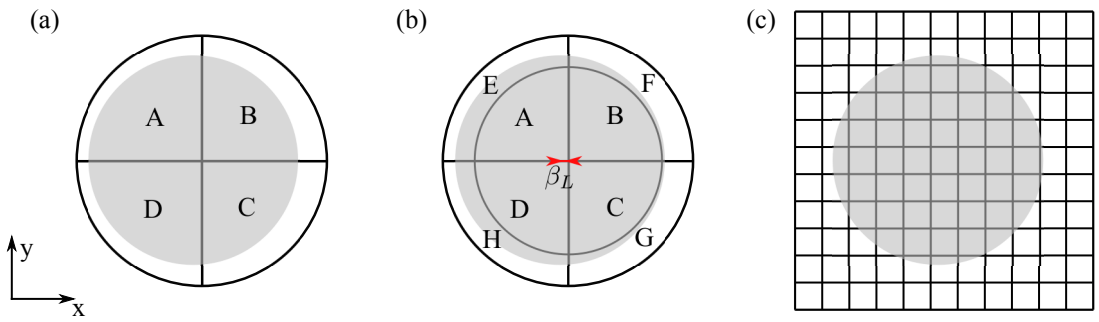

Figure 3.24: The geometry of detectors used to measure beam shifts for DPC imaging: (a) a quadrant detector, (b) annular quadrant detector and (c) a pixelated detector. The beam is shifted by β_L from the centre of each detector as indicated in (b).

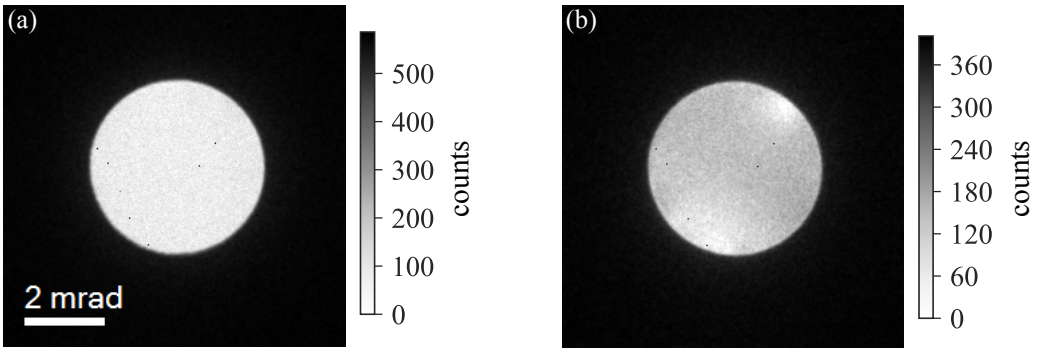

Figure 3.25: (a) A central diffraction disk with a uniform distribution of electron intensity (b) a non-uniform central disk showing common contrast variations. These images are taken from different points in the same scan of 8 nm polycrystalline Permalloy

segments E,F,G,H:

$$\beta_L(x) = \frac{\alpha\pi}{4}\frac{(E+H)-(F+G)}{A+B+...+H},$$
$$\beta_L(y) = \frac{\alpha\pi}{4}\frac{(E+F)-(H+G)}{A+B+...+H}. \tag{3.20}$$

Measurement of the beam shift in this manner relies on a number of assumptions [46, 60] (most importantly that $\beta_L \ll \alpha$) which are generally valid. One assumption that often breaks down is that the beam is incident on the detector as a flat circular disk [61], i.e. is well represented by a top hat function. See Fig. 3.25(a) for a real example of a disk that satisfies this assumption and Fig. 3.25(b) for an example that does not. Fig. 3.25(b) shows the intra-disk contrast variations that are often observed in polycrystalline materials and arise from differential Bragg scattering between grains.

Considering the detection method employed by the quadrant detector, it is clear that this intra-disk intensity redistribution leads to spurious 'deflection' measurements as the sum signal in each segment is influenced both by shifts and intensity redistributions. The annular quadrant detector was developed to address this issue. Measuring difference signals only from the four outer segments, while choosing a camera length so the disk is just larger than the inner quadrants, transfers long-range information far more efficiently than short-range information. This method was coined 'modified DPC' [61]. Modified DPC reduces but does not eliminate this

contrast and problematic diffraction contrast persists at high magnifications and always for some materials. An idealised version of modified DPC can be realised using a pixelated detector which permits both the imaging of weakly deflecting granular materials and use of the full spatial resolution offered by aberration-corrected field-free STEM [44, 59, 62].

The pixelated detector used for DPC in this thesis is a direct electron detector (DED), which is essentially a fast camera. This work used the Medipix3 with a Merlin readout system, installed on the JEOL ARM at Glasgow, which offers noiseless readout and a frame rate of 1200 fps in 12-bit mode [62, 63]. There are many exciting opportunities afforded by the recent introduction of DEDs to TEMs [64–68], but only the specific application of DEDs to DPC imaging is considered here.

With this detector the entire BF disk is collected as a 256×256 image at every scan position. STEM datasets collected in this manner are referred to as 4D datasets because a 2D image is collected at each point in a 2D scan. The images in Fig. 3.25 are single frames from different scan positions in a 4D dataset collected with the Medipix3. Access to the full image of every disk allows application of specially developed algorithms which measure deflections by essentially template matching only the edge of each disk to an idealised edge. This method is extremely efficient at separating the magnetic contrast from the diffraction contrast [59]. In this thesis, DPC imaging performed in this manner is referred to as pixelated DPC.

It must be noted that pixelated DPC can also be achieved using a traditional CCD camera, which is of course also pixelated and provides access to the entire BF disk. In fact, the first demonstration of DPC imaging using the aforementioned edge-detecting algorithm was performed on a dataset collected on a CCD camera [59]. This article also discussed the advantages offered by a DED, like the Medipix3, over a CCD camera. For DPC, the principal advantages are the increased frame-rate and high signal to noise ratio (SNR). The Orius CCD camera installed on the JEOL ARM at Glasgow has a maximum frame rate of 14 fps, far lower than the 1200 fps offered by the Medipix3 with a Merlin readout system. For STEM

imaging a fast frame-rate is essential - without it, artefacts arising from stage drift and microscope stability become prominent. For this reason, CCD cameras are generally considered ill-suited as STEM detectors. The frame-rate of the CCD camera is limited mostly by the readout system. In short, in a CCD camera, the charge deposited in each pixel must be physically shifted from each pixel to the 'readout register' where, again, the charge is shifted to the actual readout device where the charge originally deposited in each pixel is finally determined. This charge shifting process, inherent to a CCD, is the largest factor in limiting the top frame-rate possible on a CCD camera [69]. The Medipix3 requires no such charge shifting process as each pixel has its own readout system. Of course, for the acquired data to be useful, a high SNR is also required together with a high frame-rate. DEDs offer close to noiseless readout [63]. In contrast, the charge shifting readout system of CCD cameras is not perfect and introduces readout noise. Furthermore, CCD cameras suffer from cross-talk between the fibre-optic channels (used to transfer photons between the top scintillator layer and the CCD chip) which leads to charge spreading. In a DED the active layer of the detector is far thinner, and therefore lateral charge spreading is less prominent. Additionally, other cameras, including CCD cameras suffer from dark noise (where electrons are 'detected' without electrons being incident on the detector) which the Medipix3 does not. Cumulatively, these reasons make the Medipix3 detector the natural choice for STEM experiments like DPC. More technical details on the architecture of a CCD camera and the Medipix3 can be found in the literature [39, 63, 70].

With all DPC detectors, the signal can be summed over all segments (or pixels) to produce what is for all purposes a BF image - allowing the underlying structural information to be accessed simultaneous to the magnetic information.

Figure 3.26 shows a series of images generated from a 4D dataset taken from a skyrmionic multilayer sample. This sample has a total thickness of 74.4 nm, only 24 nm of this is magnetic (Co), the rest is strongly scattering non-magnetic materials. Moreover, the Co ($B_S \approx 1.2$ T) is magnetised out-of-plane and must be tilted for Lorentz microscopy imaging. When tilted by 25°, a component $B_S \sin(25°) \approx 0.5$ T

contributes to a Lorentz deflection. Tilting increases the sample thickness traversed by the beam so the magnetic thickness is 26 nm but the total thickness is 82 nm. The large total thickness of this sample, mostly composed of heavy metals, leads to severe diffraction effects that completely swamp the magnetic disk shifts using both quadrant or annular detectors. Figure 3.26(a) shows a disk representative of most scan positions in a dataset acquired from the sample. Each frame in the 4D dataset has a 1 ms acquisition time, this is the same as the disk images shown in Fig. 3.25 from 8 nm Permalloy. It is clear that there are far fewer electron counts in Fig. 3.26(a) and that the intra-disk variations are considerably more pronounced compared to Fig. 3.25. Figure 3.26(b) shows the sum image, which provides the same information as a BF image, where the crystallites are visible.

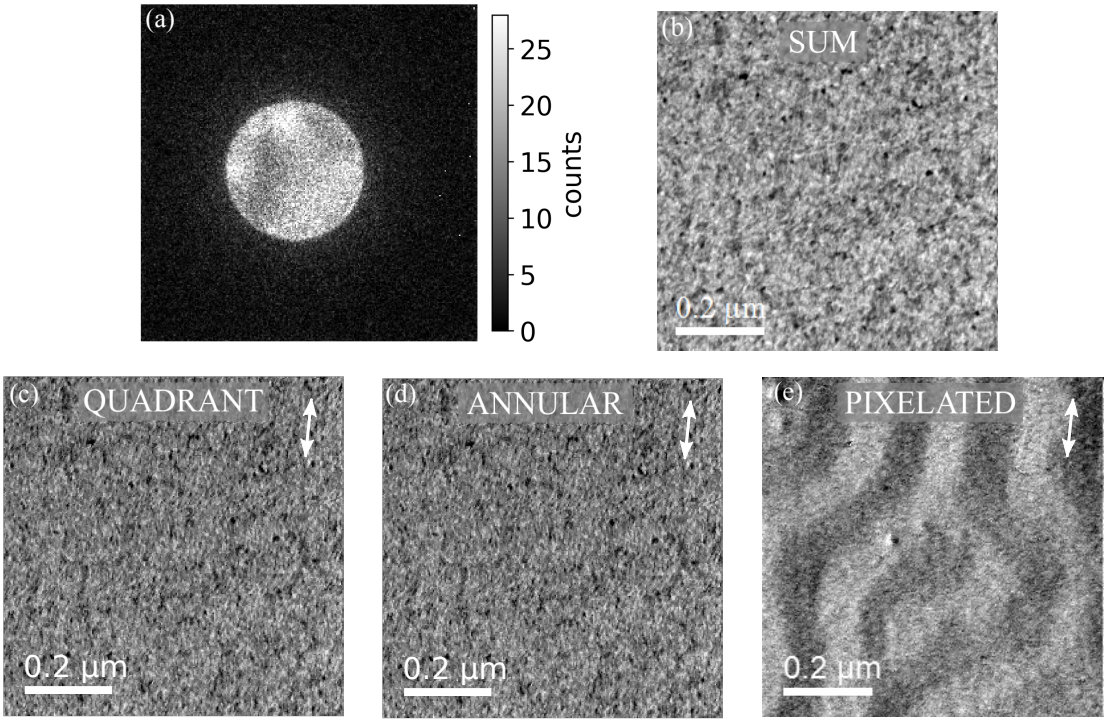

Figure 3.26: A series of images extracted or computed from a 4D dataset taken from a skyrmionic material for DPC imaging. (a) a disk representative of most scan positions, that shows strong diffraction effects from the crystallites, (b) a sum image where the crystallites themselves are visible, (c) DPC image produced from a virtual quadrant detector, (d) DPC image produced from a virtual annular quadrant detector and (e) pixelated DPC image produced by applying edge filtering and correlation algorithms that make use of the full diffraction disks made available with pixelated detectors.

Figures 3.26(c) and (d) are computed from the 4D dataset by building virtual detectors with the geometries sketched in Figs. 3.24(a) and (b) respectively and applying Eqs. 3.19 and 3.20. Therefore, the images in Figs. 3.26(c) and (d) represent DPC images acquired with quadrant and annular quadrant detectors. Both Figs. 3.26(c) and (d) show only short-range diffraction contrast, similar to Fig. 3.26(b). In striking contrast to Figs. 3.26(c) and (d) where no magnetic contrast in visible, the pixelated DPC image in Fig. 3.26(e) shows very clear magnetic contrast of meandering domains.

It is desirable to use the quadrant/annular quadrant detectors for DPC imaging wherever possible because 4D datasets from pixelated detectors come with a significant data storage cost; the 256×256 dataset behind the images in Fig. 3.26 is 8.1 GB while a 256×256 dataset collected with the annular detector has a storage cost of around 1 MB. However, all DPC images in this thesis were acquired with a pixelated detector. For skyrmionic multilayer materials, Fig. 3.26 makes the justification of this clear. The study of DMI-modified vortex cores in Chapter 7 required high magnification, high resolution images, thus again a pixelated detector was necessary to mitigate the issues prominent in Figs. 3.23(c) and (d). The pixelated DPC images in this thesis were computed from 4D datasets using code freely available online [71].

3.7.6 Other magnetic imaging modes in the TEM

Only Fresnel and DPC imaging were used in this thesis, but for completeness the other methods of Lorentz microscopy (all CTEM methods) are briefly described here together with electron holography.

The principles behind low-angle electron diffraction and Foucault imaging are in many ways similar to diffraction and dark field imaging. In the same way that Bragg scattering splits the incident beam into many beams with distinct positions on the back focal plane of the objective lens. In magnetic materials, each diffraction spot is further split into distinct positions in the back focal plane of the objective (mini) lens because of different Lorentz deflections experienced by the different parts of the

electron beam that pass though differently magnetised domains. The splitting from Bragg scattering is on the order of mrad while the splitting from Lorentz deflections is on the order of μrad. Therefore the two effects are rarely seen in the same image. The splitting of the central, undiffracted beam can be imaged directly. This technique is known as low-angle electron diffraction, or alternatively as small-angle electron scattering [72–74]. Foucault images are formed by careful placement of an objective aperture to allow only electrons experiencing similar Lorentz deflections to form an image. In this way, images relating to the magnetic induction of the domains are produced [74]. Foucault imaging is non-quantitative like Fresnel while low-angle electron diffraction is quantitative but, as the information is collected from the full illuminated area in CTEM, provides non-local information. Note that a quantitative variation of Foucault imaging exists, known as coherent Foucault imaging. It requires a highly coherent source and an aperture fabricated from a thin phase shifting film, rather than the usual electron opaque metal [41]. Coherent Foucault imaging produces interferograms (like holography which is discussed next) but not often used because it is an experimentally challenging technique to realise.

Electron holography is a CTEM technique able to provide magnetic information about a sample. In electron holography, the sample is situated so that half of the incident electron beam is transmitted though the sample and half travels through vacuum (thus is not applicable to all samples). The half that interacts with the sample is called the object beam and the half that does not is called the reference beam. Electron holography requires specialise hardware: a biprism is used to deflect and interfere the reference beam and object beam to form a hologram. The hologram is processed to reconstruct phase of the electron beam. Electron holography is quantitative, and in principle capable of high ($<$ 1 nm) resolution like DPC [75]. Practically, the resolution of holography is limited, at present, to 5 nm by the hologram processing procedures [76].

3.8 Scanning force microscopy

Scanning force microscopy (SFM) refers to a family of imaging techniques where a mechanical probe is scanned over a sample and images are built up through detection of the force between the tip and the sample. Depending on the mode of operation and the composition of the probe different forces are detected and a wealth of information can be extracted about the sample. In this thesis, atomic force microscopy (AFM) - which reveals the sample topography through detection of Van der Waals forces - and magnetic force microscopy (MFM) - which reveals the stray field above the sample through magnetostatic interactions - were used. Chapter 5 uses AFM to evaluate the surface contortion of TEM membranes and MFM to extract the magnetic domain periodicity of the samples in a magnetic ground state configuration. In Chapter 7 MFM is proposed as a method detecting the DMI-modification of vortex cores. As well as topographic and magnetic information, varieties of SFM exist that glean information on the chemical bonding [77], electric potentials [78] and polarisation [79] of the sample to name a few.

The SFM work in this thesis was performed using a Dimension 3100 microscope. Commercial SFM probes consist of a small, 3 by 5 mm, chip from which extends a cantilever with a tip on the end. The configuration of the tip and the cantilever can be seen in the diagram in Fig. 3.27. AFM tips are doped-Si. An MFM tip is doped-Si that is coated with a magnetic material (CoCr) in a manner that encourages magnetisation along the long axis of the tip. All SFM probes generally have a reflective coating on the back. A laser spot is focused on the back of the cantilever, which is reflected onto the centre of a split four-quadrant photodiode. When the tip experiences a force from the sample, the cantilever is deformed and the reflection of the laser spot on the photodiode shifts. This laser spot deflection is measured from the signal output by the photodiode in a way that is analogous to detection of Lorentz deflections by a quadrant DPC detector described in section 3.7.5. In contrast to the TEM, SFM is performed in ambient conditions and requires no special sample preparation.

AFM was performed in tapping mode, here the tip is oscillated at (or close to) its resonant frequency with a fixed oscillation amplitude, and contacts the sample once per oscillation. The Van der Waals forces felt by the tip influence the cantilever deflection which is monitored by the photodiode. A feedback loop controls the height of the tip above the sample so that the cantilever always oscillates with the same amplitude. This is repeated at each point in the scan, and the changes in height stored to produce a topographic map of the sample surface.

MFM was performed in two-pass lift mode. As the name suggests, each line in two-pass MFM is scanned twice. The first scan performs AFM, collecting topographic information. The height data collected in the first scan is used in the second scan to lift the tip a constant distance above the sample. The lift height is normally tens of nm. At this tip-sample separation the Van der Waals interactions are negligible and only the long-range (electro)magnetic interactions influence the tip [80]. Like AFM, the cantilever is driven at its resonant frequency but feedback is disabled. The principle of two-pass MFM is sketched in Fig. 3.27.

The interaction between a magnetic tip and the stray-field of a magnetic sample both deforms the cantilever and shifts its resonant frequency [81]. The former effect can be used to form MFM images (with an otherwise static cantilever) but is prone

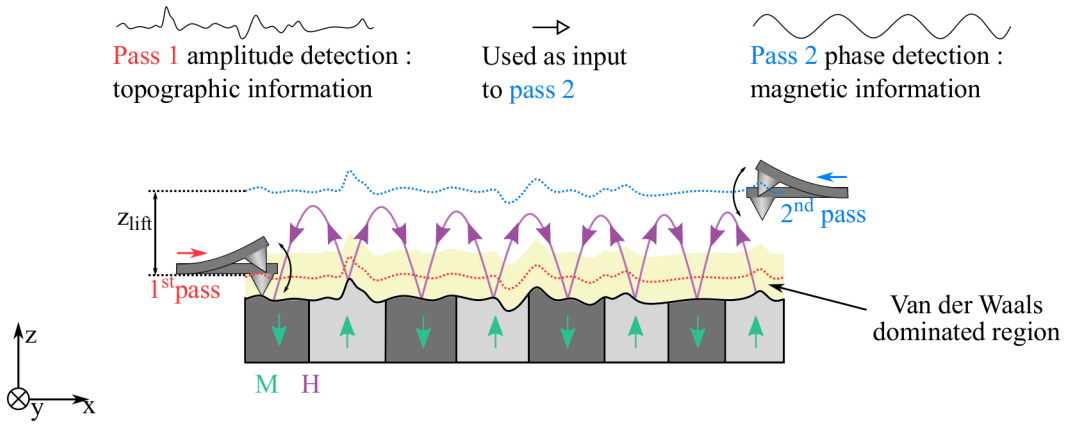

Figure 3.27: The method of two-pass MFM is sketched, AFM is performed on the first pass which collects topographic information. This is used in the second pass to maintain a constant lift height z_{lift} (tens of nm) between the tip and sample. In the second pass, this relatively large tip-sample distance ensures only long-range magnetic interactions influence the tip and Van der Waals interactions are negligible.

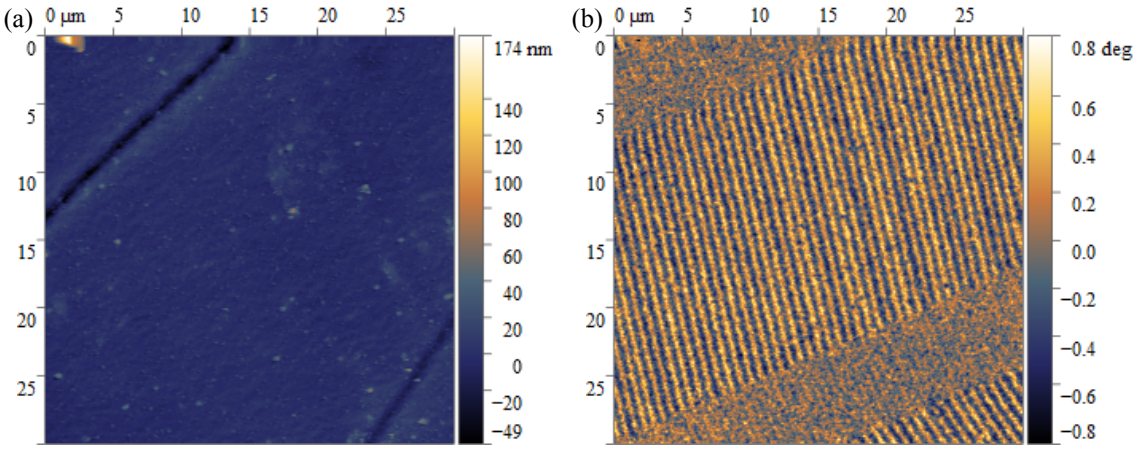

Figure 3.28: Example of AFM and MFM images recorded from a two-pass MFM scan of magnetic recording tape. (a) the AFM image shows the topography of the tape and (b) the MFM image of the sample revealing the periodic strip domains.

to serious artefacts [82]. Therefore MFM images are usually formed from the latter where shifts in the resonant frequency are detected through monitoring the phase of the cantilever oscillation relative to the phase of the original drive signal, this is called dynamic MFM. Figure 3.28 shows images taken from an MFM calibration sample (thermally evaporated magnetic recording tape of unknown composition) using two-pass MFM. Figure 3.28(a) shows the sample topography obtained from AFM performed in the first pass. Figure 3.28(b) shows the MFM image obtained with a lift height of 50 nm: periodic stripe domains are clearly visible and importantly the magnetic contrast is decoupled from the surface topography. The spatial resolution of MFM is usually $\approx$ 50 nm but 10 nm resolution has been demonstrated [80].

The shift in resonant frequency is, in the limit of a weak interaction, linearly proportional to the gradient of the magnetic force $\partial F_z/\partial z$ (note that this derivative is in z because the cantilever oscillates in z):

$$\Delta\omega = -\frac{\omega_0}{2k}\frac{\partial F_z}{\partial z} \tag{3.21}$$

where ω_0 is the original resonant frequency of the cantilever and k is the spring constant. The magnetic force is derived from the Zeeman energy of the magnetic tip in the stray field of the sample (or equivalently the magnetisation of the sample

in the stray field of the tip). The magnetic force in z is given by:

$$\begin{aligned} F_z &= \mu_0 \iiint \mathbf{M_{tip}} \cdot \frac{\partial \mathbf{H_{sample}}}{\partial z}\, dV_{tip} \\ &= \mu_0 \iiint \mathbf{M_{sample}} \cdot \frac{\partial \mathbf{H_{tip}}}{\partial z}\, dV_{sample} \end{aligned} \tag{3.22}$$

For a more intuitive picture, Eq. 3.22 can be reformulated to depend on magnetic charges [83]:

$$\begin{aligned} F_z &= \iint_A \sigma_{tip} \mathbf{H_{sample}}\, dA_{tip} + \iiint_V \rho_{tip} \mathbf{H_{sample}}\, dV_{tip} \\ &= \iint_A \sigma_{sample} \mathbf{H_{tip}}\, dA_{sample} + \iiint_V \rho_{sample} \mathbf{H_{tip}}\, dV_{sample} \end{aligned} \tag{3.23}$$

where $\sigma(= \mathbf{M} \cdot \hat{\mathbf{n}})$ and $\rho(= -\nabla \cdot \mathbf{M})$ are the surface and volume magnetic charges respectively. The second form of Eq. 3.23 is particularly useful as it allows MFM contrast to be understood from the magnetic charge distribution of the sample. MFM, sensitive to the divergence of $\mathbf{M}$, is therefore complementary to Lorentz microscopy which, as discussed in section 3.7, is sensitive to the curl of $\mathbf{M}$.

3.9 Other magnetic imaging methods

Lorentz microscopy and MFM are far from the only magnetic microscopy methods, alternative methods are briefly outlined with references to comprehensive articles and relevant applications to DMI and skyrmionic materials.

- X-ray methods based on x-ray magnetic circular dichroism (XMCD) (sensitive to $\mathbf{M}$) that can provide elemental resolution (for example scanning transmission x-ray microscopy (STXM) [84, 85] and x-ray resonant magnetic scattering (XRMS) [86, 87]).

- Scanning tunnelling methods are sensitive to the top-most atomic layer and have ultra-high (Å) lateral resolution [88] (see spin polarised scanning tunneling microscopy (SP-STM) (sensitive to $\mathbf{M}$) [89, 90]).

- Surface sensitive electron microscopy techniques based on the spin-dependence of low-energy electron scattering from magnetic surfaces (see spin polarised low energy electron microscopy (SPLEEM) [91] and scanning electron microscope with polariser analysis (SEMPA) both sensitive to **M** [92, 93]).

- Optical methods based on magneto-optical effects [94] (see magneto-optical Kerr effect (MOKE) microscopy (sensitive to **M**) [95] - can also be used for magnetometry [96]).

- Nitrogen vacancy (NV-centre) imaging (sensitive to **H**) can sense magnetic and electric fields by scanning a single-crystal diamond tip that has a single NV-centre close to the apex over a sample [97, 98]

3.10 Simulation methods

This section introduces all simulation methods used to support the experimental work presented in this thesis. Two 'categories' of simulations are discussed: (*i*) simulation of the magnetisation and (*ii*) simulation of experimental images or 'image calculation'. Category *(i)* includes micromagnetic simulations, which enable realistic magnetic structures to be calculated, as well as simple analytical models which are adequate to describe some common magnetic objects. Category (*ii*) includes calculation of Fresnel, DPC and MFM images from magnetisation configurations supplied by category (*i*) simulations.

These methods are exceedingly useful for experiment design, interpretation of results and also, in the case of micromagnetic simulations, to explore new physics.

3.10.1 Micromagnetic simulations

The exchange length l_{ex}, see Eq. 2.4, is a parameter which indicates the length-scale over which one would expect little variation of the direction of moments. In Permalloy $l_{ex} \approx 5$ nm and in Cobalt $l_{ex} \approx 4$ nm. Because l_{ex} is an order of magnitude larger than the distance between individual magnetic moments (Å) a continuum approximation can be made. This underpins the theory of micromagnetism and

enables the application of computationally efficient numerical techniques to accurately simulate magnetic materials.

Micromagnetic simulations are a ubiquitous tool in the modern study of magnetism. Among other functionality they can determine stable magnetic configurations of magnetic elements, of user-defined shape and magnetic properties, and predict the dynamic response of a magnetic system to external stimuli like applied magnetic fields or spin-polarised electric currents. There is a multitude of micromagnetic simulation software available, this thesis exclusively uses mumax^3 which offers finite difference GPU accelerated simulations [99]. Finite difference methods, like mumax^3 and OOMMF [100], sub-divide the magnetic element into cuboids and are suitable for simulation of rectangular elements and thin films (as in this thesis) but deal with more complex rounded geometries poorly. In the latter case finite element methods, like Nmag [101] or magnum.fe [102], are more suitable which subdivide the magnetic elements into arbitrary-sized tetrahedra to accurately simulate any geometry at the cost of computational efficiency. Micromagnetic simulations are used in two chapters of this thesis: in Chapter 5 to study flux-closure hybrid domain walls formed by the competition of dipolar and DMI interactions and in Chapter 7 to study DMI-modified vortex cores.

To begin, in all micromagnetic simulations, a geometry is defined and subdivided into 'cells'. In finite difference methods cells are cuboidal - as sketched in Fig. 3.29 - and each cell is assigned a separate magnetisation vector $\mathbf{M}$ where $|\mathbf{M}| = M_s$ and the only variable is the orientation. To be accurate, the simulation cell size must be below the theoretical exchange length of the material l_{ex}. The constants defining the active magnetic energy terms of the simulated material system are input. An initial magnetisation configuration must be supplied, and some care should be taken here as the system can converge erroneously to saddle points or local minima in the energy landscape. To find the global energy minima different initial states are often trialled.

Simulations employ the Landau-Lifshitz-Gilbert (LLG) equation, which is a differential equation describing the gyroscopic motion of magnetisation in response

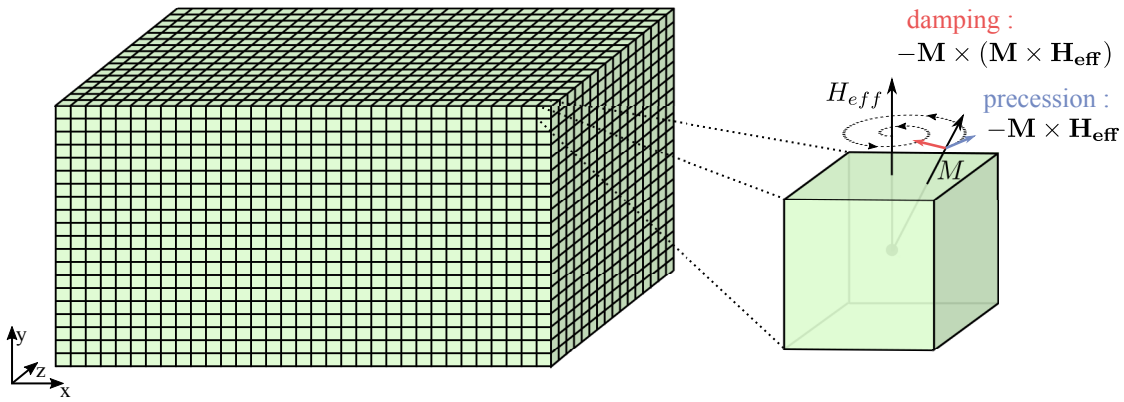

Figure 3.29: Micromagnetic simulations split the simulated materials into discrete 'cells' and solve the LLG equation which describes the damped precessional motion of magnetisation $\mathbf{M}$ about an effective field $\mathbf{H_{eff}}$.

to torques τ about an 'effective' field $\mathbf{H_{eff}}$:

$$\tau = \frac{\partial \mathbf{M}}{\partial t} = -\gamma \mathbf{M} \times \mathbf{H_{eff}} - \frac{\gamma \kappa}{|\mathbf{M}|} \mathbf{M} \times (\mathbf{M} \times \mathbf{H_{eff}}), \tag{3.24}$$

where γ is the gyromagnetic ratio and κ is the damping coefficient. Equation 3.24 has two terms: the first describes precessional motion where the second describes damping-like motion that eventually aligns $\mathbf{M}$ and $\mathbf{H_{eff}}$. The resultant motion of the magnetisation vector is sketched in the right hand side of Fig. 3.29. The effective field is given by

$$\mathbf{H_{eff}} = -\frac{1}{\mu_0} \frac{\partial \mathcal{H}_{total}}{\partial \mathbf{M}} \tag{3.25}$$

where $\mathcal{H}_{total}$ is the sum of all active energy terms. For the samples studied in this thesis, the energy terms in simulations are: exchange, dipolar (or magnetostatic), anisotropy, DMI and, for simulations under an applied field, Zeeman. The LLG equation is solved forward in time until some convergence criterion is met; for mumax^3 the criterion depends whether a dynamic or static simulation is performed [99]. Static simulations that simply aim to find an energetically stable magnetic configuration do so by 'relaxing' the simulation to minimise the total energy of the system. For this Eq. 3.24 is solved using only the second term. Dynamic simulations evaluate the full LLG equation. To simulate the interaction of electrical currents and magnetic materials, additional spin transfer torque terms are added to the LLG equation [103, 104].

To provide an example, a micromagnetic simulation was performed of the rectangular Permalloy element used as an example throughout this chapter. The simulated element has dimensions in $x \times y \times z$ of 6 μm $\times$ 2 μm $\times$ 8 nm with a cell size of $4 \times 4 \times 4$ nm^3. Only exchange and dipolar energies were included: the parameters $M_s = 860$ kAm^{-1} and $A_{ex} = 13$ pJm^{-1} were used which are typical of Permalloy. The relaxed simulation result is shown in Fig. 3.30 in which (a), (b) and (c) show the M_x,M_y and M_z components respectively and (d) shows a coloured vector plot overlaid with arrows showing the local direction of magnetisation. This is a classic flux closure domain state and is used to illustrate image calculations in sections 3.10.3 and 3.10.4.

3.10.2 Analytical models of simple magnetic configurations

In many scenarios a full micromagnetic simulation of the magnetisation is not necessary and simple analytical models suffice. In particular, this applies to Bloch and Néel walls where the magnetisation can be approximated by a 1D hyperbolic tangent model [105]. The three magnetisation components are given by:

$$M_{domain} = M_s \tanh(\frac{x}{w}) \tag{3.26a}$$

$$M_{wall} = \pm\sqrt{1 - {M_{domain}}^2} \tag{3.26b}$$

$$M_{other} = 0 \tag{3.26c}$$

where w is a measure of the domain wall width. The three components in Eqs. 3.26a- 3.26c can be assigned to M_x,M_y, M_z to model magnetisation configurations corresponding to any combination of out-of-plane or in-plane domains with Bloch or Néel type walls. Furthermore, this model was used to calculate the Lorentz image contrast expected from hybrid (Bloch-Néel) type domain walls that are the focus of Chapter 5. These 1D models can be propagated along a second dimension for image calculation, as shown in Fig. 3.31 which were calculated with $w = 10$ nm corresponding to a 18 nm wide wall. The relation between the width parameter w and the true 'domain wall width' was defined in section 2.3.1.

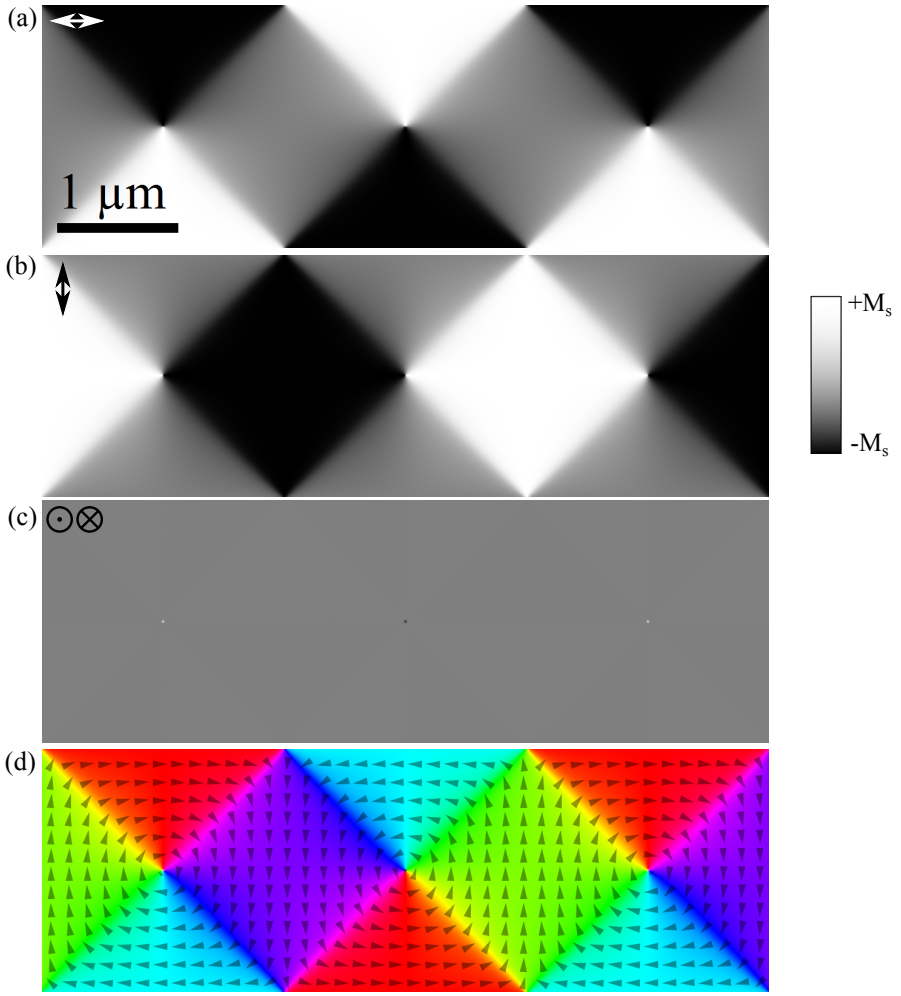

Figure 3.30: Result of mumax[3] micromagnetic simulation of a 8 nm thick Permalloy element. Respectively (a), (b) and (c) show the M_x,M_y and M_z components as defined by the icon inset in the top left of each figure. (d) presents a coloured vector plot representation of the magnetisation, arrows are overlaid giving the local magnetisation direction.

3.10.3 Calculating Lorentz microscopy images

Calculations of Fresnel and DPC images are utilised in all results chapters of this thesis and play a particularly significant role in Chapters 4 and 5. Fresnel and DPC images were calculated using scripts written by S. McVitie and G. White which implement a modified version of the algorithm originally proposed by M. Mansuripur [45, 106]. The original Mansuripur formalism provides a computationally efficient and completely general description of the phase change of an electron beam after transmission through an arbitrary thin magnetic film. Moreover, it

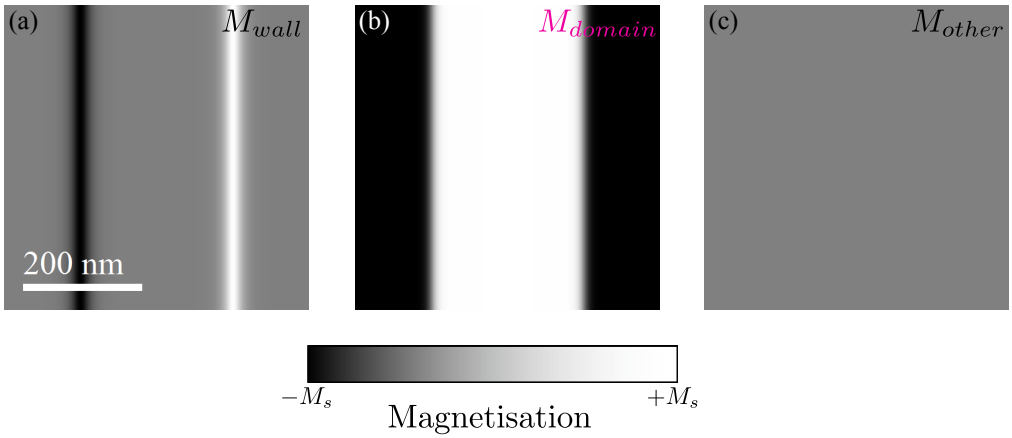

Figure 3.31: Images of magnetisation components created using an analytical hyperbolic tangent model. (a) corresponds to Eq. 3.26b, (b) to Eq. 3.26a and (c) to Eq. 3.26c with $w = 10$ nm. This model can be used for in-plane and out-of-plane magnetised films.

allows for arbitrary beam-sample geometry for image calculation of 'tilted' samples. Other open-source programs are available for this purpose such as MALTS [107]. As mentioned in section 3.7.2, all the various modes of Lorentz microscopy simply represent different means of capturing the phase change of the electron beam after its interaction with a magnetic sample: DPC contrast is linearly proportional to $\nabla\phi$ and Fresnel contrast, to the first order, relates to $\nabla^2\phi$.

The micromagnetic simulation of the multi-domain state in a rectangular permalloy element presented in section 3.10.1 (and Fig. 3.30) is used to demonstrate Lorentz microscopy image calculation (at zero tilt and 200 kV). First, Fig. 3.32(a) shows the phase change of the electron beam output by the script described in the 2004 S. McVitie and G. White paper [45].

DPC images measure the Lorentz deflection directly, therefore revisiting Eq. 3.12:

$$\nabla_{\perp}\phi = \frac{2\pi}{\lambda}\,\beta_L, \qquad \text{(3.12 revisited)}$$

it is clear that the 2D derivative of the phase provides DPC image information. Fig. 3.32(b) and (c) are two simulated DPC images, mapping the x and y components as defined by the arrows inset in the top left corner of the images. These two images are proportional to gradients in x and y of the phase (Fig. 3.32(a)) respectively. Fig. 3.32(b) and (c) can be compared to Fig. 3.21 which presents experimental DPC

images of the real 6 μm $\times$ 2 μm Permalloy element, though in the experimental DPC images the Permalloy elements supports a slightly different, higher energy magnetic configuration. This higher energy state was stabilised intentionally by field-cycling until a 180° domain wall was pinned in the patterned structure (a 180° wall was desired for that experiment).

The intensity I in Fresnel image of defocus Δ is:

$$I((x,y),\Delta) = 1 - \frac{\Delta\lambda}{2\pi}\nabla_{\perp}{}^{2}[\phi(x,y)] \tag{3.27}$$

as described in the literature [48]. Equation 3.27 is only quantitative for small

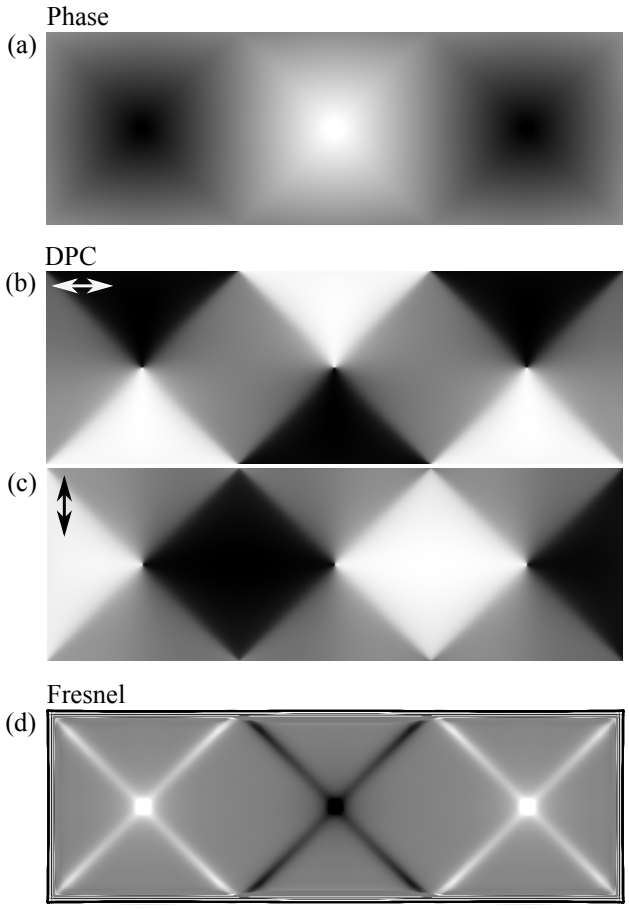

Figure 3.32: Lorentz microscopy images calculated from the micromagnetic simulation of a rectangular element, supporting a multi-domain magnetic configuration, given in section 3.10.1. (a) shows the phase calculated from the multi-domain magnetic configuration. Calculated DPC images, that map orthogonal components of integrated induction (as indicated by the double-headed arrow) are shown in (b) and (c). These are gradients of the phase in (a). The Fresnel image calculation (defocus 0.5 mm), which relates to the Laplacian of (a), is shown in (d). These calculations do not include electrostatic phase effects, which would alter the contrast at the edge of the structure.

values of Δ [48]. Otherwise Eq. 3.27, without including higher order terms [108], is a good approximation of the Fresnel image contrast. This then represents ideal or 'linear' Fresnel images but 'real' image Fresnel images can be calculated from the phase using in-house programs. A Fresnel image calculated using Eq. 3.27 and a defocus of 0.5 mm is shown in Fig. 3.32(d) which compares excellently with the experimental Fresnel image of the Permalloy element presented in Fig. 3.15(b).

Detailed discussion of contrast interpretation in Lorentz microscopy is not provided in this section because it forms a large part of the results chapters of this thesis. Chapters 4 and 5 cover in detail the contrast expected from different of domain wall structures; Chapter 6 details contrast from Néel skyrmions; and Chapter 7 details the contrast expected from magnetic vortex structures.

In this thesis, all Lorentz images are calculated from only the smoothly varying magnetic phase. In reality, as discussed in section 3.7.2, the phase is influenced by electrostatic effects together with magnetic effects. Outwith the crystallite related electrostatic phase effects detailed in section 3.7.5, the electrostatic phase does not impact this work because continuous magnetic thin films (or vortex cores located in the centre of patterned disks) are studied, where there are no large electrostatic contributions as would be associated with either changes in material or thickness as per Eq. 3.15.

3.10.4 Calculating MFM images

Basic MFM image calculations are employed in Chapter 7 to qualitatively assess the MFM contrast associated DMI-modified vortex cores. A simple script was developed to approximate MFM contrast from samples of arbitrary magnetic configuration at some lift height z_{lift}. In this calculation the lift height is calculated from the centre of film thickness. Explaination of the MFM image contrast calculation starts with the first form of Eq. 3.23, reproduced here for clarity:

$$F_z = \mu_0 \iiint \mathbf{M_{tip}} \cdot \frac{\partial \mathbf{H_{sample}}}{\partial z} \, dV_{tip}, \qquad \text{(3.23 revisited)}$$

which assumes the tip magnetisation/field and sample magnetisation/field are fixed and do not perturb each other. In the limit of a small interaction, the force gradient (measured in dynamic MFM) is:

$$\frac{\partial F_z}{\partial z} = \mu_0 \iiint \mathbf{M_{tip}} \cdot \frac{\partial^2 \mathbf{H_{sample}}}{\partial z^2}\, dV_{tip} \tag{3.28}$$

The MFM image calculation approximates the tip to be magnetised fully in z so $\mathbf{M_{tip}} = M_s\,\hat{\mathbf{z}}$ with some volume V_{tip}. Then:

$$\frac{\partial F_z}{\partial z} \propto \frac{\partial^2 \mathbf{H_{z,sample}}}{\partial z^2}. \tag{3.29}$$

This second derivative of $\mathbf{H_{z,sample}}$ is numerically approximated at the lift height using the second order difference quotient where:

$$\frac{\partial^2 \mathbf{H_{z,sample}}}{\partial z^2}|_{z=z_{lift}} \approx \frac{\mathbf{H_{z,sample}}(z_{lift}+h) - 2\mathbf{H_{z,sample}}(z_{lift}) + \mathbf{H_{z,sample}}(z_{lift}-h)}{h^2}, \tag{3.30}$$

where h is small with respect to the lift height z_{lift}. The stray field is calculated at discreet heights above the sample using a script written by G. White which implements algorithms found in the 1989 paper by I. A. Beardsley [109]. It calculates $\mathbf{H}$ from any arbitrary magnetisation distribution - be that an analytical model or the output of a micromagnetic simulation.

Figure 3.33 provides three examples of MFM images approximated by evaluating $\partial^2 \mathbf{H_{z,sample}}/\partial z^2$ at a 50 nm lift height. Examples in Fig 3.33(a) and (b) are both calculated using the hyperbolic tangent model described in section 3.10.2. From Eqs. 3.26a-3.26c, Fig. 3.33(a) uses $M_x = M_{other}$, $M_y = M_{domain}$ and $M_z = M_{wall}$ therefore simulating a material with in-plane domains and Bloch type walls. For Fig. 3.33(b) the M_x and M_z components are swapped to simulate a material with in-plane domains and Néel type walls. The magnetic configuration and the magnetic charge distribution of a Bloch wall and Néel wall are sketched respectively on the left and right of Figs. 3.33(a) and (b). Comparing the charge distributions to the corresponding MFM image, it is clear why many regard MFM as magnetic charge imaging [83]. Figure 3.33(c) shows the MFM image calculated from the micromagnetic simulation presented in section 3.10.1. The image allows Néel type walls and vortex cores to be distinguished.

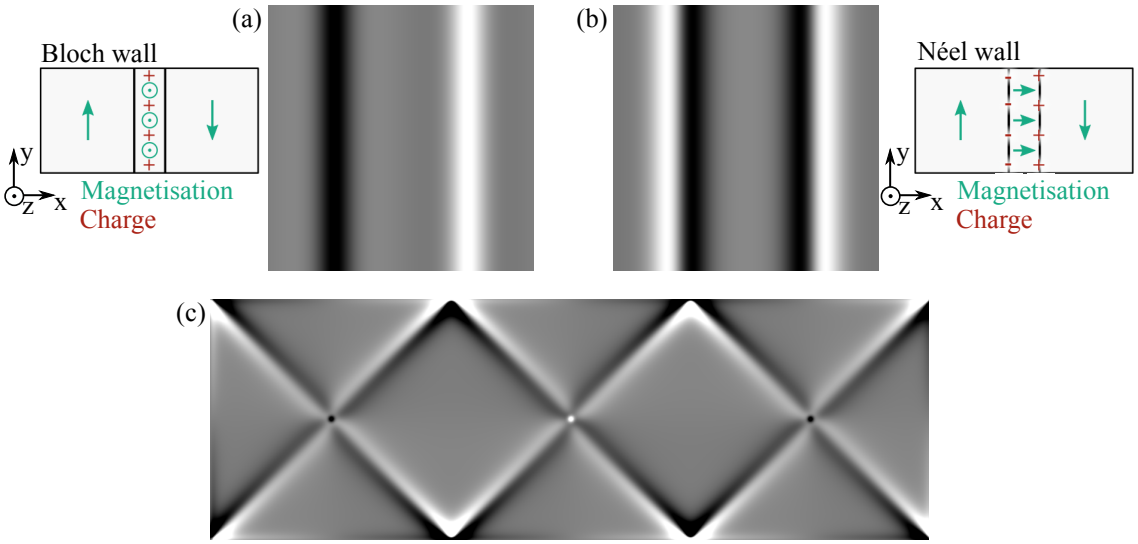

Figure 3.33: (a) MFM image calculated from a magnetic configuration with in-plane domains and Bloch type walls (the magnetisation and magnetic charge distribution is sketched on the left). (b) MFM image calculated from a magnetic configuration with in-plane domains and Néel type walls (the magnetisation and magnetic charge distribution is sketched on the right). It is clear that MFM contrast correlates well with the charge distribution but comparing the sketches to the calculated MFM images. (c) the MFM image calculated from the micromagnetic simulation of a rectangular elements supporting a multi-domain magnetic configuration given in section 3.10.1.

Bibliography

[1] P. J. Kelly and R. D. Arnell, "Magnetron sputtering: A review of recent developments and applications," *Vacuum*, vol. 56, no. 3, pp. 159–172, 2000.

[2] J. E. Greene, "Review Article: Tracing the recorded history of thin-film sputter deposition: From the 1800s to 2017," *Journal of Vacuum Science & Technology A: Vacuum, Surfaces, and Films*, vol. 35, no. 5, p. 05C204, 2017.

[3] G. Bräuer, "Magnetron Sputtering," *Comprehensive Materials Processing*, vol. 4, pp. 57–73, 2014.

[4] M. T. Johnson, P. J. Bloemen, F. J. Den Broeder, and J. J. De Vries, "Magnetic anisotropy in metallic multilayers," *Reports on Progress in Physics*, vol. 59, no. 11, pp. 1409–1458, 1996.

[5] B. Zimmermann, W. Legrand, D. Maccariello, N. Reyren, V. Cros, S. Blügel, and A. Fert, "Dzyaloshinskii-Moriya interaction at disordered interfaces from ab initio theory: Robustness against intermixing and tunability through dusting," *Applied Physics Letters*, vol. 113, no. 23, pp. 5–10, 2018.

[6] E. d. T. De Lacheisserie, D. Gignoux, and M. Schlenker, *Magnetism: II-Materials and Applications*. Springer Science & Business Media, 2012.

[7] K. Barmak and K. Coffey, *Metallic films for electronic, optical and magnetic applications: Structure, processing and properties*. Woodhead Publishing, 2014.

[8] J. I. Goldstein, D. E. Newbury, J. R. Michael, N. W. Ritchie, J. H. J. Scott, and D. C. Joy, *Scanning electron microscopy and x-ray microanalysis*. Springer, 4 ed., 2017.

[9] C. Chappert, H. Bernas, J. Ferré, V. Kottler, J. P. Jamet, Y. Chen, E. Cambril, T. Devolder, F. Rousseaux, V. Mathet, and H. Launois, "Planar patterned magnetic media obtained by ion irradiation," *Science*, vol. 280, no. 5371, pp. 1919–1922, 1998.

[10] C. T. Rettner, S. Anders, J. E. Baglin, T. Thomson, and B. D. Terris, "Characterization of the magnetic modification of Co/Pt multilayer films by He+, Ar+, and Ga+ ion irradiation," *Applied Physics Letters*, vol. 80, no. 2, pp. 279–281, 2002.

[11] C. Vieu, J. Gierak, H. Launois, T. Aign, P. Meyer, J. P. Jamet, J. Ferré, C. Chappert, T. Devolder, V. Mathet, and H. Bernas, "Modifications of magnetic properties of Pt/Co/Pt thin layers by focused gallium ion beam irradiation," *Journal of Applied Physics*, vol. 91, no. 5, pp. 3103–3110, 2002.

[12] G. J. Kusinski and G. Thomas, "Physical and magnetic modification of Co/Pt multilayers by ion irradiation," *Microscopy and Microanalysis*, vol. 8, pp. 319–332, 2002.

[13] J. Fassbender, D. Ravelosona, and Y. Samson, "Tailoring magnetism by light-ion irradiation," *Journal of Physics D: Applied Physics*, vol. 37, no. 16, pp. R179–R196, 2004.

[14] M. J. Benitez, M. A. Basith, R. J. Lamb, D. McGrouther, S. McFadzean, D. A. MacLaren, A. Hrabec, C. H. Marrows, and S. McVitie, "Engineering Magnetic Domain-Wall Structure in Permalloy Nanowires," *Physical Review Applied*, vol. 3, no. 3, pp. 1–10, 2015.

[15] S. Zhang, A. K. Petford-Long, and C. Phatak, "Creation of artificial skyrmions and antiskyrmions by anisotropy engineering," *Scientific Reports*, vol. 6, pp. 1–10, 2016.

[16] A. J. DeMarco and J. Melngailis, "Contact resistance of focused ion beam deposited platinum and tungsten films to silicon," *Journal of Vacuum Science and Technology B: Microelectronics and Nanometer Structures*, vol. 19, no. 6, pp. 2543–2546, 2001.

[17] Y. Isono, M. Kiuchi, S. Sugiyama, T. Morita, and S. Matsui, "Mechanical characteristics of FIB deposited carbon nanowire by Electrostatic Actuated nano Tensile Testing Devices (EANAT)," *Proceedings of the IEEE International Conference on Micro Electro Mechanical Systems (MEMS)*, vol. 16, no. 2, pp. 883–886, 2005.

[18] J. D. Fowlkes, R. Winkler, B. B. Lewis, A. Fernández-Pacheco, L. Skoric, D. Sanz-Hernández, M. G. Stanford, E. Mutunga, P. D. Rack, and H. Plank, "High-Fidelity 3D-Nanoprinting via Focused Electron Beams: Computer-Aided Design (3BID)," *ACS Applied Nano Materials*, vol. 1, no. 3, pp. 1028–1041, 2018.

[19] I. MacLaren, M. Nord, C. Jiao, and E. Yücelen, "Liftout of high-quality thin sections of a perovskite oxide thin film using a xenon plasma focused ion beam microscope," *Microscopy and Microanalysis*, vol. 25, no. 1, pp. 115–118, 2019.

[20] P. Tesch, N. Smith, N. Martin, and D. Kinion, "High current focused ion beam instrument for destructive physical analysis applications," *Proceedings from the 34th International Symposium for Testing and Failure Analysis (ISTFA)*, pp. 7–13, 2008.

[21] N. S. Smith, W. P. Skoczylas, S. M. Kellogg, D. E. Kinion, P. P. Tesch, O. Sutherland, A. Aanesland, and R. W. Boswell, "High brightness inductively coupled plasma source for high current focused ion beam applications," *Journal of Vacuum Science and Technology B: Microelectronics and Nanometer Structures*, vol. 24, no. 6, pp. 2902–2906, 2006.

[22] J. Li, T. Malis, and S. Dionne, "Recent advances in FIB-TEM specimen preparation techniques," *Materials Characterization*, vol. 57, no. 1, pp. 64–70, 2006.

[23] J. Li and C. Rau, "Three-dimensional, spin-resolved structure of magnetic vortex and antivortex states in patterned co films using scanning ion microscopy with polarization analysis," *Physical Review Letters*, vol. 97, no. 10, pp. 1–4, 2006.

[24] M. R. R. Azad, A. Kobs, B. Beyersdorff, P. Staeck, G. Hoffmann, R. Frömter, and H. P. Oepen, "Magnetostatic interaction of permalloy rectangles exhibiting a Landau state investigated by magnetotransport of single rectangles," *Physical Review B - Condensed Matter and Materials Physics*, vol. 90, no. 1, pp. 1–9, 2014.

[25] M. A. Basith, S. McVitie, D. McGrouther, and J. N. Chapman, "Reproducible domain wall pinning by linear non-topographic features in a ferromagnetic nanowire," *Applied Physics Letters*, vol. 100, no. 23, 2012.

[26] L. D. Ho, M. T. Tran, X. H. Cao, V. A. Dao, D. T. Ngo, and D. Q. Hoang, "Field-driven single domain wall motion in ferromagnetic nanowires," *RSC Advances*, vol. 8, no. 26, pp. 14539–14551, 2018.

[27] S. Getlawi, M. R. Koblischka, U. Hartmann, C. Richter, and T. Sulzbach, "Patterning of permalloy thin films by means of electron-beam lithography and focused ion-beam milling," *Superlattices and Microstructures*, vol. 44, no. 4-5, pp. 699–704, 2008.

[28] M. Urbanek, V. Uhlí, P. Bábor, E. Kolíbalová, T. Hrnič, J. Spousta, and T. Šikola, "Focused ion beam fabrication of spintronic nanostructures: An optimization of the milling process," *Nanotechnology*, vol. 21, no. 14, 2010.

[29] A. Aziz, S. J. Bending, H. G. Roberts, S. Crampin, P. J. Heard, and C. H. Marrows, "Angular dependence of domain wall resistivity in artificial magnetic domain structures," *Physical Review Letters*, vol. 97, no. 20, p. 206602, 2006.

[30] W. Rupp, A. Biedermann, B. Kamenik, R. Ritter, C. Klein, E. Platzgummer, M. Schmid, and P. Varga, "Ion-beam induced fcc-bcc transition in ultrathin Fe films for ferromagnetic patterning," *Applied Physics Letters*, vol. 93, no. 6, pp. 1–4, 2008.

[31] S. Shah Zaman, H. Oßmer, J. Jonner, Z. Novotný, A. Buchsbaum, M. Schmid, and P. Varga, "Ion-beam-induced magnetic transformation of CO-stabilized fcc Fe films on Cu(100)," *Physical Review B - Condensed Matter and Materials Physics*, vol. 82, no. 23, pp. 1–10, 2010.

[32] G. P. Thomson and A. Reid, "Diffraction of cathode rays by a thin film," *Nature*, vol. 119, no. 3007, p. 890, 1927.

[33] C. J. Davisson, "The Diffraction of Electrons by a Crystal of Nickel," *Bell System Technical Journal*, vol. 7, no. 1, pp. 90–105, 1928.

[34] E. Ruska, "The Development of the Electron Microscope and of Electron Microscopy (Nobel Lecture)," *Angewandte Chemie International Edition in English*, vol. 26, no. 7, pp. 595–605, 1987.

[35] O. L. Krivanek, T. C. Lovejoy, and N. Dellby, "Aberration-corrected STEM for atomic-resolution imaging and analysis," *Journal of Microscopy*, vol. 259, no. 3, pp. 165–172, 2015.

[36] B. Freitag, S. Kujawa, P. M. Mul, J. Ringnalda, and P. C. Tiemeijer, "Breaking the spherical and chromatic aberration barrier in transmission electron microscopy," *Ultramicroscopy*, vol. 102, no. 3, pp. 209–214, 2005.

[37] M. Haider, S. Uhlemann, E. Schwan, G. Rose, B. Kabius, and K. Urban, "Electron microscopy image enhanced [7]," *Nature*, vol. 392, no. 6678, pp. 768–769, 1998.

[38] O. L. Krivanek, N. Dellby, and A. R. Lupini, "Towards sub-Åelectron beams," *Ultramicroscopy*, vol. 78, pp. 1–11, 1999.

[39] D. B. Williams and C. B. Carter, *Transmission electron microscopy: Diffraction, imaging, and spectrometry*. Springer, 2016.

[40] P. D. Nellist and S. J. Pennycook, *The principles and interpretation of annular dark-field Z-contrast imaging*, vol. 113. Academic Press, 2000.

[41] S. McVitie and J. N. Chapman, "Coherent Lorentz Imaging of Soft, Thin-Film Magnetic Materials," *MRS Bulletin*, vol. 20, no. 10, pp. 55–58, 1995.

[42] A. Kohn and A. Habibi, "Adapting a JEM-2100F for Magnetic Imaging by," *JEOL News*, vol. 47, no. 1, pp. 17–22, 2012.

[43] B. Freitag, M. Bischoff, H. Mueller, P. Hartel, and H. S. V. Harrach, "Sub-nanometer resolution in field-free imaging using a titan 80-300 with lorentz lens and image cs-corrector at 300kv acceleration voltage," *Microscopy and Microanalysis*, vol. 15, no. SUPPL. 2, pp. 184–185, 2009.

[44] S. McVitie, D. McGrouther, S. McFadzean, D. A. MacLaren, K. J. O'Shea, and M. J. Benitez, "Aberration corrected Lorentz scanning transmission electron microscopy," *Ultramicroscopy*, vol. 152, pp. 57–62, 2015.

[45] S. McVitie and G. S. White, "Imaging Amperian currents by Lorentz microscopy," *Journal of Physics D: Applied Physics*, vol. 37, no. 2, pp. 280–288, 2004.

[46] J. N. Chapman, "The investigation of magnetic domain structures in thin foils by electron microscopy," *Journal of Physics D: Applied Physics*, vol. 17, no. 4, pp. 623–647, 1984.

[47] H. Hopster and H. Oepen, *Noncontact Atomic Force Microscopy*. No. 7 in NanoScience and Technology, Berlin, Heidelberg: Springer Berlin Heidelberg, 2009.

[48] S. McVitie and M. Cushley, "Quantitative Fresnel Lorentz microscopy and the transport of intensity equation," *Ultramicroscopy*, vol. 106, no. 4-5, pp. 423–431, 2006.

[49] I. S. Weir, J. N. Chapman, I. S. Molchanov, D. M. Titterington, and J. Rose, "Observation and modelling of magnetization reversal in multilayers supporting perpendicular magnetization," *Journal of Physics D: Applied Physics*, vol. 32, no. 4, pp. 395–403, 1999.

[50] T. Matsuda, K. Harada, H. Kasai, O. Kamimura, and A. Tonomura, "Observation of dynamic interaction of vortices with pinning centers by Lorentz microscopy," *Science*, vol. 271, no. 5254, pp. 1393–1395, 1996.

[51] J. Rajeswari, P. Huang, G. F. Mancini, Y. Murooka, T. Latychevskaia, D. McGrouther, M. Cantoni, E. Baldini, J. S. White, A. Magrez, *et al.*, "Filming the formation and fluctuation of skyrmion domains by cryo-Lorentz transmission electron microscopy," *Proceedings of the National Academy of Sciences*, vol. 112, no. 46, pp. 14212–14217, 2015.

[52] S. Pöllath, J. Wild, L. Heinen, T. N. Meier, M. Kronseder, L. Tutsch, A. Bauer, H. Berger, C. Pfleiderer, J. Zweck, A. Rosch, and C. H. Back, "Dynamical Defects in Rotating Magnetic Skyrmion Lattices," *Physical Review Letters*, vol. 118, no. 20, pp. 1–6, 2017.

[53] M. J. Benitez, A. Hrabec, A. P. Mihai, T. A. Moore, G. Burnell, D. Mcgrouther, C. H. Marrows, and S. McVitie, "Magnetic microscopy and topological stability of homochiral Néel domain walls in a Pt/Co/AlO x trilayer," *Nature Communications*, vol. 6, no. 1, p. 8957, 2015.

[54] S. Emori, U. Bauer, S. M. Ahn, E. Martinez, and G. S. Beach, "Current-driven dynamics of chiral ferromagnetic domain walls," *Nature Materials*, vol. 12, no. 7, pp. 611–616, 2013.

[55] A. V. Khvalkovskiy, V. Cros, D. Apalkov, V. Nikitin, M. Krounbi, K. A. Zvezdin, A. Anane, J. Grollier, and A. Fert, "Matching domain-wall configuration and spin-orbit torques for efficient domain-wall motion," *Physical Review B - Condensed Matter and Materials Physics*, vol. 87, p. 020402, 2013.

[56] W. Jiang, P. Upadhyaya, W. Zhang, G. Yu, M. B. Jungfleisch, F. Y. Fradin, J. E. Pearson, Y. Tserkovnyak, K. L. Wang, O. Heinonen, S. G. Te Velthuis, and A. Hoffmann, "Blowing magnetic skyrmion bubbles," *Science*, vol. 349, no. 6245, pp. 283–286, 2015.

[57] K. Litzius, I. Lemesh, B. Krüger, P. Bassirian, L. Caretta, K. Richter, F. Büttner, K. Sato, O. A. Tretiakov, J. Förster, R. M. Reeve, M. Weigand, I. Bykova, H. Stoll, G. Schütz, G. S. Beach, and M. Klaüi, "Skyrmion Hall effect revealed by direct time-resolved X-ray microscopy," *Nature Physics*, vol. 13, no. 2, pp. 170–175, 2017.

[58] A. Hrabec, J. Sampaio, M. Belmeguenai, I. Gross, R. Weil, S. M. Chérif, A. Stashkevich, V. Jacques, A. Thiaville, and S. Rohart, "Current-induced skyrmion generation and dynamics in symmetric bilayers," *Nature Communications*, vol. 8, p. 15765, 2017.

[59] M. Krajnak, D. McGrouther, D. Maneuski, V. O'Shea, and S. McVitie, "Pixelated detectors and improved efficiency for magnetic imaging in STEM differential phase contrast," *Ultramicroscopy*, vol. 165, pp. 42–50, 2016.

[60] J. N. Chapman, P. E. Batson, E. M. Waddell, and R. P. Ferrier, "The direct determination of magnetic domain wall profiles by differential phase contrast electron microscopy," *Ultramicroscopy*, vol. 3, no. C, pp. 203–214, 1978.

[61] J. N. Chapman, I. R. McFadyen, and S. McVitie, "Modified Differential Phase Contrast Lorentz Microscopy for Improved Imaging of Magnetic Structures," *IEEE Transactions on Magnetics*, vol. 26, no. 5, pp. 1506–1511, 1990.

[62] D. McGrouther, M. J. Benitez, S. McFadzean, and S. McVitie, "Development of aberration corrected differential phase contrast (DPC) STEM," *JEOL News*, vol. 49, no. 2, pp. 2–10, 2014.

[63] R. Plackett, I. Horswell, E. N. Gimenez, J. Marchal, D. Omar, and N. Tartoni, "Merlin: A fast versatile readout system for Medipix3," *Journal of Instrumentation*, vol. 8, no. 1, 2013.

[64] T. J. Pennycook, A. R. Lupini, H. Yang, M. F. Murfitt, L. Jones, and P. D. Nellist, "Efficient phase contrast imaging in STEM using a pixelated detector. Part 1: Experimental demonstration at atomic resolution," *Ultramicroscopy*, vol. 151, pp. 160–167, 2015.

[65] H. Yang, T. J. Pennycook, and P. D. Nellist, "Efficient phase contrast imaging in STEM using a pixelated detector. Part II: Optimisation of imaging conditions," *Ultramicroscopy*, vol. 151, pp. 232–239, 2015.

[66] K. X. Nguyen, P. Purohit, A. Yadav, M. W. Tate, C. S. Chang, R. Ramesh, S. M. Gruner, and D. A. Muller, "Reconstruction of Polarization Vortices by Diffraction Mapping of Ferroelectric PbTiO3 / SrTiO3 Superlattice Using a High Dynamic Range Pixelated Detector," *Microscopy and Microanalysis*, vol. 22, no. S3, pp. 472–473, 2016.

[67] K. Müller-Caspary, F. F. Krause, T. Grieb, S. Löffler, M. Schowalter, A. Béché, V. Galioit, D. Marquardt, J. Zweck, P. Schattschneider, J. Verbeeck, and A. Rosenauer, "Measurement of atomic electric fields and charge densities from average momentum transfers using scanning transmission electron microscopy," *Ultramicroscopy*, vol. 178, no. 2017, pp. 62–80, 2017.

[68] M. Nord, A. Ross, D. McGrouther, J. Barthel, M. Moreau, I. Hallsteinsen, T. Tybell, and I. MacLaren, "Three-dimensional subnanoscale imaging of unit cell doubling due to octahedral tilting and cation modulation in strained perovskite thin films," *Physical Review Materials*, vol. 3, no. 6, pp. 1–7, 2019.

[69] R. J. Lamb, *Exploring methods for imaging dynamics in transmission electron microscopy*. PhD thesis, University of Glasgow, 2019.

[70] R. Ballabriga, M. Campbell, E. Heijne, X. Llopart, L. Tlustos, and W. Wong, "Medipix3: A 64 k pixel detector readout chip working in single photon counting mode with improved spectrometric performance," *Nuclear Instruments and Methods in Physics Research, Section A: Accelerators, Spectrometers, Detectors and Associated Equipment*, vol. 633, no. SUPPL. 1, pp. S15–S18, 2011.

[71] M. Krajnak, "Pixelated DPC." `https://github.com/matkraj/pixelatedDPC`, 2018.

[72] J. N. Chapman and M. R. Scheinfein, "Transmission electron microscopies of magnetic microstructures," *Journal of Magnetism and Magnetic Materials*, vol. 200, pp. 729–740, 1999.

[73] Y. Togawa, T. Koyama, K. Takayanagi, S. Mori, Y. Kousaka, J. Akimitsu, S. Nishihara, K. Inoue, A. S. Ovchinnikov, and J. Kishine, "Chiral magnetic soliton lattice on a chiral helimagnet," *Physical Review Letters*, vol. 108, no. 10, pp. 21–25, 2012.

[74] H. Nakajima, A. Kotani, K. Harada, and S. Mori, "Observation of magnetic domains in uniaxial magnets via small-angle electron diffraction and Foucault imaging," *Japanese Journal of Applied Physics*, vol. 58, no. 5, 2019.

[75] H. Hopster and H. Oepen, *Magnetic Microscopy of Nanostructures*. Springer, 2007.

[76] M. R. McCartney, R. E. Dunin-Borkowski, and D. J. Smith, "Quantitative measurement of nanoscale electrostatic potentials and charges using off-axis electron holography: Developments and opportunities," *Ultramicroscopy*, vol. 203, no. February, pp. 105–118, 2019.

[77] L. Gross, F. Mohn, N. Moll, P. Liljeroth, and G. Meyer, "The chemical structure of a molecule resolved by atomic force microscopy," *Science*, vol. 325, no. 5944, pp. 1110–1114, 2009.

[78] W. Melitz, J. Shen, A. C. Kummel, and S. Lee, "Kelvin probe force microscopy and its application," *Surface Science Reports*, vol. 66, no. 1, pp. 1–27, 2011.

[79] B. J. Rodriguez, A. Gruverman, A. I. Kingon, R. J. Nemanich, and J. S. Cross, "Three-dimensional high-resolution reconstruction of polarization in ferroelectric capacitors by piezoresponse force microscopy," *Journal of Applied Physics*, vol. 95, no. 4, pp. 1958–1962, 2004.

[80] O. Kazakova, R. Puttock, C. Barton, H. Corte-León, M. Jaafar, V. Neu, and A. Asenjo, "Frontiers of magnetic force microscopy," *Journal of Applied Physics*, vol. 125, no. 6, 2019.

[81] H. Hopster and H. Oepen, *Magnetic Microscopy of Nanostructures*. Springer, 2007.

[82] X. Zhu, *Magnetic force microscopy studies of submicron and nanoscale magnet arrays*. PhD thesis, McGill University, 2002.

[83] A. Hubert, W. Rave, and S. L. Tomlinson, "Imaging Magnetic Charges with Magnetic Force Microscopy," *Physica Status Solidi (B) Basic Research*, vol. 204, no. 2, pp. 817–828, 1997.

[84] K. Zeissler, M. Mruczkiewicz, S. Finizio, J. Raabe, P. M. Shepley, A. V. Sadovnikov, S. A. Nikitov, K. Fallon, S. McFadzean, S. McVitie, T. A. Moore, G. Burnell, and C. H. Marrows, "Pinning and hysteresis in the field dependent diameter evolution of skyrmions in Pt/Co/Ir superlattice stacks," *Scientific Reports*, vol. 7, no. 1, pp. 1–9, 2017.

[85] K. Zeissler, S. Finizio, K. Shahbazi, J. Massey, F. A. Ma'Mari, D. M. Bracher, A. Kleibert, M. C. Rosamond, E. H. Linfield, T. A. Moore, J. Raabe, G. Burnell, and C. H. Marrows, "Discrete Hall resistivity contribution from Néel skyrmions in multilayer nanodiscs," *Nature Nanotechnology*, vol. 13, no. 12, pp. 1161–1166, 2018.

[86] J. Y. Chauleau, W. Legrand, N. Reyren, D. Maccariello, S. Collin, H. Popescu, K. Bouzehouane, V. Cros, N. Jaouen, and A. Fert, "Chirality in Magnetic Multilayers Probed by the Symmetry and the Amplitude of Dichroism in X-Ray Resonant Magnetic Scattering," *Physical Review Letters*, vol. 120, p. 037202, 2018.

[87] W. Legrand, J. Y. Chauleau, D. Maccariello, N. Reyren, S. Collin, K. Bouzehouane, N. Jaouen, V. Cros, and A. Fert, "Hybrid chiral domain walls and skyrmions in magnetic multilayers," *Science Advances*, vol. 4, no. 7, 2018.

[88] H. Hopster and H. Oepen, *Magnetic Microscopy of Nanostructures*. Springer, 2007.

[89] S. Heinze, K. Von Bergmann, M. Menzel, J. Brede, A. Kubetzka, R. Wiesendanger, G. Bihlmayer, and S. Blügel, "Spontaneous atomic-scale magnetic skyrmion lattice in two dimensions," *Nature Physics*, vol. 7, no. 9, pp. 713–718, 2011.

[90] N. Romming, C. Hanneken, M. Menzel, J. E. Bickel, B. Wolter, K. Von Bergmann, A. Kubetzka, and R. Wiesendanger, "Writing and deleting single magnetic skyrmions," *Science*, vol. 341, pp. 636–639, 2013.

[91] G. Chen, S. P. Kang, C. Ophus, A. T. N'Diaye, H. Y. Kwon, R. T. Qiu, C. Won, K. Liu, Y. Wu, and A. K. Schmid, "Out-of-plane chiral domain wall spin-structures in ultrathin in-plane magnets," *Nature Communications*, vol. 8, no. May, pp. 1–7, 2017.

[92] D. A. Gilbert, B. B. Maranville, A. L. Balk, B. J. Kirby, P. Fischer, D. T. Pierce, J. Unguris, J. A. Borchers, and K. Liu, "Realization of ground-state artificial skyrmion lattices at room temperature," *Nature Communications*, vol. 6, no. May, pp. 1–7, 2015.

[93] J. Lucassen, F. Kloodt-Twesten, R. Frömter, H. P. Oepen, R. A. Duine, H. J. Swagten, B. Koopmans, and R. Lavrijsen, "Scanning electron microscopy with polarization analysis for multilayered chiral spin textures," *Applied Physics Letters*, vol. 111, no. 13, 2017.

[94] N. O. Urs, B. Mozooni, P. Mazalski, M. Kustov, P. Hayes, S. Deldar, E. Quandt, and J. McCord, "Advanced magneto-optical microscopy: Imaging from picoseconds to centimeters - Imaging spin waves and temperature distributions (invited)," *AIP Advances*, vol. 6, no. 5, 2016.

[95] A. Hrabec, N. A. Porter, A. Wells, M. J. Benitez, G. Burnell, S. McVitie, D. McGrouther, T. A. Moore, and C. H. Marrows, "Measuring and tailoring the Dzyaloshinskii-Moriya interaction in perpendicularly magnetized thin films," *Physical Review B - Condensed Matter and Materials Physics*, vol. 90, no. 2, 2014.

[96] A. Fernández-Pacheco, E. Vedmedenko, F. Ummelen, R. Mansell, D. Petit, and R. P. Cowburn, "Symmetry-breaking interlayer DzyaloshinskiiMoriya interactions in synthetic antiferromagnets," *Nature Materials*, vol. 18, no. 7, pp. 679–684, 2019.

[97] P. Maletinsky, S. Hong, M. S. Grinolds, B. Hausmann, M. D. Lukin, R. L. Walsworth, M. Loncar, and A. Yacoby, "A robust scanning diamond sensor for nanoscale imaging with single nitrogen-vacancy centres," *Nature Nanotechnology*, vol. 7, no. 5, pp. 320–324, 2012.

[98] Y. Dovzhenko, F. Casola, S. Schlotter, T. X. Zhou, F. Büttner, R. L. Walsworth, G. S. Beach, and A. Yacoby, "Magnetostatic twists in room-temperature skyrmions explored by nitrogen-vacancy center spin texture reconstruction," *Nature Communications*, vol. 9, no. 1, pp. 1–7, 2018.

[99] A. Vansteenkiste, J. Leliaert, M. Dvornik, M. Helsen, F. Garcia-Sanchez, and B. Van Waeyenberge, "The design and verification of MuMax3," *AIP Advances*, vol. 4, no. 10, 2014.

[100] M. J. Donahue, "OOMMF User's Guide, Version 1.0," tech. rep., NIST, 1999.

[101] T. Fischbacher, M. Franchin, G. Bordignon, and H. Fangohr, "A systematic approach to multiphysics extensions of finite-element-based micromagnetic simulations: Nmag," in *IEEE Transactions on Magnetics*, vol. 43, pp. 2896–2898, 2007.

[102] C. Abert, L. Exl, F. Bruckner, A. Drews, and D. Suess, "Magnum.fe: A micromagnetic finite-element simulation code based on FEniCS," *Journal of Magnetism and Magnetic Materials*, vol. 345, pp. 29–35, 2013.

[103] J. C. Slonczewski, "Current-driven excitation of magnetic multilayers," *Journal of Magnetism and Magnetic Materials*, vol. 159, no. 1-2, pp. L1—-L7, 1996.

[104] S. Zhang and Z. Li, "Roles of nonequilibrium conduction electrons on the magnetization dynamics of ferromagnets," *Physical Review Letters*, vol. 93, no. 12, 2004.

[105] S. McVitie and J. N. Chapman, "Measurement of domain wall widths in Permalloy using differential phase contrast imaging in stem," *Journal of Magnetism and Magnetic Materials*, vol. 83, no. 1-3, pp. 97–98, 1990.

[106] M. Mansuripur, "Computation of electron diffraction patterns in Lorentz electron microscopy of thin magnetic films (abstract)," *Journal of Applied Physics*, vol. 69, no. 8, p. 5890, 1991.

[107] S. K. Walton, K. Zeissler, W. R. Branford, and S. Felton, "MALTS: A tool to simulate lorentz transmission electron microscopy from micromagnetic simulations," *IEEE Transactions on Magnetics*, vol. 49, no. 8, pp. 4795–4800, 2013.

[108] M. De Graef and Y. Zhu, "Quantitative noninterferometric Lorentz microscopy," *Journal of Applied Physics*, vol. 89, no. 11 II, pp. 7177–7179, 2001.

[109] I. A. Beardsley, "Reconstruction of the Magnetization in a Thin Film by a Combination of Lorentz Microscopy and External Field Measurements," *IEEE Transactions on Magnetics*, vol. 25, no. 1, pp. 671–677, 1989.

4

Imaging of Néel type domain walls in perpendicularly magnetised materials

Contents

4.1 Introduction

It was discussed in section 3.7.3 that it can be non-trivial to extract information about the wall magnetisation from Lorentz TEM images. The complications stem from the distribution of the stray field associated with the wall magnetisation. The aim of this short chapter is twofold: to explain the image contrast expected from different domain wall configurations, which is complementary to the remaining chapters; and to outline a method of extracting the direction of Néel type domain

walls from Fresnel images. The desire to extract this information was initially motivated by the fixed chirality imprinted on the wall magnetisation by an interfacial DMI interaction [1]; determination of the direction of the Néel domain walls provides access to the chirality of the magnetisation. As outlined in section 2.2.2, access to this property allows determination of the sign of the DMI in the material system thus adding to the wealth of information available from TEM imaging described in Chapter 3. In fact, systems with a strong interfacial DMI are the ideal sample to test this measurement method precisely because the direction of the domain walls is known.

First, the principle behind measurement of the Néel wall direction is demonstrated using Fresnel images calculated from analytical models of the magnetisation, before experimental work is presented. To date, experimental measurement of the Néel wall direction from Fresnel images has not been realised, the results remain inconclusive. This conclusion was reached independently by another research group [2].

4.2 Fresnel TEM image contrast from domain wall magnetisation

This chapter makes use of the analytical models of the magnetisation described in section 3.10.2. The magnetic configuration is modelled using a hyperbolic tangent with width parameter $w = 10$ nm and is then used to calculate the Fresnel image contrast expected from magnetisation configurations with Bloch and Néel type walls for a range of beam-sample orientations. Fresnel images were calculated for a sample of 0.6 nm thickness, chosen to match the experimental work, and with a defocus of 0.5 mm.

In section 2.3.1, which introduced Bloch and Néel type domain walls, it was noted that in PMA materials Bloch type domain walls are charge-less where Néel type walls are charged because of significant $\nabla \cdot \mathbf{M}$. Therefore, considering infinitely long domain walls, sketched in Fig. 4.1, Bloch walls are not associated with stray field $\mathbf{H}$ but Néel type walls are. Because of this, for Bloch walls the Lorentz

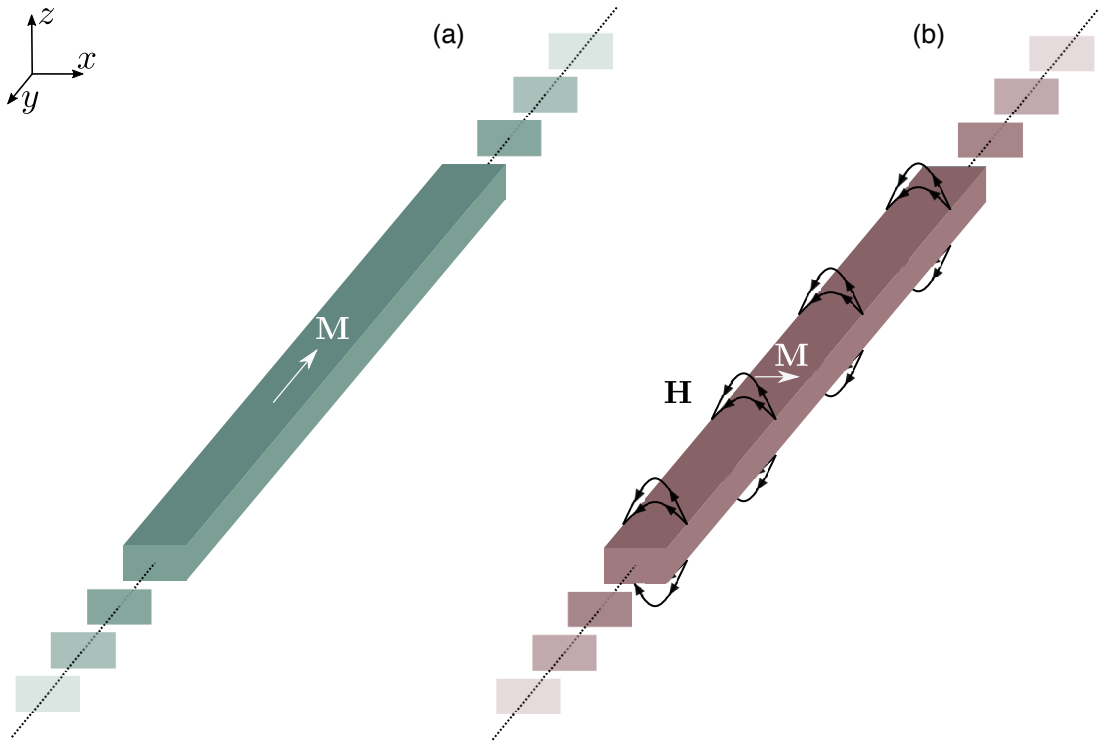

Figure 4.1: (a) In PMA systems (only considering the magnetisation at the very centre of a wall running along the $\pm y$ direction), the magnetisation **M** of a Bloch walls is parallel to the wall length and thus, in the case of an infinitely long domain wall, is not associated with any stray field **H**. (b) Néel type walls are divergent and therefore are associated with a stray field.

deflection, arising from the magnetic induction **B** ($= \mu_0(\mathbf{M} + \mathbf{H})$), correlates directly with the domain wall magnetisation. The situation for Néel walls is more complicated.

The Fresnel image contrast expected from magnetisation configurations with PMA and Bloch and Néel type domain walls is presented in Fig. 4.2. The electron beam trajectory is along the z direction. The left most column of Fig. 4.2 contains sketches that specify the magnetic configuration from which the Fresnel images, in the central and right most columns, were calculated from. The central and right most columns respectively contain Fresnel images calculated without a tilt and with a tilt of 25° about the axis indicated. As explained in section 3.7.3, when the sample is untilted (i.e. the beam is normal to the sample) out of plane magnetisation does not give any Fresnel contrast. From the second row, it is clear that the direction of a Bloch type wall is easily determined from Fresnel imaging, because the wall

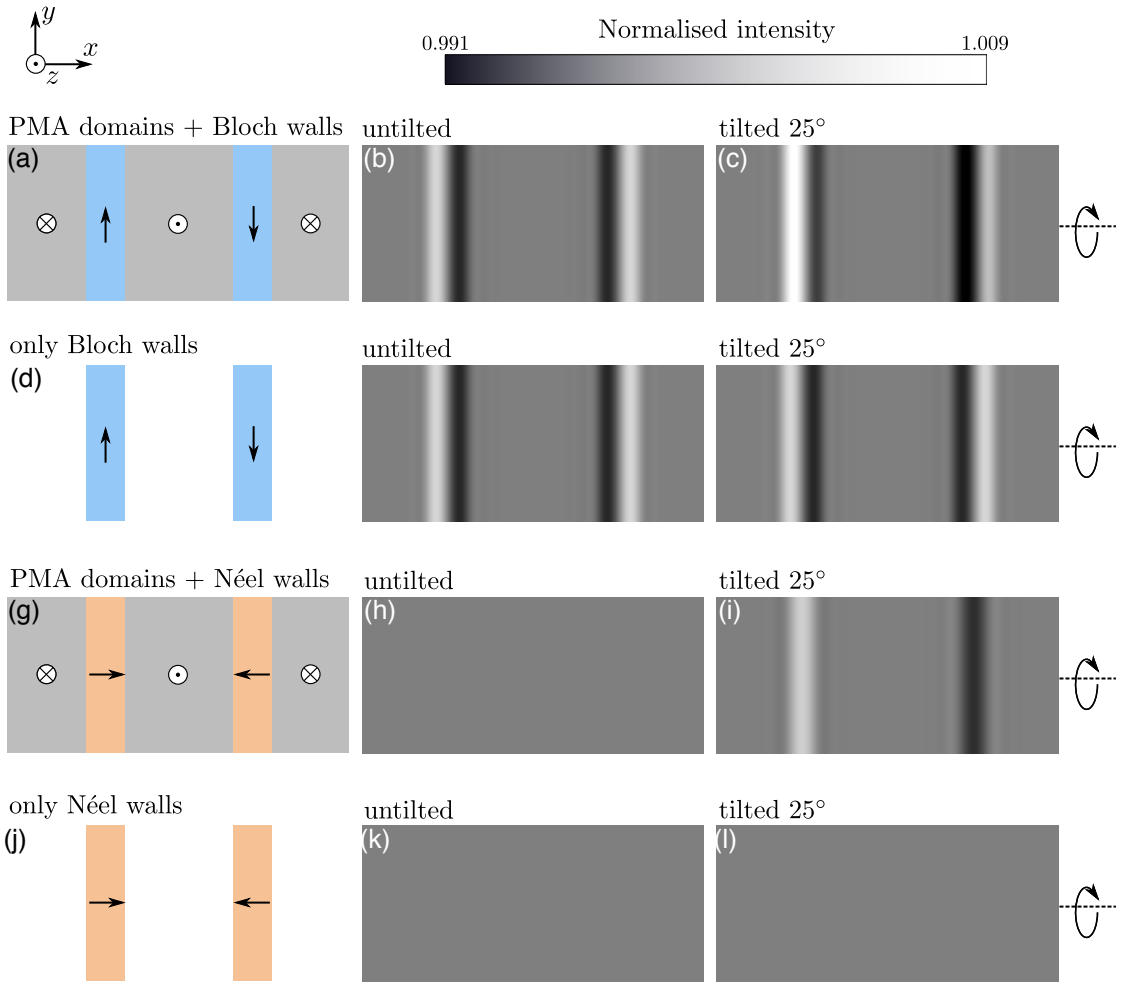

Figure 4.2: Fresnel images were calculated from samples with Bloch and Néel type walls both untilted and tilted by 25° about the axis indicated. To highlight the contrast that arises from the walls directly, two sets of calculations are performed (*i*) with the domain and wall magnetisation and (*ii*) with only the wall magnetisation. The left most column contains schematics that show the magnetisation configuration the Fresnel images in the central column (without tilt) and right most column (with tilt) were calculated from. From the second row its clear that Bloch type walls generate contrast which permits determination of the wall direction. From the bottom row, Néel type walls are not directly associated with any contrast therefore their direction cannot be determined. The third row, indicates that contrast arising from the domain magnetisation reveals the location of the walls.

magnetisation itself deflects the beam. To summarise Bloch walls are associated with bright/dark contrast, the order of which is determined by the direction of the wall magnetisation, experimental images showing this characteristic contrast can be found in the literature [3]. When the sample is tilted the contrast from the wall is present as well as contrast from the domains (see Fig. 4.2(c)).

The magnetisation of Néel type walls is purely divergent therefore (as discussed in section 3.7.3), the stray field and magnetisation cancel entirely when integrated through the thickness i.e. $\int(\mathbf{B}\times\mathbf{z})\,dz = 0$. Therefore, as is clear from the bottom row of Fig. 4.2, the wall magnetisation is not associated with any Fresnel image contrast. The location of Néel type walls can be revealed from by tilting the sample to get contrast from the domain magnetisation, this is shown in Fig. 4.2(i). The Néel nature of the walls can be inferred from the lack of contrast at zero tilt [4], but there is no information about the wall direction encoded in images taken with a sample tilt about an axis perpendicular to the wall length as is clear from Fig. 4.2(l). Next, different beam-sample geometries are considered to identify a geometry where the wall magnetisation may itself gives Fresnel image contrast.

4.3 Rationale behind extraction of Néel wall handedness using Lorentz microscopy

This section uses the curl of $\mathbf{M}$ formalism of the Lorentz deflection, given in Eq. 3.14, where the source of image contrast is considered as $\int(\nabla\times\mathbf{M})\cdot\mathbf{z}\,dz$ [5]. This is convenient as it relates directly to the magnetisation. The geometric distribution of $\nabla\times\mathbf{M}$ of a Néel wall, sketched in Fig. 4.3(a), is considered for a range of beam-sample geometries. Throughout this chapter, the beam-sample geometries are quantified using the angle Φ, which is defined as the rotation angle between the tilt axis and the local plane of the domain wall as sketched in Fig. 4.3(b). The distribution of $\nabla\times\mathbf{M}$ with respect to the z axis (i.e. the electron trajectory) for a wall tilted about different axes, as defined by Φ, is considered in Fig. 4.3(c).

With no tilt and with a tilt around a $\Phi = 0°$ axis, all curl is in the y direction and $(\nabla\times\mathbf{M})\cdot\mathbf{z} = 0$ therefore there is no contrast. By tilting about a $\Phi = 90°$ axis, $(\nabla\times\mathbf{M})\cdot\mathbf{z} \neq 0$ however it is fully compensated when projected along z and still no contrast is expected. By tilting about an intermediate axis with $\Phi = 45°$ there is $(\nabla\times\mathbf{M})\cdot\mathbf{z} \neq 0$ which is misaligned in z, therefore it is possible that this geometry provides access to image contrast pertaining to the wall itself.

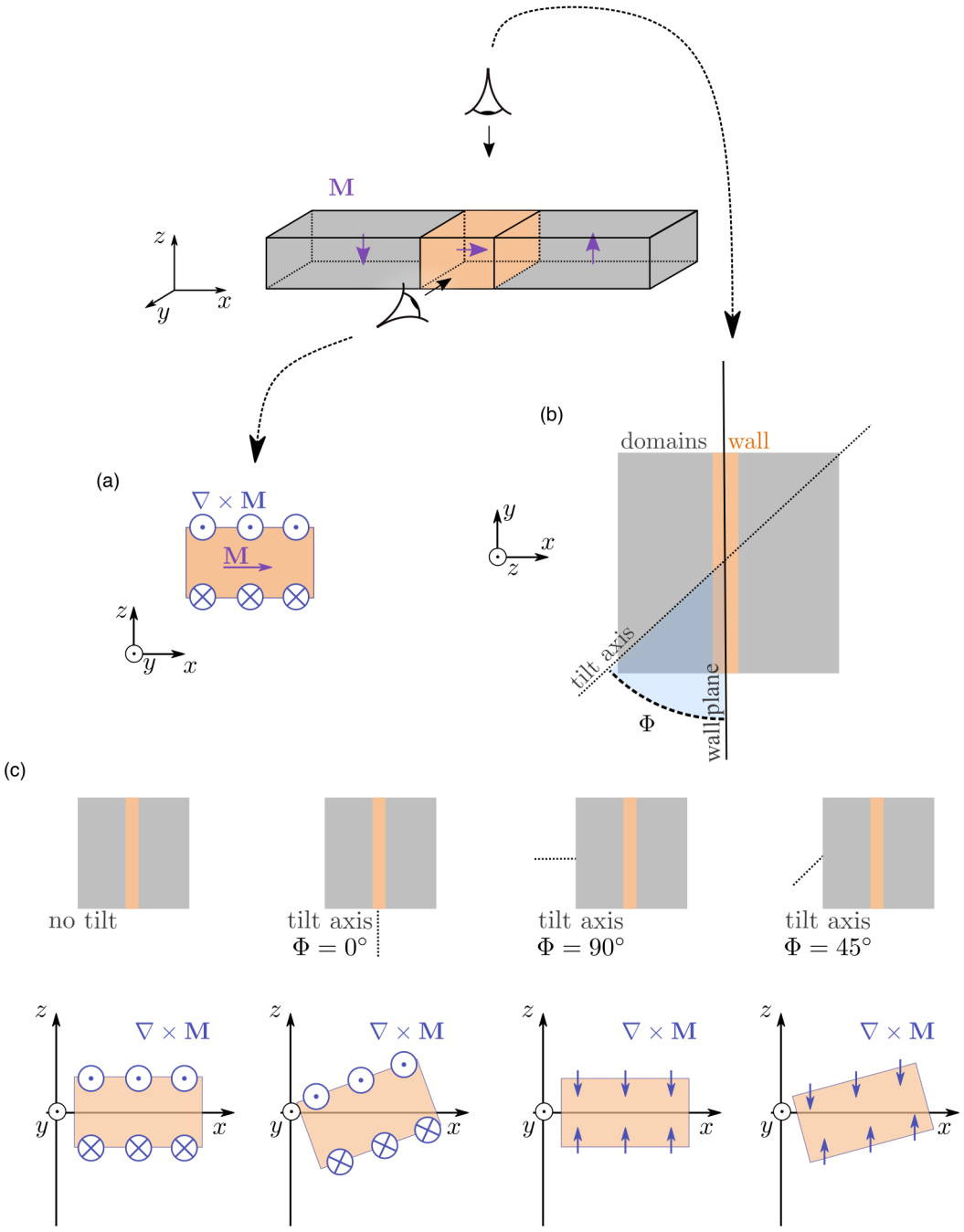

Figure 4.3: The schematic at the top of the figure is provided to aid interpretation of the two different view points considered in the rest of the figure. (a) Schematic of a Néel wall with magnetisation along $+x$ considered in cross-section together with its $\nabla \times \mathbf{M}$. (b) the angle Φ is defined as the angle between the tilt axis and the plane of the domain wall. (c) the variation of $\nabla \times \mathbf{M}$ with respect to z is considered for (from left to right) no tilt, tilt about $\Phi = 0°$, 90°,45°. Lorentz image contrast arises from $\int (\nabla \times \mathbf{M}) \cdot \mathbf{z}\, dz$ therefore images collected with tilt about a $\Phi = 45$ axis could result in image contrast from the wall itself.

4.4 Simulation

Figure 4.4 compares Fresnel images calculated, from the same analytical model of the magnetisation used for Fig. 4.2, with a tilt of 25° about axes Φ=90° (middle column) and Φ=45° (right column). The tilt of 25° was chosen as it represents the maximum tilt experimentally accessible for samples deposited on TEM membrane substrates. Though subtle, tilting about a Φ=45° axis adds a visible asymmetry to the perfectly symmetric contrast that arises from the domains. The asymmetry is more visible in Fig. 4.4(g) which displays linetraces taken through images

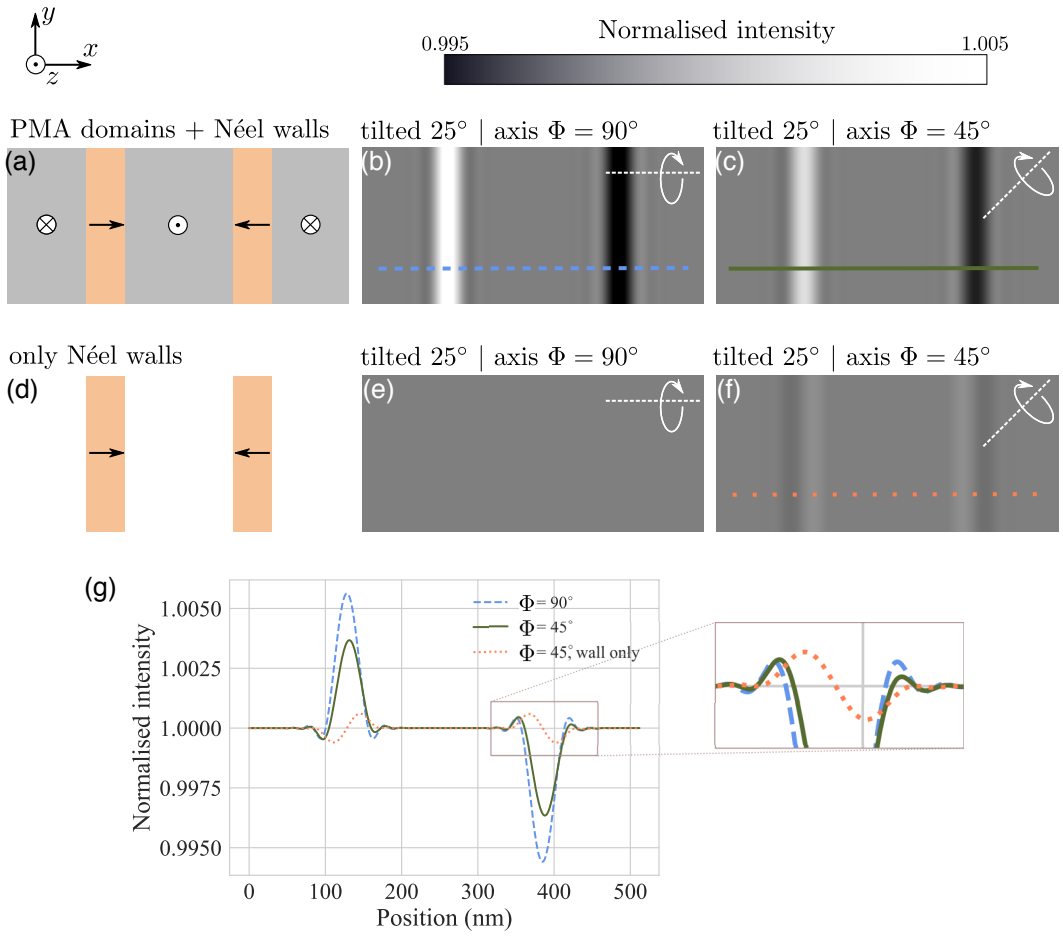

Figure 4.4: (b,c) Fresnel images calculated from Néel type walls with PMA (sketched in (a)) tilted by 25° about Φ=90° and Φ=45° axes respectively. (e,f) Fresnel images calculated from Néel type walls only (sketched in (d)) tilted by 25° about Φ=90° and Φ=45° axes respectively. A tilt about a Φ=45° axis introduces an asymmetry to the contrast which is related to the wall magnetisation - compare (c) and (f). This asymmetry is clearer from the graph in (g) which contains linetraces through (b), (c) and (f).

Fig. 4.4(b) and (c). Looking at Fig. 4.4(f), which shows Fresnel image contrast calculated only from the wall magnetisation tilted about a Φ=45° axis, proves this asymmetry arises from the wall directly. Thus, the direction of the domain wall can in theory be accessed through quantification of the asymmetry of the Fresnel image contrast compared to the angle of the tilt axis Φ.

The asymmetry is quantified using the parameter ΔI_{asym} which is labelled in Fig. 4.5(a) together with the background contrast I_0 and the domain contrast I_{dom}. The calculated variation of ΔI_{asym} for a range of Φ values shown in Fig. 4.5 where, as expected, the maximum asymmetry is found for $\Phi = 45°, 135°$. With consideration of the domain contrast type (that is convergent (bright) or divergent (dark)), the angle Φ and sign of ΔI_{asym} the wall magnetisation may, in principle, be extracted from Fresnel images.

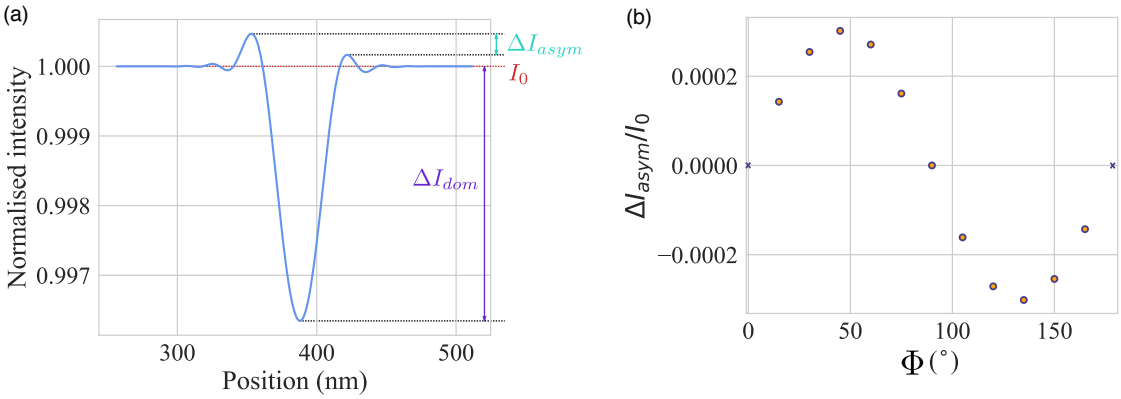

Figure 4.5: (a) Quantities used to quantify the Fresnel image contrast are labelled - that is the asymmetry ΔI_{asym}, the background contrast level I_0 and the domain contrast level I_{dom}. (b) Graph of ΔI_{asym} with Φ, tilt axis that are $\pm$ 45° from the wall axis give maximum magnitude of asymmetry. The image calculations used a magnetic configuration with thickness 0.6 nm and a wall width of $\approx$ 20 nm.

4.5 Experiment

To test the proposed method of measuring the Néel wall direction from Fresnel images, a trilayer sample was grown on a standard TEM membrane substrate by Katharina Zeissler of the University of Leeds. The sample composition was Ta(4.6)/Pt(7.5)/Co(0.6)/Ir(0.5)/Pt(7.5) where the bracketed number is the layer

thickness in nm. The walls were confirmed to be homochiral as they do not annihilate when pushed close together with an external magnetic field [4]. From a series of Fresnel images, the wall width was estimated to be $\approx$ 50 nm, this is wider than the modelled wall which was $\approx$ 20 nm wide. Furthermore, because this sample is associated with a very small Lorentz deflection ($\beta_L = 0.1$ μrad) a defocus above 10 mm is required to get sufficient magnetic contrast ($\approx$ 10% above the background contrast). This is considerably larger than the 0.5 mm defocus used to demonstrate the principle in the preceding section. Appendices A and B include details of measurement of the wall width from Fresnel images and compares Fresnel contrast calculated with realistic defocus values and from walls of realistic width. It is noted that the magnitude of the asymmetry is highly variable with both defocus and wall width.

Figure 4.6 shows a Fresnel image taken with a tilt of 25.2° about the axis marked in a field free enviroment (residual field strength less than 10 μT). The walls in the image form a large range of angles with the tilt axis, therefore one image allows access to walls of various Φ. The analysis of four segments of wall is presented in the graphs around the Fresnel image in Fig. 4.6. To analyse the wall contrast, straight segments of wall are identified and a single profile is produced by aligning and averaging each profile in the wall segment. This averaging is necessary to mitigate the effect of the background variations that primarily arise from the crystallites.

Wall segment 1 has $\Phi = 90°$ and is therefore expected to have symmetric contrast but shows strong asymmetry. Further inconsistency is found by comparing wall segments 3 and 4 which both have $\Phi = 70°$ and therefore should have the same level of asymmetry however wall segment 3 is almost symmetric where wall segment 4 is strongly asymmetric. Full analysis of $\approx$ 100 wall segments of various Φ values (expected to yield asymmetric Fresnel contrast) yielded asymmetry values that were 41% consistent with one sense of handedness, 30% consistent with the other sense of handedness and 29% showed no asymmetry. This therefore suggests the source of this experimentally detected asymmetry is not from the divergent Néel wall magnetisation. The experiment was repeated for a range of defocus values

and with different spot sizes and different condenser apertures (to improve beam coherence at the cost of electron flux) but the results remained inconsistent.

4.5.1 Modifications to experiment

Three modifications were made to the experiment in attempt to successfully extract the Néel wall direction. All were unsuccessful but they are briefly described in this section. Two new samples were prepared on standard TEM grids which permit imaging up to a tilt of 60°. As shown in Fig. 4.7, simulations show that imaging with a higher tilt angle increases the magnitude of the asymmetry (from image contrast calculations ΔI_{asym} is almost an order of magnitude larger at a 60° tilt compared to a 25° tilt). A sample of the same composition as before was prepared, as was a ten repeat sample. The latter supports narrower walls ($\delta \approx 30nm$) [6]

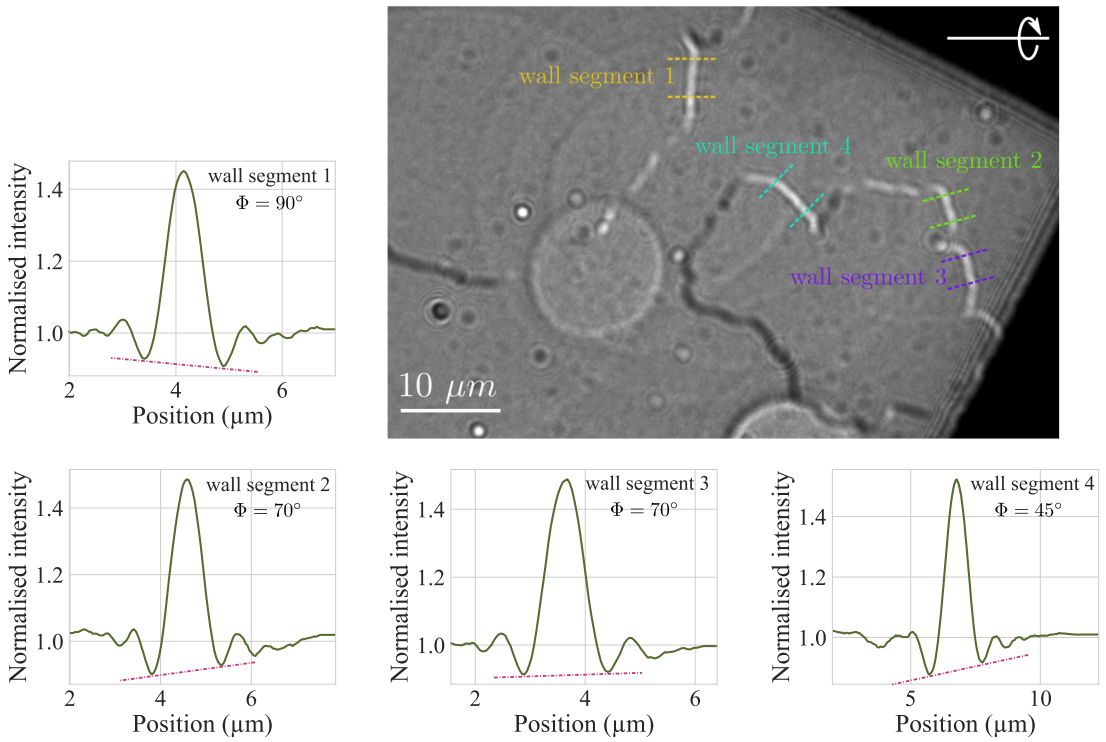

Figure 4.6: A Fresnel image, tilted around the axis indicated by 25.2°, is presented and annotated with the location of different wall segments. These are relatively straight sections of wall at some angle Φ to the tilt axis. The graphs around the Fresnel image show results of the analysis of these wall segments which are not consistent with the simulations. Segment 1, Φ = 90 ° is expected to be symmetric where segments 2 and 3, Φ = 70 ° were expected to have the same level of asymmetry.

and the larger magnetic thickness gives rise to a larger Lorentz deflection ($\beta_L \approx 1$ μrad at a 25° tilt). Consequently, it can be imaged with lower defocus (good contrast is achieved with $\Delta = 5mm$). The ten repeat sample therefore gives access to a different parameter space than the single repeat sample. The results of analysis of data sets collected from these samples at higher tilt angles were however also inconsistent.

It was thought that the background variations from the crystallites were masking the Néel wall direction related asymmetries and the cause of the spurious asymmetry measurements. Taking the Fresnel image in Fig. 4.6 as an example: the standard deviation measured in an area without magnetic contrast (or beam contamination which is the circular contrast) is ≈ 150 counts, where the asymmetry measured from wall segments 1 - 4 is between 40 and 150 counts.

To address this issue, principle component analysis (PCA) was implemented using HyperSpy [7]. PCA is a widely used data analysis tool. In the microscopy community, it is often used to aid analysis of spectroscopic images like energy dispersive spectroscopy (EDS) and electron energy loss spectroscopy (EELS) images [8–11]. In this case, PCA decomposes the dataset into a finite number of components from which each spectrum in the dataset can be described as a weighted sum. Thus PCA finds a parametric model of the dataset. The components are identified and ordered based on their variance [12]. High variance components (termed significant) are likely to be associated with useful signals where low variance components are

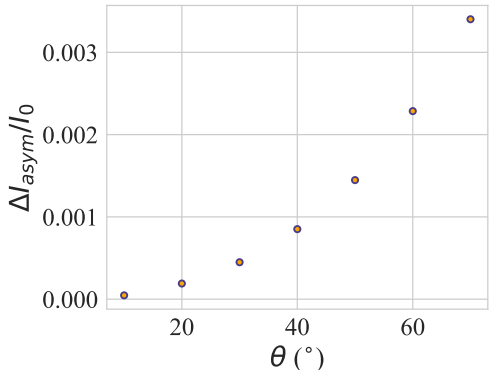

Figure 4.7: Fresnel image calculations indicate that increasing the tilt angle θ increases the magnitude of the asymmetry.

often associated with noise and can be discarded. In the case of Fresnel images, each row of the 2D image is treated as a 1D 'spectrum' (which is equivalent to a single line trace). Every line trace or 'spectrum' then, in principle, contains the same high variance magnetic signal plus low variance contrast from other sources (noise, contamination, crystallites) which differs in each line trace.

Figure 4.8 shows the result of PCA on wall segment 3 of Fig. 4.6, which is shown cropped and rotated in Fig. 4.8(a). Evaluation of the variance scree plot produced by the PCA (as described by R. Wilcox [13]), suggested there are two significant components in this Fresnel image. Figure 4.8(b) is a reconstruction of (a) using only the two most significant PCA components, where (c) is a reconstruction using the *next* 20 components. Inspection of Figs. 4.8(a,b,c) indicate PCA has successfully isolated the magnetic contrast in Fig. 4.8(a). However when the profile is averaged (as before), the exact same intensity profile is achieved from Figs. 4.8(a) and (b). This is shown in the line traces in Figs. 4.8(d) and (e), where (d) shows the line traces and (e) shows the difference between the two. The addition of PCA to the data analysis routine does not change the results of the experiment. One critical assumption of PCA is that the signal has higher variance than the noise [8]. It is therefore judged that the failure of this method to reliably extract the Néel wall direction is simply because the signal is buried in noise and crystallite contrast. Another research group, based in Argonne, independently proposed extraction of the chirality of Néel type objects from Fresnel image contrast asymmetry in work published this year [2]. Their simulations show the same characteristic asymmetry that is presented in this chapter, and their experimental work is also inconclusive.

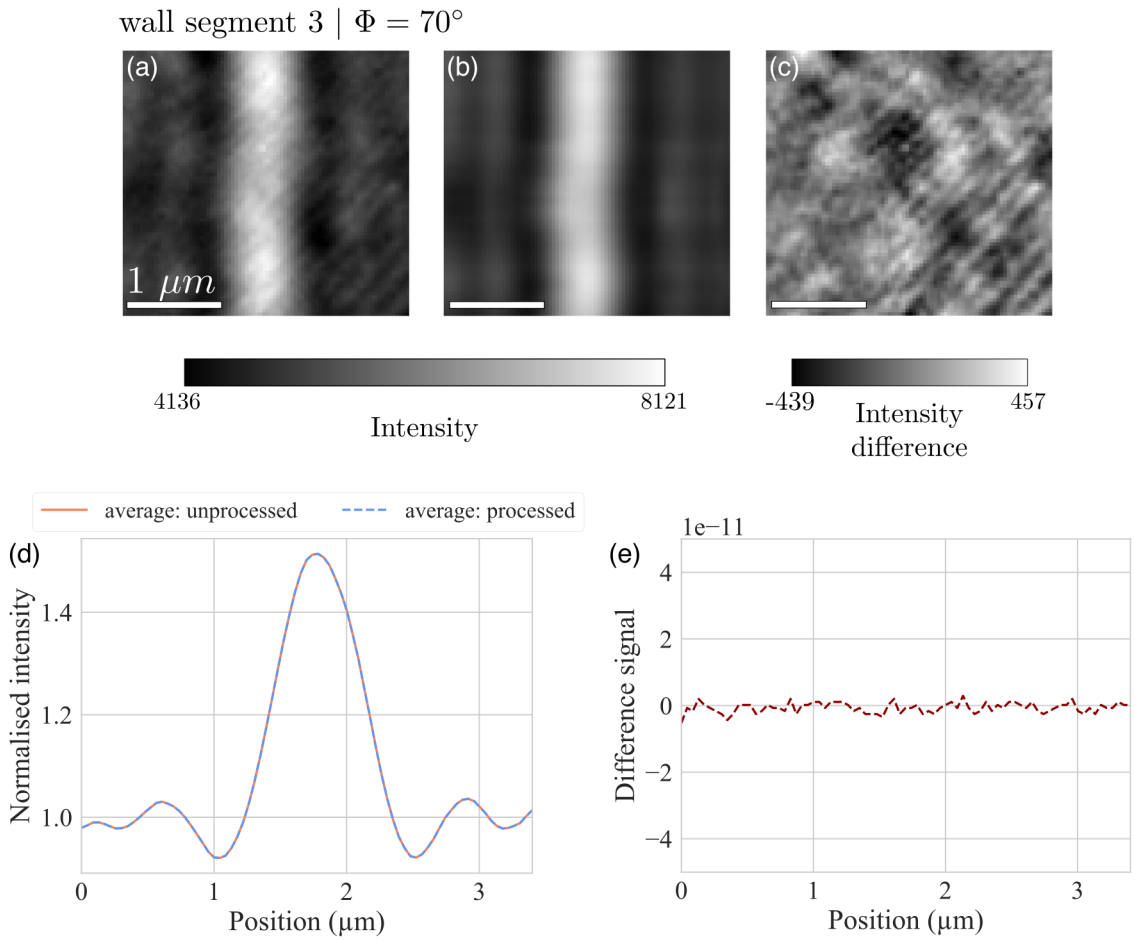

Figure 4.8: PCA was performed on Fresnel image (a) to isolate the magnetic contrast (b) from 'other' contrast (c). This procedure appears to have been successful however when the wall contrast is averaged over the wall length, no improvement is made to the final profile as is seen from the graphs in (d) and (e).

4.6 Discussion and Conclusions

The opening section of this chapter detailed how to interpret Fresnel images to extract information about the type and direction of domain walls in the sample. Bloch walls are identified easily, they give rise to a characteristic dark/bright or bright/dark contrast the order of which reveals the direction of the wall magnetisation. Néel walls on the other hand are not generally associated with any contrast. Their presence and position is revealed by contrast arising from the domain magnetisation but critically no information is encoded about the direction of the wall magnetisation.

Later sections of this chapter then present simulations showing, that with a certain angle between the incident electrons and the Néel type wall, an asymmetry can be introduced to the image contrast that correlates to the Néel wall direction. As shown in Appendix B, the magnitude of this asymmetry was found to be highly variable with both the domain wall width and the Fresnel image defocus.

Experiments were performed on two samples under a range of experimental conditions. The samples both have a strong interfacial DMI that stabilises Néel type walls of fixed handedness. The results of each experiment were inconclusive; no fixed handedness could be determined which is at odds with wealth of information on these samples and similar samples [1, 4, 14–16]. It is thought that perhaps the asymmetry is simply too small and is obscured below other contrast, such as diffraction contrast from the crystallites or additional local phase shifts caused by structural inhomogeneities (i.e. variations in layer thicknesses). This conclusion is strengthened by the failure of PCA to find the signal. Similarly, Jiang *et al.* attribute the lack of contrast to an insufficient SNR [2].

Bibliography

[1] A. Thiaville, S. Rohart, É. Jué, V. Cros, and A. Fert, "Dynamics of Dzyaloshinskii domain walls in ultrathin magnetic films," *EPL (Europhysics Letters)*, vol. 100, p. 57002, 2012.

[2] W. Jiang, S. Zhang, X. Wang, C. Phatak, Q. Wang, W. Zhang, M. B. Jungfleisch, J. E. Pearson, Y. Liu, J. Zang, X. Cheng, A. Petford-Long, A. Hoffmann, and S. G. E. te Velthuis, "Quantifying chiral exchange interaction for Néel-type skyrmions via Lorentz transmission electron microscopy," *Physical Review B*, vol. 99, p. 104402, 2019.

[3] A. Masseboeuf, C. Gatel, P. Bayle-Guillemaud, A. Marty, and J.-C. Toussaint, "Lorentz microscopy mapping for domain wall structure study in L10 FePd thin films," *Ultramicroscopy*, vol. 110, pp. 20–25, 2009.

[4] M. J. Benitez, A. Hrabec, A. P. Mihai, T. A. Moore, G. Burnell, D. McGrouther, C. H. Marrows, and S. McVitie, "Magnetic microscopy and topological stability of homochiral Néel domain walls in a Pt/Co/AlOx trilayer," *Nature Communications*, vol. 6, p. 8957, 2015.

[5] S. McVitie and G. S. White, "Imaging Amperian currents by Lorentz microscopy," *Journal of Physics D: Applied Physics*, vol. 37, no. 2, pp. 280–288, 2004.

[6] S. McVitie, S. Hughes, K. Fallon, S. McFadzean, D. McGrouther, M. Krajnak, W. Legrand, D. Maccariello, S. Collin, K. Garcia, N. Reyren, V. Cros, A. Fert, K. Zeissler, and C. H. Marrows, "A transmission electron microscope study of Néel skyrmion magnetic textures in multilayer thin film systems with large interfacial chiral interaction," *Scientific Reports*, vol. 8, p. 5703, 2018.

[7] F. de la Peña, E. Prestat, V. T. Fauske, P. Burdet, P. Jokubauskas, M. Nord, T. Ostasevicius, K. E. MacArthur, M. Sarahan, D. N. Johnstone, J. Taillon, J. Lähnemann, V. Migunov, A. Eljarrat, J. Caron, T. Aarholt, S. Mazzucco, M. Walls, T. Slater, F. Winkler, pquinn dls, B. Martineau, G. Donval, R. McLeod, E. R. Hoglund, I. Alxneit, D. Lundeby, T. Henninen, L. F. Zagonel, and A. Garmannslund, "hyperspy/hyperspy: HyperSpy v1.5.2," 2019.

[8] F. de la Peña, M.-H. Berger, J.-F. Hochepied, F. Dynys, O. Stephan, and M. Walls, "Mapping titanium and tin oxide phases using EELS: An application of independent component analysis," *Ultramicroscopy*, vol. 111, pp. 169–176, 2011.

[9] L. Yedra, A. Eljarrat, R. Arenal, E. Pellicer, M. Cabo, A. López-Ortega, M. Estrader, J. Sort, M. D. Baró, S. Estradé, and F. Peiró, "EEL spectroscopic tomography: Towards a new dimension in nanomaterials analysis," *Ultramicroscopy*, vol. 122, pp. 12–18, 2012.

[10] B. R. Jany, A. Janas, and F. Krok, "Retrieving the Quantitative Chemical Information at Nanoscale from Scanning Electron Microscope Energy Dispersive X-ray Measurements by Machine Learning," *Nano Letters*, vol. 17, pp. 6520–6525, 2017.

[11] J. F. Einsle, A. S. Eggeman, B. H. Martineau, Z. Saghi, S. M. Collins, R. Blukis, P. A. J. Bagot, P. A. Midgley, and R. J. Harrison, "Nanomagnetic properties of the meteorite cloudy zone," *Proceedings of the National Academy of Sciences*, vol. 115, pp. E11436–E11445, 2018.

[12] R. N. Cochran and F. H. Horne, "Statistically weighted principal component analysis of rapid scanning wavelength kinetics experiments," *Analytical Chemistry*, vol. 49, pp. 846–853, 1977.

[13] R. Wilcox, "Chapter 6 - Some Multivariate Methods," in *Introduction to Robust Estimation and Hypothesis Testing (Third Edition)*, pp. 215 – 289, Academic Press, Boston, third ed., 2012.

[14] S. Emori, U. Bauer, S. M. Ahn, E. Martinez, and G. S. Beach, "Current-driven dynamics of chiral ferromagnetic domain walls," *Nature Materials*, vol. 12, no. 7, pp. 611–616, 2013.

[15] A. Hrabec, N. A. Porter, A. Wells, M. J. Benitez, G. Burnell, S. McVitie, D. McGrouther, T. A. Moore, and C. H. Marrows, "Measuring and tailoring the Dzyaloshinskii-Moriya interaction in perpendicularly magnetized thin films," *Physical Review B - Condensed Matter and Materials Physics*, vol. 90, no. 2, 2014.

[16] J.-Y. Chauleau, W. Legrand, N. Reyren, D. Maccariello, S. Collin, H. Popescu, K. Bouzehouane, V. Cros, N. Jaouen, and A. Fert, "Chirality in Magnetic Multilayers Probed by the Symmetry and the Amplitude of Dichroism in X-Ray Resonant Magnetic Scattering," *Physical Review Letters*, vol. 120, p. 037202, 2018.

5

Quantitative imaging of hybrid type domain walls in skyrmionic multilayer materials

Contents

5.1 Introduction

As detailed in section 2.2.2, the Dzyaloshinskii-Moriya interaction is an antisymmetric exchange interaction which favours canting between neighbouring magnetic spins. DMI is prominent in crystalline environments with a lack of inversion symmetry and strong spin-orbit coupling - notably arising at interfaces between ferromagnets and heavy metals. This has been studied in ultrathin magnetic systems with PMA where, without any DMI, Bloch type domain walls are favoured - sketched in Fig. 5.1(a). DMI promotes rotation of the magnetisation about the DMI vector, which in this case is parallel to the plane of the interface, causing an energetically favourable reorientation of the wall magnetisation. These reorientated walls, sketched in Fig. 5.1(b), are Néel type and are homochiral, with the sense of chirality set by the sign of the DMI vector (which itself is controlled by the type of interfacial atoms adjacent to the magnetic layer) [1, 2]. The DMI promoted rotation also leads to Néel type skyrmions as well as homochiral Néel walls under the right sample conditions.

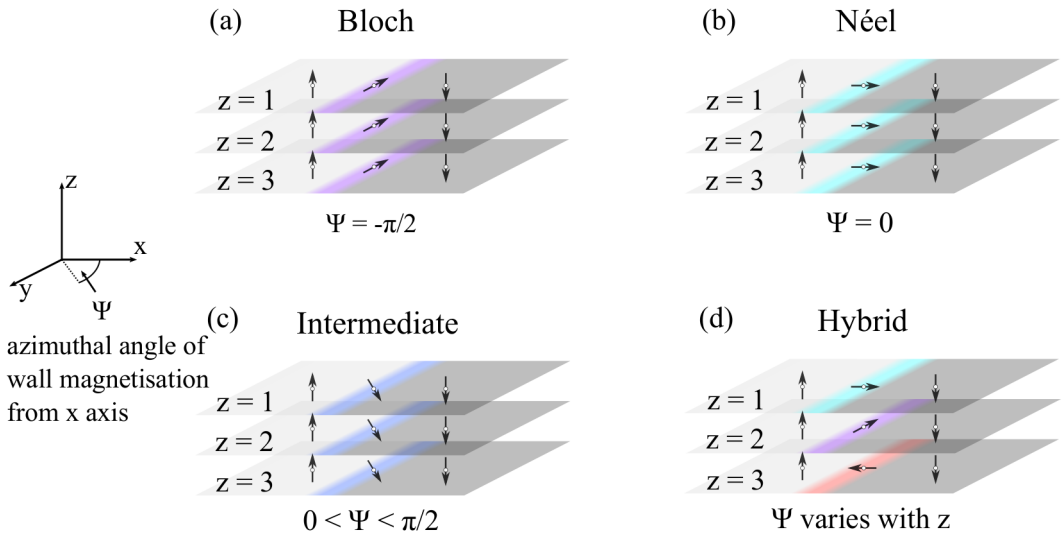

Figure 5.1: Sketches of the four types of domain walls discussed in this chapter, for simplicity depicted in a three layer system where each layer is identified by z. Drawn are (a) Bloch, (b) Néel, (c) intermediate and (d) hybrid type walls. Wall types (a-c) have no variation of ψ with z and are characterised by the different value of ψ associated with each, in contrast (d) is characterised by the variation of ψ with z.

Néel type skyrmions are of great technological interest for a multitude of reasons, including their compact size and efficient manipulation with spin transfer torques [3–5], and can be stabilised at room temperature by stacking multiple repeats of an ultrathin ferromagnetic layer sandwiched between heavy metal layers (like Pt/Co/Ir) [5–9]. This multilayer construction preserves the broken symmetry and spin-orbit coupling at each interface but increases the magnetic volume, which is thought to provide stability against the thermal fluctuations that destroy skyrmion textures in trilayer or bilayer systems at room temperature.

However, one side effect of this multilayered structure is the significant increase to the dipolar energy of the system. A number of recent studies identify that in many cases the dipolar interactions (which favour divergence-less Bloch type walls) can overcome the DMI interaction (which favours chiral Néel walls) to stabilise a three dimensional wall structure with magnetisation that twists through the thickness of the wall [10–13]. This thickness dependent wall structure is referred to as a hybrid type domain wall, sketched in 5.1(d), as it is composed of both handednesses of Néel type rotations and a Bloch type wall rotation. Thus, different chiralities are fixed on the magnetic textures in different layers of the structure. As seen in 5.1(d), the flux closure wall configuration, with Néel type walls of opposite chirality above and below central layer(s) with Bloch type wall(s), has significantly reduced the wall dipolar energy contribution compared to 5.1(b) for example. It is interesting to note that this sort of dipolar-driven, flux-closure wall structure is also observed in 80 repeat layers of Fe/Gd (antiferromagnetically coupled) [14] and in thicker ($>$ 60 nm) single-layer (therefore direct exchange coupled) magnetic systems [15, 16].

Two studies show experimental evidence of this twisted, hybrid domain wall in skyrmionic multilayer materials [10, 11]. One used nitrogen-vacancy imaging to image the stray field produced by skyrmions in a multilayer magnetic material, and by comparison with simulations, concludes that these walls must have a hybrid structure [11]. The other experimental study used x-ray resonant magnetic scattering (XRMS) [17] to compare the chirality of the Néel walls stabilised in the surface

layers of pairs of magnetic films with opposite layer stacking order. Reversing the stacking order changes the sign of the DMI vector and is expected to change the chirality of the Néel walls. This study identified the same chirality of Néel walls in the surface layers of pairs of samples with opposite stacking order, composed of 20 repeats, which is only plausible if the magnetisation twists through the thickness of the wall [10]. This study also predicts the profound impact that this hybrid chiral structure has on the current driven dynamics of skyrmions: it impacts both the skyrmion velocity and the skyrmion Hall angle. This is also predicted by the analytical study conducted by Lemesh *et al.* [12]. Furthermore, Legrand *et al.* provides a micromagnetic model which pays particular attention to the role of dipolar interactions and also studies in-depth the consequences of a hybrid wall structure on the dynamics of skyrmions under spin-polarised currents [13]. Notably, this study identifies that, in certain situations, the hybrid structure may allow the unwanted transverse motion of skyrmions under spin-polarised currents (the skyrmion Hall effect [18]) to be significantly reduced, even to zero, while maintaining a relatively high skyrmion velocity ($\approx$ 10 ms^{-1}) thus allowing for improved control over skyrmion trajectories.

In this chapter, Lorentz transmission electron microscopy is used to directly image and quantify the hybrid nature of the domain walls in three multilayer systems. This work is highly complementary to the two pre-existing experimental studies as it provides direct measurement of the Bloch twist present in the hybrid chiral domain walls.

5.2 Discussion of Néel and Bloch wall contrast separation in Lorentz TEM

In Lorentz TEM, the contribution of any Bloch type component of the walls may be separated from the Néel components through careful analysis of the variation of the contrast with sample tilt. This will be discussed in detail in this section to aid interpretation of the experimental work which follows. As discussed in section 3.7.2,

electrons travelling along the direction $\hat{\mathbf{n}}$ passing through a magnetic material with magnetic induction $\mathbf{B}$ are deflected by an angle

$$\beta_L = \frac{e\lambda}{h}\int_{-\infty}^{\infty}(\mathbf{B}\times\hat{\mathbf{n}})\,d\mathbf{l}, \qquad \text{(3.8 revisited)}$$

where the constants e and λ are the charge and wavelength of the electrons respectively and h is Planck's constant. More practically, and shown on the right hand side of equation 5.1, this means that the deflection is proportional to the product of the magnetic induction perpendicular to the electron trajectory termed B_L, and to the projected thickness of the sample traversed by the electron beam termed t':

$$\beta_L = \frac{e\lambda}{h}\int_{-\infty}^{\infty}(\mathbf{B}\times\hat{\mathbf{n}})\,dl = \frac{e\lambda}{h}\,B_L t'. \qquad (5.1)$$

For the present discussion the effects of stray fields are ignored and we consider the saturation induction $B_s = \mu_0 M_s$ where μ_0 is the permeability of free space and M_s is the saturation magnetisation. Figure 5.2 visualises the evolution of B_L and t' with sample tilt θ for in-plane (a) and out-of-plane (b) magnetic induction (magnetisation).

As seen from Fig. 5.2(a) for in-plane magnetised materials untilted $\beta_L \propto B_s t$, and when tilted by θ about the axis marked in the figure $B_L = B_s\cos(\theta)$ and

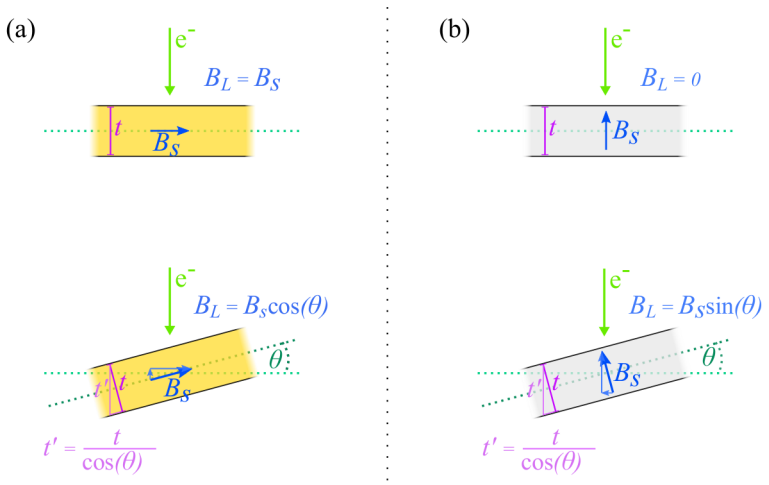

Figure 5.2: Sketches of the variation of the magnetic induction perpendicular to the electron beam trajectory, B_L, and the projected thickness, t', with sample tilt for in-plane (a) and out-of-plane (b) magnetised materials.

t'=t/cos(θ) therefore $\beta_L \propto B_s t$ and is unchanged by tilting the sample. Conversely, for out-of-plane magnetised materials, when untilted there is no deflection as $B_L = 0$, but when tilted the deflection evolves as $\beta_L \propto B_s t \tan(\theta)$. Applying this framework to the situation of hybrid type domain walls with out-of-plane domains, situation (a) describes contrast from the in-plane magnetisation associated with Bloch walls and situation (b) describes the contrast from the domains. As was the focus of chapter 4, the in-plane magnetisation of a Néel type wall is associated with a stray field which, from most projection angles, results in net $\mathbf{B} = 0$ and experimentally no contrast has been observed from this component [19–21]. Theoretically, as presented in chapter 4, certain sample-beam orientations do permit a small component of net integrated $\mathbf{B}$, where the magnetisation and the stray field do not fully cancel in projection. In any case, when tilting about the axis described above, the in-plane component of the Néel wall gives no contribution to either the tilted or untilted Lorentz TEM images. Therefore, in summary, there are two deflections to consider in this chapter when imaging hybrid domain walls: one from the Bloch component which is independent of tilt ($\beta_L \propto B_s t$) , and one from the domains which varies as $\beta_L \propto B_s t \tan(\theta)$ with tilt. Note that in these equations, t is not necessarily the total magnetic thickness but instead is the portion of the thickness associated, in the first case, with Bloch type wall magnetisation and in the second case with the magnetisation of the domains.

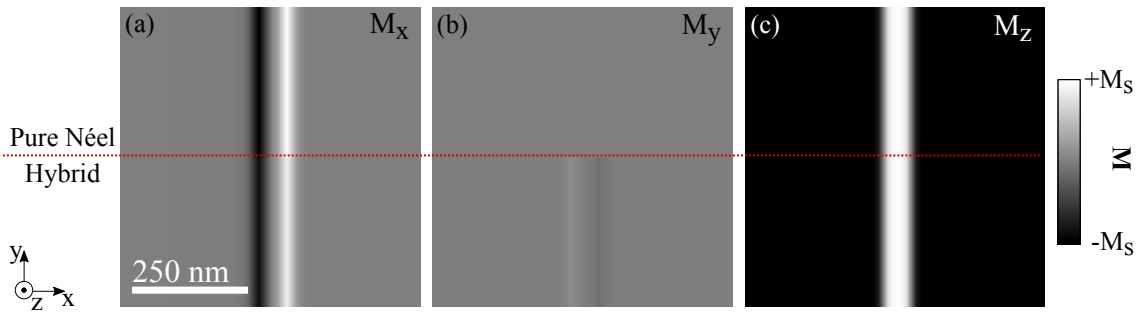

Figure 5.3: (a) M_x, (b) M_y and (c) M_z components, constructed from a simple 1D hyperbolic tangent model, of two closely spaced domain walls. The upper half, above the red dividing line, models pure Néel walls whilst the lower half models hybrid Bloch/Néel walls, with a Bloch to Néel ratio of 0.1 to 0.9.

The rest of this section discusses what to expect from Fresnel and DPC images which were calculated from a magnetisation model provided in Fig. 5.3 using the method outlined in section 3.10.3. The magnetisation model is based on a one dimensional hyperbolic tangent, where $M_z = \tanh(x/w)$ and w is the width parameter, chosen to be 15 nm in this case. A pair of closely spaced domain walls (three domains) was modelled to best match the experimental work that follows. In the top half of Fig. 5.3 the walls are Néel type and in the bottom half they are hybrid type. The model for the hybrid wall has a ratio of 10% Bloch to 90% Néel (representing for example a ten-repeat multilayer with nine layers Néel type and one layer Bloch type) with $|M_x| \leq 0.9M_s$ and $|M_y| \leq 0.1M_s$. These are simple one-layer, thickness-averaged models as Lorentz TEM measures a projection of magnetic induction through the thickness. Thus, it must be noted that a Lorentz TEM image of a hybrid domain wall (the in-plane wall angle ψ varies with z as in Fig. 5.1(d)) is identical to an intermediate domain wall (constant ψ that is between conventional Néel and Bloch types but fixed in z as in Fig. 5.1(c)). The model was designed to have magnetic induction of 1 T and to be 24 nm thick to match experimental results given later.

Figure 5.4 shows Fresnel images with (a), (b) and (c) calculated with a sample tilt of +20°, 0 and -20° respectively, and a defocus of 1 mm. With the same split as Fig. 5.3, above the red line shows Fresnel images from the pure Néel wall model and below the red line shows Fresnel images from the hybrid wall model. Clearly seen in upper Fig. 5.4(b), and covered in chapter 4, for pure Néel walls there is no image contrast at zero sample tilt. At +(-) tilt the domains generate, from left to right, white/black(black/white) contrast which reverses with tilt either side of zero. The lower half of Fig. 5.4(b) of hybrid walls untilted has clear contrast albeit of lower intensity than images (a) and (c). This contrast arises from the Bloch component of the walls, which represents 10% of the total magnetic thickness t, giving an integrated magnetic induction of $0.1B_st$. This is compared to the domains, which at a tilt of 20°, give an integrated magnetic induction of $0.36B_st$ resulting in the contrast seen in (a) and (c).

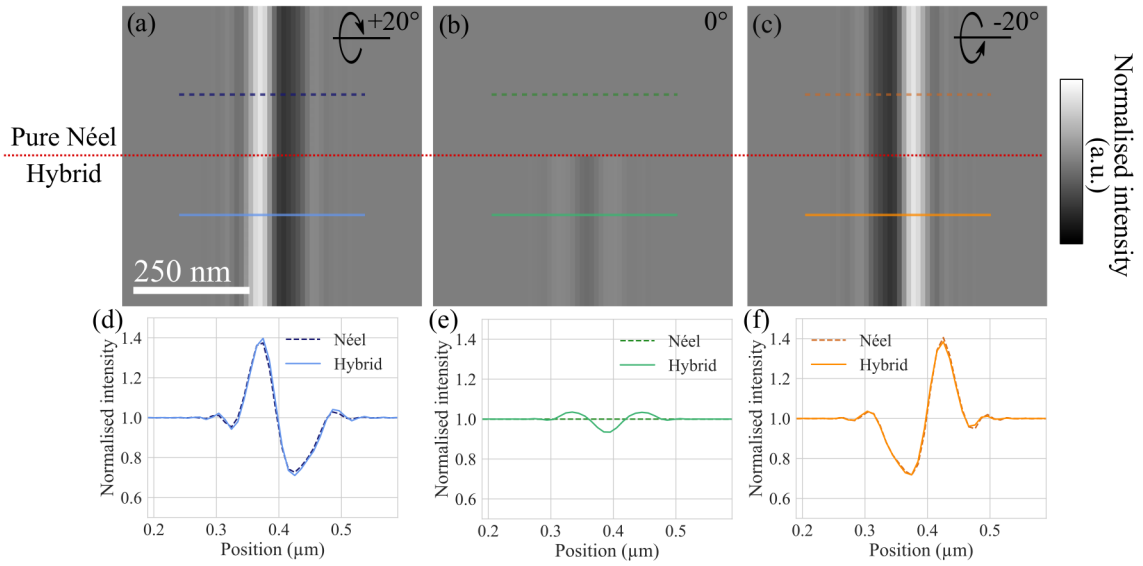

Figure 5.4: Fresnel images calculated with +20°, 0 and -20° sample tilt in images (a), (b) and (c) respectively. The top half shows the contrast expected from sample pure Néel walls and the lower half shows the contrast expected from a sample with hybrid type walls, with a Bloch to Néel ratio of 0.1 to 0.9. Line traces were taken from the upper and lower parts of images (a-c) and are shown in (d-f).

These Fresnel images have been normalised to the background intensity level, to allow for comparison between images of different magnetic structures at different sample tilts. For the model with hybrid domain walls, the contrast from the Bloch portion of the wall does not change with tilt and is added to the contrast gained with sample tilt from the domains. As is most clear from the line traces in Fig. 5.4(d) and (f), the effect of the Bloch portion on the overall signal at ± 20° tilt is very weak. At these tilt levels the domain contrast dominates, and the only effect of the Bloch nature is to add a slight asymmetry to the line trace from the hybrid walls compared to the trace from Néel walls. These calculated images indicate that Fresnel imaging can certainly be used to ascertain if there is some Bloch component to the domain walls by determining if there is any Fresnel image contrast at zero sample tilt. However, in general, the contrast in Fresnel images is not quantitative and cannot be relied upon for precise measurement of the amount of Bloch layers in the hybrid domain walls.

As described in section 3.7.4, DPC is an in-focus scanning Lorentz TEM technique that provides quantitative measurement of β_L and consequently of the in-

tegrated magnetic induction of the sample. Figure 5.5 is analogous to Fig. 5.4 but shows calculated DPC images at tilts +20°, 0 and -20° in (a-c), with line traces from these images displayed in (d-f). As with the Fresnel images, there is a clear difference between images of the Néel and hybrid wall structures at zero tilt (compare upper/lower Fig. 5.4(b)). And from (d) and (f) it is visible that line traces from images with ± 20° tilt of the hybrid walls are asymmetric compared to the Néel walls. At ± 20° tilt the domain contrast clearly dominates over the Bloch wall contrast as the overall contrast level between the Néel and hybrid line traces is comparable. In this limit, a set of DPC images at different tilt angles, including zero, can be used to quantitatively determine the Bloch-like thickness of the hybrid domain wall without making any assumption of B_s of the material (other than that it is constant). This is because the tilted images provide a measure of $B_s t \tan\theta$ which can be compared to untilted images with $B_s t_B$ to extract t_B, where t_B is the Bloch-like thickness of the wall.

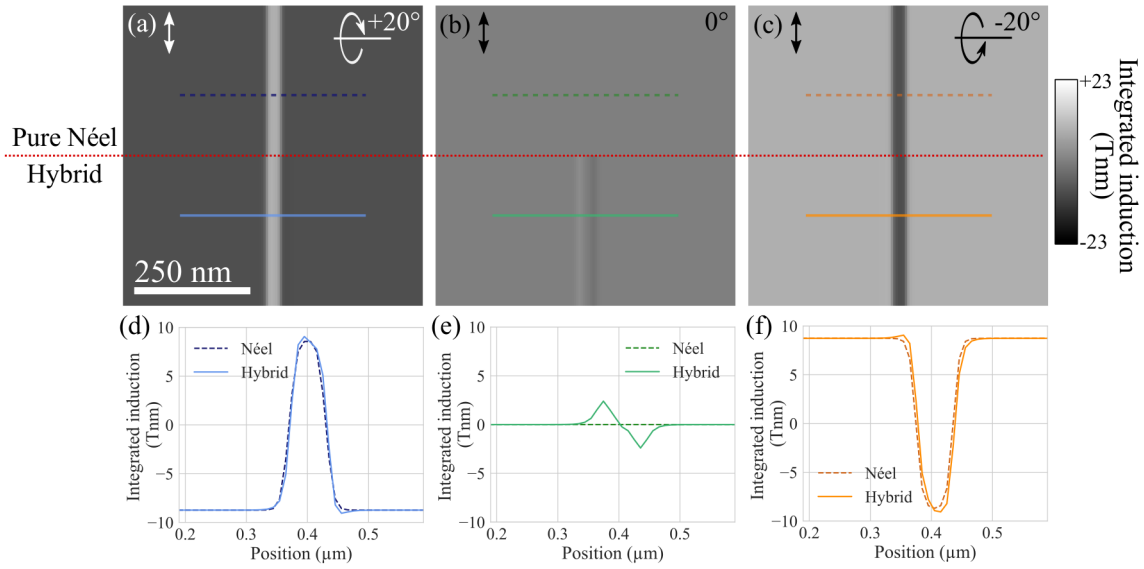

Figure 5.5: DPC images (mapping the component of induction indicated by the double-headed arrow) calculated with +20°, 0 and -20° sample tilt in images (a), (b) and (c) respectively. The top half shows the contrast expected from a sample with pure Néel walls and the lower half shows the contrast expected from a sample with hybrid type walls, with a Bloch to Néel ratio of 0.1 to 0.9. Line traces were taken from the upper and lower parts of images (a-c) and are shown in (d-f).

5.3 Samples

For TEM investigations, three multilayer samples were deposited by DC magnetron sputtering by William Legrand at CNRS/Thales on Si_3N_4 membrane samples with a 100 μm by 100 μm electron transparent window suspended from a thicker Si frame. The layer structure of the three samples is given in table 5.1.

Alternating gradient field magnetometry (AGFM) (performed by colleagues at CNRS/Thales) suggests that all three samples support out-of-plane domains; for the samples 1 and 2 the origin is PMA from the interface but in sample 3, because of the Co thickness, the magnetic anisotropy favours in-plane magnetisation and out-of-plane domains are stabilised by dipolar interactions. The multilayers were deposited on top of Ta(10)/Pt(8) buffer layers to control their PMA and are capped with 3nm of Pt to prevent oxidation. The 1.4 nm Ru layer is used in conjunction with varying Co layer thickness to ensure ferromagnetic (RKKY) coupling between the individual Co layers in each multilayer [22]. As RKKY coupling is an interfacial effect the samples with thinner Co layers experience the strongest interlayer coupling: sample 3 (with 1.6 nm Co layers) has a weaker coupling than sample 1 (with 1.2 nm Co layers). However, in any case, the interlayer exchange coupling is small compared to the intra-layer direct exchange. Increasing the number of repeats and increasing the Co layer thickness both increase the strength of the dipolar field and therefore increase the likelihood that hybrid walls are formed over chiral Néel type walls. From previous studies of similar multilayers, it is expected that samples 2 and 3 have hybrid type walls and sample 1 has Néel type walls [10, 17].

Sample	Multilayer structure	Expectation
1	Ta(10)/Pt(8)[Co(1.2)/Ru(1.4)/Pt(0.6)]$_{\times 5}$/Pt(2.4)	*homochiral Néel walls*
2	Ta(10)/Pt(8)[Co(1.4)/Ru(1.4)/Pt(0.6)]$_{\times 10}$/Pt(2.4)	*hybrid walls*
3	Ta(10)/Pt(8)[Co(1.6)/Ru(1.4)/Pt(0.6)]$_{\times 15}$/Pt(2.4)	*hybrid walls*

Table 5.1: Summary of the sample composition - the numbers in brackets give the layer thickness in nm and the subscript gives the number of repeats - and the expectations of each sample based on input from colleagues at CNRS/Thalés. The samples differ in the thickness of the Co layer and the number of repeats, therefore these qualities are coloured to make this easier to see.

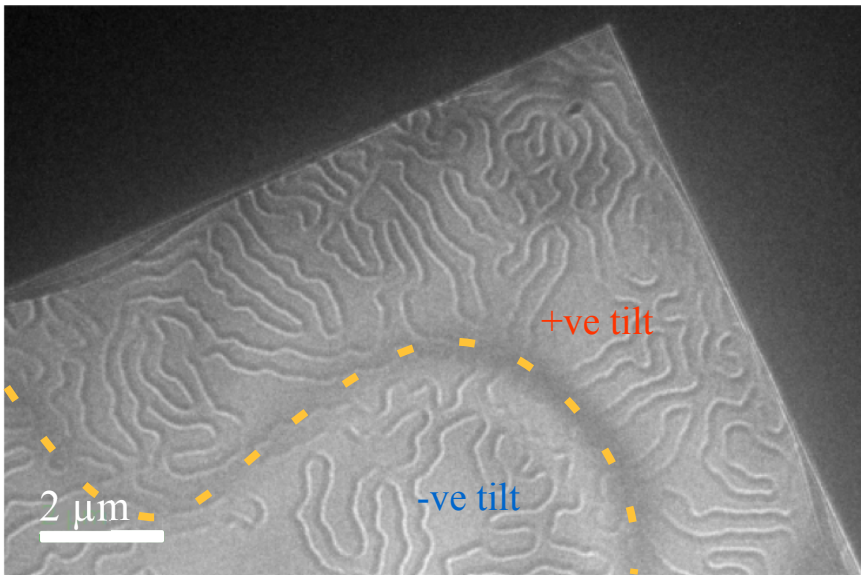

Figure 5.6: Fresnel image of sample 3 taken with zero rod tilt. The large amount of magnetic contrast that reverses either side of a bend contour (dark s-shaped curve traversing the image highlighted by the yellow dashed line) suggests the sample surface is extremely contorted with the area above the contour at a positive angle to the electron beam and the area below at a negative angle.

Figure 5.6 shows a low magnification Fresnel image from sample 3 taken with the sample nominally untilted - i.e. the sample is flat with respect to the thicker membrane frame with no explicit rod tilt. Part of the electron opaque frame is visible in Fig. 5.6 as the black region on the top and right of the image. In this image the sample is in a 270 mT out-of-plane field. This field is applied to stabilise long isolated worm domains which are much more convenient for wall contrast analysis than the labyrinth-like remanent state of the sample. The curved dark line that traverses the image, highlighted by the yellow dashed line, is a bend contour separating regions of opposite local tilt. This is further evidenced by the contrast reversal either side of this bend contour. The contrast is, from left to right, white/black above the contour and black/white below, and matches the domain contrast calculated in Figs. 5.4(c) and (a) respectively. Therefore, we conclude that the electron transparent window of the sample is severely buckled, which effectively results in local tilting of the film with respect to the electron beam - with the yellow line separating areas of opposite local tilt. This conclusion is supported by AFM data presented in 5.7.

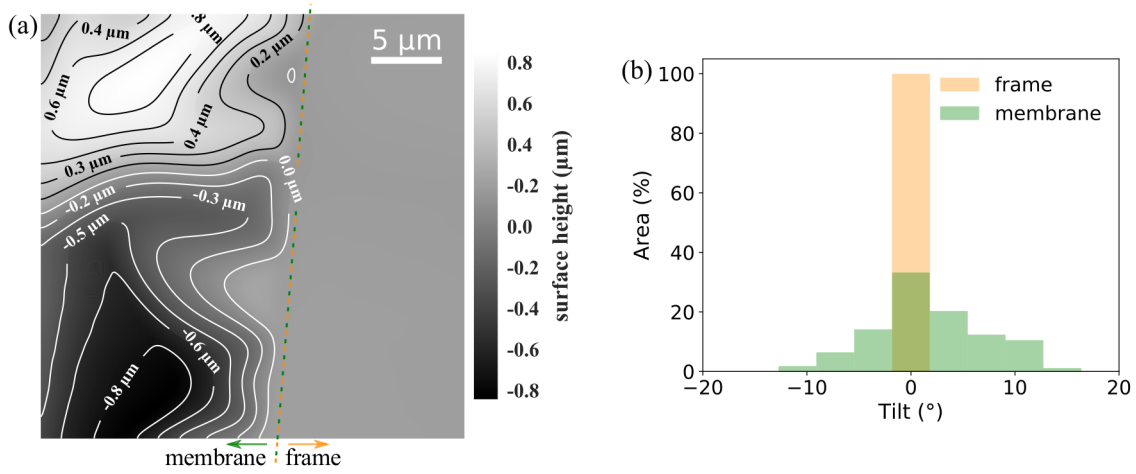

Figure 5.7: (a) AFM image of sample 3 taken from an area straddling the boundard between the membrane and the thicker Si frame showing the severe contortion of the membrane relative to the frame. (b) provides analysis of the local tilts present in this image indicating that the membrane has surface tilts between approximately ±15°.

Figure 5.7(a) is an AFM image showing the surface topography of the electron transparent on the membrane on the left and the thick Si frame on the right. This image confirms that the membrane surface is extremely contorted compared to the flat Si frame, with height variations of ± 0.8 μm across the membrane section of the AFM image in (a). Figure 5.7(b) shows quantitative analysis of the local tilts of the surface confirming membrane surface tilt between approximately ± 15°. The AFM data was taken using a Veeco Dimension 3100 Scanning Probe Microscope operated in tapping mode with a standard non-magnetic tip. The membranes on samples 1 and 2 also show similar buckling.

As discussed in section 5.2, interpreting the image contrast at different tilt angles is imperative to isolate the contrast from Bloch component of the hybrid walls. The buckled sample surface adds a layer of complexity to this experiment as the absolute value of the tilt of the multilayered structure with respect to the beam thus corresponds to the local tilt due to buckling combined with to the microscope rod tilt. Also shown in section 5.2 is that the contrast from the out-of-plane domains reverses either side of zero tilt, therefore by slowly varying the rod tilt, the local tilt due to buckling can be identified as the cross-over point between reversed domain contrast.

5.4 Lorentz TEM imaging

All of the Lorentz microscopy images were taken using a JEOL ARM 200cF probe corrected microscope. A direct electron detector, Medipix3, was used for acquiring both the Fresnel images and the DPC images presented in this section. The reasons for using a pixelated detector to acquire 4D STEM datasets for DPC of skyrmionic multilayer materials are covered extensively in section 3.7.5. The Medipix3 was used for the Fresnel images as well because of its superior signal to noise performance compared to the standard CCD detector normally used for the acquisition of Fresnel images [23]. Critically, this means high quality images can be obtained with a short exposure time [24]. For example, Fig. 5.6 was acquired with the CCD camera with an acquisition time of 5s, and the Fresnel images in section 5.4.1 were acquired with the Medipix3 with an acquisition time of 1s. The Fresnel contrast from these skyrmionic multilayer materials is somewhat weak, due to the large total thickness relative to the magnetic thickness, therefore with the CCD camera long exposure times are needed for good contrast. As explained in section 5.3, for these samples, local zero tilt must be identified by finding the cross-over point where the domain contrast reverses. Therefore, to understand how the image contrast evolves with tilt, a reasonable image update time is required while changing the rod tilt in real-time; in this sense the use of the Medipix3 was critical in locating the rod tilt that corresponds to local zero tilt required to isolate the Bloch component (if present).

5.4.1 Identifying hybrid type domain walls with Fresnel imaging

In Fresnel imaging, the important feature is the contrast level relative to the background, therefore the line traces taken from all Fresnel images have been normalised to the background intensity level to allow for meaningful comparison of the information contained across different Fresnel images. Furthermore, all Fresnel images were taken with a defocus between 1 and 5 mm. Such large values are required because of the small deflection angles expected, for example if a sample

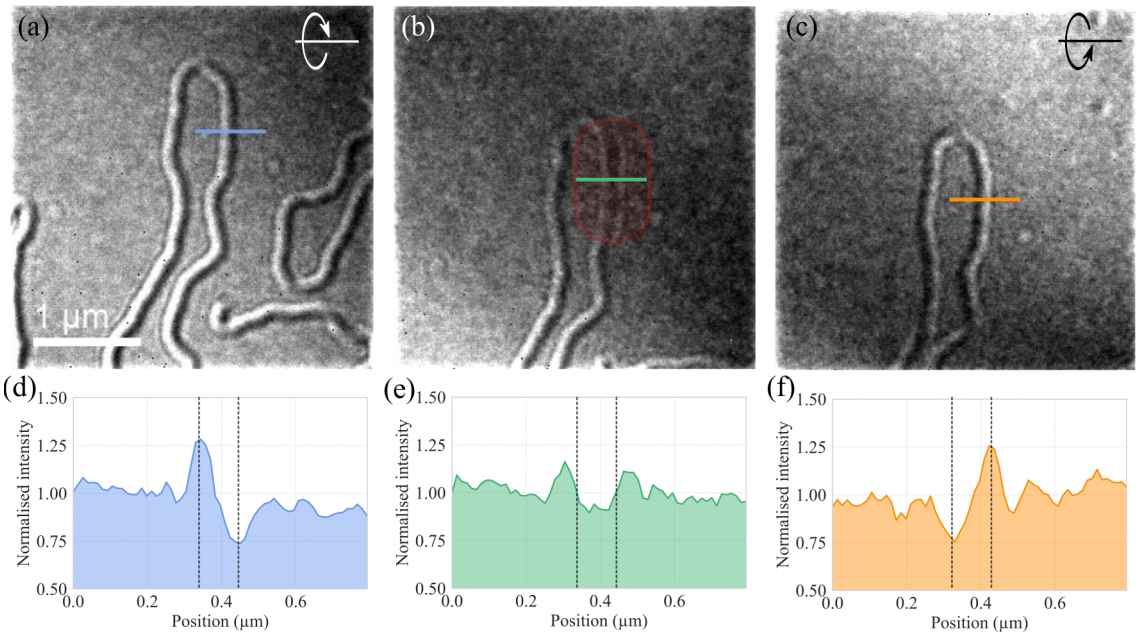

Figure 5.8: Fresnel images of sample 3 with closely spaced pairs of domain walls with local tilt at the coloured lines of (a) +5°, (b) 0° and (c) -5°. The corresponding intensity line traces from these images, averaged over 10 lines, are shown in (d-f). These line traces have been normalised to the background intensity level. The vertical lines on the images indicate the position of the centre of the domain wall.

with 1.4 nm thick Co layers has one Bloch-type layer, at zero tilt $\beta_L \approx 1$ μrad. As described in relation to Fig. 5.6, an out-of-plane field was applied to the samples during imaging to ensure they support isolated worm domains rather than the dense maze-like domain structure present at zero field.

Figure 5.8 shows Fresnel images taken from sample 3 at three different tilt angles. Figure 5.8(b) is the 'zero' tilt image, taken with a rod tilt of -9.8°. Only the area of the image indicated by the transparent red oval is at zero tilt; the rest of the image is at varying levels of positive tilt relative to the electron beam. Images (a) and (c) are at +5° and -5° tilt relative to image (b). As expected, at the area marked by the coloured lines in images (a) and (c), the contrast reverses either side of zero tilt. Significantly, there is still contrast visible at the area at zero local tilt in image Fig. 5.8(b). To illustrate the variation of contrast with tilt more clearly, intensity line traces taken from the three images are shown in Fig. 5.8(d-f). These line traces are in excellent agreement with traces from calculated Fresnel images presented in Fig. 5.4(d-f). Although Fresnel images are not quantitative, given

the relatively weak contrast level in the zero tilt image compared to the images with tilt (tilt of 5° corresponds to $0.09B_st$), it is concluded that these walls are of hybrid type and are not pure Bloch type walls.

Fresnel images from sample 2 show the same magnetic contrast variation with tilt as sample 3, indicative of the film supporting hybrid domain walls. These images are shown in Fig. 5.9(a-c). The Fresnel image contrast is weaker from this sample compared to the images from sample 3 due to the reduced total magnetic thickness. As with sample 3, sample 2 is severely buckled thus only some regions of Fig. 5.9(b) are untilted with respect to the electron beam - one such region is indicated by the red circle on the left of the image (the image was taken with a rod tilt of 16.3°). Images Fig. 5.9(a) and (c) are taken at relative tilts of -10° and +10° compared to image (b). The line traces shown in Fig. 5.9(d) and (f) show the characteristic domain contrast which reverses with tilt. The line trace in Fig. 5.9(e) is of lower contrast and symmetric indicating that this sample has

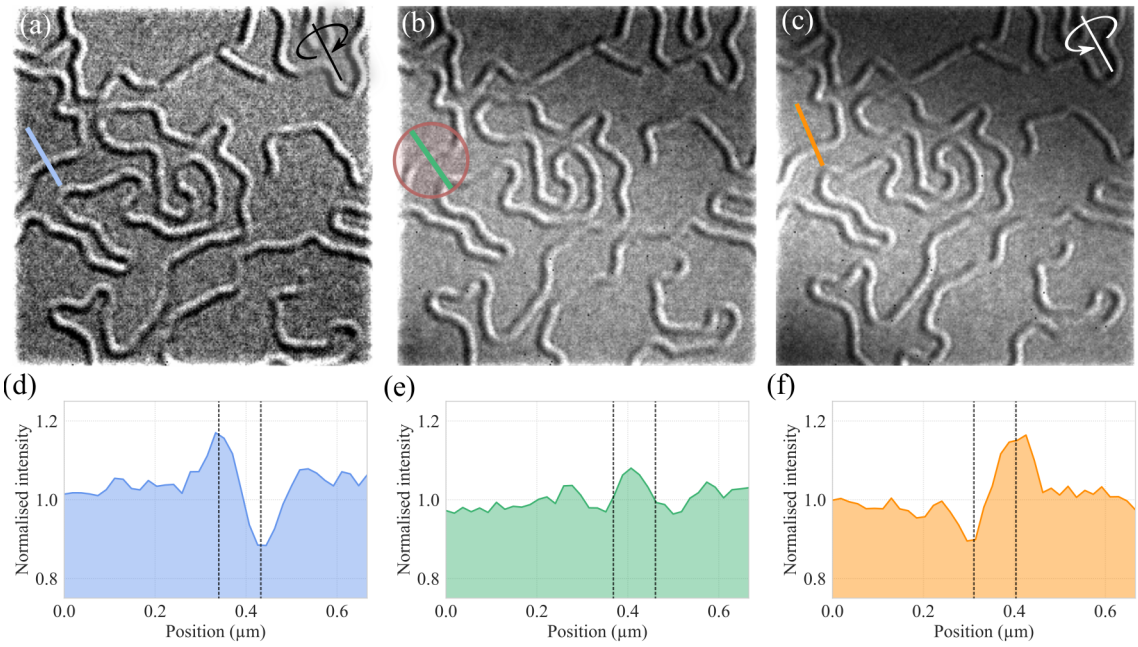

Figure 5.9: Fresnel images of sample 2 with closely spaced pairs of domain walls with local tilt at the coloured lines of (a) +10°, (b) 0° and (c) -10°. The corresponding intensity line traces from these images, averaged over 10 lines, are shown in (d-f). These line traces have been normalised to the background intensity level. The vertical lines on the images indicate the position of the centre of the domain wall.

walls with partial Bloch character.

For sample 1, the Fresnel image contrast does not provide clear evidence that the sample supports hybrid domain walls. The images are shown in Fig. 5.10(a-c) and have only weak contrast as expected from a sample with 5 nm of magnetic material in a total thickness of 31 nm. Image 5.10(b) is at approximate zero tilt (rod tilt of +6.0°), with image 5.10(a) at relative -9° and 5.10(c) at relative +8°. Line traces taken across the same wall region of each Fresnel image are shown in Fig 5.10(d-f). This area was chosen to analyse because in images 5.10(a) and 5.10(c) it shows unambiguous contrast reversal with tilt. The line traces in 5.10(d) and 5.10(f) show contrast above the background intensity variation which reverses with tilt, and is therefore consistent with contrast from out-of-plane domains. The line trace in 5.10(e), through the same area at zero tilt, has no clearly discernable contrast above the background intensity variation. The contrast in images 5.10(a) and

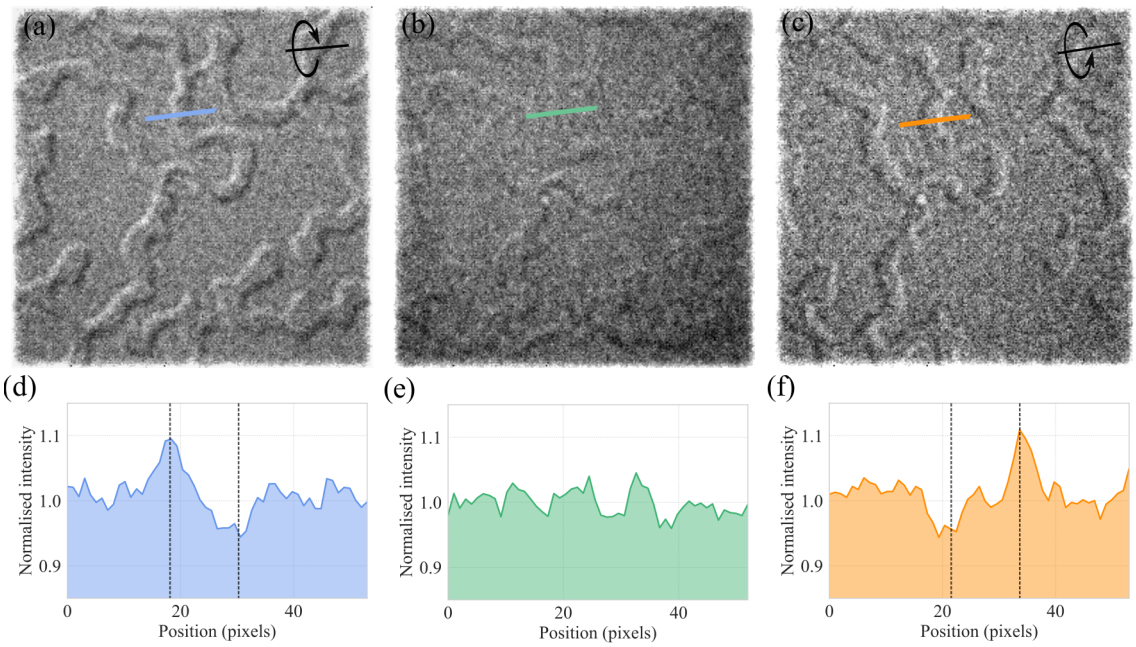

Figure 5.10: Fresnel images of sample 1 with pairs of domain walls with local tilt at the coloured lines of (a) +9°, (b) 0° and (c) -8°. The corresponding intensity line traces from these images, averaged over 10 lines, are shown in (d-f). These line traces have been normalised to the background intensity level. Note that these images are not calibrated and the position scale is in pixels - the key point here is to demonstrate the nature of the contrast not to measure any quantitative spatial extent of the walls. The vertical lines on the images indicate the position of the centre of the domain wall.

5.10(c) arises from an electron beam deflection proportional to $\approx 0.14 B_s t$ (from out-of-plane domains tilted at 8°/9°). If this sample possessed hybrid walls even with only one Bloch type layer, at zero tilt this would lead to a deflection proportional to $0.2 B_s t$. Hence, it is expected that contrast from a Bloch type wall in one layer would lead to contrast in 5.10(b) at least as strong as images 5.10(a) and 5.10(c). For this reason it is concluded that the walls in sample 1 do not have the same twisted structure as the walls in samples 2 and 3.

5.4.2 Quantifying the Bloch component of the hybrid walls with DPC imaging

As demonstrated in the previous section, Fresnel images can be used to determine if the domain walls in a sample are hybrid, pure Bloch or pure Néel type walls. However, Fresnel imaging is not quantitative and the exact hybrid nature of the walls cannot be determined by this method. To measure how much of the multilayer the Bloch core (identified in samples 2 and 3) occupies, DPC imaging is used. As explained in sections 3.7.4 and 5.2, DPC is a quantitative imaging method that directly measures β_L which, as per Eq. 5.1, gives quantitative measurement of magnetic induction of the sample integrated along the electron path. Thus by taking DPC images at two tilt angles, one at zero tilt and the other at a tilt where the domain contrast dominates, the Bloch thickness t_B can be measured.

Figure 5.11 shows two DPC images collected from the same area of sample 3 at two different tilt angles. The images map the component of integrated induction in the direction indicated by the double-headed arrow inset on the top right of the images. These DPC images were acquired with a probe forming aperture of 50 μm (probe size 1.4 nm and resolution 0.7 nm) at a magnification of 80k× giving a pixel size of 9 nm and, as with the images in Fig. 5.6 and section 5.4.1, the sample was in an out-of-plane field to stabilise long isolated worm domains during imaging. The area under the green line in Fig. 5.11(a) was determined to be at zero tilt (the rod tilt was 12.2°). This area of local zero tilt was identified in the Fresnel mode prior to DPC imaging - the rest of the image is at various levels of positive

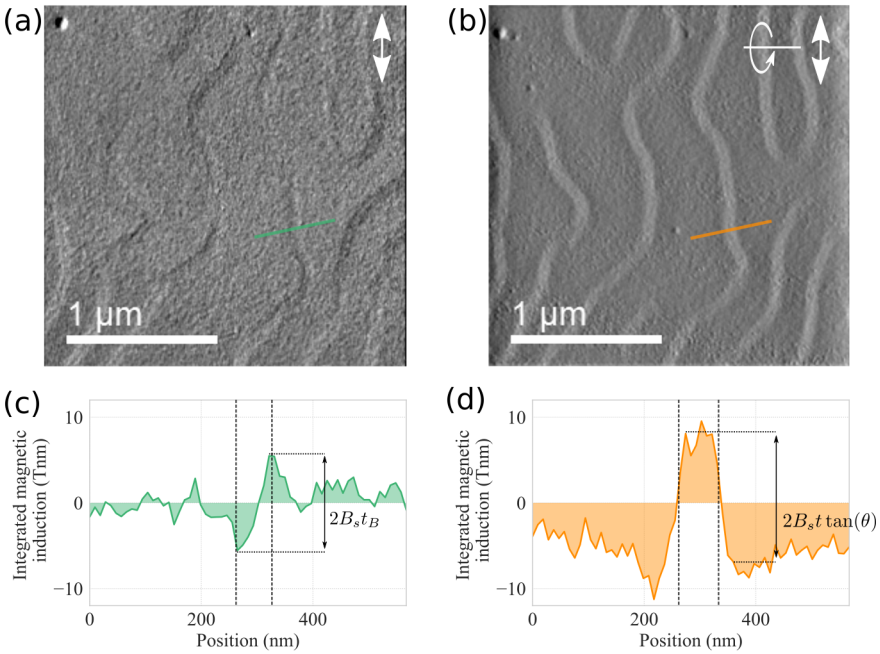

Figure 5.11: DPC images of sample 3 taken at two different tilts. The local tilt at the coloured lines is (a) 0° and (b) +13.2°. The component of induction mapped is indicated by the double headed arrow. The corresponding line traces, averaged over 20 lines, of the integrated induction from these images are shown in (c) and (d). The salient values of integrated magnetic induction, originating from the Bloch core of thickness t_B in (c) and from the domains in (d), are marked on the line traces. The vertical lines on the images indicate the position of the centre of the domain wall.

and negative tilt to the electron beam as evident from the bright and dark domain contrast visible in different areas of the image. Fig. 5.11(b) was taken at a tilt 13.2° relative to image (a) and the domain contrast clearly dominates at all points in this image. Figs. 5.11 (c) and (d) show line traces taken through the area marked by the coloured lines in images (a) and (b) respectively. As with the Fresnel images, the contrast in Figs. 5.11(a) and (b) is in excellent agreement with the DPC images calculated from the model of a hybrid wall structure presented in Fig. 5.5. The line traces displayed in (c) and (d) were averaged over 20 pixels. The contrast in image (a) and line trace (c) is, from peak to trough, $2B_s t_B$ (i.e. $\pm B_s t_B$) and conversely the contrast in image (b) and line trace (d) is from $2B_s t \tan(\theta)$, where t_B is the Bloch thickness, t is the total magnetic thickness and θ is the local sample tilt with respect to the electron beam. For clarity these two quantities are marked on the line traces. Thus by dividing the integrated induction measured from the two images,

the ratio t_B/t can be extracted. From sample 3 the ratio t_B/t was calculated to be 0.18 ± 0.02 where the error originates from the background fluctuations due to residual polycrystalline contrast (see section 3.7.5). Alternatively, this corresponds to an equivalent 2.7 of the 15 layers being of Bloch type. The same experiment performed on sample 2 gave a t_B/t ratio of 0.16 ± 0.02 which equates to 1.6 of the 10 layers having Bloch nature.

Because the methods of Lorentz TEM innately measure quantities related to the projection of the magnetic induction through the thickness, we cannot determine how many layers have pure Bloch type wall orientation (with azimuthal wall angle $|\psi| = \pi/2$) or how many layers have walls with an intermediate wall magnetisation between conventional the Néel and Bloch type (azimuthal wall angle $0 < |\psi| < \pi/2$). For the same reasons, and as mentioned in section 5.4.1, images of an intermediate wall configuration (Fig. 5.1(c)) would appear identical to images of hybrid type walls (Fig. 5.1(d)). However, taken in conjunction with the surface sensitive measurements by x-ray magnetic scattering experiments from similar samples in [10] - which measured opposite handedness of Néel walls on, effectively, the top and bottom surfaces of the samples - allows us to be certain we are imaging hybrid domain walls. As with the Fresnel images we were unable to obtain any measureable Bloch signal from sample 1 at zero tilt as is consistent with the walls being purely Néel in character.

5.4.3 Measurement of the thickness projected domain wall width and domain periodicity

The spatial resolution of DPC allows the profile of the narrow domain walls to be imaged and the wall width to be measured. The DPC images for this purpose were acquired with a probe forming aperture of 40 μm (giving a 1.8 nm probe and 0.9 nm resolution), and at a magnification of 250k$\times$ giving a pixel size of 3 nm. In Fig. 5.12(a), we show a DPC image of sample 3 in a demagnetised state close to remanence together with an integrated induction profile in Fig. 5.12(b). After deconvolution with a Gaussian function matching the imaging probe, the line

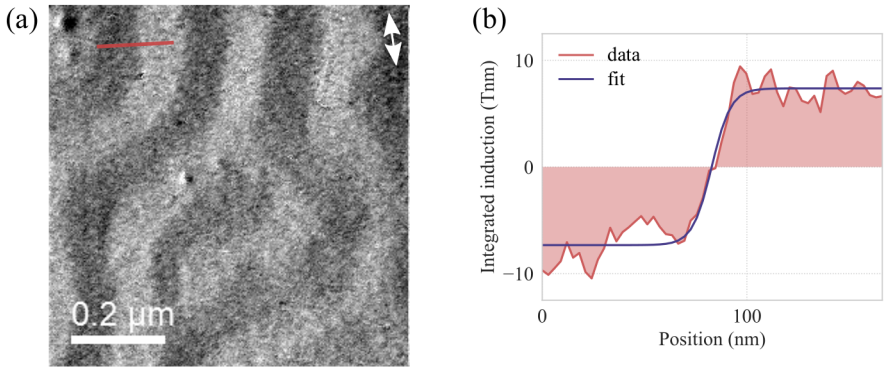

Figure 5.12: (a) DPC image taken of sample 1 tilted and in a demagnetized state close to remanence, with the component of induction mapped indicated by the double headed arrow on the top right of (a). The sample is tilted to provide strong contrast from the out-of-plane domains. (b) Integrated induction line trace taken from red line in (a) showing domain wall profile and its fit to a hyperbolic tangent function of form $B_y = B_s \tanh(x/w)$.

trace can be fitted to a standard hyperbolic tangent function, $B_y = B_s \tanh(x/w)$, giving a measure of the thickness-averaged domain wall width by the fit parameter w. This procedure identified an average $w = 11 \pm 1$ nm in sample 3 and $w = 5 \pm 1$ nm in sample 2. The DPC images from sample 1 contain strong polycrystalline contrast which obscures the magnetic contrast and prevents reliable extraction of the wall width - this is due to the small magnetic thickness and the issues discussed in section 3.7.5.

Experimental access to the domain wall width is of particular interest firstly because it provides another parameter with which to evaluate the correlation between experiments and micromagnetic simulations (which follow in the next section) and secondly because it allows indirect access to the exchange stiffness A of the material. A is the only material parameter not experimentally measured for input to the micromagnetic simulations. As defined in section 2.3.1, the width parameter we measure, w is equal to $(1/1.76)\,\delta$ where δ is the wall width. In the classical continuous film case $\delta = \sqrt{(A/K)}$, where K is the anisotropy constant [25]. Determination of w is hence interesting as it provides access to A. The above equation is overly simplistic for this material system: with the variation in wall type through the thickness there is certainly also variation in wall width.

Therefore, in reality, δ must be some function of the thickness z, and 'K' requires a thickness dependent modification which relates to the impact of the dipolar fields in each layer. It is however safe to assume A is identical in each layer. There are some interface effects that give rise to short-range (Å-scale) variations in A [26] however as each layer has the same interfaces, A in each layer should be equivalent. To estimate A we have performed a set of micromagnetic simulations to compare with the experimentally measured values of w. Further discussion of this is left to section 5.5 which focuses on micromagnetic simulations.

Also indicative of the energetics in these magnetic systems is the domain periodicity p. In this work domain periodicity was measured from low magnification Fresnel images of the samples in a demagnetised state - such an image is shown Fig. 5.13(a) taken from sample 3. The domain period is extracted from this image by taking a fast Fourier transform which is shown in Fig. 5.13(b). The spatial frequencies corresponding to p are extracted by taking a radial integral around the rings in the Fourier transform, indicated by the shaded blue segment in Fig. 5.13(b). The results of the radial integral are shown in the line trace inset on the bottom left of Fig. 5.13(b). This method identified $p = 660 \pm 10$ nm, 230 ± 10 nm and 200 ± 10 nm for samples 1, 2 and 3 respectively. p was then used as an input to the micromagnetic simulations as is described in the following paragraph.

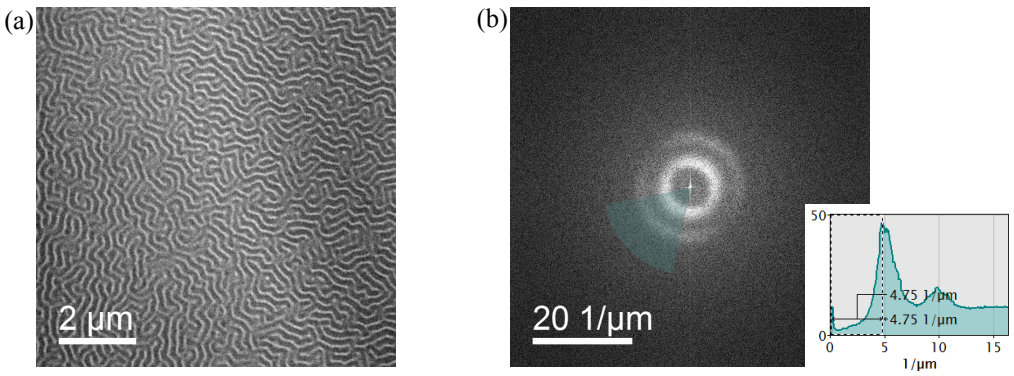

Figure 5.13: (a) Low magnification Fresnel TEM image of sample 3 in a demagnetised labyrinth domain state. (b) Fast Fourier transform of (a) showing spatial frequency information of the magnetic structure. The inset shows the intensity from which the domain spatial frequency is extracted.

5.5 Micromagnetic simulations

Micromagnetic simulations were performed using MuMax3 [27] and are based on scripts originally written by William Legrand of CNRS/Thalés. For all simulations, the cell size was fixed as 0.25 × 0.25 × 0.2 nm along the x, y and z directions, respectively. The length of the wall runs along the y direction and periodic boundary conditions were used in the both the x and y directions. The magnetisation was initialised in a three domain (two wall) configuration - with the domain periodicity set to the p values measured by Lorentz TEM - and then relaxed to the minimum energy state.

As much as possible the simulations parameters were experimentally determined. For all simulations outside section 5.5.2 the Heisenberg exchange was set as $A = 10$ pJm^{-1}, a typical value for Co thin films [6, 10, 20, 28–31]. All of the metrology measurements detailed below were performed by collaborators at CNRS/Thalés and are summarised in table 5.2. The saturation magnetisation M_s was measured experimentally, with SQUID, to be $M_s = 1.2$ MAm^{-1}. Extracting M_s from SQUID magnetometry relies on assumption of the magnetic volume and there is some evidence that the Co/Ru interface may lower M_s to 1.0 MAm^{-1} in these multilayers [32]. Therefore, simulations were trialled with different values of M_s, over the range 1.0 - 1.2 MAm^{-1}, and values were chosen that best fit the experimental data - for samples 1 and 2 this was $M_s = 1.0$ MAm^{-1} and for sample 3 it was $M_s = 1.2$ MAm^{-1}. The thickness of the magnetic layers and vacuum spacing (which, in the simulation, represents the non-magnetic layers of the sample) were chosen to match that of each multilayer. Uniaxial perpendicular anisotropy $K_u = 0.829$ MJm^{-3}, 0.711 MJm^{-3} and 0.622 MJm^{-3}; DMI parameter $D = 0.825$ mJm^{-2}, 0.707 mJm^{-2} and 0.619 mJm^{-2} were chosen for samples with Co layer thickness 1.2 nm, 1.4 nm and 1.6 nm respectively. They thus match with the interfacial perpendicular anisotropy and interfacial DMI value measured from a similar sample with thickness 1.1 nm considering an inverse thickness dependence.

Sample	$p^{\dagger}$ (nm)	A (pJm^{-1})	$M_s{}^{\star}$ (MAm^{-1})	$K_u{}^{\dagger}$ (MJm^{-3})	$D^{\dagger}$ (mJm^{-2})
5×	660	10	1.0	0.829	0.825
10×	230	10	1.0	0.711	0.707
15×	200	10	1.2	0.622	0.619

Table 5.2: Summary of input parameters for the micromagnetic simulations of each sample. The superscript on the quantity label indicates if it is experimentally measured (†) or experimentally guided ($\star$). The exchange stiffness A has no superscript as, for the initial simulations, its value was assumed.

5.5.1 Simulated domain wall profiles

This section presents results of the micromagnetic simulations, with the parameters detailed above, for each sample. Figure 5.14 relates to sample 1, the five repeat multilayer. Figure 5.14(a) shows an arrow plot indicating the direction of the magnetisation in each layer. In this projection, M_x and M_z are given by the length and direction of the arrows and M_y is given by the red to blue colour scale displayed to the right of the figure. The background colour gradient relates to the layer where red is the bottom layer, yellow is the middle layer and blue is

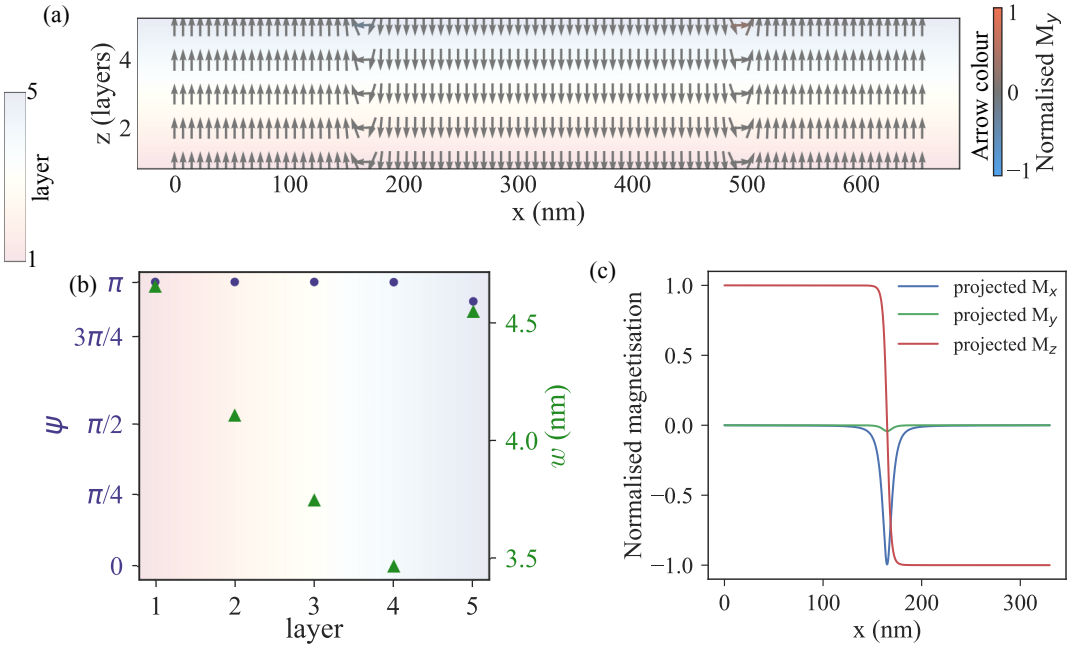

Figure 5.14: Results of simulation of domain walls in sample 1. (a) arrow plot of the cross-section of simulated domain wall, (b) graph showing the azimuthal wall angle ψ and the wall width parameter w in each layer and (c) graph of the thickness projected and normalised M$_x$, M$_y$ and M$_z$ components.

the top layer. The same background shading is on Fig. 5.14(b) to provide a visual link between different information about the same magnetic layer. This plot shows the evolution of the azimuthal wall angle ψ and the wall width parameter w with thickness through the sample. $\psi = \pi, 0$ both correspond to Néel walls (with opposite chiralities) and $\psi = \pi/2$ is a Bloch wall. w was extracted from fit the M_z profile of each layer to a $M_s \tanh(x/w)$ function (using the same fitting procedure detailed in section 5.4.3). Fig. 5.14(b) provides prediction of the thickness variation of the wall angles and width, information that is not seen in Lorentz TEM images which provide information related to the projection of the magnetisation through the thickness. Figure 5.14(c) shows M_x, M_y and M_z averaged through the thickness, therefore more related to quantities measurable from Lorentz TEM images.

For sample 1, all experimental images were consistent with the sample having homochiral Néel walls and no wall width could be extracted from the DPC data (which for this sample was dominated by non-magnetic contrast from the polycrystallites). The micromagnetic simulations largely agree with what was measured experimentally. As is most visible from Figs. 5.14(b) and (c) there is a slight twist (by 12° or 0.2 radians) away from pure Néel structure towards a Bloch structure in the topmost layer (layer 5). This surface twist occurs in simulations just below the threshold were the DMI induced field overcomes the dipolar interlayer field to stabilise pure homochiral Néel type walls. This corresponds to a t_B/t ratio of 0.04 (t_B/t is the peak of the M_y contrast in Fig. 5.14(c)). A low magnitude twist away from a pure Néel structure may well be present in the experimental images, but is likely not detectable above the contrast from the crystallites. In line traces averaged over 10 lines (Figs. 5.10(d-f)), the crystallites are responsible for background fluctuations with a standard deviation of 0.02. By scaling the contrast in Figs. 5.10(d) and (f), it can be estimated that a magnetic thickness of $0.04t$ would result in Fresnel contrast of ± 0.02 (i.e. a intensity minimum of 0.98 and maximum of 1.02). Hence a small signal from a partial Bloch twist could be present but not detectable with any certainty. The w value measured from the thickness projected M_z profile in Fig. 5.14(c) is 4 nm.

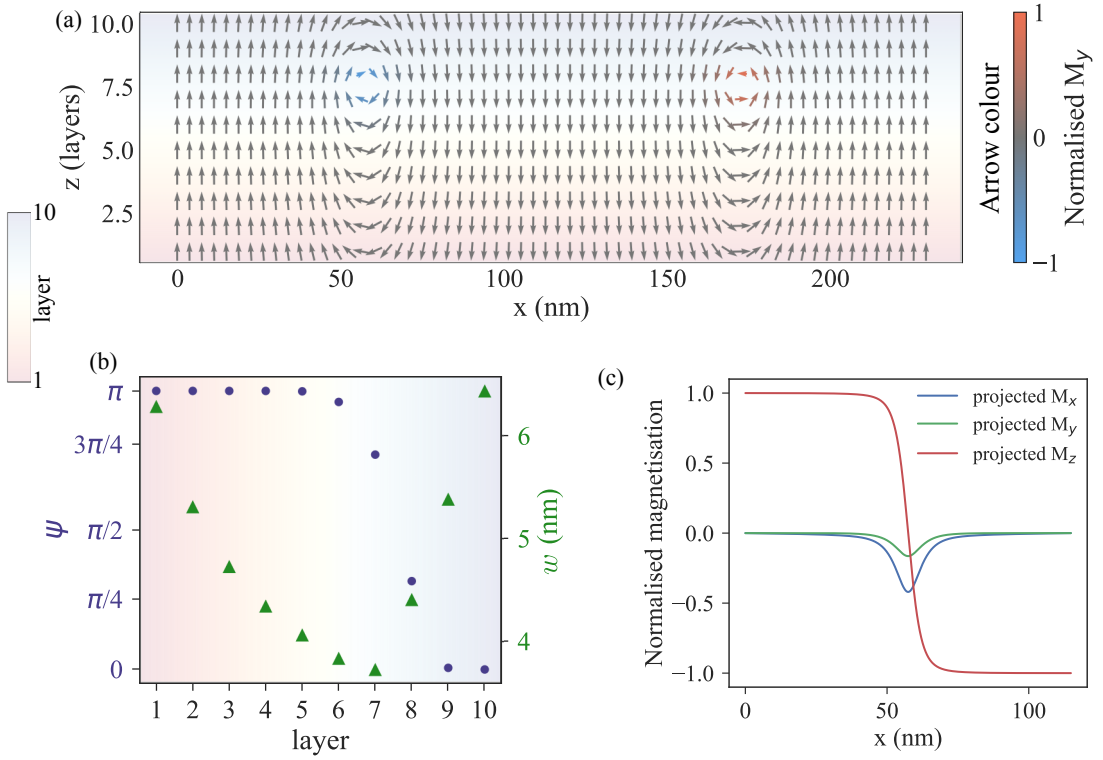

Figure 5.15: Results of simulation of domain walls in sample 2. (a) arrow plot of the cross-section of simulated domain wall, (b) graph showing the azimuthal wall angle ψ and the wall width parameter w in each layer and (c) graph of the thickness projected and normalised M_x, M_y and M_z components.

Figure 5.15 shows the same figures as 5.14 but related to simulations of sample 2, the ten repeat sample. These simulations indicate a Bloch twist extending through two layers (layers 7 and 8) near the top surface of the sample; five layers have the chirality promoted by the DMI and three have the opposite chirality. As is seen in Fig. 5.15(b) there is significant variation in the wall width throughout the different layers of the simulation. The surface layers (Néel) are significantly wider than the inner, more Bloch like, layers. This is also noted in [10, 13]. The peak of the M_y curve in graph in Fig. 5.15(c) predicts a t_B/t ratio of 0.16, the same as the experimentally measured value. Additionally, the w value measured from the thickness projected M_z profile in Fig. 5.15(c) is 5 nm, which is also in excellent agreement with the experimentally measured value of 5 $\pm$ 1 nm.

Figure 5.16 relates to simulations of sample 3, the 15 repeat sample. These simulations indicate a Bloch twist extending through three layers (layers 8, 9 and

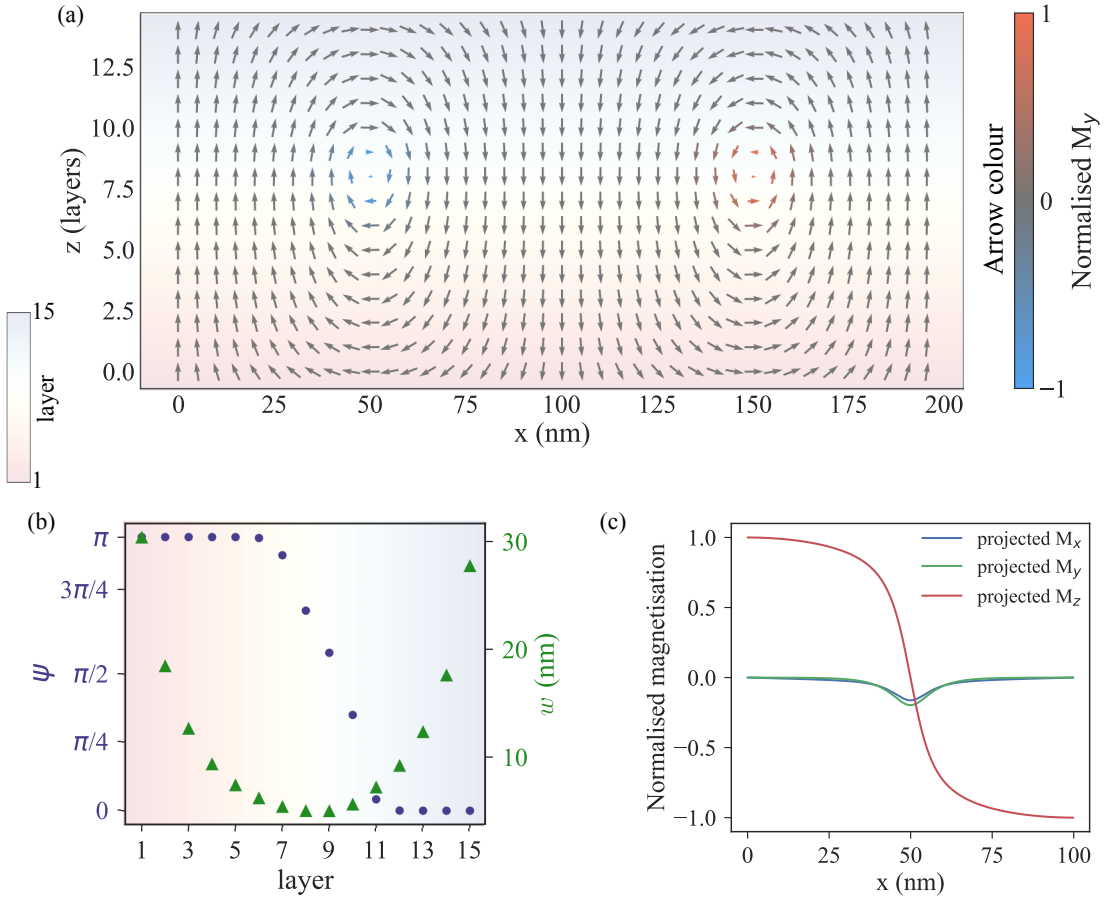

Figure 5.16: Results of simulation of domain walls in sample 3. (a) arrow plot of the cross-section of simulated domain wall, (b) graph showing the azimuthal wall angle ψ and the wall width parameter w in each layer and (c) graph of the thickness projected and normalised M_x, M_y and M_z components.

10) near the centre of the sample; seven layers have the chirality promoted by the DMI and five have the opposite chirality. The peak of the M_y curve in graph in Fig. 5.15(c) predicts a t_B/t ratio of 0.19, in agreement with the experimentally measured value of 0.18 ± 0.02. Additionally w measured from the thickness projected M_z profile in Fig. 5.15(c) is 10 nm, which is also in excellent agreement with the experimentally measured value of 11 ± 1 nm.

These values of t_B/t and w from simulations of all three samples are summarised, along with the corresponding experimental measurements, in table 5.3.

5.5.2 Variation of A with w and comparison to experiment

A is measured directly from the dispersion curve of spinwaves using methods such as Brillouin light scattering, inelastic neutron scattering or ferromagnetic resonance [33–36]. As summarised in [37], these methods become challenging for measuring A in Co films with thicknesses below 30 nm. Study [37] uses comparison of the experimental response of an 'exchange spring' to an external magnetic field with simulations to deduce $A = 7$ pJm^{-1} in 2 nm thick Co layers, increasing to 15 pJm^{-1} in 7 nm thick Co layers. The value of 10 pJm^{-1} used for the simulations in section 5.5.1, matches the value used for micromagnetic simulations of similar Co-based multilayer samples [6, 10, 20, 28–31].

As introduced at the end of section 5.4.3, here micromagnetic simulations were used in conjunction with experimentally measured wall widths to give a measure of the exchange stiffness A of the samples. The wall width and the exchange stiffness are related through $\delta = \sqrt{(A/K)}$ where K is some effective 'anisotropy' that in this system, as discussed in section 5.4.3, varies with thickness. Because of this, determination of 'K' is a complex analytical problem and therefore, to estimate A we have performed two sets of micromagnetic simulations. The simulation use the parameters outlined in table 5.2 for samples 2 and 3 except A which was varied between 3 and 20 pJm^{-1}. For every value of A, the system was allowed to relax and then from each relaxed state the thickness averaged w was measured to produce the curves of A versus w shown in Fig. 5.17 which follow the expected square root trend.

	Experiment		Simulation	
Sample	w (nm)	t_B/t	w (nm)	t_B/t
5×	-	-	4	0.04
10×	5 ± 1	0.16 ± 0.02	5	0.16
15×	11 ± 1	0.18 ± 0.02	10	0.19

Table 5.3: Summary of the width parameter w, and ratio of Bloch thickness to total magnetic thickness t_B/t, measured from each sample experimentally and calculated from micromagnetic simulations of each sample.

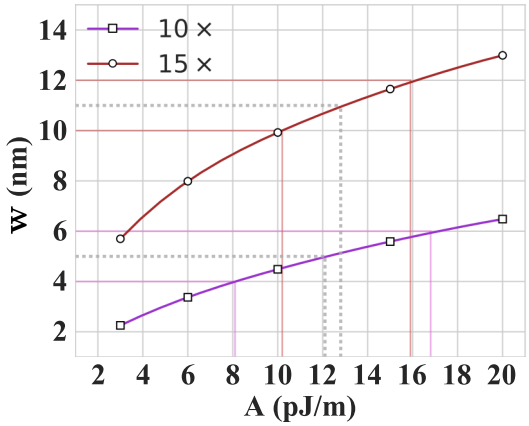

Figure 5.17: Graph of domain wall width parameter w versus A generated from micromagnetic simulations based on the structures of sample 2 ($\times$ 10 repeat) and sample 3 ($\times$ 15 repeat) the dashed grey lines relate the experimental measurement of w width, to the value of A predicted by best fit to the curves produced by micromagnetic simulation.

These graphs suggest that A in these magnetic multilayer systems is 12 pJm^{-1} for sample 2 and 13 pJm^{-1} for sample 3, in the expected range for such films. However, because w varies slowly with A, the error bound on these values (shown by the cross over of thin red and purple lines with the x-axis of the graph in Fig. 5.17) are quite large ($\pm$ 4 pJm^{-1} for sample 2 and $\pm$ 2 pJm^{-1} for sample 3). A slight increase in A does not change the t_B/t ratio measured from simulation of either sample 2 or 3 - in fact over the A range simulated, the t_B/t ratio only differed significantly for the lowest value of A (= 3 pJm^{-1}).

5.6 Discussion and Conclusion

In this chapter results were presented which provide unambiguous and quantitative determination of the nature of hybrid domain walls in ultrathin multilayer stacks using Lorentz microscopy. The measurements are consistent with recent experimental studies, which in contrast to this work measured only the Néel component, and also with simulations of such structures [10–13]. Firstly, the magnitude of Fresnel image contrast from the magnetic multilayers at zero tilt was used to indicate whether the walls are Néel, Bloch or Hybrid Néel/Bloch type. The Fresnel images suggested that the two thicker samples (samples 2 and 3) have hybrid type domain walls, and that the thinnest sample (sample 1) has homochiral Néel walls. The precise fraction

of the thickness occupied by Bloch type domain walls was quantitatively measured by DPC imaging (therefore indirectly also providing the thickness occupied by Néel type walls). As expected from considering the strength of the dipolar interactions in each sample, the magnitude of the Bloch twist was observed to increase with thickness with: no experimental measurement of a twist in sample 1 (five repeats of 1.2 nm Co), 1.6 layers Bloch in sample 2 (ten repeats of 1.4 nm Co), and 2.7 layers Bloch in sample 3 (15 repeats of 1.6 nm Co). We note that the critical number of repeat layers required to generate hybrid domain wall textures also depends on the material parameters, such as the saturation magnetisation and strength of DMI, and not simply the number of repetitions.

It was addressed that, because Lorentz TEM measures a projection of the integrated magnetic induction, these measurements themselves cannot distinguish a domain wall with thickness invariant ψ between Néel and Bloch configurations and a hybrid wall where ψ varies through the thickness. It is noted that Lorentz TEM tomography techniques could provide this missing information and reveal the full variation of the Bloch component through the thickness of the multilayer [38]. The surface sensitive measurements of by Legrand *et al.* effectively found Néel walls of opposite chirality on the top and bottom surfaces of multilayers similar to those studied in this chapter [10]. Therefore we conclude with certainty that we have measured Bloch twists residing in the central layers of hybrid type domain walls between Néel layers with opposite chirality. Furthermore, the micromagnetic simulations of the samples (in section 5.5) are in excellent agreement with the experimental work and provide further certainty that the walls are hybrid type.

Experimental quantification of the internal structure of these recently discovered hybrid domain walls, stabilised instead of homochiral Néel walls in samples with strong enough dipolar fields, is critical if skyrmionic materials are to be used for spintronic applications. In this chapter we have shown that Lorentz TEM can be used both to identify the presence of hybrid walls and quantify 'how hybrid' they are. This is valuable information because, as explained in 5.1, hybrid textures have significant - though not necessarily negative - consequences on the motion of

skyrmions under spin-polarised currents. Interestingly, the hybrid structure also explains some phenomena already noted in literature, such as the dependence of skyrmion velocity on the strength of the DMI interaction [5, 39]. This was explained by Legrand *et al.* as a consequence of hybrid skyrmions because increasing the DMI strength increases the net chirality of the skyrmion which in turn increases its velocity under spin-polarised currents [10].

Bibliography

[1] A. Fert and P. M. Levy, "Role of anisotropic exchange interactions in determining the properties of spin-glasses," *Physical Review Letters*, vol. 44, no. 23, pp. 1538–1541, 1980.

[2] M. Heide, G. Bihlmayer, and S. Blügel, "Dzyaloshinskii-Moriya interaction accounting for the orientation of magnetic domains in ultrathin films: Fe/W(110)," *Physical Review B - Condensed Matter and Materials Physics*, vol. 78, p. 140403, 2008.

[3] S. Heinze, K. Von Bergmann, M. Menzel, J. Brede, A. Kubetzka, R. Wiesendanger, G. Bihlmayer, and S. Blügel, "Spontaneous atomic-scale magnetic skyrmion lattice in two dimensions," *Nature Physics*, vol. 7, no. 9, pp. 713–718, 2011.

[4] W. Jiang, P. Upadhyaya, W. Zhang, G. Yu, M. B. Jungfleisch, F. Y. Fradin, J. E. Pearson, Y. Tserkovnyak, K. L. Wang, O. Heinonen, S. G. Te Velthuis, and A. Hoffmann, "Blowing magnetic skyrmion bubbles," *Science*, vol. 349, no. 6245, pp. 283–286, 2015.

[5] S. Woo, K. Litzius, B. Krüger, M. Y. Im, L. Caretta, K. Richter, M. Mann, A. Krone, R. M. Reeve, M. Weigand, P. Agrawal, I. Lemesh, M. A. Mawass, P. Fischer, M. Kläui, and G. S. Beach, "Observation of room-temperature magnetic skyrmions and their current-driven dynamics in ultrathin metallic ferromagnets," *Nature Materials*, vol. 15, pp. 501–506, 2016.

[6] C. Moreau-Luchaire, C. Moutafis, N. Reyren, J. Sampaio, C. A. Vaz, N. Van Horne, K. Bouzehouane, K. Garcia, C. Deranlot, P. Warnicke, P. Wohlhüter, J. M. George, M. Weigand, J. Raabe, V. Cros, and A. Fert, "Additive interfacial chiral interaction in multilayers for stabilization of small individual skyrmions at room temperature," *Nature Nanotechnology*, vol. 11, no. 5, pp. 444–448, 2016.

[7] G. Yu, P. Upadhyaya, X. Li, W. Li, S. K. Kim, Y. Fan, K. L. Wong, Y. Tserkovnyak, P. K. Amiri, and K. L. Wang, "Room-Temperature Creation and Spin-Orbit Torque Manipulation of Skyrmions in Thin Films with Engineered Asymmetry," *Nano Letters*, vol. 16, no. 3, pp. 1981–1988, 2016.

[8] A. Soumyanarayanan, M. Raju, A. L. Oyarce, A. K. Tan, M. Y. Im, A. P. Petrovic, P. Ho, K. H. Khoo, M. Tran, C. K. Gan, F. Ernult, and C. Panagopoulos, "Tunable room-temperature magnetic skyrmions in Ir/Fe/Co/Pt multilayers," *Nature Materials*, vol. 16, no. 9, pp. 898–904, 2017.

[9] K. Zeissler, M. Mruczkiewicz, S. Finizio, J. Raabe, P. M. Shepley, A. V. Sadovnikov, S. A. Nikitov, K. Fallon, S. McFadzean, S. McVitie, T. A. Moore, G. Burnell, and C. H. Marrows, "Pinning and hysteresis in the field dependent diameter evolution of skyrmions in Pt/Co/Ir superlattice stacks," *Scientific Reports*, vol. 7, no. 1, pp. 1–9, 2017.

[10] W. Legrand, J. Y. Chauleau, D. Maccariello, N. Reyren, S. Collin, K. Bouzehouane, N. Jaouen, V. Cros, and A. Fert, "Hybrid chiral domain walls and skyrmions in magnetic multilayers," *Science Advances*, vol. 4, no. 7, 2018.

[11] Y. Dovzhenko, F. Casola, S. Schlotter, T. X. Zhou, F. Büttner, R. L. Walsworth, G. S. Beach, and A. Yacoby, "Magnetostatic twists in room-temperature skyrmions explored by nitrogen-vacancy center spin texture reconstruction," *Nature Communications*, vol. 9, no. 1, pp. 1–7, 2018.

[12] I. Lemesh and G. S. Beach, "Twisted domain walls and skyrmions in perpendicularly magnetized multilayers," *Physical Review B*, vol. 98, no. 10, pp. 1–8, 2018.

[13] W. Legrand, N. Ronceray, N. Reyren, D. MacCariello, V. Cros, and A. Fert, "Modeling the Shape of Axisymmetric Skyrmions in Magnetic Multilayers," *Physical Review Applied*, vol. 10, no. 6, p. 1, 2018.

[14] S. A. Montoya, S. Couture, J. J. Chess, J. C. Lee, N. Kent, D. Henze, S. K. Sinha, M. Y. Im, S. D. Kevan, P. Fischer, B. J. McMorran, V. Lomakin, S. Roy, and E. E. Fullerton, "Tailoring magnetic energies to form dipole skyrmions and skyrmion lattices," *Physical Review B*, vol. 95, no. 2, pp. 1–10, 2017.

[15] A. E. LaBonte, "Two-dimensional Bloch-type domain walls in ferromagnetic films," *Journal of Applied Physics*, vol. 40, no. 6, pp. 2450–2458, 1969.

[16] A. Hubert, "Stray-Field-Free and Related Domain Wall Configurations in Thin Magnetic Films (II)," *Physica Status Solidi (B)*, vol. 38, no. 2, pp. 699–713, 1970.

[17] J. Y. Chauleau, W. Legrand, N. Reyren, D. Maccariello, S. Collin, H. Popescu, K. Bouzehouane, V. Cros, N. Jaouen, and A. Fert, "Chirality in Magnetic Multilayers Probed by the Symmetry and the Amplitude of Dichroism in X-Ray Resonant Magnetic Scattering," *Physical Review Letters*, vol. 120, p. 037202, 2018.

[18] W. Jiang, X. Zhang, G. Yu, W. Zhang, X. Wang, M. Benjamin Jungfleisch, J. E. Pearson, X. Cheng, O. Heinonen, K. L. Wang, Y. Zhou, A. Hoffmann, and S. G. Te Velthuis, "Direct observation of the skyrmion Hall effect," *Nature Physics*, vol. 13, no. 2, pp. 162–169, 2017.

[19] M. J. Benitez, A. Hrabec, A. P. Mihai, T. A. Moore, G. Burnell, D. Mcgrouther, C. H. Marrows, and S. McVitie, "Magnetic microscopy and topological stability of homochiral Néel domain walls in a Pt/Co/AlO x trilayer," *Nature Communications*, vol. 6, no. 1, p. 8957, 2015.

[20] S. McVitie, S. Hughes, K. Fallon, S. McFadzean, D. McGrouther, M. Krajnak, W. Legrand, D. MacCariello, S. Collin, K. Garcia, N. Reyren, V. Cros, A. Fert, K. Zeissler, and C. H. Marrows, "A transmission electron microscope study of Néel skyrmion magnetic textures in multilayer thin film systems with large interfacial chiral interaction," *Scientific Reports*, vol. 8, p. 5703, 2018.

[21] W. Jiang, S. Zhang, X. Wang, C. Phatak, Q. Wang, W. Zhang, M. B. Jungfleisch, J. E. Pearson, Y. Liu, J. Zang, X. Cheng, A. Petford-Long, A. Hoffmann, and S. G. Te Velthuis, "Quantifying chiral exchange interaction for Néel-type skyrmions via Lorentz transmission electron microscopy," *Physical Review B*, vol. 99, p. 104402, 2019.

[22] P. J. Bloemen, H. W. Van Kesteren, H. J. Swagten, and W. J. De Jonge, "Oscillatory interlayer exchange coupling in Co/Ru multilayers and bilayers," *Physical Review B*, vol. 50, no. 18, pp. 13505–13514, 1994.

[23] J. A. Mir, R. Clough, R. MacInnes, C. Gough, R. Plackett, I. Shipsey, H. Sawada, I. MacLaren, R. Ballabriga, D. Maneuski, V. O'Shea, D. McGrouther, and A. I. Kirkland, "Characterisation of the Medipix3 detector for 60 and 80ăkeV electrons," *Ultramicroscopy*, vol. 182, pp. 44–53, 2017.

[24] J. Song, C. S. Allen, S. Gao, C. Huang, H. Sawada, X. Pan, J. Warner, P. Wang, and A. I. Kirkland, "Atomic Resolution Defocused Electron Ptychography at Low Dose with a Fast, Direct Electron Detector," *Scientific Reports*, vol. 9, no. 1, p. 3919, 2019.

[25] A. Hubert and R. Schäfer, *Magnetic Domains: the analysis of magnetic microstructures*. Berlin, Heidelberg: Springer, 2009.

[26] C. Eyrich, "Exchange Stiffness in Thin-Film Cobalt Alloys," Master's thesis, Simon Fraser University, 2010.

[27] A. Vansteenkiste, J. Leliaert, M. Dvornik, M. Helsen, F. Garcia-Sanchez, and B. Van Waeyenberge, "The design and verification of MuMax3," *AIP Advances*, vol. 4, no. 10, 2014.

[28] T. N. A. Nguyen, R. Knut, V. Fallahi, S. Chung, Q. T. Le, S. M. Mohseni, O. Karis, S. Peredkov, R. K. Dumas, C. W. Miller, and J. Åkerman, "Depth-Dependent Magnetization Profiles of Hybrid Exchange Springs," *Physical Review Applied*, vol. 2, p. 044014, 2014.

[29] R. H. Liu, W. L. Lim, and S. Urazhdin, "Dynamical Skyrmion State in a Spin Current Nano-Oscillator with Perpendicular Magnetic Anisotropy," *Physical Review Letters*, vol. 114, p. 137201, 2015.

[30] M. Cubukcu, J. Sampaio, K. Bouzehouane, D. Apalkov, A. V. Khvalkovskiy, V. Cros, and N. Reyren, "Dzyaloshinskii-Moriya anisotropy in nanomagnets with in-plane magnetization," *Physical Review B*, vol. 93, p. 020401, 2016.

[31] S. D. Pollard, J. A. Garlow, J. Yu, Z. Wang, Y. Zhu, and H. Yang, "Observation of stable Néel skyrmions in cobalt/palladium multilayers with Lorentz transmission electron microscopy," *Nature Communications*, vol. 8, p. 14761, 2017.

[32] W. Legrand. Private communication, 2018.

[33] S. P. Vernon, S. M. Lindsay, and M. B. Stearns, "Brillouin scattering from thermal magnons in a thin Co film," *Physical Review B*, vol. 29, no. 8, pp. 4439–4442, 1984.

[34] A. Yoshihara, Y. Haneda, Y. Shimada, and T. Fujimura, "Brillouin scattering from spin waves in sputtered Co-Zr films," *Journal of Applied Physics*, vol. 66, no. 1, pp. 328–335, 1989.

[35] H. A. Alperin, O. Steinsvoll, G. Shirane, and R. Nathans, "Observation of the dispersion relation for spin waves in hexagonal cobalt," *Journal of Applied Physics*, vol. 37, no. 3, pp. 1052–1053, 1966.

[36] P. E. Tannenwald and R. Weber, "Exchange integral in cobalt from spin-wave resonance," *Physical Review*, vol. 121, no. 3, p. 715, 1961.

[37] C. Eyrich, A. Zamani, W. Huttema, M. Arora, D. Harrison, F. Rashidi, D. Broun, B. Heinrich, O. Mryasov, M. Ahlberg, O. Karis, P. E. Jönsson, M. From, X. Zhu, and E. Girt, "Effects of substitution on the exchange stiffness and magnetization of Co films," *Physical Review B - Condensed Matter and Materials Physics*, vol. 90, p. 235408, 2014.

[38] C. Phatak and D. Gürsoy, "Iterative reconstruction of magnetic induction using Lorentz transmission electron tomography," *Ultramicroscopy*, vol. 150, pp. 54–64, 2015.

[39] K. Litzius, I. Lemesh, B. Krüger, P. Bassirian, L. Caretta, K. Richter, F. Büttner, K. Sato, O. A. Tretiakov, J. Förster, R. M. Reeve, M. Weigand, I. Bykova, H. Stoll, G. Schütz, G. S. Beach, and M. Klaüi, "Skyrmion Hall effect revealed by direct time-resolved X-ray microscopy," *Nature Physics*, vol. 13, no. 2, pp. 170–175, 2017.

6

Controlled individual skyrmion nucleation at room temperature at artificial defects formed with ion irradiation

Contents

6.1 Introduction

Chapter 5 presented an investigation of the three dimensional wall structure in multilayered samples which support skyrmion magnetic textures. The experiments identified that, in samples with certain multilayer stack geometries, a number of the

central layers support a Bloch type wall rotation. Comparison with previous studies and micromagnetic simulations confirms that the central Bloch type layers are situated between Néel type wall rotations of opposite handedness. This thickness varying wall structure influences the current induced motion of skyrmions therefore full profiling of the three dimensional wall structure is critical to fully capitalise on the potential of skyrmions for spintronic applications. This chapter studies another critical component required to realise a skyrmion based device: reliable nucleation of skyrmions at room temperature and low applied magnetic fields.

A multitude of nucleation methods have been proposed in recent years which fit largely into three categories based on: spin transfer torques [1–7]; laser pulses [8–10]; and locally applied electric fields [11, 12]. It is also recognised that naturally occurring defects also serve as a nucleation point for skyrmions [13, 14], however the precise nature of the defect is variable and there is no control over the placement of such defects. In this chapter, an original method of nucleating skyrmions using a focused ion beam (FIB) microscope to create nanoscale defects is proposed.

In multilayer systems based on Pt/Co/Pt, ion irradiation is well documented to have a dose dependent effect on both the perpendicular magnetic anisotropy and coercivity of the material (resulting in decreased anisotropy and increased coercivity) [15–19]. These effects have been exploited to engineer or tailor the local behaviour of magnetic systems [20, 21]. For example a study found that extended circular areas of FIB irradiation (diameter 300 nm to 1 µm) in multilayers of Pt/Co/Pt can stabilise anti-skyrmions and Bloch skyrmions [21]. In contrast to the aforementioned study, here point-like FIB defects are purposed to nucleate Néel type skyrmions.

6.2 Samples

The efficiency of using FIB irradiation to nucleate skyrmions was tested on four distinct multilayered samples known to support homochiral Néel walls and/or skyrmions using a range of TEM imaging modes. The structure of the four multilayer samples is provided in table 6.1:

The structural impact of the defects and the magnetic response of the sample at the defects was studied extensively for sample 1. The structural impact of the defects was studied both in plan view and in cross-section. The magnetic behaviour at the defects as a function of applied magnetic field was studied by *in situ* Fresnel magnetising experiments and details of the magnetic textures at the defects were studied with high resolution DPC images. The reproducibility of the technique and sensitivity to multilayer composition was tested on samples 2-4 (which were the focus of chapter 5). For these three additional samples, the magnetic response of the sample at the defect sites was imaged as a function of applied magnetic field using Fresnel TEM. Chapter 5 identified samples 3 and 4 as having hybrid type domain walls (as opposed to the usual Néel type walls commonplace in multilayer thin films with DMI) but the internal wall structure is not thought to be of significance in this study.

For clarity it should be mentioned that two 'sample 1's were purposed for this experiment which have identical layer composition but were grown in different sputtering machines. Sample 1a was deposited by DC magnetron sputtering by Katharina Zeissler at the University of Leeds on a 3 nm thick amorphous carbon substrate suspended from a standard TEM grid, and was used for all of the presented work except the cross-sectional study. The cross-sectional study was performed on sample 1b which was deposited by DC magnetron sputtering by William Legrand at CNRS/Thalés on Si_3N_4 membrane samples where the cross-section was extracted from the thicker Si frame. As discussed in chapter 5 samples 2-4 were also deposited by DC magnetron sputtering by William Legrand at

Sample	Multilayer structure
1	$Pt(10)/[Ir(1)/Co(0.6)/Pt(1)]_{\times 10}/Pt(3)$
2	$Ta(10)/Pt(8)[Co(1.2)/Ru(1.4)/Pt(0.6)]_{\times 5}/Pt(2.4)$
3	$Ta(10)/Pt(8)[Co(1.4)/Ru(1.4)/Pt(0.6)]_{\times 10}/Pt(2.4)$
4	$Ta(10)/Pt(8)[Co(1.6)/Ru(1.4)/Pt(0.6)]_{\times 15}/Pt(2.4)$

Table 6.1: Summary of the sample composition where the numbers in brackets give the layer thickness in nm and the subscript gives the number of repeats.

CNRS/Thales on Si_3N_4 membrane samples. All samples are polycrystalline and support out-of-plane magnetisation.

6.3 Sample properties before defect creation

This section details magnetic and structural measurements made from the samples prior to defect creation which provide a useful point of reference for the rest of the chapter.

6.3.1 Evolution of magnetisation with field prior to defect creation

Figure 6.1 presents Fresnel images which summarise the magnetic behaviour of all four samples with applied magnetic field prior to the creation of FIB defects. The samples were each saturated in a positive out-of-plane magnetic field (supplied by the objective lens of the microscope), then imaged as the strength field was reduced to zero at which point the samples were then turned upside down and imaged as the field strength was again increased until the samples saturate. From the reference frame of the sample, this procedure allows imaging of the magnetic reversal from saturation in a positive field to saturation in a negative field. This positive and negative field convention is used throughout the rest of this chapter. Samples 3 and 4 are respresented by one set of images because they have extremely similar behaviour (the only difference is an offset in field values). The images shown in Fig. 6.1(f) and (g) are from sample 4. As explained in section 5.2 of chapter 5, samples with out-of-plane domains and (predominantly) Néel type walls must be tilted with respect to the electron beam to get magnetic contrast in Fresnel TEM images. The images of sample 1 were taken with a 20° tilt about the axis indicated in the top right corner of Fig. 6.1(a). The tilt is implicit for samples 2-4 because, as explained in section 5.3 of chapter 5, the membrane windows suffer from considerable buckling which alone provides a sufficiently large angle between the sample surface and the electron beam for magnetic contrast. For this reason the tilt axis is not marked on any images from samples 2-4, as it varies locally in the imaged region.

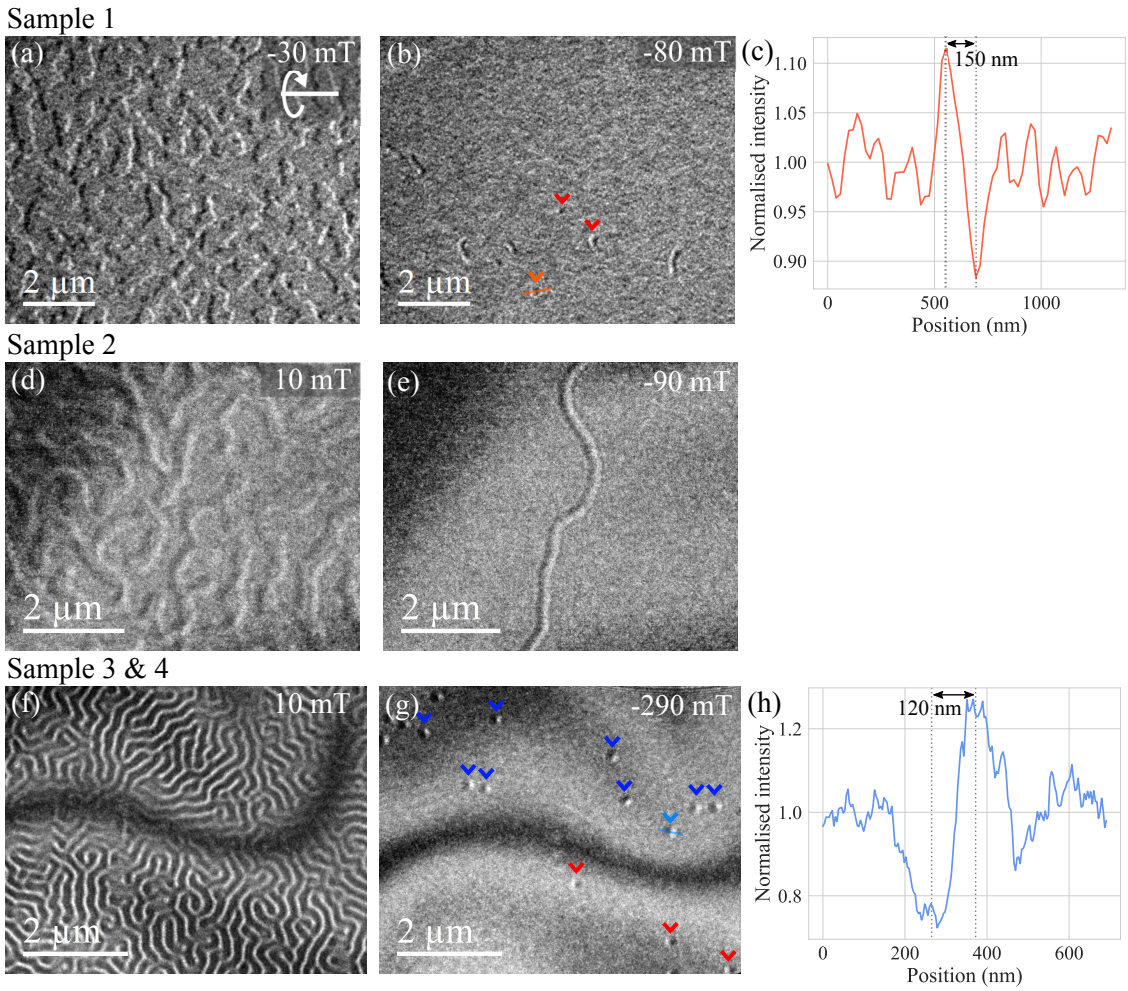

Figure 6.1: Fresnel images of (a-b) sample 1, (d-e) sample 2 and (f-g) sample 4 at two different field values. Sample 1 is tilted 20° about axis labelled, where for samples 2 and 4 tilt is provided by surface contortion. The images of sample 4 are also representative of sample 3 - albeit at skyrmions form at a lower field value. The left most column shows (close to) the coercive state of the samples where the central column shows the magnetic configuration just before saturation where samples 1, 3 and 4 support skyrmions (highlighted by coloured arrows). No skyrmions were observed in sample 2. (c) and (h) show line traces through skyrmions in samples 1 and 4 respectively. The diameter of the skyrmion is marked on each line trace.

The left most column of images shows the samples close to their coercive state supporting a labyrinth-like domain configuration in all cases. As the field is increased in strength, domains in the same direction as the field grow while the other domains shrink. Isolated skyrmions are supported in samples 1, 3, and 4 just before saturation. Néel type skyrmions appear in Fresnel images as dot-like objects with contrast which is black on one side and white on the other; their

location is highlighted by a small coloured arrow above the skyrmion. In sample 1 the skyrmions are very sparse with only three present in the field of view - a line trace through one of the skyrmions, averaged over five pixels, is shown in Fig. 6.1(c). For sample 2 sparse thread-like domains, as shown in Fig. 6.1(e), remain just before saturation at ≈ -100 mT. No skyrmions were observed in sample 2. Samples 3 and 4 stabilise a far larger number of skyrmions than sample 1 though in a significantly stronger out-of-plane field. The images in Fig. 6.1(f) and (g) are traversed by a dark band which is non-magnetic contrast arising from a bend contour symptomatic of the contorted membrane windows. On either side of this boundary, the sample surface presents an opposite sign of tilt to the electron beam and consequently the black/white nature of the skyrmion contrast reverses. Skyrmions indicated by red arrows, below the boundary, are at positive tilt to the electron beam where the skyrmions with blue arrows, above the boundary, are at negative tilt to the electron beam. Figure 6.1(h) presents a line trace, averaged over 10 pixels, through a skyrmion in Fig. 6.1(g). After saturation, on reduction of the applied magnetic field strength, sample 1 does not form any domains until in a field of ≈ + 20 mT where sample 2 begins to form domains just under - 10 mT. Samples 3 and 4 also briefly support skyrmions when reducing the field from saturation. These skyrmions are not stable as the field is reduced, and quickly expand via worm-like domains to reform the labyrinth-like demagnetised state visible in Fig. 6.1(f) at ≈ - 95 mT and - 200 mT for samples 3 and 4 respectively. Key magnetic parameters that were estimated from these *in situ* Fresnel magnetising experiments such as the coercivity H_c, the remanence M_r and the field range over which skyrmions are stable are summarised in table 6.2.

Measuring skyrmion diameter from Fresnel images

The line traces presented in Fig. 6.1(c) and (h) are taken from Fresnel images (which are defocussed images with broadened features) and mark the skyrmion diameters to be 150 nm and 120 nm respectively. As will be shown in the following, the skyrmion diameter can be quantitatively measured from Fresnel images as

Sample	H_c (mT)	M_r/M_s	Skyrmion stability range (mT)
1	-25	1	-50 to -80
2	0	0	n/a
3	0	0	-170 to -190
4	0	0	-270 to -350

Table 6.2: Summary of key magnetic properties of the samples estimated from *in situ* Fresnel magnetising experiments in which each sample was saturated in a positive field and imaged during its reversal to saturation in a negative field.

distance between the maxima of the bright contrast and the minima of the dark contrast. Figure 6.2(a) shows a coloured vector image of the magnetisation of a Néel type skyrmion, with ≈ 130 nm diameter. Figure 6.2(b) shows the M_z configuration constructed to represent the skyrmions in sample 1: it is a circle of diameter ≈ 130 nm with a narrow transitional wall (between $\pm M_z$) chosen to match the width of the profile experimentally measured with DPC later in the chapter. As discussed in

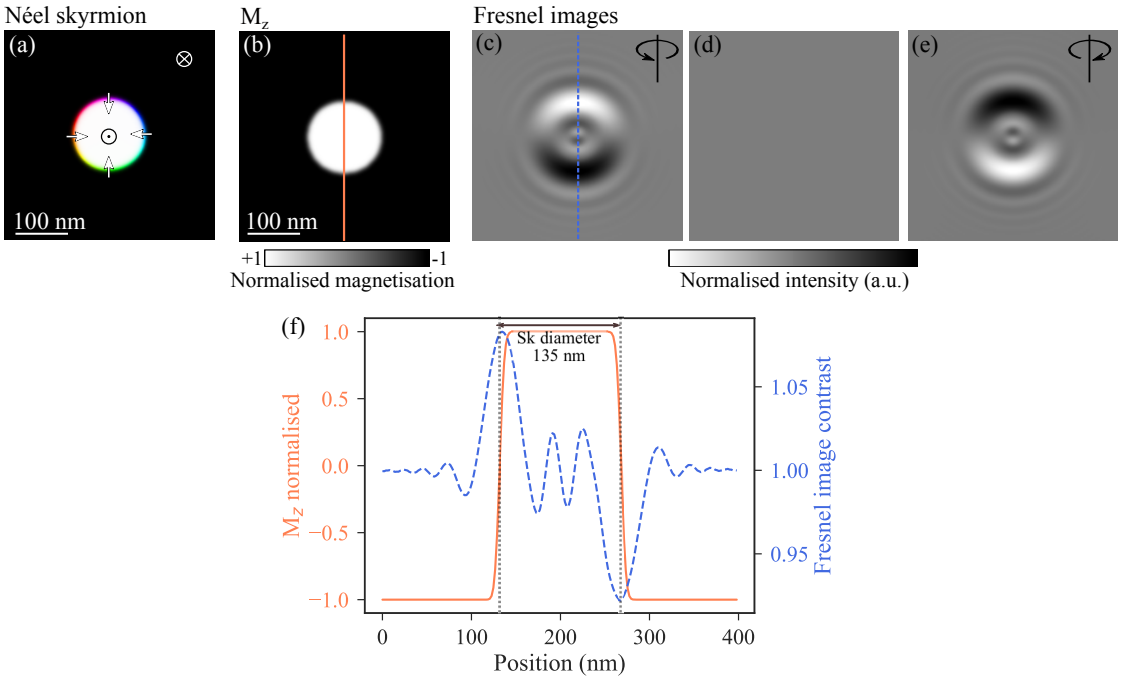

Figure 6.2: (a) schematic of the magnetisation of a Néel type skyrmion where the colour represents the direction of the magnetisation. (b) shows the M_z component of the skyrmion which is used to calculate of Fresnel images. (c-e) Fresnel images calculated with a defocus of 5 mm and with a sample tilt of +25°, 0° and -25° respectively. (f) shows the profile of M_z overlaid with the Fresnel image contrast - the distance between the extrema of the Fresnel images matches the skyrmion diameter determined from M_z.

chapter 4, the in-plane magnetisation associated with Néel type objects (walls and skyrmions) does not contribute to Lorentz microscopy images. Therefore without lack of accuracy the image calculations used only the domain magnetisation M_z. Example Fresnel images, calculated with a tilt of 25°, 0° and -25° about the axis indicated and with a defocus of 5 mm (chosen to match the experimental defocus used to image sample 1) are shown in Figs. 6.2(c-e) respectively. The Fresnel images show the white/black contrast characteristic of a Néel type skyrmion which reverses with tilt, as seen in Fig. 6.2(c) and (e), and with no visible contrast without tilt Fig. 6.2(d). Here, the diameter of the skyrmion is defined as the distance between the two zeros of a M_z profile which passes through the centre of the skyrmion (e.g. the orange line in Fig. 6.2(f) taken from Fig. 6.2(b)). On the graph in Fig. 6.2(f), the two zeros of M_z are highlighted by the vertical grey lines. Also shown on this graph is a line trace taken from the Fresnel image of the skyrmion, where it is clear that the distance between the extrema of the Fresnel images is equivalent to the skyrmion diameter. Further evidence that this is valid is encountered later in this chapter where the same skyrmion diameter is measured from both Fresnel images and DPC images (which are in-focus).

For comparison with skyrmions nucleated at artificial defects, presented later in this chapter, the evolution of the skyrmion size with applied field strength was analysed for sample 1 and is presented in Fig. 6.3. The error bars represent the

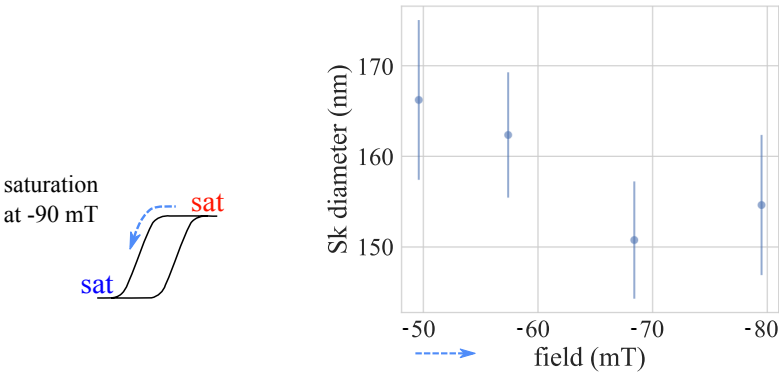

Figure 6.3: Summary of the skyrmion size supported by sample 1 before artificial defect creation. Skyrmions are stable between -50 and -80 mT with diameter between 170 and 150 nm.

standard error on each measurement which is the average of 5 measurements. The sample size is not larger due to the sparse nature of the skyrmions in sample 1. The skyrmions 'naturally' supported by the sample are first stablised in an applied out-of-plane field of -50 mT with a diameter around 165 nm, with the skyrmion size decreasing with increasing applied field to around 155 nm at -80 mT, this trend matches that observed in similar studies [22].

6.3.2 Grain size analysis

The grain size was measured for the Ir/Co/Pt trilayer sample studied in chapter 4. This trilayer sample was grown in the same sputtering machine, under the same deposition conditions and on the same substrate as sample 1. It is therefore expected that the grain distribution of the single trilayer is representative of sample 1 [23]. The grain size measurement is included here for two reasons: (*i*) the grain size impacts skyrmion motion [6] and (*ii*) the grain size is enlarged by FIB irradiation [24–26]. With regard to point (*i*) skyrmions are most likely to be pinned at grains which are same size as the skyrmion. It is therefore useful to compare the size of FIB enlarged grains to the distribution of grain sizes normally present in the sample to give an indication of the increased likelihood of pinning at defects.

The grain size is measured by taking multiple high resolution BF images of different areas, an example is given in Fig. 6.4(a) where the 0.5 nm pixel size limits the resolution. In BF images, as explained in section 3.6, grains which meet any Bragg condition are dark. A threshold is applied to the BF images to isolate contrast from the dark grains before the grain size is measured using the DigitalMicrograph particle analysis tool. Grains were measured from 20 images to give reasonable statistics with the size of ≈4000 grains measured. A histogram of the measured grain sizes is given in Fig. 6.4(b). From this distribution, it can be seen that most of the grains are below about 7 nm in diameter but a small amount of larger grains, up to ≈ 15 nm diameter, are also measured. The grain size distribution can be fitted to a lognormal distribution as described elsewhere [27] to estimate the mean size of the grains. The lognormal fit is provided in Fig.

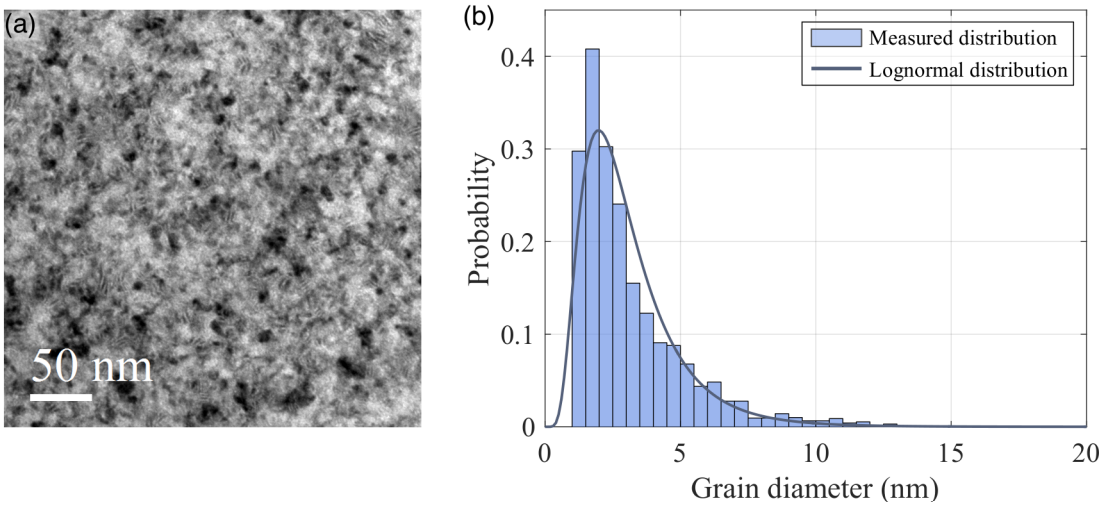

Figure 6.4: (a) a high resolution BF image showing the polycrystalline grains and (b) histogram of measured grain sizes overlaid with the best fit to a lognormal distribution which identifies a mean grain size of 3±1 nm.

6.4(b) and identified a mean grain size of 3±1 nm. This is far smaller than the ≈150 nm diameter skyrmions supported by sample 1, and even the largest grains are still an order of magnitude smaller than the skyrmion size.

6.4 Defect creation

As discussed earlier, FIB irradiation can alter the magnetic and structural properties of magnetic multilayer films. To explore this effect for skyrmion nucleation, FIB defects were made using a FEI Nova NanoLab 200 scanning electron microscope (SEM) and FIB with a 30 keV Ga^+ beam energy and beam current of 10 pA - giving an ion beam diameter of around 10 nm. This diameter is defined as the FWHM, but it should be noted the probe has tails that extend a larger distance [20]. A wide range of defects were made on sample 1 with the geometry shown in Fig. 6.5. The irradiation was controlled with the dwell time T and number of passes n to deliver doses between 10^{14} and 10^{18} ions/cm^2. The dose is not provided by the microscope but calculated from known parameters using the formula:

$$dose = \frac{JTn}{Q_{ion}A_{beam}} \tag{6.1}$$

where J is the beam current, Q_{ion} is the charge of the ions and A_{beam} is the area

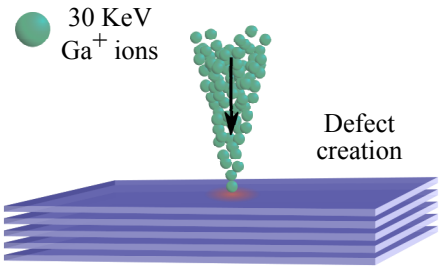

Figure 6.5: Schematic of the geometry of fabricating point-like defects with a Ga^+ focussed ion beam.

of the ion beam. Three methods of creating point-like defects with the FIB were trialled, two using in-built patterning routines (the line tool and the circle tool) and one using stream files. As described in section 3.4.2 a stream file is a user created list of dwell times and beam coordinates which precisely defines the beam scan path - in this case the stream file contains only one line, defining precisely one point of irradiation. The line tool was set to irradiate a 10 nm line and the circle tool was set to irradiate a 10 nm diameter circle. SEM images of defects created with the three methods are shown in Fig. 6.6. The defects were created with (a) a stream file, (b) the line tool and (c) the circle tool. All defects were calculated to have a dose of 1×10^{18} ions/cm^2, however there are stark differences between the SEM

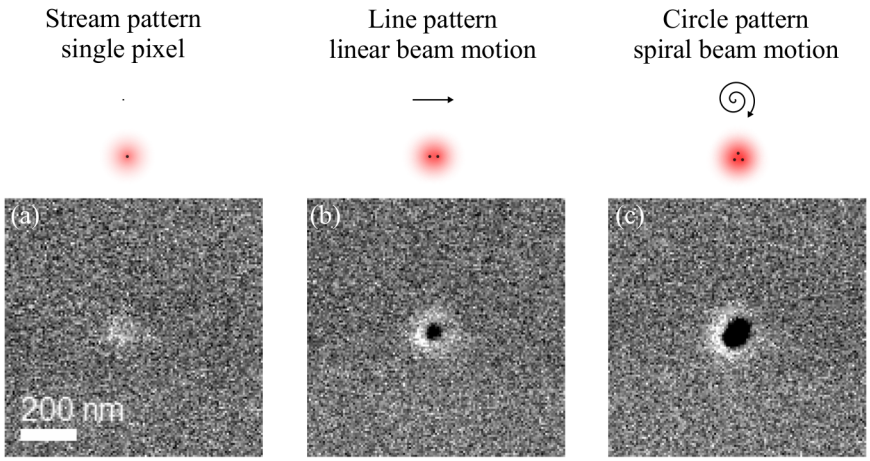

Figure 6.6: SEM images of point defects created with different methods on the FIB with identical beam current, dwell time and number of passes: (a) irradation of a single point with a stream file, (b) 10 nm line with in-built line tool and (c) 10 nm diameter circle with in-built circle tool. The 'notational' dose of each defect is 1×10^{18} ions/cm^2, but clearly the sample is receiving different ion doses with each method.

images of the defects. In (a) the central lighter area indicates visible influence of the ion irradiation on the sample, while the black region in both (b) and (c) indicates that a hole has been milled through both the multilayer and the substrate.

The line tool moves the ion beam linearly along the path defined (here 10 nm) with an inherent beam overlap of 50%. Similarly, the circle tool moves the ion beam in a spiral motion over the circular area specified by the user. The intent of the beam overlap is to deliver constant dose over the pattern despite the Gaussian shape of the beam. The full width half maximum of the 10 pA beam used here is 10 nm and it is thought that the discrepancies shown in Fig. 6.6 occur when attempting to make point-like defects about the size of the beam diameter. It appears that even though one beam position would be sufficient for such small patterns, the microscope moves the beam to multiple spots within the small pattern following the predesignated linear or spiral motion resulting in a higher local 'effective' dose than intended. This idea is sketched above the SEM images in Fig. 6.6 where the diffuse red dot represents the ion beam and the black dot shows its centre. The difference in opacity of the graphics represents the unintended higher 'effective' dose caused by beam overlap. To give context on the magnitude of the discrepancy in delivered dose discussed in this section, using the procedure in Fig. 6.6(a) (with no beam overlap and therefore unambiguous determination of dose) a 70 nm diameter hole is milled with a dose of 5×10^{18} ions/cm^2. This is compared to the 60 and 110 nm diameter holes milled with the procedures in Fig. 6.6(b, c) respectively with a notational ion dose of 1×10^{18} ions/cm^2. Possibly this effect could be mitigated by overwriting the default beam overlap parameter. However, to be sure of the dose we have supplied to the sample, unless otherwise stated, all defects were created using the stream file method.

6.5 Structural impact of defects

The structural impact of the defects on sample 1 was studied in both plan view, with bright field (BF) images, and in cross-section, with high angle annular dark field (HAADF) images. For the plan view study, point-like defects were made on the

electron transparent window. Conversely, for the cross-sectional study, line defects (fabricated with a stream file) were made on the thicker Si frame of the sample. A cross-sectional electron transparent lamella was prepared from this region using a Xe^+ plasma FIB. To protect the sample from damage during the fabrication process, the region was first coated with carbonaceous gold and platinum.

A selection of BF and HAADF images from defect sites made with different ion dose are shown in Fig. 6.7. The left column of Fig. 6.7 shows the BF images in which the granular structure of the polycrystalline sample is visible. The right column shows the HAADF images in which the discrete layer structure of the sample is visible. As discussed in section 3.6, HAADF imaging is essentially atomic number Z imaging, where brighter image contrast corresponds to a higher Z material, hence in these images, in the area corresponding to the multilayer, Ir and Pt are bright (Z=77,78 respectively) and Co is dark (Z=27). Each row of the figure relates to a different dose. The top row shows the sample without any defect and the bottom shows a defect created with a dose of 1×10^{17} ions/cm^2. The orange arrows and lines are provided to guide the eye to the centre of the defect in both the BF and HAADF images.

A defect of dose 1×10^{16} ions/cm^2 is shown in the second row of images, Fig. 6.7(c,d). With comparision to Fig. 6.7(b) there is little evidence of damage from this defect in the HAADF image, with each layer of the structure resolvable. The centre of the BF image shows perhaps slight grain enlargement compared to Fig. 6.7(a) - a known effect of ion irradiation on polycrystalline films [24–26] - but no grain growth outwith the normal distribution of sizes identified in section 6.3.2. The 5×10^{16} ions/cm^2 defect causes visible damage to the layer structure, Fig. 6.7(f); there is intermixing of the layers in a 'u'-shape extending to a diameter 70 nm in the top layers and to a depth of 7 layers at the centre of the defect. The corresponding BF image shows similar grain growth to the 1×10^{16} ions/cm^2 defect; the largest grain at the defect region was measured to have a diameter $\approx$ 20 nm which is only slightly outside the size range expected from this sample per section 6.3.2. There is a considerable area of grain enlargement associated with the 1×10^{17}

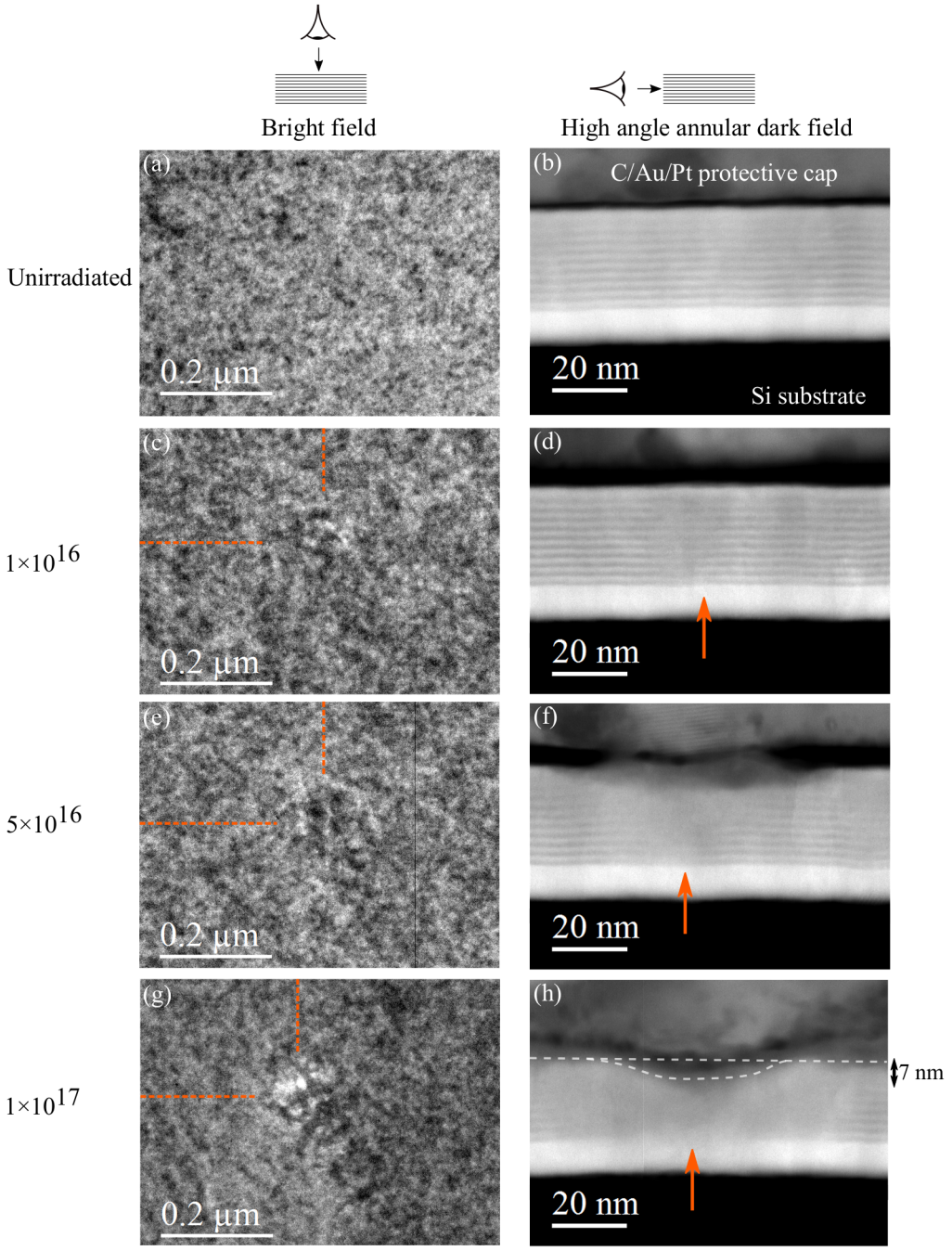

Figure 6.7: Bright field (BF) images sample in plan view - looking straight down on the sample - in the left hand column (a,c,e,g), and high angle annular dark field (HAADF) images of the sample in cross-section in the right hand column (b,d,f,h). The top row shows the sample without defects, the images in the second row show defects created with ion dose of 1×10^{16} ions/cm^2, third row with 5×10^{16} ions/cm^2, and bottom row with ion dose of 1×10^{17} ions/cm^2. The orange lines on the BF images and arrows on the HAADF images are to guide the eye to the centre of the defect. The HAADF image of the highest dose shows signs of milling - as annotated in (h) about 7 nm of the multilayer has been removed.

ions/cm^2 defect, Fig. 6.7(g,h), and the layer structure has been fully erased over a diameter of 80 nm - additionally this defect causes milling ≈ 7 nm into the sample, judging by the infill of the protective layers as marked on the image. It is noted that defects smaller than 10^{16} ions/cm^2 showed no visible signs of damage when judged by the grain size and the uniformity of the layer structure. Defects created with doses larger than 10^{18} ions/cm^2 resulted in clearly defined holes through the multilayer stack due to milling.

6.6 Magnetic behaviour with field after defect creation

Figure 6.8(a) shows a Fresnel image of sample 1, patterned with an array of defects created with dose between 10^{16}-10^{17} ions/cm^2. This image shows the sample in a field-free environment immediately after the sample was saturated in an out-of-plane field of ≈ 2 T. Strikingly in Fig. 6.8(a) single skyrmions can be observed at the defect sites in a zero field environment at room temperature. Compared to the spot defects in Fig. 6.5 these are extended defects (created using the circle tool), purposed in this section for two reasons: to demonstrate the separation of non-magnetic defect contrast and magnetic skyrmion contrast; and to evaluate the relationship between defect size and skyrmion size. Figures 6.8(b) and (c)

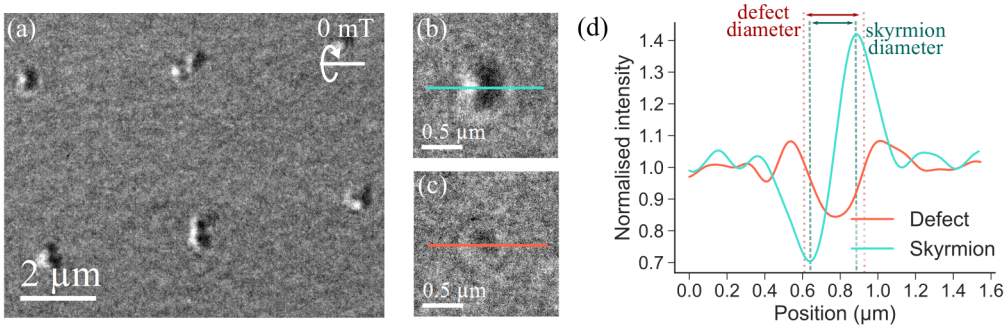

Figure 6.8: (a) Fresnel image of sample 1 after defect creation with circle pattern tool on FIB, imaged in a field free environment - skyrmions are clearly visible at most defect sites. (b) enlarged image of a defect with skyrmion for comparison with (c) enlarged image of a saturated defect. Line trace in (d) indicates the distinction between a skyrmion and defect is easily made and shows the skyrmion to be ≈ 250 nm in diameter and the defect 300 nm. All Fresnel images taken with sample tilt of 20° about the axis indicated.

illustrate the contrast from a defect site with and without a skyrmion respectively. The changed physical structure of the defect results in non-magnetic image contrast even after the skyrmion has been removed (by saturating the defect site) as shown in Fig. 6.8(c). The line traces taken from the defects are shown in Fig. 6.8(d), these indicate that the contrast from a saturated defect site is symmetric compared to a defect site with a skyrmion. Moreover, as shown in Fig. 6.2, because the magnetic contrast is generated by the sample tilt (here +20°), any magnetic contrast will reverse with tilt, i.e. at -20° black becomes white and vice versa. Therefore, in ambiguous cases (as shown later), to help separate the magnetic and non-magnetic contrast the tilt angle can be reversed.

The diameter of the skyrmion in Fig. 6.8(b) is 250 nm and the defect size is 300 nm. Figure. 6.8(a) shows part of the array of defects, when averaged over all nucleated skyrmions in the array the average skyrmion size at zero applied field is 300 ± 10 nm. Similarly, the average defect size is 250 ± 30 nm. This skyrmion diameter is outwith the distribution of sizes presented in Fig. 6.3 which was between 150 nm and 170 nm. The skyrmion diameter depends on the strength of the applied field - the diameter is larger in a smaller applied field - therefore, it is not surprising that the diameter of these zero field skyrmions is larger than measured in section 6.3.1. Alternatively, this discrepancy may suggest that the skyrmion size is linked to the defect size which in this case is similarly large - this will be revisited in section 6.6.1.

To be technologically advantageous the defects should cause a minimal increase to the depinning current required to move a skyrmion from the defect site. Whilst this is not studied here directly, it is known that local changes in anisotropy increase the pinning field [6], and that higher ion doses cause a larger modification of the anisotropy [15–19]. The enlargement of the grains is thought less likely to be problematic as a previous study identifies the most severe pinning for grain sizes which are the same size as the skyrmions [6] and the FIB enlarged grains are still an order of magnitude smaller than the skyrmions. Hence, the lowest dose required to cause low field, room temperature nucleation was determined though

a systematic study of the magnetic response of defects created with dose spanning from 10^{14} to 10^{18} ions/cm^2. This was repeated on all four samples introduced in section 6.2. For this set of experiments, all defects were created using the stream file method to ensure the dose is accurately known and that defects are laterally as small as possible.

Figure 6.9 summarises the results of this experiment on sample 1. A sequence of Fresnel images are shown in Fig. 6.9(a-c). Fig. 6.9(a) shows the sample just after saturation in a field of 90 mT, where any non-magnetic contrast associated with the defects is visible. The field of view of Figs. 6.9(a-c) includes five doses vertically, ranging from 5×10^{16} ions/cm^2 at the top to 5×10^{18} ions/cm^2 at the bottom - the three highest dose defects show clear non-magnetic contrast, there is little evidence of the defects made with the two lowest doses. Horizontally, there are five repeats of each dose. After saturation, the applied field was reduced steadily and the changes in magnetisation monitored. Figure 6.9(b) shows the sample in a

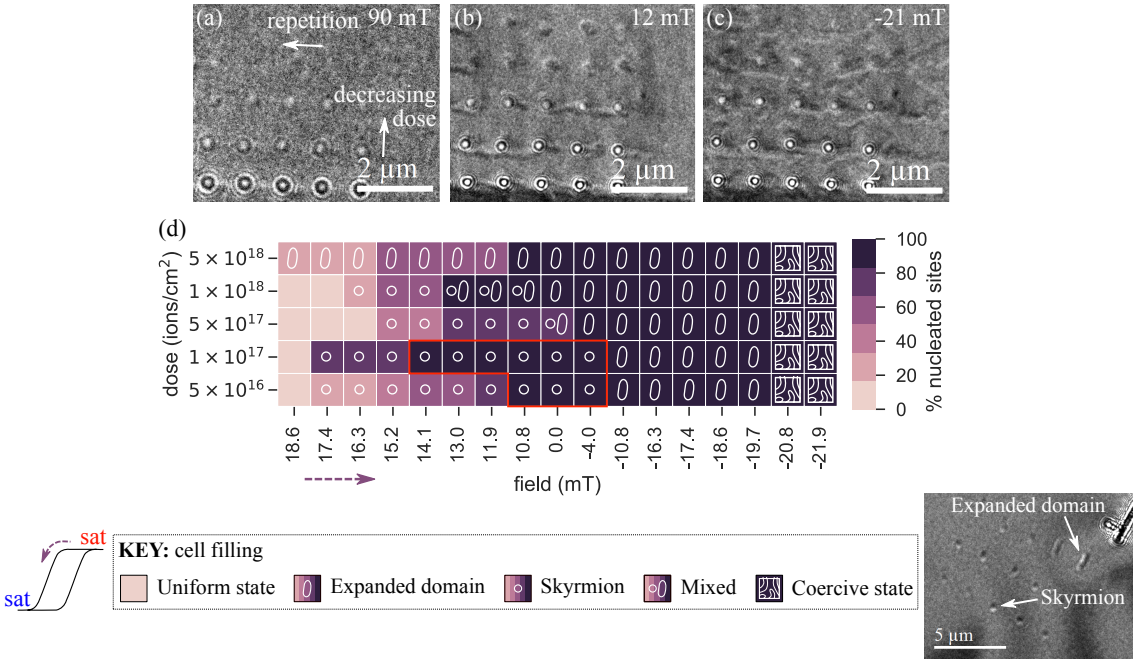

Figure 6.9: (a-c) Fresnel images showing defects on sample 1 in (a) a saturated state, (b) a 12 mT field and (c) near the coercive state. (d) Chart presenting the detailed behaviour of defect sites as a function of ion dose and applied field on sample 1. This chart is explained by the colourbar and key. Squares outlined in red highlight the most interesting parts of the chart that have 100% skyrmion nucleation. The Fresnel image (from sample 2) provides examples of the different magnetic states in the key.

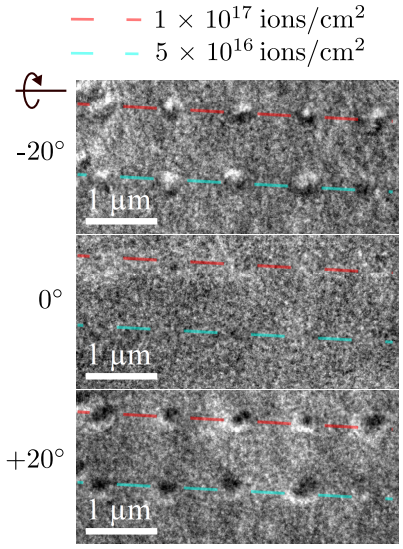

Figure 6.10: A tilt sequence of Fresnel images taken of low dose defects made on sample 1. The circular contrast that reverses at ± tilts and lack of magnetic contrast at zero tilt is consistent with Néel skyrmions.

12 mT field, where the two lowest dose defect sites (the top two rows) are occupied by skyrmions. The magnetic contrast is not strong in these images, therefore to aid interpretation the tilt was varied between +20°, 0° and -20°. These images are shown in Fig. 6.10, where it is clearer that the contrast matches that expected from Néel type skyrmions (as simulated in 6.2).

Figure 6.9(d) contains a chart which summarises the behaviour of the defect sites with field. Note that the field scale is not linear between ± 10.8 mT because the objective lens field cannot be varied smoothly between these values. To image between ± 10.8 mT the sample must be removed and the objective lens field set manually with a Hall probe. The colour of the box indicates what percentage of the defect sites (of a given dose) have a magnetic object local to them - the lightest colour means none of the five, 0%, defect sites have any magnetic object local to them where the darkest colour means five of the five, 100%, defect sites have a magnetic object local to them. The icon inset on each square indicates the nature of the magnetic object local to the defect: a circle indicates all occupied sites have skyrmions; a bean shape indicates all occupied sites have expanded domains; both a circle and bean indicate a mixture of the above; and the maze icon indicates the sample is in a state close to remanence with labyrinth domains (as in Fig. 6.9(c)),

where it is meaningless to evaluate the behaviour local to the defect sites. The description 'expanded domain' refers to a chiral bubble that has an extended size, only compact magnetic objects have been identified as skyrmions - examples of both are marked in the Fresnel image to the right of the key. Expanded domains are also present, together with skyrmions, in the Fresnel image in Fig. 6.1(b) which shows sample 1, unmodified, in a field of -80 mT. To be clear, objects are classified as skyrmions if they are circular with simple bright-dark contrast, where, alternatively, structures are classified as expanded domains if they are associated with either a more complex contrast distribution or are elongated. Hence the areas of most interest (outlined in red) are those with a circle on a dark background, indicating all defect sites with that dose have stabilised skyrmions, i.e. 100% success rate of skyrmion nucleation.

Figure 6.11 shows the results of the experiment repeated on sample 2. Fresnel images are shown in Fig. 6.11(a-c) with (a) showing the sample in a saturated state indicating that these defects, made with dose between 5×10^{15} and 5×10^{16}

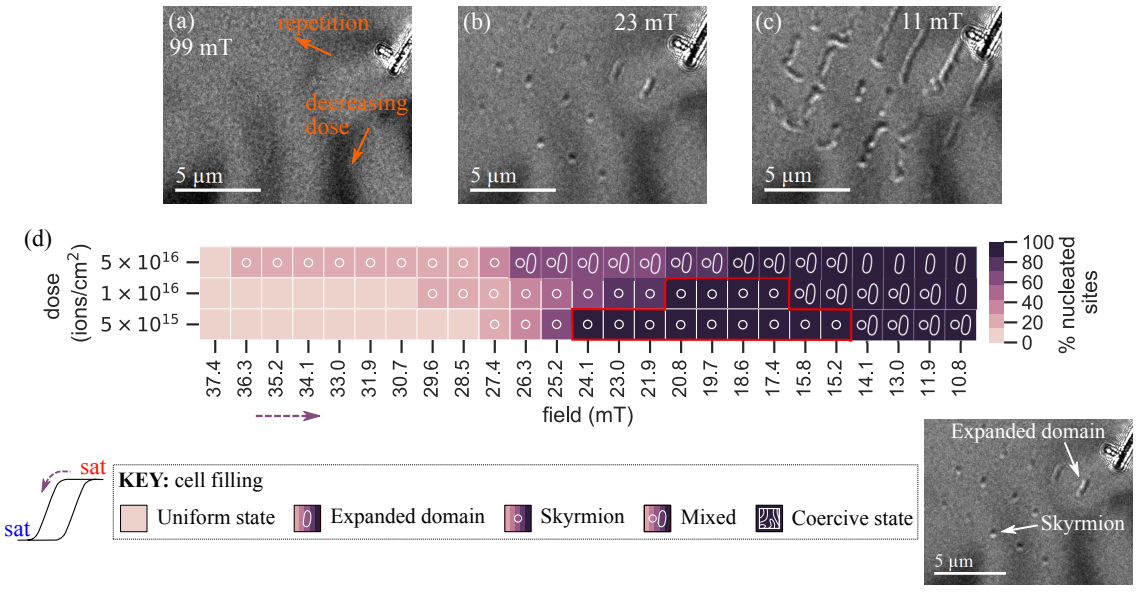

Figure 6.11: (a-c) Fresnel images showing defects on sample 2 in (a) a saturated state, (b) a 23 mT field and (c) a 11 mT field where all skyrmions have expanded. (d) Chart presenting the detailed behaviour of defect sites as a function of ion dose and applied field on sample 2. This chart is explained by the colourbar and key. Squares outlined in red highlight the most interesting parts of the chart that have 100% skyrmion nucleation. The Fresnel image provides examples of the different magnetic states in the key.

ions/cm^2, are not associated with any non-magnetic contrast. After saturation the strength of the out-of-plane field was reduced, Fig. 6.11(b) shows the sample in a 23 mT out-of-plane field where compact skyrmions are visible at many of the defect sites. Figure 6.11(c) shows the sample in an 11 mT out-of-plane field where almost all of the initially compact skyrmions have expanded into elongated domains. The chart in Fig. 6.11(d) shows a summary of the magnetic response of the defects in sample 2 with out-of-plane field as it is reduced from saturation to $\approx$ 10 mT. The key is the same as for Fig. 6.9(e). Like sample 1, there are combinations of defect dose and applied field that result in 100% skyrmions nucleation for sample 2; these are highlighted by the areas of the chart outlined in red. Unlike sample 1, the nucleated skyrmions do not remain stable in zero applied field. As is seen in Fig. 6.11(c), they are unstable and expand into larger domains as is expected from a sample with low remanence. This result is particularly interesting as these artificial defects have resulted in skyrmion stabilisation in a material system that, as detailed in 6.3.1, did not previously support skyrmions on field-cycling alone.

Samples 3 and 4 do not show the same behaviour as samples 1 and 2. The results of the experiments are shown in Figs. 6.12 and 6.13 which are structured in the same way as Fig. 6.11, with Fresnel images in (a-c) and a detailed chart in (d). On both samples, defects made with 5×10^{17} ions/cm^2 show consistent early nucleation of domains - with domain formation starting $\approx$ 50 mT earlier local to the defect sites than on the unmodified film for both samples. Unlike samples 1 and 2, there is no combination of applied field and defect dose that causes 100% skyrmion nucleation - the skyrmions exhibit the same behaviour as in the unmodified film: they nucleate and immediately expand to worm-like domains as seen in Figs. 6.12(b) and 6.13(b).

This study proves that it is possible to reproducibly nucleate skyrmions local to FIB defects in zero field at room temperature in samples with a hysteresis loop tuned to have high remanence - like sample 1. Furthermore, it shows these artificial defects can stabilise skyrmions in materials that support homochiral walls but do not 'naturally' support skyrmions - like sample 2. Table 6.3 provides details of the

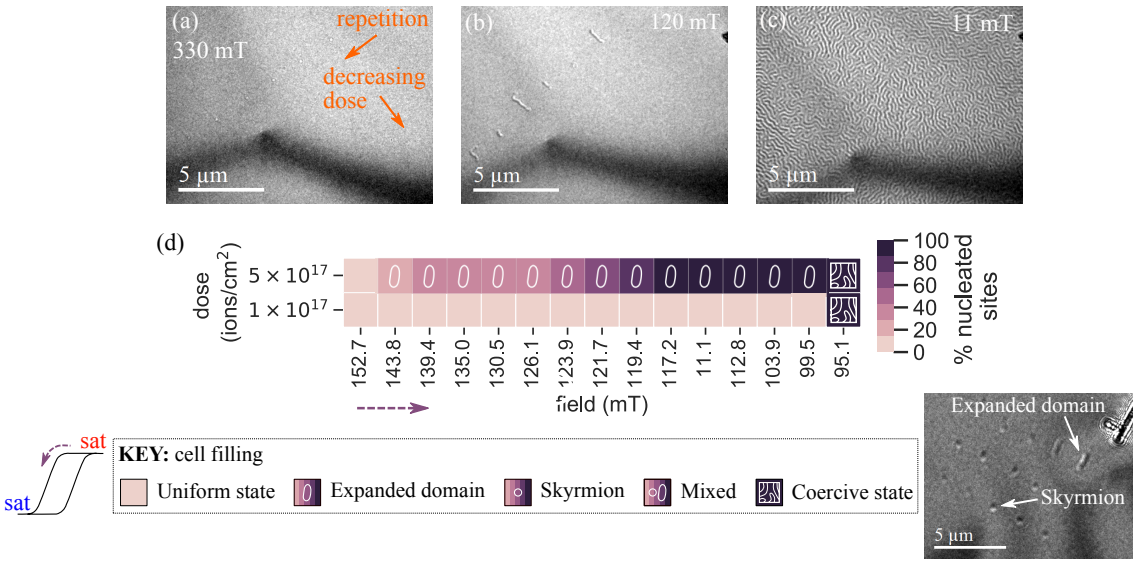

Figure 6.12: (a-c) Fresnel images showing defects on sample 3 in (a) a saturated state, (b) a 120 mT field and (c) a coercive state. (d) Chart presenting the detailed behaviour of defect sites as a function of ion dose and applied field on sample 3. This chart is explained by the colourbar and key. Squares outlined in red highlight the most interesting parts of the chart that have 100% skyrmion nucleation. The Fresnel image (from sample 2) provides examples of the different magnetic states in the key.

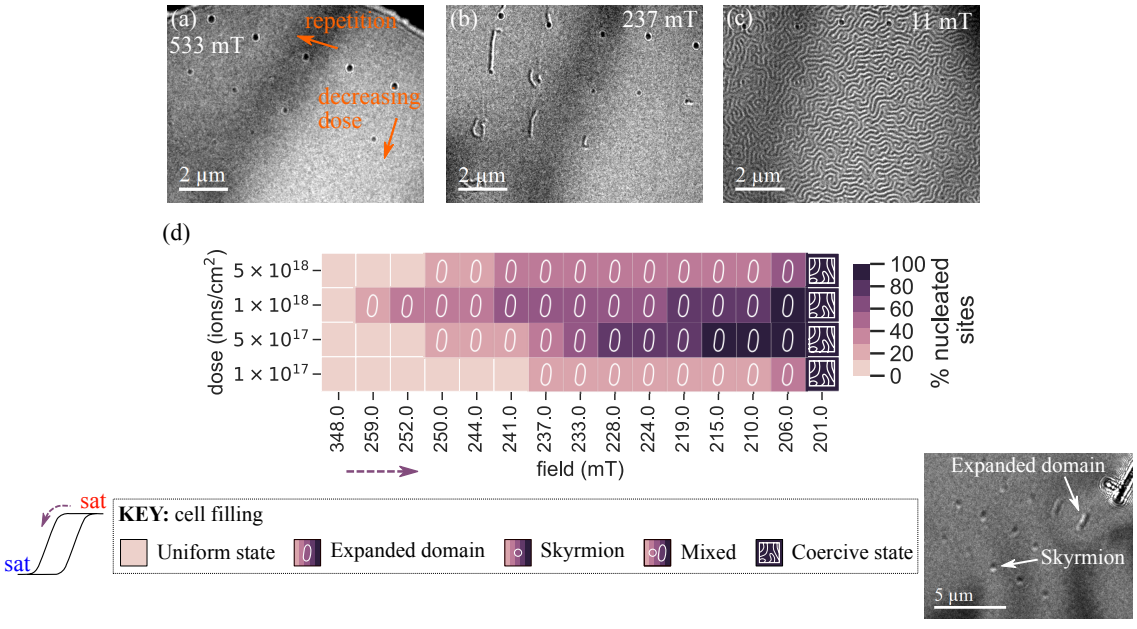

Figure 6.13: (a-c) Fresnel images showing defects on sample 4 in (a) a saturated state, (b) a 237 mT field and (c) a coercive state. (d) Chart presenting the detailed behaviour of defect sites as a function of ion dose and applied field on sample 4. This chart is explained by the colourbar and key. Squares outlined in red highlight the most interesting parts of the chart that have 100% skyrmion nucleation. The Fresnel image (from sample 2) provides examples of the different magnetic states in the key.

Table 6.3: Summary of artificial defect types that cause 100% skyrmion nucleation at room temperature - detailed is the dose associated with each successful defect and field range over which the nucleated skyrmions remain stable.

Sample	Defect dose (ions/cm^2)	Range of stability (mT)
1	5×10^{16}	10.8 to -4.0
1	1×10^{17}	14.1 to -4.0
2	5×10^{15}	24.1 to 15.8
2	1×10^{16}	20.8 to 17.4

'ideal' artificial defects found to cause 100% skyrmion nucleation in samples 1 and 2. The dose required to nucleate skyrmions is an order of magnitude smaller for sample 2 compared to sample 1 - demonstrating the extreme sensitivity of this nucleation method to the sample structure. As seen in the cross-sectional images presented in Fig. 6.7(f,h), the energy imparted in the sample by the ions causes damage and intermixing of the multilayer structure: alloying the multilayer. Given the different elemental composition of the two multilayer stacks studied, the magnetic properties of the resulting alloy are certainly different. For example, an older study [28] characterises the magnetisation of binary alloys of Co and various transition metals. It shows that the magnetisation of Co is more sensitive to alloying with Ru than either Ir or Pt - giving a possible explanation for the greater sensitivity of sample 2 to ion dose than sample 1.

6.6.1 Skyrmion size evolution with field

The size of the skyrmions stabilised over the range of doses and field presented in table 6.3 was analysed in the same way as in section 6.3.1. The results of this analysis are presented in Fig. 6.14, where Fig. 6.14(a) pertains to sample 1 and (b) to sample 2. Each measurement is an average of the skyrmion sizes measured from all five defect sites of the same dose and the error bar is the standard error.

Before defect creation, section 6.3.1 shows that sample 1 supported skyrmions with mean diameter between $\approx$ 150 and 170 nm over the field range -50 to -80 mT, after passing through the coercive state and just before saturation. It has been shown that skyrmions can be stabilised at artificial defect sites in lower applied

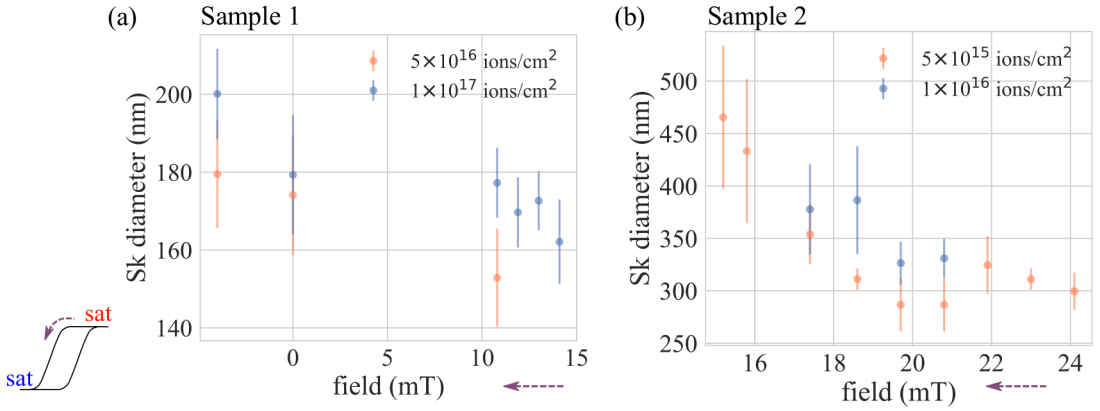

Figure 6.14: Evolution of the size of the skyrmions nucleated at the artificial defect sites with applied field for (a) sample 1 and (b) sample 2.

fields before the coercive state is reached. On sample 1, these skyrmions are stable in the field range 15 mT to -4 mT. Figure 6.14(a) shows that at defect sites of dose 1×10^{17} ions/cm^2, when the skyrmions first nucleate at 15 mT, the mean skyrmion diameter is $\approx$ 160 nm which increases steadily to $\approx$ 180 mT in a field of 10 mT. There is a gap in the graph between $\approx$ 10 mT and 0 mT because, as explained above in reference to Fig. 6.9(e), sample must be removed and the field strength set manually for each measurement between $\pm$ 10.8 mT. At 0 mT the mean skyrmion size is 180 nm, increasing to 200 nm at -4.0 mT. The mean skyrmion size at the 5×10^{16} ions/cm^2 defects increases from 155 nm at 10.8 mT to 180 nm at -4.0 mT. The mean skyrmion size at the higher dose defects is always larger than the skyrmion size measured at the lower dose defects, however the two sizes are almost always within the measured error of one another.

Prior to defect creation, no skyrmions were observed in sample 2: while increasing the applied field strength towards saturation the domains narrowed into long worm-like domains then disappeared with no intermediate skyrmion state observed. As detailed earlier in this section, compact skyrmions can be stabilised at artificial defect sites created with ion doses of 5×10^{15} and 1×10^{16} ions/cm^2 between fields of $\approx$ 25 mT and 15 mT in sample 2. For 5×10^{15} ions/cm^2 defects, skyrmions are first nucleated at 24.1 mT with a mean diameter of 300 nm, this increases to $\approx$ 560 nm at 15.2 mT. Similarly, at the 1×10^{16} ions/cm^2 defects skyrmions

are first nucleated at 20.8 mT with a mean diameter of ≈ 330 nm, increasing to ≈ 400 nm at 17.4 mT.

From Fig. 6.8, at defects made with the circle pattern rather than with stream files, a mean skyrmion size of 300 nm was measured at zero field and room temperature. It was remarked that this skyrmion size was outwith the range of sizes presented in Fig. 6.3 and two possible reasons for this were given: that the skyrmion size may be this large in zero applied field because the skyrmion diameter depends on the strength of the applied field or that the skyrmion size is linked to the defect size. All defects analysed in this section were made using stream files and the mean size of skyrmions measured at zero field is ≈ 175 nm. This diameter is more in keeping with the 'inherent' skyrmion size measured from the sample before defects were created, this size is controlled by the material parameters such as: the strength of the DMI, the anisotropy, the exchange stiffness and the saturation magnetisation of the material [29]. Although not the focus of the experiments (and therefore there is limited data), it does seem that defects larger than the inherent skyrmion size stabilise artificially large skyrmions. For example, Fig. 6.8 shows a 300 nm diameter defect stabilising a 250 nm diameter skyrmion, this is compared to the HAADF images in 6.7(f, h), of the 5×10^{16} and 1×10^{17} ions/cm^2 stream file defects which have diameters 70 nm and 80 nm respectively and both stabilise mean skyrmion diameters of ≈ 175 nm. Further evidence in support of this conclusion is the larger difference in diameter of skyrmions measured from sample 2 compared to sample 1. The ion dose required to make defects that cause successful skyrmion nucleation in sample 2 is an order of magnitude smaller than for sample 1. The images of these defects in sample 2 show no visible non-magnetic phase contrast, like presented in the Fresnel image in Fig. 6.8(c), or obvious grain growth, like shown in the BF images in Figs. 6.7(c,e,g). Consequently, although not measured, the lateral size of the defects is almost certainly smaller than measured for sample 1 but the skyrmions are larger. This offers additional evidence that for small defects the skyrmion size is determined by the sample properties and not the defect itself.

6.7 DPC of a skyrmion at an artificial defect site

Using a pixelated detector to reduce the extraneous polycrystalline contrast, DPC images were taken of sample 1 which allows measurement of the saturation induction B_s of the film near a defect. As explained in section 3.7.4, DPC is a quantitative imaging method that directly measures the beam deflection β_L.

Before introducing the experimental images, to aid interpretation, calculated DPC images of a Néel type skyrmion are presented in Fig. 6.15 in analogy to Fig. 6.2. As discussed frequently in this thesis, perpendicularly magnetised materials

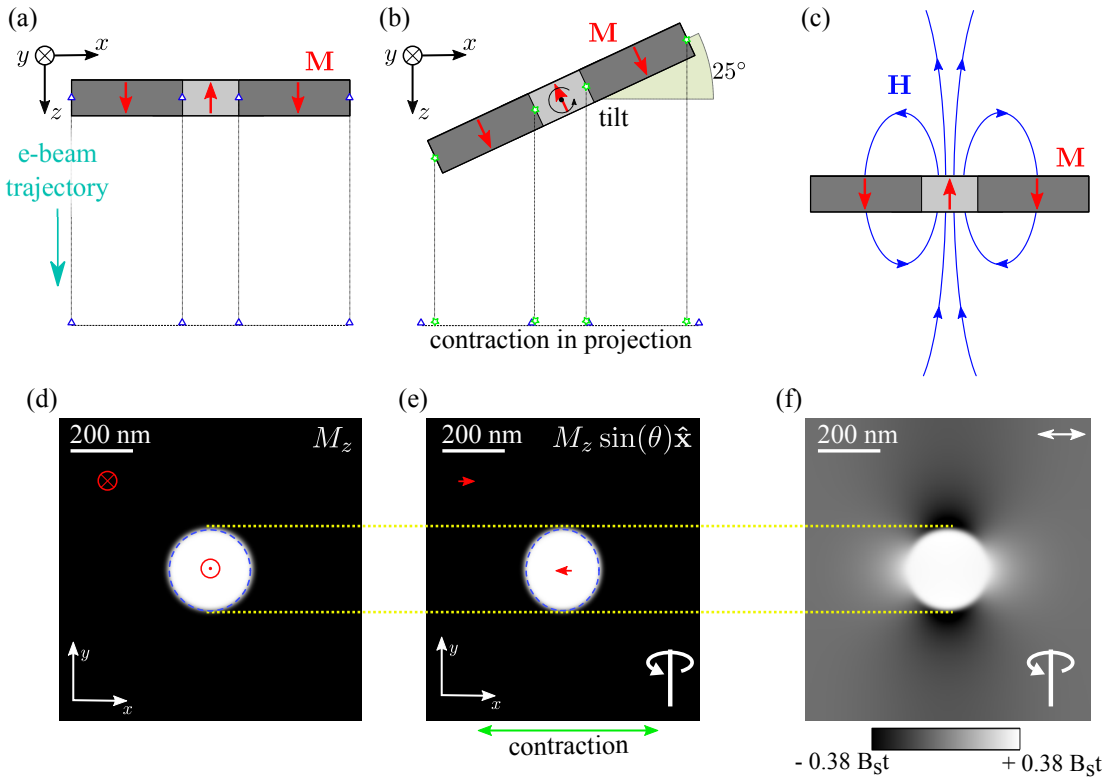

Figure 6.15: (a) geometry of skyrmion sample (depicted in cross-section) in a TEM at normal incidence to the electrons travelling along the $+\hat{z}$ direction. (b) geometry of skyrmion sample tilted by 25° around an axis along y direction: the object is contracted in the x direction when projected back onto the xy plane (i.e. when forming an image on a detector in the TEM). (c) a skyrmion is associated with a dipole-like **B** field consisting of the magnetisation **M** and the stray field **H**. Consider (d) the M_z of a skyrmion, when tilted and projected onto the xy plane, a component $\sin(\theta)$ of M_z is projected onto the xy plane and the shape is distorted to an ellipse (e). (f) DPC images **B** and, at the skyrmion and parallel to the tilt axis, **H** and **M** cancel significantly leading to an exaggerated elliptical shape. Note that the ellipse in (e) is not seen in (f) which appears elliptical in an orthogonal direction.

with Néel type objects must be tilted to produce any contrast in Lorentz microscopy images. Both the sensitivity of Lorentz microscopy to **B** (not **M**) and the necessity to tilt, leads to elliptical contrast from a circular Néel skyrmion in DPC images. Figures 6.15(a) and (b) depict the geometry of a skyrmion containing sample (in cross-section) in the TEM both in untilted and tilted positions respectively, where the electrons travel along $+\hat{\mathbf{z}}$. Tilting the structure and projecting back on the xy plane (i.e. a detector in the microscope) leads to contraction of the object in the direction perpendicular to the tilt axis. For a circular skyrmion, represented only by its M_z component (Fig. 6.15(d)), this results in elliptical shaped magnetisation that corresponds to the skyrmion, see Fig. 6.15(e). As denoted by the red arrows in 6.15(e), a component $\sin(\theta)$ of the original sample M_z is projected in the xy plane of the microscope. The skyrmion is associated with a stray field **H** as well as magnetisation **M**, as sketched in Fig. 6.15(c). DPC images are then this dipole-like **B** ($= \mu_0(\mathbf{M} + \mathbf{H})$) field projected through the sample thickness onto the xy plane. The **H** field cancels much of the **M** sketched in Fig. 6.15(e), preferentially reducing the DPC contrast perpendicular to the tilt axis again leading to elliptical contrast. Note that sense of ellipticity in 6.15(f) is orthogonal to the ellipticity caused by contraction. Parallel to the tilt axis the skyrmion size is undistorted (as highlighted by the yellow dashed line).

The DPC image calculation was designed to accurately represent the experimental conditions. It uses the same M_z component for the image calculation as was used for Fig. 6.2. The image calculation is, however, of a perfect system with no sources of contrast other than the smoothly varying magnetisation. The real samples are polycrystalline, therefore experimental DPC images also contain shorter-range electrostatic grain contrast as well as contrast from the skyrmion.

If one were to ignore the effect of the stray field (i.e. assuming the contrast only arises from the magnetisation in the sample), the difference between the maximum and minimum values in the DPC image (which occur parallel to the tilt axis) would correspond to $2B_s t \tan(\theta)$ where $B_s = \mu_0 M_s$. For a tilt of 24.6°, this is 0.92 $B_s t$. In the simulation, where the effects of the stray field are properly accounted for,

the difference between the maximum and minimum values in the DPC image is measured as 0.76 $B_s t$. Therefore, in order to extract B_s (and M_s) experimentally we apply a stray-field-compensating scaling factor of (0.76/0.92 =) 0.83 to the experimental measurements[1]. In conclusion, three things should be understood: (*i*) DPC images of perfectly circularly symmetric skyrmions have elliptical contrast; in the direction perpendicular to the tilt axis, (*ii*) the skyrmion diameter can be measured, (*iii*) as can M_s (assuming the sample thickness is known).

Figure 6.16(a) shows a DPC image of a $5{\times}10^{16}$ ions/cm^2 defect site on sample 1 in a field of 10 mT taken with a sample tilt of 24.6°. The lighter area in the centre of the image is a skyrmion, measured to have diameter 150 nm; this experimental DPC image has significant background undulations arising from the crystallites but otherwise matches Fig. 6.15(f) well. A white circle, diameter 70 nm, is overlaid at the position of the defect with size matching the area of physical damage associated with this dose, as identified from Fig. 6.7(f). A line trace was taken from the area marked in Fig. 6.16(a), near to the defect, and is shown next to the DPC image. By fitting a hyperbolic tangent function to this line trace (the dotted line in Fig. 6.16(b)), the deflection due to the domains was determined as 1.7±0.2 μrad. From this B_s was calculated, using the procedure detailed above, to be 1.2±0.1 T. This is compared to magnetometry measurements, performed by Katharina Zeissler of

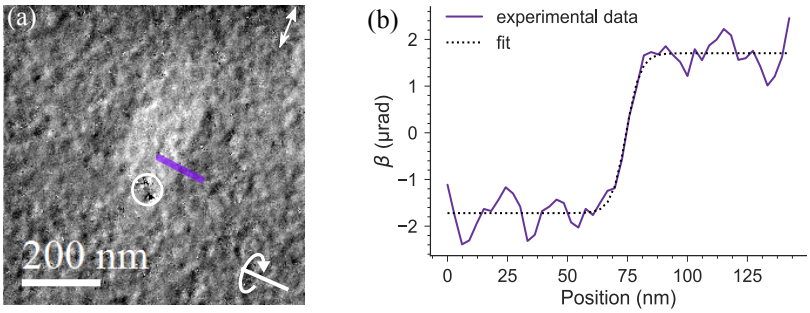

Figure 6.16: (a) DPC image of sample 1, tilted by ≈ 25 ° about the axis indicate, with a 150 nm skyrmion nucleated at a 5 × 10^{16} ions/cm^2 defect site. The circle gives the size and position of the defect and the line shows where the line trace (b) was taken from. The line trace was averaged over 15 pixels.

[1]Note that such a correction is not needed in the case of long domain walls such as those encountered in chapter 5.

the University of Leeds, on the sample before irradiation which measured M_s as 1.0±0.1 MAm^{-1} - equivalent to 1.2±0.1 T. This quantitative analysis suggests that the defect has caused skyrmion nucleation in all layers, and not just in the surface layers most impacted by the irradiation.

6.8 Discussion and conclusion

This chapter demonstrates that nanoscale artificial defects (created with FIB irradiation) can be used to nucleate isolated, single skyrmions in polycrystalline magnetic multilayer systems at room temperature in low, even zero, applied magnetic field. This effect was studied in four multilayer systems with different layer structures. As detailed in table 6.3, compact skyrmions are consistently nucleated in sample 1 at defects fabricated with ion dose 5×10^{16} and 1×10^{17} ions/cm^2 which remain stable over a field range including zero; sample 2 stabilises compact skyrmions at defects created with dose 5×10^{15} and 1×10^{16} ions/cm^2 although a bias field is required. Sample 1 has a higher magnetic remanence of almost M_s, compared to sample 2 which has a remanence close to zero; high remanence is vital to retaining compact skyrmions at zero applied field. As observed in sample 2, these artificial defects can even stabilise skyrmions in samples with lower DMI strength that naturally support homochiral Néel walls but never stabilise skyrmions on field cycling alone. The method was unsuccessful for samples 3 and 4. Here the defects nucleate unstable skyrmions which quickly expand into worm-like domains - the same behaviour observed in the unmodified films, albeit at an earlier point in the hysteresis loop.

From the observations made, the size of the nucleated skyrmions appears uninfluenced by the defect itself so long as it is smaller than the inherent skyrmion size. The skyrmion size in a multilayer system is determined by the interplay of various magnetic energy terms controlled by: the strength of the DMI, the anisotropy, the exchange stiffness and the saturation magnetisation of the material [29]. Hence, even though the skyrmions observed in this study are larger than 100 nm, we expect this nucleation method to successfully nucleate technologically relevant sub-100 nm skyrmions in an optimised material system. To this end it must be mentioned that

it is possible to create smaller FIB defect sites; for example, this work used a 30 keV, 10 pA focused Ga^+ beam which has a beam diameter of $\approx$ 10 nm but a 35 keV, 10 pA focused He^+ beam has a beam diameter an order of magnitude smaller and can mill sub-10 nm features [30, 31].

Critically, the mobility of these FIB nucleated skyrmions remains to be studied. The structural imaging of the defects, Fig. 6.7, indicates that nucleation is most successful at defects with partial layer intermixing - undoubtedly this intermixing is associated with local lowering of the perpendicular anisotropy and DMI strength as both originate from the layer interfaces. Both of these effects will likely increase the depinning field, as will the local reduction in M_s predicted by alloying [6, 28].

It is expected that new device technologies are more likely to be utilised if they mould into current fabrication methods. A relevant example is that polycrystalline systems are desirable over single crystal systems as they fit with current deposition technologies. Focused ion beam microscopes are widely used in device fabrication (for example in fabrication of semiconductor devices and disk read/write heads) hence controlled skyrmion nucleation at artificial FIB defects is certainly a promising mechanism for reproducible generation of room temperature, isolated skyrmions.

Bibliography

[1] N. Romming, C. Hanneken, M. Menzel, J. E. Bickel, B. Wolter, K. von Bergmann, A. Kubetzka, and R. Wiesendanger, "Writing and deleting single magnetic skyrmions," *Science*, vol. 341, no. 6146, pp. 636–639, 2013.

[2] J. Sampaio, V. Cros, S. Rohart, A. Thiaville, and A. Fert, "Nucleation, stability and current-induced motion of isolated magnetic skyrmions in nanostructures," *Nature Nanotechnology*, vol. 8, no. 11, pp. 839–844, 2013.

[3] J. Iwasaki, M. Mochizuki, and N. Nagaosa, "Current-induced skyrmion dynamics in constricted geometries," *Nature Nanotechnology*, vol. 8, no. 10, pp. 742–747, 2013.

[4] W. Jiang, P. Upadhyaya, W. Zhang, G. Yu, M. B. Jungfleisch, F. Y. Fradin, J. E. Pearson, Y. Tserkovnyak, K. L. Wang, O. Heinonen, S. G. Te Velthuis, and A. Hoffmann, "Blowing magnetic skyrmion bubbles," *Science*, vol. 349, no. 6245, pp. 283–286, 2015.

[5] A. Hrabec, J. Sampaio, M. Belmeguenai, I. Gross, R. Weil, S. M. Chérif, A. Stashkevich, V. Jacques, A. Thiaville, and S. Rohart, "Current-induced skyrmion generation and dynamics in symmetric bilayers," *Nature Communications*, vol. 8, p. 15765, 2017.

[6] W. Legrand, D. Maccariello, N. Reyren, K. Garcia, C. Moutafis, C. Moreau-Luchaire, S. Collin, K. Bouzehouane, V. Cros, and A. Fert, "Room-Temperature Current-Induced Generation and Motion of sub-100 nm Skyrmions," *Nano Letters*, vol. 17, no. 4, pp. 2703–2712, 2017.

[7] S. Finizio, K. Zeissler, S. Wintz, S. Mayr, T. Weßels, A. J. Huxtable, G. Burnell, C. H. Marrows, and J. Raabe, "Deterministic Field-Free Skyrmion Nucleation at a Nanoengineered Injector Device," *Nano Letters*, vol. 19, no. 10, pp. 7246–7255, 2019.

[8] T. Ogasawara, N. Iwata, Y. Murakami, H. Okamoto, and Y. Tokura, "Submicron-scale spatial feature of ultrafast photoinduced magnetization reversal in TbFeCo thin film," *Applied Physics Letters*, vol. 94, no. 16, pp. 1–4, 2009.

[9] M. Finazzi, M. Savoini, A. R. Khorsand, A. Tsukamoto, A. Itoh, L. Duò, A. Kirilyuk, T. Rasing, and M. Ezawa, "Laser-induced magnetic nanostructures with tunable topological properties," *Physical Review Letters*, vol. 110, no. 17, pp. 1–5, 2013.

[10] S. G. Je, P. Vallobra, T. Srivastava, J. C. Rojas-Sánchez, T. H. Pham, M. Hehn, G. Malinowski, C. Baraduc, S. Auffret, G. Gaudin, S. Mangin, H. Béa, and O. Boulle, "Creation of Magnetic Skyrmion Bubble Lattices by Ultrafast Laser in Ultrathin Films," *Nano Letters*, vol. 18, no. 11, pp. 7362–7371, 2018.

[11] P. J. Hsu, A. Kubetzka, A. Finco, N. Romming, K. Von Bergmann, and R. Wiesendanger, "Electric-field-driven switching of individual magnetic skyrmions," *Nature Nanotechnology*, vol. 12, no. 2, pp. 123–126, 2017.

[12] T. Srivastava, M. Schott, R. Juge, V. Kižáková, M. Belmeguenai, Y. Roussigné, A. Bernand-Mantel, L. Ranno, S. Pizzini, S. M. Chérif, A. Stashkevich, S. Auffret, O. Boulle, G. Gaudin, M. Chshiev, C. Baraduc, and H. Béa, "Large-Voltage Tuning of Dzyaloshinskii-Moriya Interactions: A Route toward Dynamic Control of Skyrmion Chirality," *Nano Letters*, vol. 18, no. 8, pp. 4871–4877, 2018.

[13] F. Büttner, I. Lemesh, M. Schneider, B. Pfau, C. M. Günther, P. Hessing, J. Geilhufe, L. Caretta, D. Engel, B. Krüger, J. Viefhaus, S. Eisebitt, and G. S. Beach, "Field-free deterministic ultrafast creation of magnetic skyrmions by spin-orbit torques," *Nature Nanotechnology*, vol. 12, no. 11, pp. 1040–1044, 2017.

[14] S. Woo, K. M. Song, X. Zhang, M. Ezawa, Y. Zhou, X. Liu, M. Weigand, S. Finizio, J. Raabe, M. C. Park, K. Y. Lee, J. W. Choi, B. C. Min, H. C. Koo, and J. Chang, "Deterministic creation and deletion of a single magnetic skyrmion observed by direct time-resolved X-ray microscopy," *Nature Electronics*, vol. 1, no. 5, pp. 288–296, 2018.

[15] C. Chappert, H. Bernas, J. Ferré, V. Kottler, J. P. Jamet, Y. Chen, E. Cambril, T. Devolder, F. Rousseaux, V. Mathet, and H. Launois, "Planar patterned magnetic media obtained by ion irradiation," *Science*, vol. 280, no. 5371, pp. 1919–1922, 1998.

[16] C. T. Rettner, S. Anders, J. E. Baglin, T. Thomson, and B. D. Terris, "Characterization of the magnetic modification of Co/Pt multilayer films by He+, Ar+, and Ga+ ion irradiation," *Applied Physics Letters*, vol. 80, no. 2, pp. 279–281, 2002.

[17] C. Vieu, J. Gierak, H. Launois, T. Aign, P. Meyer, J. P. Jamet, J. Ferré, C. Chappert, T. Devolder, V. Mathet, and H. Bernas, "Modifications of magnetic properties of Pt/Co/Pt thin layers by focused gallium ion beam irradiation," *Journal of Applied Physics*, vol. 91, no. 5, pp. 3103–3110, 2002.

[18] G. J. Kusinski and G. Thomas, "Physical and magnetic modification of Co/Pt multilayers by ion irradiation," *Microscopy and Microanalysis*, vol. 8, pp. 319–332, 2002.

[19] J. Fassbender, D. Ravelosona, and Y. Samson, "Tailoring magnetism by light-ion irradiation," *Journal of Physics D: Applied Physics*, vol. 37, no. 16, pp. R179–R196, 2004.

[20] M. J. Benitez, M. A. Basith, R. J. Lamb, D. McGrouther, S. McFadzean, D. A. MacLaren, A. Hrabec, C. H. Marrows, and S. McVitie, "Engineering Magnetic Domain-Wall Structure in Permalloy Nanowires," *Physical Review Applied*, vol. 3, no. 3, pp. 1–10, 2015.

[21] S. Zhang, A. K. Petford-Long, and C. Phatak, "Creation of artificial skyrmions and antiskyrmions by anisotropy engineering," *Scientific Reports*, vol. 6, pp. 1–10, 2016.

[22] W. Jiang, S. Zhang, X. Wang, C. Phatak, Q. Wang, W. Zhang, M. B. Jungfleisch, J. E. Pearson, Y. Liu, J. Zang, X. Cheng, A. Petford-Long, A. Hoffmann, and S. G. Te Velthuis, "Quantifying chiral exchange interaction for Néel-type skyrmions via Lorentz transmission electron microscopy," *Physical Review B*, vol. 99, p. 104402, 2019.

[23] K. Zeissler, M. Mruczkiewicz, S. Finizio, J. Raabe, P. M. Shepley, A. V. Sadovnikov, S. A. Nikitov, K. Fallon, S. McFadzean, S. McVitie, T. A. Moore, G. Burnell, and C. H. Marrows, "Pinning and hysteresis in the field dependent diameter evolution of skyrmions in Pt/Co/Ir superlattice stacks," *Scientific Reports*, vol. 7, no. 1, pp. 1–9, 2017.

[24] C. M. Park and J. A. Bain, "Focused-ion-beam induced grain growth in magnetic materials for recording heads," *Journal of Applied Physics*, vol. 91, no. 10 I, pp. 6830–6832, 2002.

[25] M. A. Basith, S. McVitie, D. McGrouther, J. N. Chapman, and J. M. Weaver, "Direct comparison of domain wall behavior in permalloy nanowires patterned by electron beam lithography and focused ion beam milling," *Journal of Applied Physics*, vol. 110, p. 083904, 2011.

[26] C. Ferguson, *Imaging spin textures in advanced magnetic nanostructures using Lorentz microscopy.* PhD thesis, University of Glasgow, 2016.

[27] G. Vallejo-Fernandez, L. E. Fernandez-Outon, and K. O'Grady, "Antiferromagnetic grain volume effects in metallic polycrystalline exchange bias systems," *Journal of Physics D: Applied Physics*, vol. 41, p. 112001, 2008.

[28] J. Crangle and D. Parsons, "The magnetization of ferromagnetic binary alloys of cobalt or nickel with elements of the palladium and platinum groups," *Proceedings of the Royal Society of London. Series A. Mathematical and Physical Sciences*, vol. 255, no. 1283, pp. 509–519, 1960.

[29] O. Boulle, J. Vogel, H. Yang, S. Pizzini, D. De Souza Chaves, A. Locatelli, T. O. Mente, A. Sala, L. D. Buda-Prejbeanu, O. Klein, M. Belmeguenai, Y. Roussigné, A. Stashkevich, S. Mourad Chérif, L. Aballe, M. Foerster, M. Chshiev, S. Auffret, I. M. Miron, and G. Gaudin, "Room-temperature chiral magnetic skyrmions in ultrathin magnetic nanostructures," *Nature Nanotechnology*, vol. 11, no. 5, pp. 449–454, 2016.

[30] N. Bassim, K. Scott, and L. A. Giannuzzi, "Recent advances in focused ion beam technology and applications," *MRS Bulletin*, vol. 39, no. 4, pp. 317–325, 2014.

[31] J. A. Notte and D. S. Pickard, "Helium ion microscopy," *Handbook of Physics in Medicine and Biology*, vol. 32(2), no. 020801, pp. 39–1–39–11, 2010.

7

Investigating the Dzyaloshinskii-Moriya interaction in thin films with planar magnetisation

Contents

7.1 Introduction

The previous three chapters focused on materials with ultrathin magnetic layers and an interfacial DMI. As discussed, these materials are the subject of intensive global research as they can support technologically exciting magnetic skyrmions

[1–3]. This chapter investigates interfacial DMI from a different perspective and explores the effect of DMI on 'thicker' thin films, with a thickness on the order of the exchange length of the material, that have in-plane magnetisation. In particular, we study bilayer and trilayer systems based on 8 nm thick permalloy (Py), composition $Ni_{81}Fe_{19}$, with the geometry shown in Fig. 7.1.

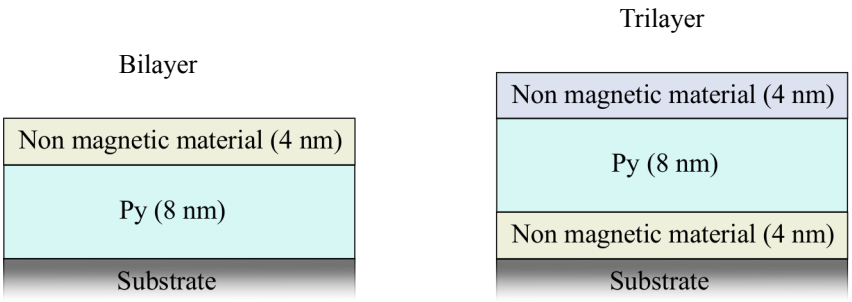

Figure 7.1: Geometry of material system studied in this chapter (7).

There are a handful of experimental and theoretical studies reporting on interfacial DMI in Py based material systems [4–8]. Im *et. al* investigate magnetic vortex formation in 100 nm thick Py nano disks, of diameter 500 nm defined by electron-beam lithography, and finds a statistically significant lack of degeneracy between the four possible vortex configurations (discussed later) and attributes this to DMI [4]. However, the study also identified that other less exotic effects, like surface roughness and edge defects, may play a role in the broken vortex degeneracy. It has also been predicted theoretically [5, 7] and measured experimentally, in a Py/Pt bilayer system [6], that DMI induces an asymmetry to the spin-wave propagation in thin in-plane magnetised materials. Another study uses micromagnetics to show that the presence of DMI in a spin transfer nano-oscillator device based on a Py nanodisk causes the vortex to precess with a frequency three times larger than predicted in an equivalent nanodisk without DMI [8]. In this chapter, the effect of interfacial DMI on magnetic vortices is studied first using micromagnetic simulations and then experimentally with the methods of Lorentz TEM.

As detailed in section 2.2.2, in systems with both strong spin-orbit coupling and a lack of inversion symmetry an additional antisymmetric exchange interaction,

DMI, contributes to the total energy of the system. This additional contribution to the Hamiltonian has the form:

$$\mathcal{H}_{DMI} = -\mathbf{D} \cdot (\mathbf{S_i} \times \mathbf{S_j}), \tag{7.1}$$

where $\mathbf{D}$ is the DMI vector, and $\mathbf{S_{i,j}}$ are two neighbouring magnetic spins. $\mathcal{H}_{DMI}$ is minimised by perpendicular neighbouring spins, where the relative sense of rotation is defined by the sign of $\mathbf{D}$. The direction of $\mathbf{D}$ is set by the local crystal symmetry and, in systems where the DMI originates from an interface, is parallel to the plane defined by the interface [9]. Consequently, in order to decrease DMI energy, the cross product of two neighbouring spins must also be parallel to this interface. This leads to the reason we chose to focus on magnetic vortices in this study of DMI in planarly magnetised materials.

We will study a continuous film which supports in-plane domains separated by Néel type walls as sketched in Fig. 7.2(a). If DMI is generated by an interface, the associated energy can only be lowered by pulling either the magnetisation of the domains or the wall out-of-plane. Both options would be associated with a significant increase to the magnetostatic energy, so the effect, if any, is expected to be slight. Micromagnetic simulations (the details are given in section 7.2) indicate that, with a moderate DMI strength of 1 $\mathrm{mJm^{-2}}$ the magnetisation is pulled out-of-plane by $\approx 0.0002°$. This effect is drawn exaggerated in Fig. 7.2(b) where the domains have both in-plane and out-of-plane magnetisation components. Note the purpose of Fig. 7.2 is to discuss the different influence DMI may have on a wall structure compared to a vortex structure from a conceptual point of view. However to be clear by 'moderate $\mathbf{D}$' we mean a realistic interaction strength of around 1 $\mathrm{mJm^{-2}}$, and by 'high $\mathbf{D}$' we mean something unrealistic like $|\mathbf{D}| > 3$ $\mathrm{mJm^{-2}}$ at which point the DMI energy begins to dominate over the other energy terms.

If the geometry of the system is confined to a disk, the energetically favoured configuration is a magnetic vortex. Magnetic vortices are characterised by circling in-plane magnetisation, classified by the circularity c which is assigned +1 for a clockwise rotation or -1 for counter-clockwise rotation. To avoid the highly

energetic situation of anti-parallel neighbouring spins, at the centre of the vortex a nanoscale area of magnetisation points out-of-plane - this is the vortex core which is classified by the polarity p, and assigned +1 for a core pointing up and -1 for a core pointing down. The four possible combinations of circularity and polarity leads to four 'types' of magnetic vortices, thought to be degenerate in energy before study [4]. One of these configurations, with (c,p) = (-1,+1), is sketched in Fig. 7.2(d). We propose that the out-of-plane magnetisation naturally associated with a vortex core may provide an interaction point for DMI, where it may cause a local chiral twisting that lowers the total energy of the vortex structure (this is sketched in 7.2(e)). Hence, the effect of DMI on a magnetic vortex could be probed even at low **D** strengths that cause a negligible modification to the wall structure. Above a certain **D** threshold, a spin spiral with fixed handedness (sketched in Fig. 7.2(c,f)) will be the energetically favoured configuration as the lowering of $\mathcal{H}_{DMI}$ is greater than the increase to other energy terms such as the anisotropy and standard symmetric exchange. Spin spirals are observed in other material systems

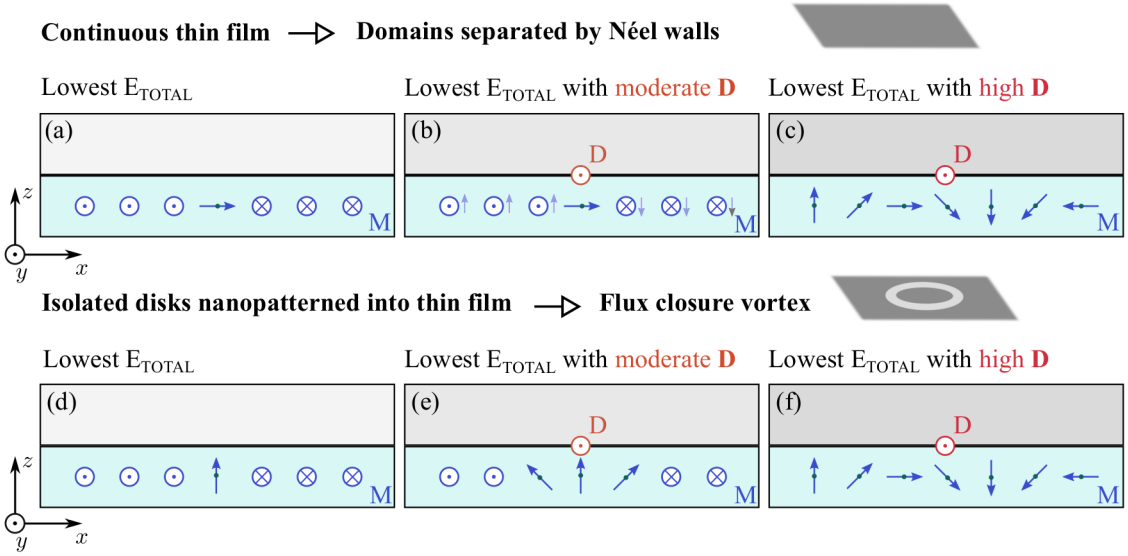

Figure 7.2: Cross-sectional sketches of the spin configuration in an in-plane magnetic material (blue), relative to the interfacial DMI (**D**) that may be expected at an interface to a non-magnetic material (grey). Sketched are the spin configurations in a continuous thin film (a-c), which predominately forms Néel type walls, and a disk (d-f), which stabilises a magnetic vortex. Through energy considerations, it is expected that the structure of magnetic vortex will be influenced by DMI at lower **D** strength than Néel walls.

with interfacial and bulk DMI systems [10–13]. Micromagnetic simulations suggest that, in this system, a spin spiral will be stabilised for unphysically high DMI strengths of $|\mathbf{D}| > 3.5$ mJm^{-2}.

It must also be noted that interface between a heavy non-magnetic metal and ferromagnet is also associated with PMA. The effect of interface induced anisotropy in films of this thickness is expected to be small because, as explained in 2.2.4, the surface/interface anisotropy strength scales inversely with thickness. However to study the DMI, careful consideration must also be given to the possible effect of PMA [6, 14].

7.2 Micromagnetic simulation and calculation of observable effects of DMI

To begin with, the effect of interfacial DMI in thin film systems with in-plane magnetisation was simulated using MuMax3 [15]. To simulate Permalloy the following material parameters were used: saturation magnetisation M_s of 8.6 $\times$ 10^5 Am^{-1}, exchange stiffness A of 1.3 $\times$ 10^{-11} Jm^{-1} and damping constant of 0.02. No anisotropy was included in any simulation results presented outside section 7.2.3. The simulations have cell size 1 nm $\times$1 nm $\times$ t for $x \times y \times z$, where t is the thickness in nm. One cell in the z direction was deemed sufficient to simulate a one layer direct exchange coupled material with t close to the exchange length (6 nm in Permalloy [16]). All simulations presented in this chapter have $t = 8$ nm, chosen to match the experimental work, however simulations performed with thickness ranging from 2 nm to 10 nm show the same effect albeit more pronounced for the thinner systems - as is expected from an interface effect.

Figure 7.3 shows vector plots of the magnetisation local to a vortex core, simulated from a 1 μm diameter disk with (a,c) no DMI, (b,d) $\mathbf{D} = 1.5$ mJm^{-2} and (c,f) $\mathbf{D} = 3$ mJm^{-2}. The first row shows the magnetisation in plan view, and the second row shows it in cross-sectional view. As is most obvious from Fig. 7.3(f) of $\mathbf{D} = 3$ mJm^{-2} in cross-section, the addition of DMI to the simulation of a vortex does indeed introduce a chiral twisting of the magnetisation around the core. The

magnetisation of the vortex core without DMI has only curl and no divergence; DMI adds a divergence to the curl of the vortex as sketched at the bottom of Fig. 7.3. These simulations were of a (c,p)=(+1,+1) type vortex; simulations were performed of the other three vortex types and found the DMI induced divergence is independent of c but reverses with p, this is as expected (and clear from looking at the homochiral spin spiral sketched Fig. 7.2(c,f)). Furthermore, all four vortex types, with and without DMI, were found to be degenerate.

Figure 7.4 details the relationship between $\mathbf{D}$ and $\nabla\cdot\mathbf{M}$ (again for a (c,p)=(+1,+1) type vortex). Figures 7.4(a) and (b) plot the divergence $\nabla \cdot \mathbf{M}$ of a vortex core without DMI and with $\mathbf{D} = 3$ mJm^{-2} on the same greyscale. The curl $\nabla \times \mathbf{M}$ of the same two structures is given in Figs. 7.4(c) and (d). It must be noted that the divergence at the core is always compensated by equal but opposite divergence spread around the edge of the disk, hence the total divergence of the magnetic disk is always zero. Between $\pm$ 2.5 mJm^{-2} there is a linear relationship between $\mathbf{D}$ and $\nabla \cdot \mathbf{M}$, as seen from graph Fig. 7.4(e) which plots $\nabla \cdot \mathbf{M}$ summed over an area 300

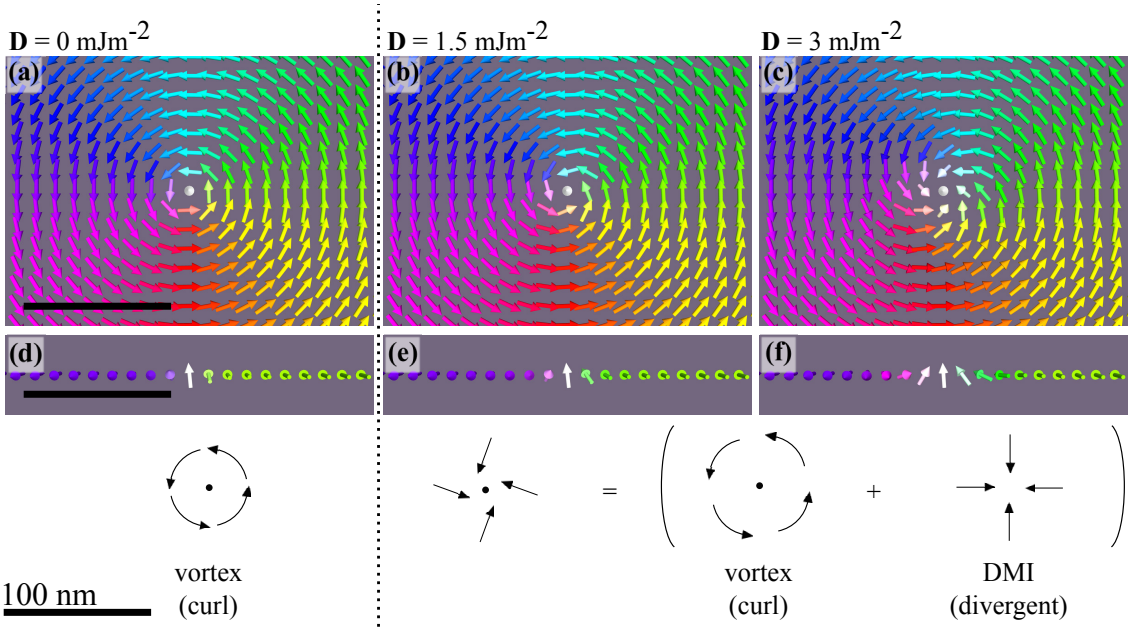

Figure 7.3: Plan and cross-sectional views of vector plots of the magnetisation local to a vortex core from simulations of disks, diameter 1 μm, with (a,c) no DMI, (b,d) $\mathbf{D}$ = 1.5 mJm^{-2} and (c,f) $\mathbf{D} = 3$ mJm^{-2}. DMI adds divergence to the pure curl structure of a standard vortex (as sketched at the bottom of the figure).

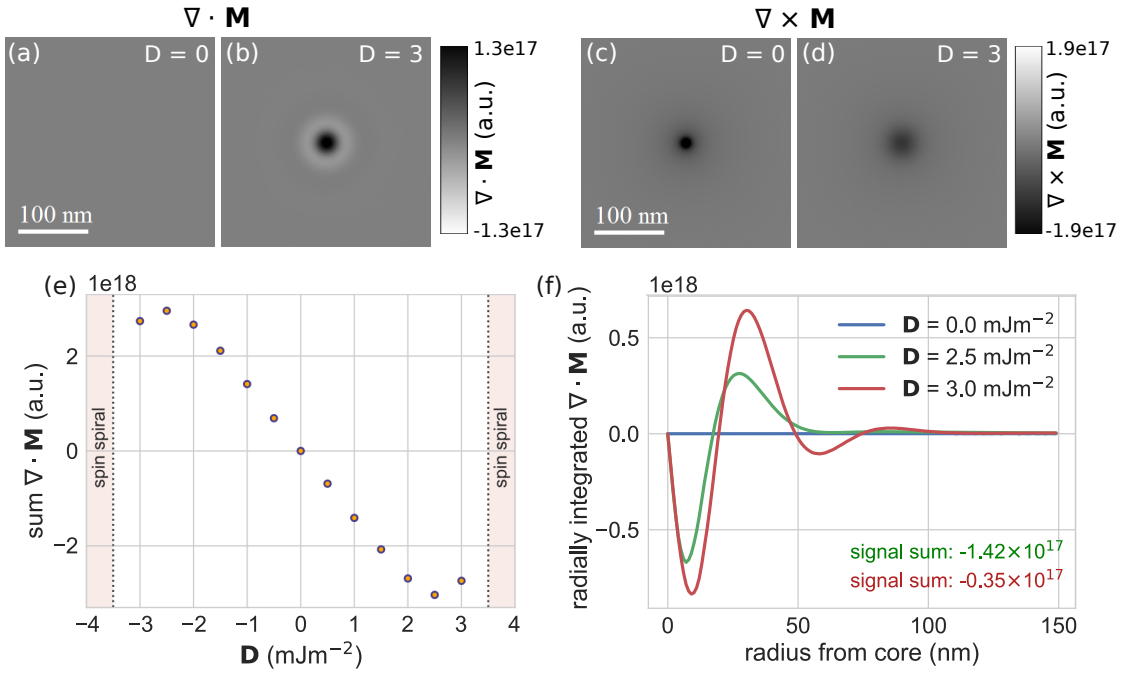

Figure 7.4: Interfacial DMI adds a divergent component to vortex core (compare (a) with $\mathbf{D} = 0$ mJm^{-2} and (b) $\mathbf{D} = 3$ mJm^{-2} presented on the same greyscale). For comparison, (c) and (d) show the associated curl of the magnetisation. (e) shows a graph of $\nabla \cdot \mathbf{M}$ summed over an area 300 × 300 nm^2 around the centre of the core and shows that $\nabla \cdot \mathbf{M}$ varies linearly with $\mathbf{D}$ between ± 2.5 mJm^{-2} with a spin spiral above 3.5 mJm^{-2}. The linear relationship breaks down at $|\mathbf{D}| = \pm$ 3 mJm^{-2} as the DMI causes more than one twist around the core as seen from the radially integrated profiles presented in (f).

× 300 nm^2 around the core. For $|\mathbf{D}| \geq 3.5$ mJm^{-2} the magnetic disks support a homochiral continuous spin spiral. $|\mathbf{D}| = 3$ mJm^{-2} has less $\sum(\nabla \cdot \mathbf{M})$ than $|\mathbf{D}|$ = 2.5 mJm^{-2} because, as a precursor to a continuous spin spiral, there is already additional chiral twists outside the core. This is clear from Fig. 7.4(f) which plots radially integrated profiles of $\nabla \cdot \mathbf{M}$ for $\mathbf{D}$=0, 2.5 and 3 mJm^{-2}. As expected from energy considerations discussed in section 7.1, simulations of a two domain structure show far smaller alterations to the wall structure: the magnetisation cants out-of-plane by a maximum of 0.0004° before a spin spiral is stabilised at $|\mathbf{D}| = 3.5$ mJm^{-2}.

The remainder of this section deals with prediction of experimentally measurable effects of interfacial DMI in magnetic disks from simulation.

7.2.1 Low-field expulsion of vortex core from disks with DMI

The divergent magnetisation at the vortex core can be thought of as a local magnetic charge compensated by magnetic charges of opposite 'polarity' at the edge of the disk. This is associated with significant magnetostatic energy and likely affects the magnetisation dynamics of the disk. To explore this, disks of diameter 1 μm and thickness 8 nm with a (c,p)=(+1,+1) vortex (as above) were simulated and an in-plane external magnetic field applied increasing in steps of 0.1 mT. Figure 7.5 shows the results of these simulations. It is evident that DMI reduces the strength of the magnetic field required to push the vortex core out of the disk (the 'vortex expulsion field'). The top half of the figure (Figs. 7.5(a-c)) shows the path of vortex core as it is expelled from the disk for three values of

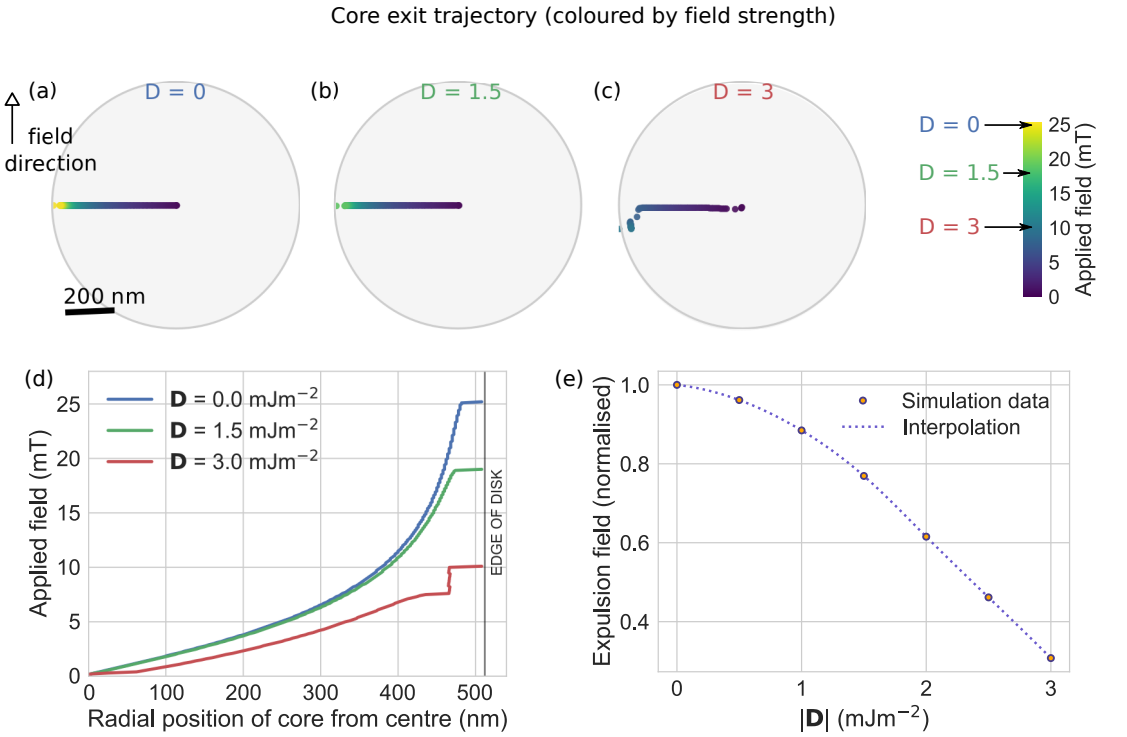

Figure 7.5: The path of the vortex core as it is pushed from a disk by an external field is shown in (a) for $\mathbf{D} = 0$, (b) $\mathbf{D} = 1.5$ and (c) 3 mJm^{-2}. The path is coloured by the field strength and hence gives the position of the core at each field strength and it is seen that (a) leaves at 25 mT, (b) at 18 mT and (c) at 10 mT by the colour of the path at the edge of the disk. This is also clear from the graph in (d). (e) shows the relationship between the expulsion field and $\mathbf{D}$ - the expulsion field is independent of the sign of $\mathbf{D}$.

D. The path is coloured by the strength field and it is apparent that there is a relationship between **D** and the vortex expulsion field as, at the point of exit, the core is yellow in (a), green in (b) and blue in (c). For $\mathbf{D} = 0$ and 1.5 $\mathrm{mJm^{-2}}$ the core takes a simple path straight out of the disk, however the high **D** value takes a more complex path. Figure 7.5(c) details the relationship between the vortex expulsion field and **D** - the markers are the discrete values calculated by simulation and the dashed line is a cubic interpolation of this data included to guide the eye. When normalised to the zero DMI expulsion field, disks of diameter 0.5, 1, and 2 μm show the same trend between expulsion field and **D**.

In situ magnetising experiments can be performed in the TEM (detailed in section 3.7.1) hence, using the Fresnel imaging mode, the motion of the vortex core under an applied field is easily observed and could provide a straightforward method of estimating the strength of **D** in this material system. It should be noted, however, that for realistic DMI strengths ($|\mathbf{D}| < 2$ $\mathrm{mJm^{-2}}$) this method is not sensitive to the sign of **D**.

7.2.2 Distortion of vortex core structure with DMI

The most striking effect of the DMI on a vortex core is the chiral twisting visible in Fig. 7.3. In this section we present two possible methods of detecting the DMI from the static vortex core structure: first discussed is imaging the vortex core using MFM and secondly using DPC Lorentz STEM.

Direct imaging of DMI induced divergence

MFM perhaps provides the ideal method to directly measure the DMI induced divergence. As discussed in detail in section 3.8, MFM can be thought of as magnetic charge imaging [17]. There are two contributions: one from surface charges $\sigma = \mathbf{M} \cdot \hat{\mathbf{n}}$ where **M** is the sample magnetisation and $\hat{\mathbf{n}}$ is a unit vector normal to the sample surface; and one from volume charges $\rho = -\nabla \cdot \mathbf{M}$. Therefore MFM images should be acutely sensitive to the $\nabla \cdot \mathbf{M}$ induced by DMI. The image contrast will be based on a combination of this DMI induced ρ, and σ which

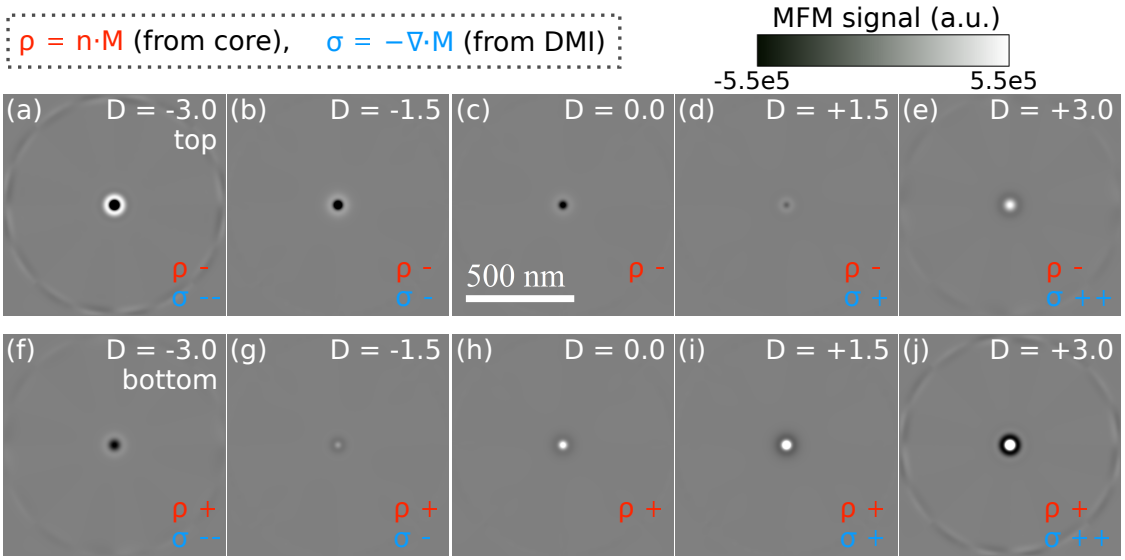

Figure 7.6: Calculation of MFM images from micromagnetic simulations of a 1 μm disk supporting a (c, p)=(+1,+1) type vortex. (a-e) is images calculated with a range of **D** values from a sample imaged from the top. (f-j) is MFM image contrast expected from the same vortex structures imaged 'upside down'. All images are shown on the same greyscale. DMI induces contrast asymmetry between images of the top and bottom surfaces which could be used to measure, at least qualitatively, the sign and strength of the DMI at the interface.

originates from the M_z inherent to vortex cores. Figure 7.6 displays an array of simulated MFM images (see section 3.10.4 for details) which show that, by imaging the top and bottom surface of the disk, the image contributions from DMI and from the core can be decoupled to allow measurement both of the sign and, at least qualitatively, the strength of the interface induced DMI. These images are displayed on the same greyscale and were calculated from the output of micromagnetic simulations of a 1 μm disk supporting a (c, p) =(+1,+1) vortex and simulate a MFM images taken with a lift height of 30 nm and dipole-like tip magnetised in the $-z$ direction.

Figures 7.6 (c) and (h) show the MFM image contrast expected when imaging the top and bottom surfaces of an unmodified magnetic vortex respectively. The contrast originates from the stray field generated by the vortex core and simply reverses when the sample is imaged 'upside down' - i.e. the modulus of these two images is identical. Significant asymmetry between images of the top and bottom surfaces emerges when DMI is added to the simulations. This is because

the core contrast, from ρ, reverses when the sample is imaged upside down but the DMI contrast, from σ, does not - leading to addition of the contributions in one orientation but subtraction in the other. The presence and sign of ρ and σ are noted in the bottom left of each MFM image.

It is expected that there will be a natural mixture of the four possible vortex states stabilised in an array of disks. It may seem that comparing images of disks with opposite p would provide the same information, however, imaging the top and bottom surfaces is the only way to detect this DMI induced asymmetry. This is because reversing p also reverses the divergence (and consequently σ), hence a p=−1 vortex with $\mathbf{D} = 3$ mJm^{-2} imaged from the top will have the same contrast as (a) which has contrast exactly the inverse of a p=+1 vortex with $\mathbf{D} = 3$ mJm^{-2} imaged from the top shown in (e) - therefore there is no asymmetry.

Effective vortex core broadening in DPC

The quantitative, in-focus scanning Lorentz TEM method of DPC is advantageous because of its impressively high spatial resolution of about 1 nm [18]. It is sensitive to the component of the magnetic induction **B** of the sample that is perpendicular to the electron beam trajectory. However, as underpins most of the Lorentz imaging in this thesis, at normal incidence, no image contrast is observed from the divergent component of the magnetisation. Divergent **M** and the associated **H**-field, when integrated along the electron path, completely cancel each other leading to zero integrated **B** and no deflection to measure in Lorentz microscopy. However, for the divergent magnetisation induced by DMI, the *lack* of integrated **B** may still provide a quantitative measurement of the strength of **D**. This manifests in DPC images as diffuseness around the vortex core as seen in bottom row of Fig. 7.7

Figures 7.7 (a-c) show the y-component of the magnetisation of a vortex with (a) $\mathbf{D} = 0.0$ mJm^{-2}, (b) $\mathbf{D} = 1.5$ mJm^{-2} and (c) $\mathbf{D} = 3.0$ mJm^{-2}. In Fig. 7.7(a) the contrast is symmetric about the axis drawn in light blue through the core, with increasing asymmetry observed in Fig. 7.7(b) then Fig. 7.7(c) from the chiral twisting induced by DMI. This is in contrast to Figs. 7.7(d-f) which are

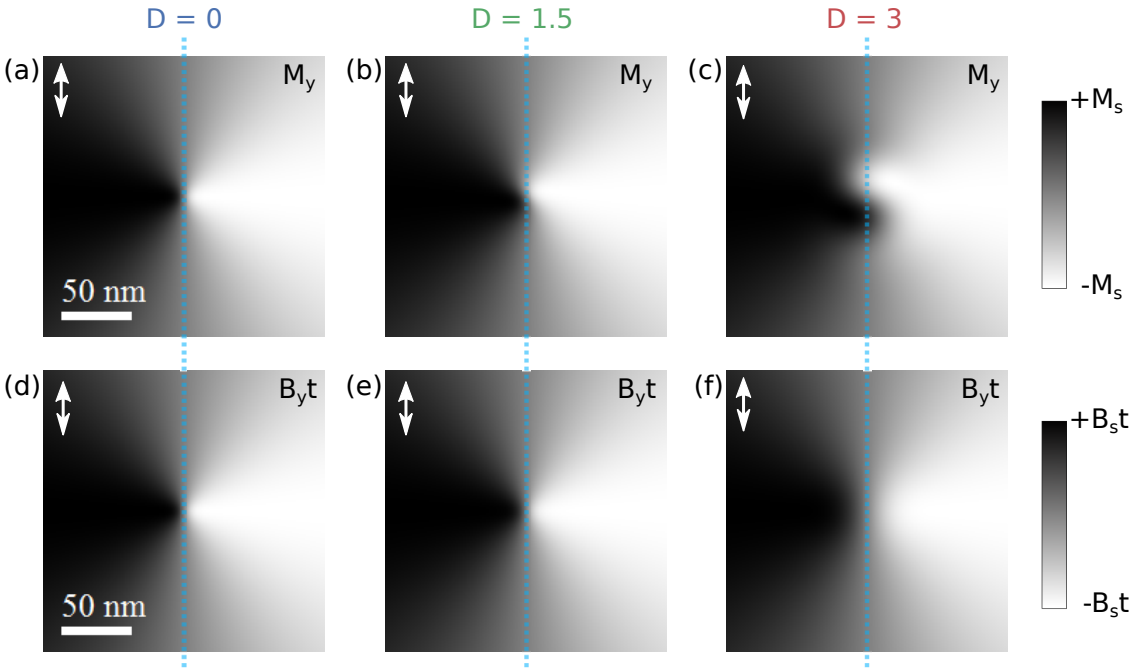

Figure 7.7: The variation of M_y with **D** is shown for (a) no DMI, (b) **D** = 1.5 mJm^{-2} and (c) 3 mJm^{-2}. In these images DMI adds a charactaristic swirl. Conversely, (c-e) shows of a DPC image mapping the integrated **B** in the y-direction for the same DMI values - these DPC images show none of the charactaristic asymmetry seen in the images of the magnetisation. Instead DMI is associated with an effective broadening of the vortex core. A dashed blue line, through the centre of the core, is included to make the symmetry of the images more obvious.

all symmetric - these images are simulated DPC images (mapping the y-direction of the integrated magnetic induction) for the same **D** values as Figs. 7.7(a-c). Instead, in DPC images, the effect of DMI is visible as an effective broadening of the contrast associated with the vortex core which arises because of local reduction of the integrated **B**. Figure 7.8 (a) compares line traces taken horizontally through the centre of the images in Fig. 7.7(d-f). The width of a vortex core is measured the same way as a domain wall: by fitting a one-dimensional hyperbolic tangent function (form: $y = \tanh(x/w)$) to profiles extracted from DPC images. The fitted parameter w then gives a measure of the core width. The relationship between the width parameter w and **D** is plotted in Fig. 7.8(b). The markers represent each individual measurement and the dashed line is an interpolation included to guide the eye. The values of w have been normalised to the width parameter from a vortex core without DMI. The highest experimentally measured value of **D** from an

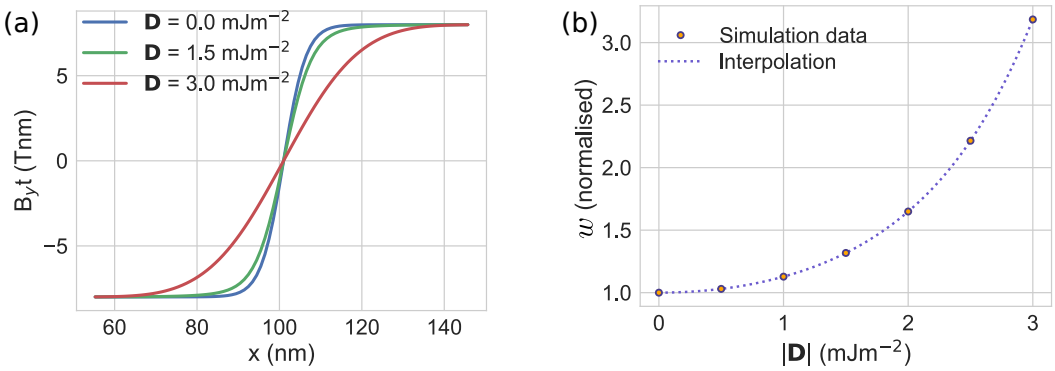

Figure 7.8: (a) profiles of the integrated magnetic induction from simulated DPC images for three values of **D**. (b) shows the relationship between the width parameter w (measured by fitting the profiles to a function of the form: $\tanh(x/w)$) and the strength of **D**. The markers are the discreet measurements made from simulations and the dashed line is a cubic interpolation of this data included to guide the eye. The values in this graph have been normalised to the w parameter measured from a zero DMI vortex which, for these simulation parameters, was 5.4 nm.

interface is 1.9 mJm^{-2} [3], and in these simulations $\mathbf{D} = 2$ mJm^{-2} was measured to cause a broadening of 60% (from 5.4 nm to 8.6 nm). Given that this value represents the maximum realistic broadening, the detection of core broadening from experimental DPC images is likely to be a challenging measurement, but one that is certainly within the methods capabilities.

7.2.3 Evaluation of the effect of interface induced anisotropy

As mentioned earlier in this chapter, interfaces that have strong spin-orbit coupling between the magnetic material and adjacent non-magnetic metal are also associated with a surface induced perpendicular uniaxial anisotropy as well as DMI. The energy associated with this surface anisotropy is generally an order of magnitude smaller than the energy associated with DMI [14]. Hence, for films 8 nm thick the effect of this anisotropy will certainly be small, however for transparency, this section simulates the effect of a uniaxial magnetic anisotropy on the magnetism of a vortex core and discusses any possible influence on the **D** measurements proposed above.

As seen in Fig. 7.9, the addition of an out-of-plane uniaxial anisotropy is associated with only a slight broadening of the vortex core. The maximum anisotropy

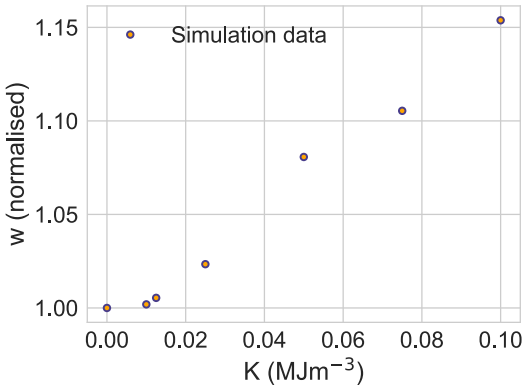

Figure 7.9: Graph (b) showing the relationship between the strength of perpendicular uniaxial anisotropy, K, and the width parameter w measured from simulated DPC images. The values in this graph have been normalised to the w parameter measured from a zero anisotropy vortex core - which for these simulation parameters was 5.4 nm.

included on the graph is 0.1 MJm^{-3}, simulations with 0.5 MJm^{-3} relax into a stripe domain state and above 1 MJm^{-3} the magnetisation is fully out-of-plane. The width parameter w was measured from simulated DPC images in an identical manner to section 7.2.2. Perpendicular anisotropy of 0.1 MJm^{-3} was associated with a broadening of 0.82 nm (2%) relative to the zero anisotropy width. Stashkevich *et al.* [6] measured a surface anisotropy of 0.4 mJm^{-2} at the interface between Permalloy and platinum and, assuming an inverse thickness relationship, in an 8 nm thick Permalloy film this would be associated with a uniaxial anisotropy of 0.05 MJm^{-3} which in simulations caused a broadening of 0.4 nm (1%) relative to the zero anisotropy width. Therefore, this effect is small but certainly needs to considered if estimating DMI from core broadening in DPC images. The anisotropy has no influence on the measurement of DMI from vortex expulsion experiments or from MFM images.

7.3 Experimental

The rest of this chapter explores experimental realisation of the experiments proposed in section 7.2.

7.3.1 Samples

The experimental work focuses on three samples, two bilayer samples and one trilayer sample based on $Ni_{81}Fe_{19}$ Permalloy - the details of which are summarised in table 7.1. These polycrystalline samples were deposited by dc magnetron sputtering onto electron transparent substrates by Sinan Azzawi of the University of Durham. The samples were deposited onto a 3 nm thick amorphous carbon substrate on a

Sample	Expected **D** type	Comment
Py(8)/Cu(4)	none	*control sample*
Py(8)/Ir (4)	-	-
Ir(4)/Py(8)/Pt(4)	+	*additive DMI from double interface?*

Table 7.1: Summary of the sample composition, the numbers in brackets give the layer thickness in nm, and the expectations of each sample.

standard TEM grid. This decision was made because, unlike the standard Si_3N_4 window substrates, the geometry of the TEM grid should permit MFM on both surfaces of the sample as is required to perform the experiment proposed in section 7.2.2. The geometry of the different substrates is sketched in Fig. 3.1.

The reasons these three sample geometries were chosen to study is explained in the following. Interfaces between Ir and Pt and a magnetic material are arguably the most studied interfaces regarding interfacial DMI. The two interfaces are associated with **D** vectors of opposite sign - i.e. that favour opposite handednesses of chiral twisting [19]. Here we define a $+(-)\mathbf{D}$ vector to be is associated with counter-clockwise (clockwise) spin rotation. Furthermore, heavy metal layers associated with opposite **D** vectors arranged either side of a magnetic layer gives rise to an 'additive' DMI as described in section 2.2.2 [3, 20, 21]. Therefore, we expect the interface between Py and Ir to be associated with $-\mathbf{D}$ and the trilayer sample with successive interfaces between Py and both Ir and Pt to be associated with $+\mathbf{D}$ of possibly greater magnitude. Although, any effects of 'additive' DMI will be small as the two interfaces in this study are almost one order of magnitude further apart than in the original studies of additive DMI [3, 20]. We include Py/Cu as a control

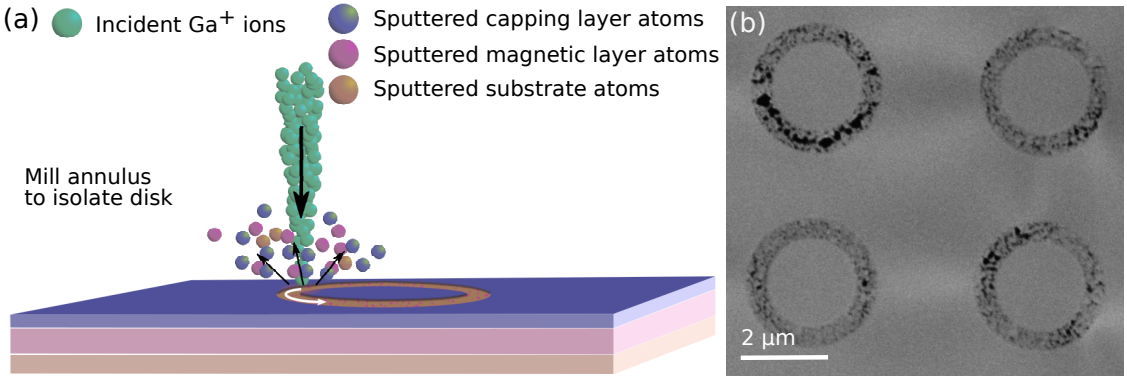

Figure 7.10: (a) schematic of using a FIB to isolate disks of magnetic material from a continuous film. (b) SEM image of some disks, 2 μm diameter, which have been separated from the continuous films by milling an annulus 0.5 μm wide.

sample because the Py/Cu interface is expected to cause negligible DMI but the Cu layer will prevent oxidation of the magnetic layer.

Disks were defined in these continuous thin films using a FIB, as described in section 3.4.2. A schematic of this process is sketched in Fig. 7.10 (a). The focused ion beam is used to mill out an annulus of material (stopping at the substrate) to leave a disk of magnetic material isolated from the continuous film. Here we used an FEI Nova NanoLab 200 scanning electron microscope (SEM) and FIB operated at a 30 keV Ga^+ beam energy and with a beam current of 10 pA. The beam motion during milling is kept parallel to the edge of the feature being defined to ensure the least edge artefacts - this is shown by the white arrow in Fig. 7.10 (a). An array of 2 μm disks were defined by milling an annulus of width 0.5 μm. The centre to centre distance between the disks was 5 μm. An SEM image of part of an array of disks is shown in Fig. 7.10 (b). Polycrystalline samples are subject to preferential milling and, because the substrate is extremely thin, in some places it was necessary to mill holes through the substrate (black areas in Fig. 7.10 (b)) to ensure the disk was magnetically separate from the rest of the film.

7.3.2 Vortex expulsion observed by *in situ* Fresnel imaging

The Fresnel mode of Lorentz TEM, provides a straightforward method of measuring the vortex expulsion field for the three samples. A Fresnel image of a magnetic

vortex is characterised by a bright or dark spot at the position of the vortex core. This contrast arises as the in-plane circling magnetisation associated with a vortex acts like a lens, either focusing or spreading the transmitted electrons resulting in a bright or dark spot respectively. This is sketched in Fig. 7.11 for a vortex with $c = +1$ on the left and -1 on the right. Therefore, despite appearances, the Fresnel contrast from a magnetic vortex arises from c and contains no information about the sign of p.

Nevertheless, Fresnel images provide the position of the vortex core. As described in section 3.7.1, the objective lens of the microscope was used to perform *in situ* magnetising experiments. For this experiment, the objective lens was excited to produce a field of 25 mT at the sample oriented along the optic axis. The strength of the in-plane magnetic field experienced by the sample is then controlled by the sample tilt θ and varies as $(25 * \sin(\theta))$ mT. A tomography sample rod was used to permit high tilt angles. Micromagnetic simulations predict that, for this field strength, the component of the field perpendicular to the disks does not influence the normalised expulsion field trend with DMI. Figure 7.12(a) shows an untilted Fresnel image of four disks in the Py/Ir sample. As the tilt is increased, and the in-plane field strength increased, the cores move to the edge of the disk as seen in image Fig. 7.12(b) where the core positions highlighted by orange circles. At some

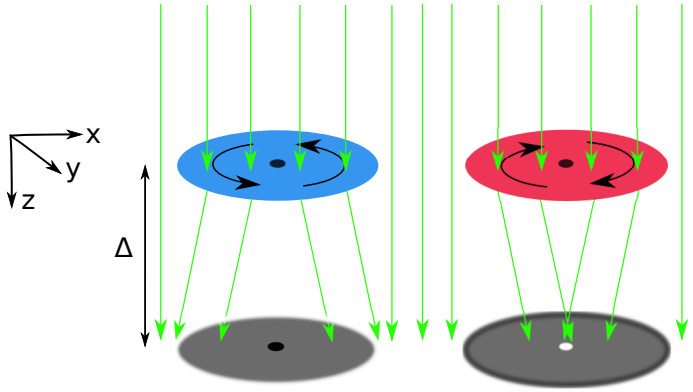

Figure 7.11: The Fresnel image contrast from a magnetic vortex relates to the in-plane magnetisation of the vortex which either focuses or spreads the transmitted electrons leading to a bright or dark spot at the position of the core which is not related to the polarity of the vortex core.

tilt angle the in-plane field will have pushed the vortex core out of the disk as seen in Fig. 7.12(c) where no vortex Fresnel contrast remains. The bright and dark spots in Fig. 7.12(a) are not centred which suggests the sample is not completely flat therefore, to remove any artefact originating from residual tilts, the expulsion field measured from one disk is recorded as an average of the field measured from positive and negative tilt angles.

Each sample was patterned with arrays of 4 × 4 disks of 2μm diameter, and the experiment was repeated a total of four times for both tilt directions. This leads to 64 measurements of the vortex expulsion field from each sample. The results of these experiments are shown in table 7.2, where the expulsion field is the mean of these repeated measurements and the error quoted is the standard error on the mean. The values presented in table 7.2 show that there is a statistically

Sample	Expulsion field (mT)	Expulsion field (normalised)
Py/Cu	14.9 ± 0.2	1.00
Py/Ir	13.8 ± 0.2	0.93 ± 0.02
Ir/Py/Pt	13.6 ± 0.1	0.91 ± 0.01

Table 7.2: Results of vortex expulsion experiment.

significantly reduction of the vortex expulsion field compared to the control sample, however there is little difference between the two DMI samples. Comparing the

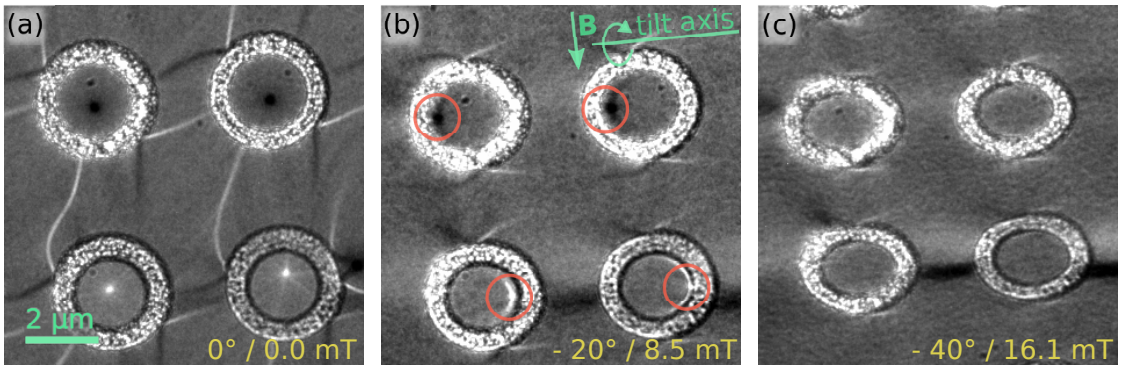

Figure 7.12: Fresnel images of FIB defined disks imaged at different sample tilts. At 0° tilt in (a) the core is positioned at the bright or dark spot near the centre of the disk. As a field is applied by tilting the sample, the cores move towards the edge of the disks (b) before being expelled (c). The orange circles in (b) are to make the position of the vortex core more obvious.

normalised experimental values to the graph in 7.5(e) allows us to estimate the strength of the DMI in the Py/Ir sample as $|\mathbf{D}| = 0.8 \pm 0.3$ mJm^{-2} and in the Ir/Py/Pt sample as $|\mathbf{D}| = 0.9 \pm 0.1$ mJm^{-2}. These values are of the expected order of magnitude. The error on $|\mathbf{D}|$ was estimated using the simulated dataset in Fig. 7.5(e) and the experimental error on the expulsion field values.

7.3.3 Vortex core broadening measured by DPC

The width of the vortex cores in the three samples was measured using DPC imaging. As mentioned previously in this chapter, the core broadening is expected to be only a few nanometers and will be a challenging measurement at the limit of the resolution of DPC. The images were taken in a low field environment, with the objective lens off, using a probe forming aperture of 50 μm (resolution 0.7 nm) at a magnification of $\times$400k to give a pixel size of 0.9 nm. As discussed in section 3.7.5, at high magnifications, the crystallites of polycrystalline samples add a great deal of non-magnetic diffraction contrast to DPC images collected with a segmented detector. While the effect for this material system is much milder than for the materials studied in chapters 5 and 6, this non-magnetic polycrystalline contrast would certainly hamper detection of core broadening in this system. Therefore, as in the earlier chapters, a pixelated detector was used to collect the DPC datasets. This allows application of an algorithm which is very efficient at separating the image contributions from the crystallites from the underlying magnetic contrast [22]. High magnification DPC images of a vortex core in the Ir/Py/Pt sample are shown in Fig. 7.13(a) and (c) which map two orthogonal directions of integrated magnetic induction given by the double headed arrows inset on the top left of the images. The lines traces taken through the centre of the core in images (a) and (c) are shown respectively in (b) and (d). These graphs include the experimental data and the fit to a tanh function. The width parameter w is then extracted from the tanh fit, so each DPC dataset provides two measurements of the core width. The mean width measurement from all three samples is presented in table 7.3

Sample	Width parameter (nm)	Width parameter (normalised)
Py/Cu	10.5 ± 0.8	1.0
Py/Ir	11.7 ± 0.7	1.1 ± 0.1
Ir/Py/Pt	12.3 ± 0.9	1.2 ± 0.1

Table 7.3: Results of measuring the width of the vortex core from DPC images.

Pixelated DPC datasets are gigabytes in size and therefore we do not have the same large sample size as the vortex expulsion measurements - the values in table 7.3 are the average of about 10 measurements. The error on the core width measured from the Py/Cu and Py/Ir samples overlap. However, there is a definite broadening of the core in the Ir/Py/Pt sample. Comparing the normalised mean experimental measurements to the graph in 7.8(b) predicts a $|\mathbf{D}| = 0.9 \pm 0.6$ mJm^{-2} for the Py/Ir sample and a $|\mathbf{D}| = 1.2 \pm 0.3$ mJm^{-2} the Ir/Py/Pt sample. Note that the proportionally large error on the Py/Ir measurement arises because, as seen in Fig. 7.8(b), the vortex core width varies slowly for $|\mathbf{D}| < 1$ mJm^{-2}.

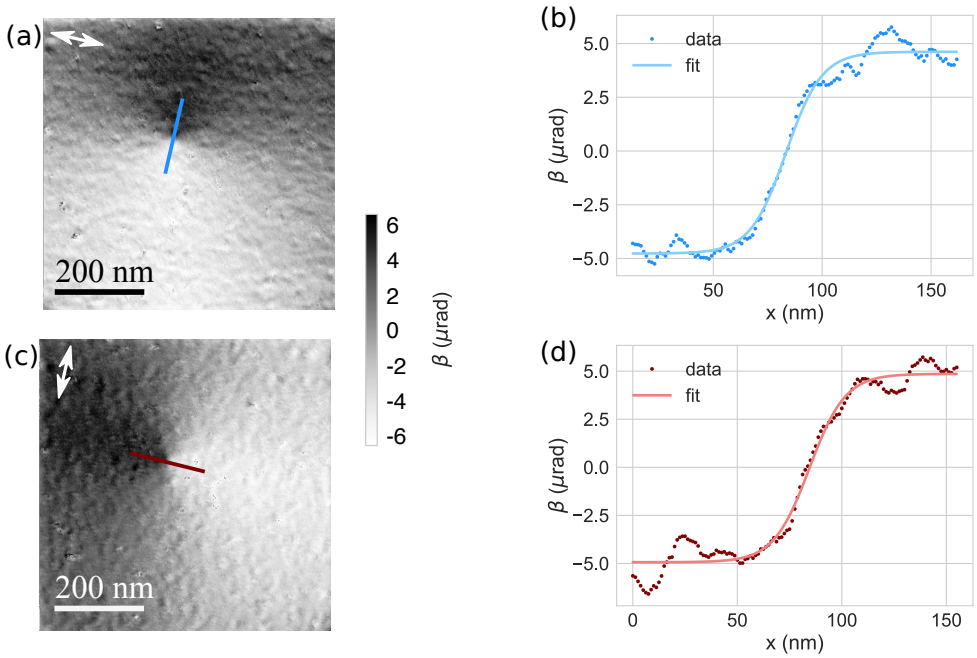

Figure 7.13: DPC images of a vortex core in the Ir/Py/Pt sample. Images (a) and (c) map two orthogonal direction of the integrated magnetic induction as indicated by the arrows inset on the top left of the images. (b) and (d) show line traces taken across the vortex core from both of these images together with the fitted hyperbolic tangent function the core width is determined from.

These values are within the error bounds of the measurement of $|\mathbf{D}|$ from the vortex expulsion field in section 7.3.2.

As discussed in section 7.2.3, interfaces may induce a perpendicular surface anisotropy that also with broadens vortex cores. One might expect that the surface anisotropy will depend critically on the interface quality and likely varies with the sample deposition environment. However, as a guide, study [14] measures an interface anisotropy of 0.1 $\mathrm{mJm^{-2}}$ (equivalent to a uniaxial anisotropy of 0.01 $\mathrm{MJm^{-3}}$ in a 8 nm thick film) at the interface between Cu and Py; and study [6] measures an interface anisotropy of 0.4 $\mathrm{mJm^{-2}}$ (equivalent to 0.05 $\mathrm{MJm^{-3}}$) at the interface between Pt and Py; no equivalent study was found for polycrystalline bilayer films with Ir and Py. Using these values of uniaxial anisotropy, micromagnetic simulations indicate that the width of a core in a simulation with 0.05 $\mathrm{MJm^{-3}}$ uniaxial perpendicular anisotropy, normalised to the width of a core in a simulation with 0.01 $\mathrm{MJm^{-3}}$ is only 1.02. Therefore, because this value is approximately one order of magnitude smaller than the detected broadening, we can be relatively certain that any surface anisotropy effects only contribute a small amount to the measured widths.

7.4 Discussion and Conclusion

This chapter presents two independent measurements of the strength of the DMI in bilayer and trilayer in-plane magnetised material systems by both 'dynamic' and 'static' means. In in-plane magnetised materials systems, micromagnetic simulations predict that DMI introduces a chiral swirling of the magnetisation local to the vortex core. This chiral swirl is best classified as divergence of magnetisation, added to the normally divergence-free vortex strucure, which varies linearly with $\mathbf{D}$ over the range $\pm$ 2.5 $\mathrm{mJm^{-2}}$. The end of section 7.2 proposes three methods of measuring this effect experimentally - two of which have been realised.

Experimentally, Py/Ir and Ir/Py/Pt material systems were studied along with Py/Cu as a zero DMI reference sample. For the Py/Ir sample we estimate $|\mathbf{D}|$ = 0.8 $\pm$ 0.3 $\mathrm{mJm^{-2}}$ from the vortex expulsion measurement and $|\mathbf{D}|$ = 0.9 $\pm$

0.6 $\mathrm{mJm^{-2}}$ from the DPC core width experiment. For the Ir/Py/Pt sample the same experiments estimate $|\mathbf{D}| = 0.9 \pm 0.1$ $\mathrm{mJm^{-2}}$ and $|\mathbf{D}| = 1.2 \pm 0.3$ $\mathrm{mJm^{-2}}$ respectively. These values were determined by comparison with simulation. Figures 7.5(e) and 7.8(b) contain graphs detailing the variation of the vortex core expulsion field and the vortex core width in DPC with $|\mathbf{D}|$ (normalised to the zero DMI case). The experimental measurements from the Py/Ir and Ir/Py/Pt samples, normalised to the measurement from the Py/Cu sample (assumed to have negligable DMI), were compared to the interpolated functions on the graphs in Figs. 7.5(e) and 7.8(b) to estimate the DMI value, and error on this value, for both material systems. Furthermore, the measured values from both methods are in agreement with each other and are similar to [6] which measures $\mathbf{D} = 1.2$ $\mathrm{mJm^{-2}}$ (using Brillouin light scattering to measure DMI induced non-reciprocal spin-wave propagation) in Py(4 nm)/Pt(6 nm) bilayer nanowires.

Section 7.2.3 highlighted the need for caution when interpreting the DPC core broadening experiment because interfaces with spin-orbit coupling are also associated with a surface induced perpendicular anisotropy that also broadens the vortex core profile. By comparing simulations to experimental values of the surface anisotropy, found in the literature from similar material systems, the effect of any anisotropy induced broadening was deemed unlikely to influence the outcome of the experiment.

Focused ion beam milling is a highly energetic process known to cause damage to the edge of FIB defined structures. This damage includes (for polycrystalline materials) grain growth and possible intermixing of the layers at the edges of structures, as well as irregularities in the defined shape. The simulations of the vortex expulsion field experiment simulate a 'perfect' disk free of these artefacts - therefore, the influence of these structural effects on the experimental measurement of the expulsion field cannot be ruled out. However, the disks on all three samples are prepared identically and are likely subject to the same damage hence, the relative lowering of the expulsion field of the Py/Ir and Ir/Py/Pt samples compared to the Cu/Py sample is thought to be meaningful and attributable to DMI.

Section 7.2.2 proposes that both the sign and strength of the DMI could be measured using MFM. To perform this experiment the samples were deposited on standard TEM grids, the geometry of which allows MFM on both surfaces. However, in experiment these substrates proved far too mobile for any scanning probe microscopy; it was impossible to track the surface well with the tip, leading to poor images and ripped samples. Therefore to perform this experiment another set of samples is required: the ideal set of samples would include pairs of samples with reverse layer geometry deposited on thicker substrates. Imaging the pairs of samples from the top would mimic imaging one sample from the top and bottom as proposed in section 7.2.2.

In conclusion, this chapter details methods of possibly measuring the Dzyaloshinskii-Moriya interaction in 'thicker' thin films with in-plane magnetisation. Simulations show that the vortex core structure is modified at low DMI strengths where a comparatively negligible modification is seen to the static domain wall structure - although a number of studies do detect DMI in the modification of the dynamic properties of domain walls such as spin-wave propagation [5–7]. In the present study, the interaction of DMI with the vortex core was measured through changes in the applied magnetic field required to expel a vortex from a disk and from a perceived broadening of DPC image contrast associated with the core. It was also identified that MFM could be another method of measuring DMI from a vortex core. This study was primarily curiosity-driven. However Chen *et al.* identified, through micromagnetic simulations, that the addition of DMI to Py nanodisks modifies the (spin-polarised current driven) precession of the vortex in ways that improve its functionality as a spin transfer nano-oscillator [8]. In nanodisks with DMI, the vortex precesses with a higher frequency and with narrower linewidth than without DMI. This therefore provides an additional motivating factor for the experimental quantification of the effect of DMI on the magnetic behaviour of Py disks.

Bibliography

[1] W. Jiang, P. Upadhyaya, W. Zhang, G. Yu, M. B. Jungfleisch, F. Y. Fradin, J. E. Pearson, Y. Tserkovnyak, K. L. Wang, O. Heinonen, S. G. Te Velthuis, and A. Hoffmann, "Blowing magnetic skyrmion bubbles," *Science*, vol. 349, no. 6245, pp. 283–286, 2015.

[2] G. Chen, A. Mascaraque, A. T. N'Diaye, and A. K. Schmid, "Room temperature skyrmion ground state stabilized through interlayer exchange coupling," *Applied Physics Letters*, vol. 106, no. 24, 2015.

[3] C. Moreau-Luchaire, C. Moutafis, N. Reyren, J. Sampaio, C. A. Vaz, N. Van Horne, K. Bouzehouane, K. Garcia, C. Deranlot, P. Warnicke, P. Wohlhüter, J. M. George, M. Weigand, J. Raabe, V. Cros, and A. Fert, "Additive interfacial chiral interaction in multilayers for stabilization of small individual skyrmions at room temperature," *Nature Nanotechnology*, vol. 11, no. 5, pp. 444–448, 2016.

[4] M. Y. Im, P. Fischer, K. Yamada, T. Sato, S. Kasai, Y. Nakatani, and T. Ono, "Symmetry breaking in the formation of magnetic vortex states in a permalloy nanodisk," *Nature Communications*, vol. 3, no. 1, pp. 983–986, 2012.

[5] J. H. Moon, S. M. Seo, K. J. Lee, K. W. Kim, J. Ryu, H. W. Lee, R. D. McMichael, and M. D. Stiles, "Spin-wave propagation in the presence of interfacial Dzyaloshinskii-Moriya interaction," *Physical Review B - Condensed Matter and Materials Physics*, vol. 88, no. 18, pp. 1–6, 2013.

[6] A. A. Stashkevich, M. Belmeguenai, Y. Roussigné, S. M. Cherif, M. Kostylev, M. Gabor, D. Lacour, C. Tiusan, and M. Hehn, "Experimental study of spin-wave dispersion in Py/Pt film structures in the presence of an interface Dzyaloshinskii-Moriya interaction," *Physical Review B - Condensed Matter and Materials Physics*, vol. 91, no. 21, pp. 1–9, 2015.

[7] J. Xia, X. Zhang, M. Yan, W. Zhao, and Y. Zhou, "Spin-Cherenkov effect in a magnetic nanostrip with interfacial Dzyaloshinskii-Moriya interaction," *Scientific Reports*, vol. 6, pp. 1–7, 2016.

[8] S. Chen, S. Zhang, Q. Zhu, X. Liu, C. Jin, J. Wang, and Q. Liu, "Effect of Dzyaloshinskii-Moriya interaction on the magnetic vortex oscillator driven by spin-polarized current," *Journal of Applied Physics*, vol. 117, no. 17, 2015.

[9] A. Fert and P. M. Levy, "Role of anisotropic exchange interactions in determining the properties of spin-glasses," *Physical Review Letters*, vol. 44, no. 23, pp. 1538–1541, 1980.

[10] X. Z. Yu, Y. Onose, N. Kanazawa, J. H. Park, J. H. Han, Y. Matsui, N. Nagaosa, and Y. Tokura, "Real-space observation of a two-dimensional skyrmion crystal," *Nature*, vol. 465, no. 7300, pp. 901–904, 2010.

[11] A. Tonomura, X. Yu, K. Yanagisawa, T. Matsuda, Y. Onose, N. Kanazawa, H. S. Park, and Y. Tokura, "Real-space observation of skyrmion lattice in helimagnet MnSi thin samples," *Nano Letters*, vol. 12, no. 3, pp. 1673–1677, 2012.

[12] M. Bode, M. Heide, K. Von Bergmann, P. Ferriani, S. Heinze, G. Bihlmayer, A. Kubetzka, O. Pietzsch, S. Blügel, and R. Wiesendanger, "Chiral magnetic order at surfaces driven by inversion asymmetry," *Nature*, vol. 447, no. 7141, pp. 190–193, 2007.

[13] P. Ferriani, K. Von Bergmann, E. Y. Vedmedenko, S. Heinze, M. Bode, M. Heide, G. Bihlmayer, S. Blügel, and R. Wiesendanger, "Atomic-scale Spin spiral with a unique rotational sense: Mn monolayer on W(001)," *Physical Review Letters*, vol. 101, no. 2, pp. 1–4, 2008.

[14] J. O. Rantschler, P. J. Chen, A. S. Arrott, R. D. McMichael, W. F. Egelhoff, and B. B. Maranville, "Surface anisotropy of permalloy in NM/NiFe/NM multilayers," *Journal of Applied Physics*, vol. 97, no. 10, pp. 1–4, 2005.

[15] A. Vansteenkiste, J. Leliaert, M. Dvornik, M. Helsen, F. Garcia-Sanchez, and B. Van Waeyenberge, "The design and verification of MuMax3," *AIP Advances*, vol. 4, no. 10, 2014.

[16] G. S. Abo, Y. K. Hong, J. Park, J. Lee, W. Lee, and B. C. Choi, "Definition of magnetic exchange length," *IEEE Transactions on Magnetics*, vol. 49, no. 8, pp. 4937–4939, 2013.

[17] A. Hubert, W. Rave, and S. Tomlinson, "Imaging magnetic charges with magnetic force microscopy," *physica status solidi (b)*, vol. 204, pp. 817–828, 1997.

[18] S. McVitie, D. McGrouther, S. McFadzean, D. A. MacLaren, K. J. O'Shea, and M. J. Benitez, "Aberration corrected Lorentz scanning transmission electron microscopy," *Ultramicroscopy*, vol. 152, pp. 57–62, 2015.

[19] H. Yang, A. Thiaville, S. Rohart, A. Fert, and M. Chshiev, "Anatomy of Dzyaloshinskii-Moriya Interaction at Co/Pt Interfaces," *Physical Review Letters*, vol. 115, no. 26, p. 267210, 2015.

[20] A. Hrabec, N. A. Porter, A. Wells, M. J. Benitez, G. Burnell, S. McVitie, D. McGrouther, T. A. Moore, and C. H. Marrows, "Measuring and tailoring the Dzyaloshinskii-Moriya interaction in perpendicularly magnetized thin films," *Physical Review B - Condensed Matter and Materials Physics*, vol. 90, no. 2, 2014.

[21] B. Dupé, M. Hoffmann, C. Paillard, and S. Heinze, "Tailoring magnetic skyrmions in ultra-thin transition metal films," *Nature Communications*, vol. 5, no. May, pp. 1–6, 2014.

[22] M. Krajnak, D. McGrouther, D. Maneuski, V. O'Shea, and S. McVitie, "Pixelated detectors and improved efficiency for magnetic imaging in STEM differential phase contrast," *Ultramicroscopy*, vol. 165, pp. 42–50, 2016.

8
Summary and outlook

In this thesis, a number of studies relating to the effects of an interface-driven Dzyaloshinskii-Moriya interaction on the magnetisation of thin films were presented, with a special focus on Lorentz microscopy. This chapter summarises the main outcomes of these pieces of research and suggests relevant future research avenues.

Chapter 4, using models, discussed the interpretation of Fresnel images to extract information on the magnetisation of the domain wall and then proposed a method of determining the direction of the Néel wall magnetisation in Lorentz TEM. Image calculations were presented that show, under certain imaging conditions, the Néel wall magnetisation causes a signature asymmetry to the otherwise symmetric Fresnel image contrast. Experimentally this was tested on PMA samples consisting of ultrathin Co layer(s) sandwiched between Ir and Pt. Such samples support homochiral domain walls, stabilised by an interfacial DMI, and therefore provide the ideal magnetic configuration to test the proposed method. However the experimental results were inconclusive, likely due to non-magnetic contrast contributions.

To increase the stability of skyrmions against thermal fluctuations, multilayers of many repetitions (up to ≈ 20) are often designed and fabricated. Recent studies indicated that the inclusion of so many repeats, while increasing skyrmion stability, can promote a dipolar-driven reorientation of the domain wall structure: rather than being homochiral Néel type, the wall is composed of opposite handedness of

Néel type walls either side of a Bloch type central region thus leading to a flux-closure structure through the thickness of the multilayer. As Lorentz microscopy is a transmission technique it is ideally suited to study the internal domain wall structure. Using the framework outlined in Chapter 4, Chapter 5 uses Fresnel images to identify walls with 'hybrid' chirality. Then DPC images were used to quantify hybrid walls by determining what proportion of the wall structure is Bloch type in the systems studied: the 15 repeat sample a total 2.7 layers had Bloch type structure; the a 10 repeat sample a total 1.6 layers had Bloch type structure; and in the five repeat sample there was no experimental evidence of a hybrid chirality. For ease of image interpretation the hybrid structure was studied in domain wall configurations, but the structure of skyrmions will be similarly impacted. Nevertheless, it would be interesting to study the hybrid skyrmion structure with high resolution and quantitative DPC images, as such studies have not been reported. A hybrid structure impacts the spin-polarised current induced motion of skyrmions: it affects both the velocity and the skyrmion Hall angle [1, 2]. Therefore, the quantification of the wall structure enabled by Lorentz microscopy and presented in Chapter 5 provides key information required for the design of spintronic devices that harness the full potential of skyrmions as information carriers.

The use of skyrmions as 'bits' in spintronic devices also requires a reliable nucleation method. To this end, Chapter 6 investigated the use of nanoscale artificial defects, fabricated with FIB irradiation, as skyrmion nucleation points. The chapter studied the field-induced nucleation of skyrmions both before and after defect creation on four different samples . A detailed study was performed on one of these samples to probe the structural impact of the defects on the multilayer structure and correlate this with their magnetic behaviour. The results of Chapter 6 show that the effectiveness of this nucleation method is highly dependent on the multilayer system, this is however expected as different systems have different sensitivity to ion irradiation. For all samples the point-like defects caused localised early reversal of the magnetisation. On two samples, unstable skyrmions are

nucleated that almost immediately deform into elongated worm-like domains, this behaviour is inherent to these samples and was also observed prior to defect creation. Therefore, for these two samples this nucleation method was deemed unsuccessful in terms of compact skyrmion nucleation. For the remaining two samples the nucleation method was successful. In one of these samples, upon reversal from positive to negative saturation, skyrmions were observed prior to defect formation in fields between -50 to -80 mT. At artificial defects, made with ion dose 5×10^{16} ions/cm^2, skyrmions nucleate and remain stable in a lower field range of +10 to -5 mT, notably including zero applied field. The skyrmion size in the -50 to -80 mT range was about 160 nm and in the lower field, the defect stabilised regime, the skyrmion size is about 180 nm and therefore appears unaffected by the defects themselves. The structural study was also performed on this sample. Plan-view images identified a minimal increase to the grain size compared to the grain size distribution that is representative of this sample prior to defect formation. Cross-sectional images show that the successful defects are associated with partial intermixing of the layers. In the other sample only homochiral Néel walls were observed prior to defect creation, and interestingly skyrmions were nucleated and stabilised at the artificial defects, ion dose 5×10^{15} ions/cm^2, and remain stable over a field range of 10 mT.

The work in Chapter 6 is somewhat preliminary and there are many possible avenues of future work. Firstly, it would be interesting to quantify the depinning current required to move the skyrmions from the defect sites, and also to study their stability when moved away from the defect (particularly in a sample that did not previously support skyrmions on field-cycling alone). Secondly, the mechanism of this skyrmion nucleation method is unknown. This could possibly be determined using carefully designed micromagnetic simulations that use information determined from transport of ions in matter (TRIM) simulations [3, 4], correlated with magnetometry measurements taken from irradiated samples. Furthermore, to produce the smallest (most technologically relevant) skyrmions in interfacial DMI systems, research focus is beginning to shift towards synthetic antiferromagnetic

(SAF) systems [5]. In ferromagnetically coupled systems, the dipolar interactions fundamentally limit the skyrmion size to $\approx$ 100 nm. In SAF systems the dipolar interactions are reduced to essentially zero, therefore permitting smaller skyrmions. It would be interesting to study this nucleation method in such a system, though it is quite possible that the ion irradiation will destroy the RKKY coupling that stabilises the antiferromagnetic textures.

Chapter 7 presented a different flavour of study on interfacial DMI. Here the influence of DMI on the vortex structure stabilised in 8 nm thick Py disks was studied through micromagnetic simulations and Lorentz TEM measurements. Simulations indicated that DMI caused a chiral twisting of the magnetisation about the vortex core. Furthermore, it was predicted that two measurable consequences of this chiral twist are (*i*) to decrease the strength of external field required to push a vortex core out of the disk, and (*ii*) to effectively broaden the measured signal variation associated with the vortex core in DPC images. Both of these effects were detected experimentally and, with comparison to simulation, are consistent with a DMI strength in the system of about 1 mJm^{-2}.

On a more general note, despite the recent advances in DPC imaging enabled by pixelated detectors [6], the residual contrast from crystallites still prevents application of quantitative DPC imaging to some of the multilayered samples studied in this thesis (Chapters 4 and 5). Therefore it is proposed that the influence of the crystallite contrast could still be reduced. To this end it is suggested that precession electron diffraction (PED) systems could be utilised to reduce this contrast [7, 8]. In PED systems the beam is scanned over the sample and, at each scan position, is precessed around the optic axis (precession angle is tens of mrad maximum). This leads to slightly different diffraction conditions being met as the beam precesses. The Lorentz deflection will also vary, but only slightly (by $\approx 0.01 B_s t$ μrad with a 20 mrad precession angle), but this variation should be periodic and could be taken into account in post-processing. Thus, in principle, the central undiffracted spot should become more like a top-hat function as crystallite contrast is averaged out. Consequently, the balance of the crystallite contrast to magnetic contrast (that

at present limits the quality of DPC images of polycrystalline materials) could be further shifted towards magnetic contrast.

Bibliography

[1] W. Legrand, J. Y. Chauleau, D. Maccariello, N. Reyren, S. Collin, K. Bouzehouane, N. Jaouen, V. Cros, and A. Fert, "Hybrid chiral domain walls and skyrmions in magnetic multilayers," *Science Advances*, vol. 4, no. 7, 2018.

[2] I. Lemesh and G. S. Beach, "Twisted domain walls and skyrmions in perpendicularly magnetized multilayers," *Physical Review B*, vol. 98, no. 10, pp. 1–8, 2018.

[3] J. Biersack and L. Haggmark, "A Monte Carlo computer program for the transport of energetic ions in amorphous targets," *Nuclear Instruments and Methods*, vol. 174, pp. 257–269, 1980.

[4] W. Möller and W. Eckstein, "Tridyn A TRIM simulation code including dynamic composition changes," *Nuclear Instruments and Methods in Physics Research Section B: Beam Interactions with Materials and Atoms*, vol. 2, pp. 814–818, 1984.

[5] W. Legrand, D. Maccariello, F. Ajejas, S. Collin, A. Vecchiola, K. Bouzehouane, N. Reyren, V. Cros, and A. Fert, "Room-temperature stabilization of antiferromagnetic skyrmions in synthetic antiferromagnets," *Nature Materials*, pp. 1–23, 2019.

[6] M. Krajnak, D. McGrouther, D. Maneuski, V. O. Shea, and S. McVitie, "Pixelated detectors and improved efficiency for magnetic imaging in STEM differential phase contrast," *Ultramicroscopy*, vol. 165, pp. 42–50, 2016.

[7] E. F. Rauch, J. Portillo, S. Nicolopoulos, D. Bultreys, S. Rouvimov, and P. Moeck, "Automated nanocrystal orientation and phase mapping in the transmission electron microscope on the basis of precession electron diffraction," *Zeitschrift für Kristallographie*, vol. 225, pp. 103–109, 2010.

[8] G. Brunetti, D. Robert, P. Bayle-Guillemaud, J. L. Rouvière, E. F. Rauch, J. F. Martin, J. F. Colin, F. Bertin, and C. Cayron, "Confirmation of the Domino-Cascade Model by LiFePO/FePO4 Precession Electron Diffraction," *Chemistry of Materials*, vol. 23, pp. 4515–4524, 2011.

Appendices

A

Wall width measurement from Fresnel images

This appendix pertains to the content of Chapter 4.

The wall width is ideally measured from DPC images. However, because this sample is associated with only a small Lorentz deflection (0.6 nm of Co magnetised out of plane gives rise to a deflection of ≈ 0.1 μrad at 25° tilt) no magnetic contrast was detected in DPC mode, which is more sensitive to the effects of crystallites than Fresnel mode. Fresnel imaging is a defocused imaging technique therefore the width of the intensity associated with a wall is wider than the wall itself. A simple relationship exists [1] for divergent (dark) wall contrast where the measured signal width, W, is linearly related to the true wall width δ through the defocus Δ:

$$W = m\Delta + \delta. \tag{A.1}$$

Therefore, the wall width δ is the intercept of a graph of the width W plotted against the defocus Δ. Figure. A.1(a) shows the graph produced from data relating to the Ta(4.6)/Pt(7.5)/Co(0.6)/Ir(0.5)/Pt(7.5) sample. The defocus values are recorded as the objective mini-lens DAC values subtracted from the value at focus. This gives a more direct measure of the defocus than the method outlined in section

3.7.3 (which gives the defocus in distance) and is therefore more accurate for this calculation. As defined in the literature [1], W is measured as the width of the wall contrast at the intensity value midway between the background intensity and the intensity at the centre of the wall, an example is shown in the inset in Fig. A.1(b). The wall width δ was measured as 50 ± 20 nm. The large error bound arises from significant uncertainty in the measurement of W; as seen from Fig. A.1(b) there is strong background fluctuations arising from the crystallites. Furthermore, the original demonstration of this method used a maximal defocus value of 4 mm [1] but, here, because of the small deflection, the defocus is an order of magnitude larger. Simulations indicate that for the range defocus used in this experiment, this method of measurement overestimates the width (by ≈10 nm for a 50 nm wide wall). While being far from ideal this measurement does provide a useful order of magnitude estimate of the wall width in the sample.

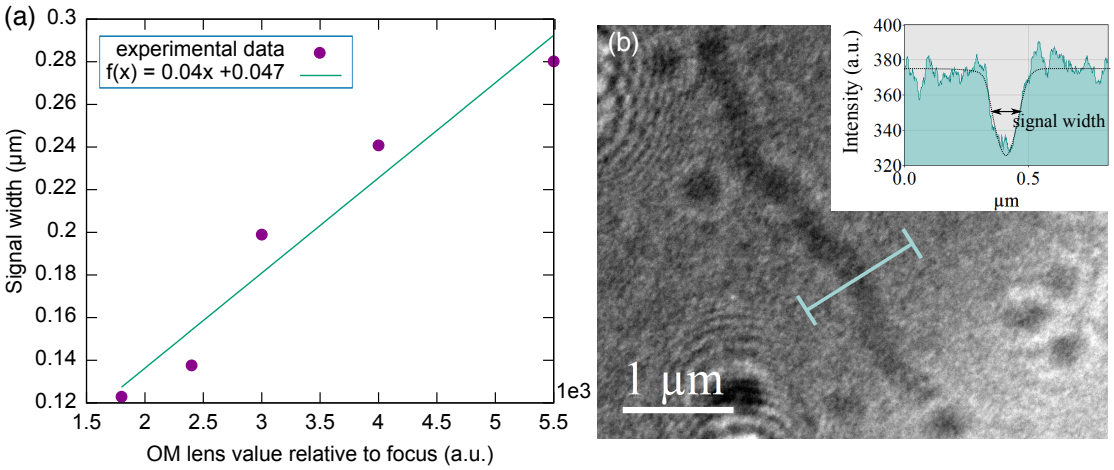

Figure A.1: (a) Graph of the signal width W measured from divergent domain wall contrast as a function of the imaging lens defocus. (b) Fresnel image of the domain wall from which the measurements in (a) were taken from. The inset in (b) shows an intensity line trace (taken through the region marked by the light blue line and averaged over 30 pixels) which is annotated with the signal width measurement W.

Bibliography

[1] H. Gong and J. Chapman, "On the use of divergent wall images in the Fresnel mode of Lorentz microscopy for the measurement of the widths of very narrow domain walls," *Journal of Magnetism and Magnetic Materials*, vol. 67, pp. 4–8, 1987.

B

Calculated Fresnel images representative of experiment

This appendix pertains to the content of Chapter 4.

Fresnel images were calculated from modelled Néel walls of width 30, 50 and 70 nm and with a defocus of 10, 20 and 30 mm to explore the contrast asymmetry for parameters close to the experimental values. In all cases the images were calculated with a tilt of 25° about a $\phi = 45°$ axis. Figure B.1 compares the Fresnel contrast calculated from different wall widths δ with a fixed defocus Δ of 20 mm. Figure B.2 compares the Fresnel contrast calculated from a 50 nm wide wall with different defocus values. On each line trace in Figs.B.1 and B.2, a dashed line is drawn to highlight the asymmetry of the contrast.

Figure B.1 shows almost no asymmetry for the narrowest walls, and a slight asymmetry for the 50 and 70 nm wide walls for a defocus of 20 mm. Figure B.1 which compares the effect of the defocus on a 50 nm wide wall shows a considerably larger asymmetry for the smallest defocus value. These images are not intended to represent experiment fully, for example the beam coherence is not controlled for and the crystallite contrast is not included. They are simply intended to demonstrate how sensitive magnitude of the asymmetry is to two critical parameters: wall width

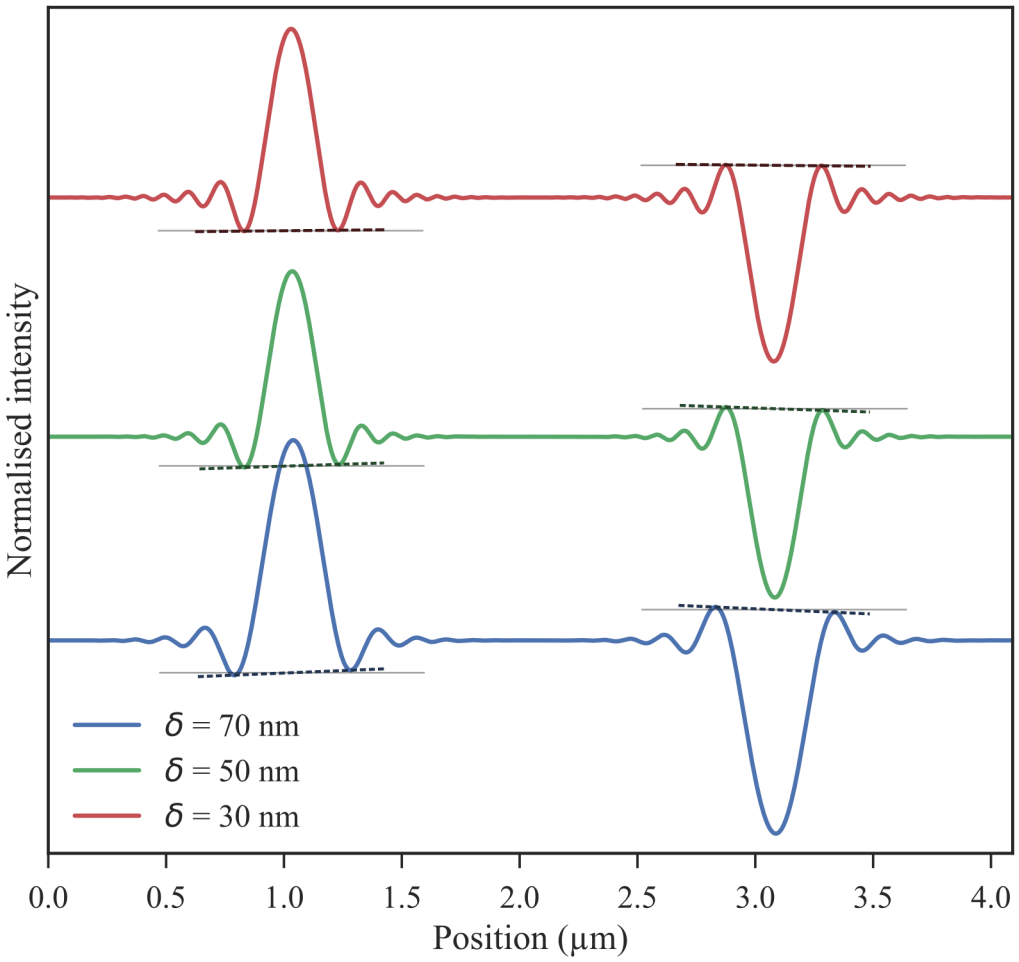

Figure B.1: Fresnel image contrast (normalised to the background contrast level) calculated from an analytical model of a Néel wall at a defocus of 20 mm for wall width of $\delta = 30, 50, 70$ nm. The widest wall shows the largest asymmetry for this defocus value.

and defocus. Therefore for each sample, with a different wall width, a wide range of defocus values must be trialled.

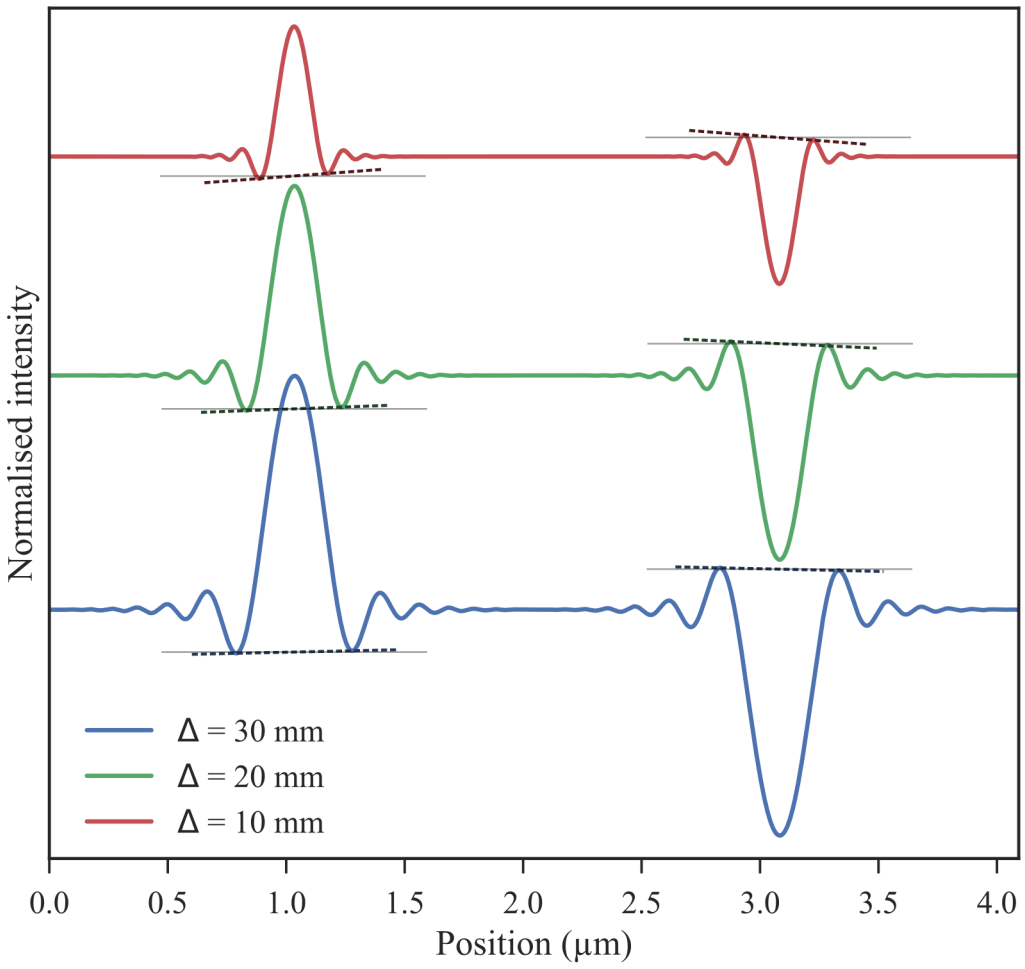

Figure B.2: Fresnel image contrast (normalised to the background contrast level) calculated from an analytical model of a Néel wall with a wall width of $\delta = 30$ nm and a defocus of $\Delta = 10, 20, 30$ mm. The smallest defocus values shows the largest asymmetry for this wall width.